Simulating the Performance
of a Heat Exchanger During Frosting

Y. Wu, P. Verma, C. W. Bullard, and P. S. Hrnjak

Abstract

Factors affecting frost distribution are explored using a finite element model, developed and validated using a full-scale 8-row heat exchanger in a wind tunnel. The heat exchanger is typical of the type used in supermarket display cases; so face velocities and air inlet temperatures were varied from 0.5-2.3 m/s and 0 to -20 °C, respectively, and inlet humidities from 70-90%. In order to focus on frost distribution, the prototype was designed to have a simple geometry and single-phase refrigerant to provide maximum certainty on parameters not directly related to frost. Measured and predicted total and sensible heat transfer agreed within RMS 6% and 8%, respectively, over the range of operating conditions. For latent heat, there was more scatter due to frost non-uniformities induced by the experimental apparatus. The simulation model was used to illustrate how the point of maximum frost thickness moved from the front to the rear of the heat exchanger, depending on face velocity, inlet humidity and fin surface temperature. Heat transfer and pressure drop were calculated from standard correlations, with fin thickness and tube diameter increasing as a function of frost thickness. The model was further extended to simulate the performance of the heat exchanger under the effect of a fan curve. A comparison is made between DX and indirect refrigeration system performance with respect to capacity, pressure drop and air flow variations under frosting conditions.

Table of Contents

List of Figures

List of Tables

Nomenclature

A_{fin}	fin surface area , m^2
A_{free}	free flow area, m^2
$A_{frontal}$	frontal area, m^2
A_o	total heat transfer area, m^2
A_{ref}	refrigerant side area, m^2
A_t	tube outer surface area, m^2
b_w	constant used in calculating effective heat transfer coefficient
c_p	specific heat, $kJ/kg \cdot K$
D_{ab}	binary diffusion coefficient for water in air, m^2/s
D_c	tube outer diameter, m
D_{eff}	effective diameter, m
dP_{duct}	pressure drop across the duct, Pa
dP_{evap}	airside pressure drop across the evaporator, $in.H_2O$
dP_{fan}	fan pressure drop, $in.H_2O$
d_i	tube inner diameter, m
F_s	fin spacing, m
F_{th}	fin thickness, m
f	friction factor
G_{max}	maximum air velocity (based on minimum flow area), $kg/m^2 s$
H	height of heat exchangers, m
h_a	airside heat transfer coefficient, $kW/m^2 \cdot K$
h_D	mass transfer coefficient, $kg/m^2 \cdot s$
h_{eff}	effective heat transfer coefficient, $kW/m^2 \cdot K$
h_{ref}	refrigerant heat transfer coefficient, $kW/m^2 \cdot K$
h_{sg}	Enthalpy of sublimation of water, kJ/kg
j	Colburn j factor
k_{fin}	thermal conductivity of fins, $kW/m \cdot K$
k_{tube}	thermal conductivity of tubes, $kW/m \cdot K$
k_{fr}	thermal conductivity of frost, $kW/m \cdot K$
K_c	entrance loss coefficient
K_e	exit loss coefficient
L	depth of the evaporator, m
L	parameter in Sector Method, m
$Le = \dfrac{a}{D_{ab}}$	Lewis number

M	parameter in Sector Method, m
m	fin parameter
$\dot{m}$	mass flow rate, kg/s
$\dot{m}_{fr}$	frosting rate, kg/s
N_{tube}	number of tubes
N_{fin}	number of fins
NT	number of tubes perpendicular to air flow direction
NP	number of tubes on air flow direction
Nu	Nusselt number
P_l	horizontal tube spacing, m
P_t	vertical tube spacing, m
P_{wa}	water partial pressure in ambient conditions, Pa
P_{ws}	saturation pressure of water at surface temperature, Pa
Q	total load, kW
Q_{latent}	latent load, kW
Q_{sens}	sensible load, kW
Q_{min}	minimum capacity required, kW
Re	Reynolds number
r_i	inner radius in Sector Method, m
r_{oo}	outer radius in Sector Method, m
R_n	radius ratio in Sector Method
S_n	surface area of each sector in Sector Method, m^2
T_{ain}	air inlet temperature, ^oC
T_{am}	average air temperature, ^oC
T_{aout}	air outlet temperature, ^oC
T_{so}	outer frost surface temperature, ^oC
T_{si}	base temperature of fin, ^oC
T_{rin}	refrigerant inlet temperature, ^oC
T_{rout}	refrigerant outlet temperature, ^oC
T_{ref}	average refrigerant temperature, ^oC
U	heat transfer coefficient, $kW/m^2 \cdot K$
$\dot{V}$	volumetric flow rate, CFM
v_1	specific volume of inlet air, m^3/kg
v_2	specific volume of outlet air, m^3/kg
v_m	mean specific volume, m^3/kg
vel	velocity, m/s
W	width of heat exchanger, m
W_{blower}	power blower, kW

w_i	air inlet absolute humidity, kg/kg
w_o	air outlet absolute humidity, kg/kg
w_a	average air humidity, kg/kg
w_s	saturated air humidity at surface, kg/kg

Greek Symbols

a	thermal diffusivity, m^2/s
d_{fr}	frost thickness, m
r_{fr}	frost density, kg/m^3
r_a	density of air, kg/m^3
$r_{v,\infty}$	partial density in freestream, kg/m^3
$r_{v,s}$	partial density on surface, kg/m^3
s	ratio of free flow area to frontal area, dimensionless
b	constant parameter used in calculating frost thickness
h_f	fin efficiency
h_{suf}	fin surface efficiency
m	viscosity, $kg/s \cdot m$
ΔT_w	temperature change across the frost layer, ^oC
ΔT_∞	temperature change from freestream to frost surface , ^oC
Δr_v	partial density change, kg/m^3

Subscripts:

a, air	air
amb	ambient
avg	average
Dc	based on tube outer diameter
eff	effective
fin	fin
fr	frost
i	inner
min	minimum
max	maximum
o	outer
ref	refrigerant
tube	tube
s	surface

Chapter 1: Introduction

1.1 Introduction

When moist air passes over cold heat exchanger surfaces with surface temperatures below dew point, the moisture in the air begins to condense. Also, if the surface temperature is below freezing, frost starts to form.

Frost growth on heat exchangers is a common problem with refrigeration and air-conditioning equipment. It causes the performance of heat exchanger to decline, firstly as frost accumulation blocks the airflow path causing an increase in the airside pressure drop and a consequent decrease in the airflow rate. Secondly, the capacity of heat exchangers is also detrimentally affected by the insulating effect of frost. Eventually, the heat exchangers need be defrosted to maintain adequate performance. However, the defrosting process itself causes an additional penalty of energy consumption.

1.2 Objective

The purpose of this report is to study, experimentally and analytically, the frost deposition patterns on the heat exchangers and to develop models to simulate different frost deposition patterns in order to find better ways to obtain a more uniform frost distribution. Uneven frost distribution along the airflow direction blocks the air free flow area quickly and leads to tremendous decrease in the capacity of the heat exchanger. It occurs even though little or no frost grows on the other parts of the heat exchanger. This report focuses on understanding what factors affect the frost deposition pattern, in order to help find ways to control the frost distribution and increase heat exchanger efficiency. The simulation model presented in this report helps us achieve this goal.

1.3 Literature review

This literature review includes three classes of frost research: studies on frost properties such as frost density and thermal conductivity; studies on frost formation on simple geometries (flat plates or tubes) and heat exchangers; and studies on models to simulate the frost growth or the performance of heat exchangers under frosted conditions.

1.3.1 A review of studies on frost properties

Substantial literature is available on frost properties such as frost formation stages, density and thermal conductivity.

O'Neal and Tree (1985) have provided a comprehensive review of frost research in simple geometries (flat plate, cylinders, tubes, parallel plates and annuli) for the 50 years before 1984.

Hoke et al. (2000) studied the microscopic frost deposition on a variety of substrates. He provided a comprehensive review of the research results of frost formation, experimental and numerical frost growth studies. He concluded that there are usually two different frost growth scenarios: condensation frosting and ablimation frosting. The former one is generally the scenario encountered on a refrigeration evaporator. There are three regimes in condensation frosting—condensation period, early frost growth period (almost constant frost thickness growth rate) and mature growth period (increase in frost thickness is proportional to the square root of time).

There exist some attempts to model the early crystal growth period, for example Tao et al. (1993), but it is believed that modeling the early crystal growth is not necessary for the present problem of frost growth over many hours especially on full-scale heat exchanger. So, only mature growth period is considered in this study.

<u>1.3.2 A review of studies on frost formation</u>

There are several correlations in the literature to predict frost thickness, density and conductivity as a function of environmental parameters.

Mao et al. (1999) correlated the thickness, density and conductivity as a function of environmental parameters, location on a flat plate, and Reynolds number, for conditions similar to those found in a freezer with the cold plate temperature from –20 °C to –41 °C and the supply air temperature range from –10 °C to –26 °C. The frost surface was characterized as being either smooth or rough and correlations predicting frost properties for both types of frost were presented.

Storey and Jacobi (1999) developed another model for frost thickness. This model was based on frost surface heat flux and mass continuity. It was found that the non-dimensional frost thickness was proportional to the square root of the environmental time, t. This behavior has been observed in mature frost growth by many investigators, such as Ostin and Andersson (1991).

Storey and Jacobi (1999) evaluated their model using data and assuming frost surface temperature equal to the freezing point. The experimental data were consistent with the equation. This model captures the essential physics of mature frost growth and is a useful tool for data interpretation. However their model is valid only when the frost surface temperature is close enough to freezing point.

Kondepudi and O'Neal (1987) provided a comprehensive review of the literature available during the 30 years before 1987 on the effects of frost growth on extended surface heat exchanger performance. They concluded that:

- Frost growth is detrimental to the heat exchanger performance.
- Fin efficiency increases initially with frost growth and then tends toward a constant value.
- The overall heat transfer coefficient first increases as a result of increased surface areas and surface roughness but soon decreases due to the thermal resistance of frost layer when the air flow rate was maintained constant.
- Surface roughness is helpful to coil performance only in the early stage of frost growth.

After that, several experimental studies have been done to investigate heat exchanger performance under frosting conditions.

Kondepudi and O'Neal (1989) investigated the frost growth effects on the performance of heat exchangers with flat and louvered fins. It was found that a constant mass flow rate of air, high inlet humidity, low refrigeration temperature and high fin density leads to increased frost accumulation, large pressure drop and high energy transfer.

Ostin and Andersson (1991) studied the formation of frost in an experimental apparatus simulating the conditions in a counter flow heat exchanger. The air temperature in their experiments was about 20 °C and relative humidity from 30% to 75%. The cold plate temperature varied from –20 °C to –7 °C.

Two categories of frost formation—monotonic growth and cyclic growth—were observed. Frost thickness increased monotonically with time in the monotonic growth. In the cyclic growth, frost stopped growing after a couple of hours and the thickness stayed almost constant for about one and a half hours, then frost resumed to grow with time. The cyclic growth was observed under conditions that the air humidity ≥ 50% and the surface temperature

≤ -10 °C. They concluded that melting at the frost surface was the reason for the cyclic increase of the thickness and the abrupt increase of density.

Frost mass was found to increase linearly with time under their test conditions. For the monotonic growth, frost thickness increased with the square root of time as shown in Eqn. (1.6) according to:

$$\boldsymbol{d} = a_o + a_1\sqrt{t} \qquad\qquad (1.1)$$

Where t is the time from onset of frosting [s]. They did not find universal values of a_0 and a_1.

Frost density was found to increase fast initially and then tends to a constant value. The relationship of frost conductivity and density was obtained from the test but the conductivity is lower than the results of other investigators, such as Yonko and Sepsy (1967).

It was also found that the condensed water vapor from the air stream contributes in equal amounts to increases in the frost thickness and density. This conclusion agrees with the findings of White and Cremers (1974), Fukada and Inoue (1999): approximately half the mass increases the density and the other half contributes directly to increasing the frost thickness. The effect of air velocity on the frost thickness was found to be negligible, which is in agreement with previous research results.

Ogawa, Tanaka, and Takeshita (1993) studied ways to improve the performance of plate-fin-tube heat exchangers, which were typically used for refrigerators and heat pump air conditioners, under frosted conditions. They realized that the blockage problem of airflow at the leading edge caused by the frost growth was a big concern in heat exchanger design. Several methods—fin staging, fin width extension and partial cutting of fins—were studied to decrease the frost formation at the leading edge to improve the performance of heat exchangers. A series of experiments were conducted to observe frost formation, changes in heat transfer coefficient and airside pressure drop etc. using different methods. It was found that front staging, side staging and fin width extension were all effective to reduce the blockage effect at the leading edge and reduce airside pressure drop, thus improve the performance of the heat exchangers.

Although these studies provide a clearer picture of the effect of frost formation on the performance of heat exchangers, they were not concerned with developing comprehensive models to simulate the frost growth. Rather, they were aimed at measuring the performance of typical heat exchangers when frost growth occurred.

1.3.3 A review of studies on model development

Numerous models have been developed trying to predict frost growth in simple geometries (such as a single fin, flat plate etc.) as well as heat exchangers.

Tao et al. (1993) developed a mathematical model to predict frost deposition on a cold surface, which is exposed to warm moist airflow at about 20 °C. They used a one-dimensional, transient formulation based on the local volume averaging technique. Frosting rate, the time variation of frost thickness, frost density, and both spatial and temporal variations of temperature were predicted. The frost growth was divided into two phases. In the early growth phase, the frost was modeled as ice columns. In the mature growth phrase, the frost was modeled as a homogeneous porous medium with a distributed porosity and expanding boundary. They assumed diffusion to be the only mechanism for internal water transport. The Yonko and Sepsy (1967) correlation for frost conductivity was

employed. The initial conditions for the mature frost growth phrase were taken from the solutions of the early crystal growth model. From this model, the frost density distribution in the full-growth period depends on the distribution during the early growth period. It was found that the maximum densification rate occurred near the warm side of the frost layer. The heat flux was found to increase initially but then decrease monotonically in the full growth period.

Padki et al. (1989) proposed a simple method of computing both the spatial and temporal variations of heat transfer, frost growth rate, frost thickness and surface temperature for a horizontal flat plate and a horizontal cylinder in both free and forced convection. An iterative quasi-steady-state approach was employed. It was assumed that steady-state conditions exist for sufficiently small time intervals, but the overall analysis was transient. The surface temperature, frost thickness, density and conductivity, were computed. A correlation between frost density and the surface temperature provided by Hayashi et al. (1977) and two correlations between frost density and conductivity from Sanders (1974) and Marinyuk (1980) were used. Model results were compared with existing experimental data in the literature and good agreement was obtained.

Oskarsson et al. (1990) developed three models—finite element model, three-region model, and a parametric model— for plate-finned-tube evaporators used in heat pump systems. The models predict evaporator performance under dry, wet and frosted conditions. It was assumed that a quasi-steady state at one time step could be used for analysis at the next time step. Some assumptions made in these models were:

- Airside heat transfer coefficients on the wet and frosted coils are the same as that on the dry coil surface.
- Possible increase in fin efficiency on frosted coils is assumed to be negligible.

Model results were compared with experimental results for two evaporators in heat transfer rates, dehumidification rate, etc. However, the frost thickness was not compared.

Chen et al. (2000) developed a numerical model to simulate frost growth on plate-fin heat exchangers for typical freezer conditions with air supply temperature from −10 °C to −21 °C, constant relative humidity at 92% and base plate temperature from −31 °C to −38 °C. The frost layer was treated as a one-dimensional transient porous medium, including a two-dimensional transient heat conduction model for in the fins. Frost properties are different over the fin surfaces. Most of the simulation results for heat transfer rate, frost thickness and density are within the experimental uncertainty of the measured data. However, the model cannot predict the pressure drop accurately when the frost blockage effects are large. It was also found that the selection of correlations for the calculation of effective thermal conductivity of frost is important to predict the frost thickness and density accurately.

Chapter 2: Numerical Model

2.1 Numerical model

An EES model has been developed to study the frost deposition patterns for a refrigerated display case heat exchanger under different running conditions.

The heat exchanger is a plain-fin-tube evaporator with aluminum fins and copper tubes, about 0.80 m wide, 0.343 m high, and 0.264 m deep. It has eight tube rows along the airflow direction and nine cross counter flow refrigerant circuits perpendicular to the airflow direction as shown in Figures 2.1 and 2.2. Each circuit starts at the air exit side of the heat exchanger and exits after eight passes at the front of the heat exchanger. Each of the nine circuits is confined to a single row in the horizontal plane (Carlson, 2001).

For the experiments conducted to validate the model, a single-phase refrigerant is used to permit real-time monitoring of heat exchanger mass (including frost). Hydroflouroether (HFE) 7100 was selected to ensure that flow was turbulent so the refrigerant-side heat transfer could be accurately characterized.
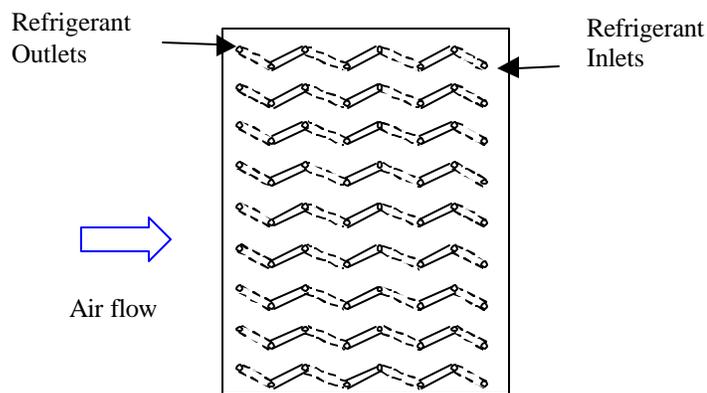
Figure 2.1 Side view of the heat exchanger

In order to simulate the frost deposition patterns, the heat exchanger is divided into eight finite elements, shown with dotted lines in Figure 2.2, along the air flow direction in the model. Total load, sensible load, latent load, air side temperature gradient and humidity gradient, refrigerant side temperature gradient as well as air side pressure drops are calculated in each row for a given time interval. So are the frost mass, thickness, density and conductivity.
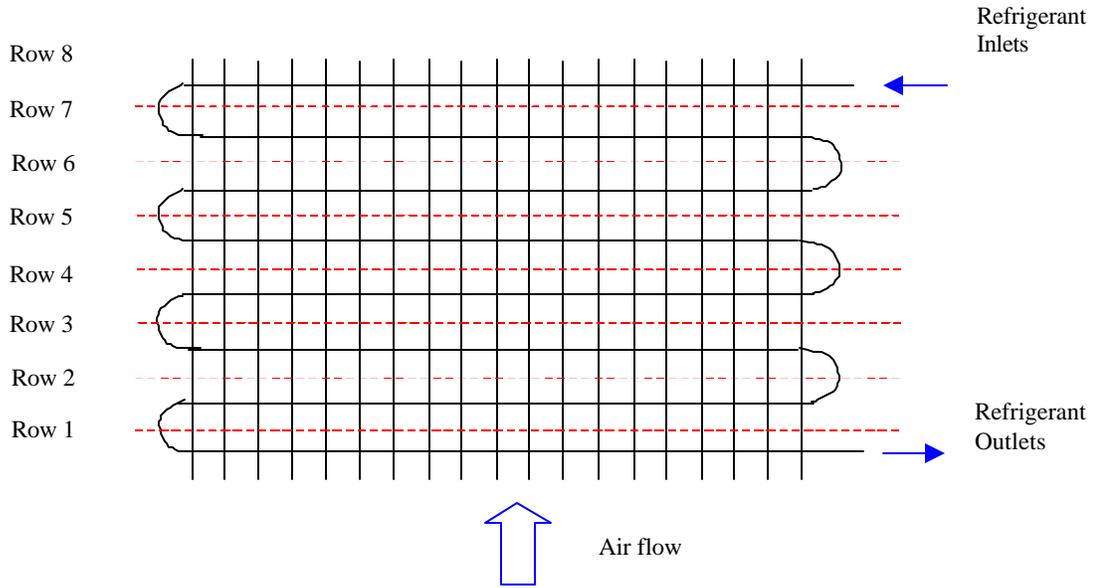
Figure 2.2 Top view of the heat exchanger

The model assumes that (1) the effect of refrigerant-side pressure drop on heat exchanger performance is negligible; (2) frost is evenly distributed on the surface of the tubes and fins in each row; (3) the transient frosted heat exchanger performance is analyzed assuming a quasi-steady state where calculations at one time step can be used for analysis at the next time step.

2.2 Fin surface efficiency

The fin surface efficiency is calculated using the sector method (Pira, Bullard and Jacobi, 2000), as described in Appendix A. Since the literature available on the fin efficiency of the frosted heat exchangers offers very limited information, the fin is analyzed for the heat flow due to conduction through the frost layer owing to temperature gradient across the frost layer, plus the heat flow along the fin from tip to the base. More details of the fin surface efficiency analysis can be found in Appendix A.

2.3 Air side heat transfer coefficient

Three air side heat transfer correlations for plain-fin heat exchangers namely, Wang and Chang (1998), Wang, Chang, Hsieh, and Lin (1996), and Kim, Youn and Webb (1999) were compared with the experimental results to obtain the best air side heat transfer correlation for the current heat exchanger (Carlson, 2001)

Carlson (2001) found that the latter correlation was the best in describing the performance of our heat exchanger. This had been expected, due to the range of geometric and operating parameters involved. Since this report will focus on frost distribution, we will use Carlson's best fit correlation, as described in Equation 2.1, obtained by simple scaling of the Kim, Youn and Webb (1999) correlation, based on dry-surface wind tunnel data with our heat exchanger.

$$j_{Carlson} = \frac{0.1484}{0.1896} j_{Kim} = 0.78 j_{Kim}$$

(2.1)

6

2.4 Air side pressure drop

The airside pressure drop was calculated using the following equation (Kays and London, 1998):

$$\Delta P = \frac{G_{max}^2}{2} \cdot v_1 \cdot \left[\left(K_c + 1 - s^2\right) + 2 \cdot \left(\frac{v_2}{v_1} - 1\right) + f \cdot \frac{A_o}{A_{free}} \cdot \frac{v_m}{v_1} - (1 - s^2 - K_e)\frac{v_2}{v_1} \right] \quad (2.2)$$

K_c (entrance loss coefficient) and K_e (exit loss coefficient) were determined according to Kays and London (1998) as : $K_c = 0.6$, $K_e = 0.15$.

The Kim, Youn and Webb (1999) airside friction factor correlation for plain fin heat exchangers with round tubes was used in the model. It is applicable to the range of geometry and operating conditions used in the display case. Refer to Appendix B for a detailed description of this correlation.

2.5 Refrigerant side heat transfer coefficient

The Gnielinski correlation for fully developed (hydro dynamically and thermally) turbulent flow in a smooth circular tube was used. Using the method of Kays and Crawford (1993), it was found that the effect of thermal entry length was less than 1% for the relevant range of Re and Pr, so it was neglected. For details see Appendix B.

2.6 Frosting rate

The frosting rate can be obtained from the air inlet and outlet humidity:

$$\dot{m}_{fr} = \dot{m}_{air}(w_{in} - w_{out}) \quad (2.3)$$

Where $\dot{m}_{air} =$ air mass flow rate, kg / s

         $w_{in} =$ air inlet absolute humidity, kg/kg of dry air

         $w_{out} =$ air outlet absolute humidity, kg/kg of dry air

For each element of the heat exchanger, the one-dimensional mass transfer equation is used:

$$\dot{m}_{fr} = h_D \cdot A_o \cdot (w_a - w_s) \quad (2.4)$$

Considering the analogy between the heat transfer and mass transfer at the surface (Incropera and DeWitt (1996)):

$$h_D = \frac{h_a}{c_{pm}} \cdot Le^{-\frac{2}{3}} \quad (2.5)$$

So, the final form for the frosting rate can be written as:

$$\dot{m}_{fr} = \frac{h_a}{c_{pm}} \cdot Le^{-\frac{2}{3}} \cdot A_o \cdot (w_a - w_s) \quad (2.6)$$

Where $h_a =$ airside heat transfer coefficient, $kW / m^2 \cdot K$

c_{pm} = specific heat of moist air, $kJ/kg \cdot K$

w_a = average air absolute humidity

w_s = air absolute humidity saturated at frost surface

In the model, both equations are solved simultaneously in order to get the frosting rate, $\dot{m}_{fr}$ as well as the air outlet humidity, w_{out}.

2.7 Frost thickness and density

(A): Thickness

Many investigators, e.g. Ostin and Andersson (1991), Storey and Jacobi (1999), have found the frost thickness increases linearly with the square root of time during the mature frost growth period. There have been several models proposed in the literature to normalize the effects of environmental conditions and predict the frost growth observed in experiments. However, the Storey and Jacobi non-dimensional procedure for determining frost density could not be used in our case for two reasons:

(i) as the surface temperature of the frost is well below freezing point for most of the cases.

(ii) The initial frost conductivity term (k_o) cannot be neglected from the relation

$$k_f = k_o + \boldsymbol{b}\boldsymbol{r}_f \qquad (2.7)$$

because it accounts for as much as 20 % of the total.

The one selected for our analysis is a model for frost height determined with the help of one dimensional heat and mass transfer governing equations presented in section 2.9 with the frost properties (density and conductivity) presented in 2.8
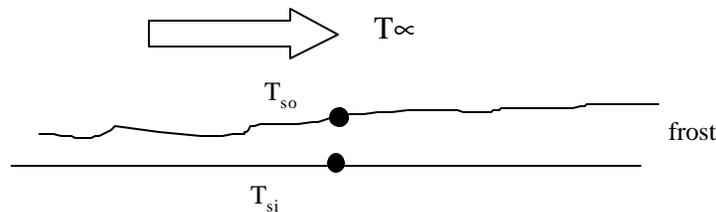
Figure 2.3 Single fin frosting

In the model, T_{si} (base temperature of the fin is determined after considering the surface efficiency of the frosted fin.

The thickness of the frost layer is computed by dividing the accumulated frost mass (m_{frost}) by the product of average frost density ($\mathbf{r}_{fr}$) and surface area ($A_{o,dry}$, fin area and tube area under dry conditions) given by Eqn. (2.8).

$$\mathbf{d}_{fr} = \frac{m_{frost}}{\mathbf{r}_{fr} \cdot A_{o,dry}} \qquad (2.8)$$

Here it is assumed that the changes in the frost density along the thickness of the frost (from base to surface) are negligible. This was observed by Chen (2000) during their experiments except for frost thickness below 0.4 mm as shown in Figure 2.4. Since our model is used to predict the mature frost growth over a long period of time assuming that a thin layer of frost is already present on the surface of the fins and the tubes, the assumption of constant frost density (along the base to the surface) for frost thickness greater than 0.4 mm is valid for our model.
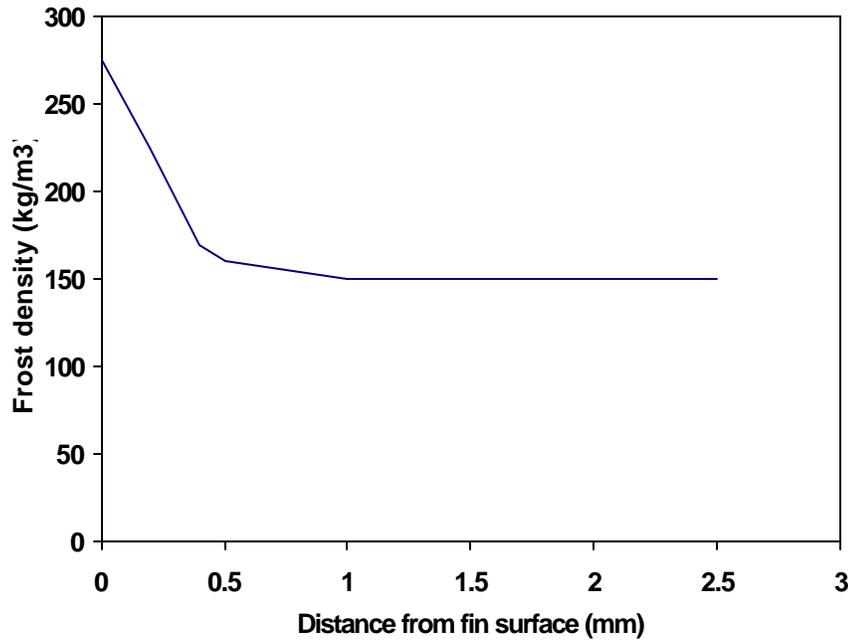
Figure 2.4 Variation of frost density within the frost layer, Chen (2000)

(B) Density

For air inlet temperatures near 0 °C, Hayashi's (1976) empirical correlation of frost density with respect to the surface temperature of the frost is used.

$$\mathbf{r}_{fr} = 650 \, e^{0.277 \, T_{so}} \qquad (2.9)$$

Figure 2.5 shows the variation of frost density with the surface temperature expressed by Eq. (2.9). This expression was developed for frost surface temperatures between -25 to 0 °C, air stream velocities between 2 and 6 m/s and an air stream humidity ratio of 0.0075 kg/kg of dry air (corresponding to $T_{dp} = 9.5$ °C). However for our experiments with lower air velocities (0.6 to 2.2 m/s), the expression is compatible only for 0 °C air supply

temperatures and the correlation breaks down for air inlet temperatures of –20 °C with the frost surface temperatures falling below –25 °C.
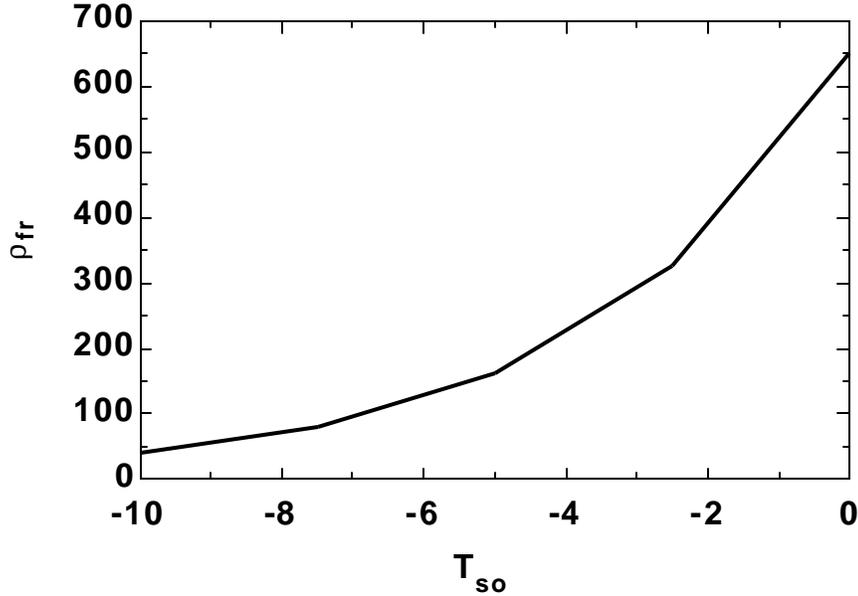
Figure 2.5 Variation of frost density with surface temperature, Hayashi (1976)

Chen (2000) measured frost characteristics on heat exchanger fins for typical freezer operating conditions with base temperatures form –31 to –38 °C and air supply temperatures from –13 to –21 °C and found that the frost density varied from 100 to 145 kg/m^3 along the air flow for air supply temperature of –15 °C and plate temperatures of –35 °C. Since very little is known about density of frost at lower surface temperatures (below –25 °C), a constant frost density of 130 kg/m^3 is used for the analysis of the cases with air supply temperatures of – 20 °C for our model.

2.8 Frost conductivity
Several researchers have conducted experiments to develop empirical relationships to express frost conductivity as a function of its density. The relations are generally of the form: $k_{fr} = k_0 + b \cdot r_{fr}$. Of course, the relationship is highly dependent on the structure of the frost, which in turn depends on the operating conditions during which it is formed. For example, Storey and Jacobi (1999) assumed $k_o = 0$ and obtained $8.7 \times 10^{-4} W \cdot m^2 / kg \cdot K$. However, most of their experiments were done with the air temperature around 20 °C and they assumed the frost surface temperature to be the freezing point. This is very different from our experiments in which the air temperature varied from –20 °C to 0 °C and surface temperature was always far below the freezing point.

To evaluate k_{fr} (kW/m-K), we use the Yonko and Sepsy (1967) correlation for frost density and conductivity:

$$k_{fr} = (0.02422 + 7.214 \cdot 10^{-4} \cdot r_{fr} + 1.1797 \cdot 10^{-6} \cdot r_{fr}^2)/1000 \qquad (2.10)$$

This equation implies that $\beta = 7.214 \times 10^{-4} W \cdot m^2 / kg \cdot K$. We assume it to be constant. Actually, $\beta = 7.214 \times 10^{-4} (1 + r_{fr})$, which means β should vary with r_{fr}. However, there will be only 0.07% change in β for our entire range of $r_{fr} = 40 \sim 450$ kg/m^3 (predicted by the model).

Yonko and Sepsy (1967) also tested a wide range of surface temperature from $-30\,°C$ to $-5.7\,°C$, which is very similar to our surface temperature. And their correlation is limited to $r_{fr} < 576$ kg/m^3, which was fully satisfied in all the data sets.

2.9 Governing equations

Note that frost surface is initially rough and uneven due to the random nature of the deposition of the frost. The roughness and actual surface area of the frost surface are usually difficult to predict. It might contribute to an enhancement of the heat transfer to
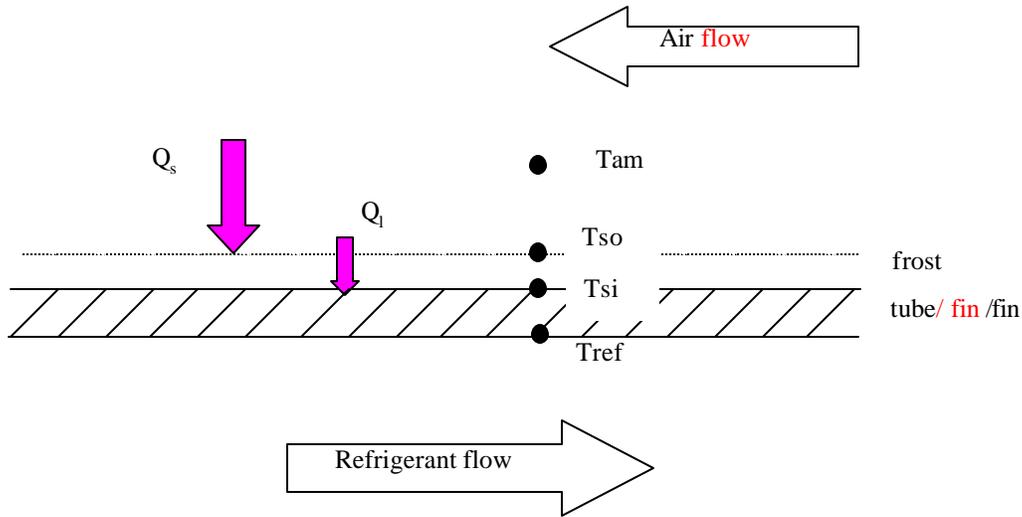
Figure 2.6 One dimensional heat transfer from the air through the frost layer, tubes and fins to the refrigerant

the heat exchanger. But as Sanders (1974) has found, the surface roughness effect of enhancing the heat transfer has a significant effect only in the early stages of frost formation. Later the insulation effect makes it inconsequential. Since our model usually describes a long period of frosting on a full-scale heat exchanger, most of the time should be outside the early stage of frost formation. Therefore surface roughness is not considered in the model.

Figure 2.6 describes the process of the one dimensional heat transfer from the air through the frost layer, tubes and fins to refrigerant.

The one-dimensional governing equations to describe the heat and mass transfer process for each element are listed below:

Heat transfer from the air to the surface of the frost:

$$T_{am} - T_{so} = \frac{Q_{sens}}{h_{a,dry} \cdot A_{o,fr}}$$

(2.11)

11

Heat transfer through the frost layer:

$$T_{so} - T_{si} = \frac{Q_{sens} + Q_{latent}}{\frac{k_{fr}}{d_{fr}} \cdot A_{o,fr} h_{suf}}$$

(2.12)

Heat transfer from the frost layer to the refrigerant:

$$T_{si} - T_{ref} = \frac{Q_{sens} + Q_{latent}}{h_{ref} \cdot A_{ref}}$$

(2.13)

T_{am} is the average air temperature of each element, T_{so} is the outer surface temperature of the frost layer in the middle of each element and T_{si} is the base temperature of the fin and T_{ref} is the average refrigerant temperature.

The sensible load is obtained from the airside temperature drop:

$$Q_{sens} = \dot{m}_{air} c_{p,air}(T_{ain} - T_{aout})$$

(2.14)

The latent load comes from the formation of frost on the surface of tubes and fins:

$$Q_{latent} = \dot{m}_{fr} h_{sg}(T_{so})$$

(2.15)

The total load of the heat exchanger is the sum of these two parts:

$$Q = Q_{sens} + Q_{latent}$$

(2.16)

Refrigerant side temperature rise and mass flow rate could also be used to calculate the total load:

$$Q = \dot{m}_{ref} c_{p,ref} (T_{rin} - T_{rout})$$

(2.17)

2.10 Time Interval

The time interval used in the model is 3 minutes, the same as the time interval used to collect data in the experiments. Actually, time interval will affect the accuracy of the prediction. Carlson (2001) studied four time intervals and concluded that the three-minute increment yields solutions within 1% of the one-minute increment in all cases, except for frost thickness at the beginning of the run where it is off by 2%. So, the 3-minute time interval is used throughout the model.

2.11 Model

It is necessary to estimate initial values of frost thickness and frost density in order to start calculations. These initial guess values only affect the predictions at the first time step but will not have any impact on the results later on for frost thickness from 0.02 mm to 0.05mm and density from 40 kg/m^3 to 100 kg/m^3. 40 kg/m^3 of frost density and 0.02 mm frost thickness were used in this study.

Figure 2.7 describes the algorithm for the proposed numerical model.

For row i (i=1~8):

Kim (1999): $j \rightarrow h_{a,i}$ & f $\rightarrow dP_i$

Gnielinski $:$ $h_{ref, i}$
Sector method: $\mathbf{h}_{f,i}$

At one time step j
Input parameter:
geometry
operating conditions

Q_i
$Q_{sens,i}$
$Q_{latent,i}$
$T_{aout,i}$
$T_{rout,i}$
$T_{so,i}$
$T_{si,i}$

Governing Eqns

next time step, j+1

Frost
conductivity

Hayashi's
Frost Density

Frost
mass

Geometry updated
due to frost layer
$Dc_{,j}=Dc_{,0} + 2*\delta_{fr}$
$F_{th,j} = F_{th,0} +2*\delta_{fr}$

Frost Thickness
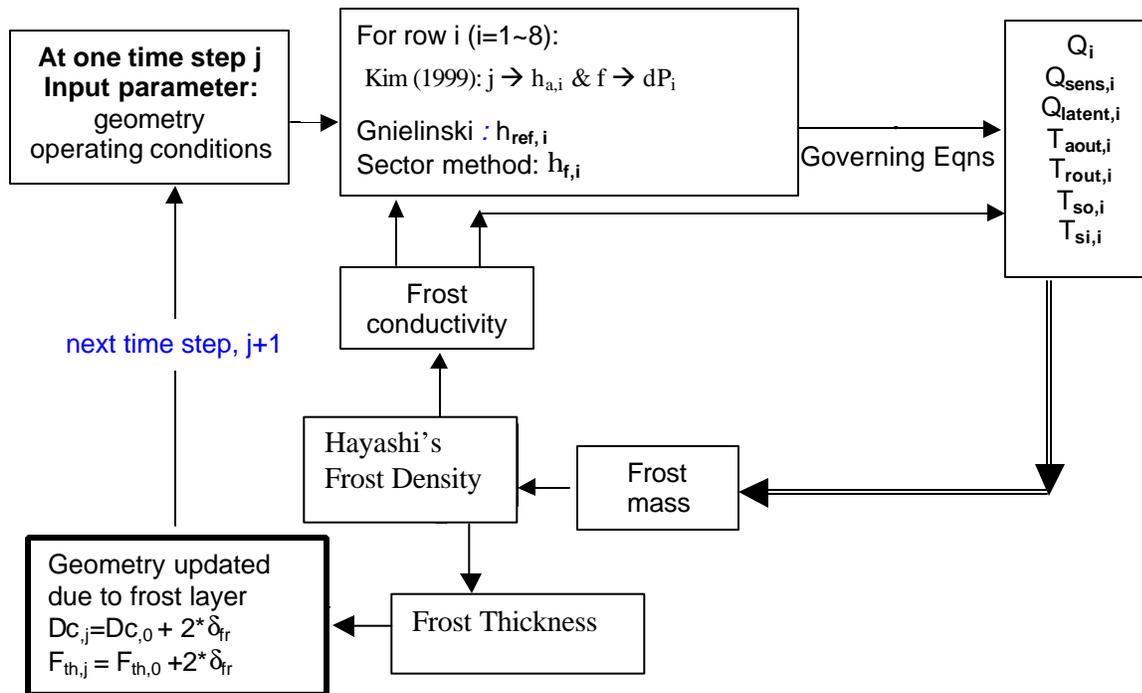
Figure 2.7 Structure of the numerical model

Chapter 3: Model Validation and Discussion

3.1 Model validation under dry conditions

The model for predicting the performance of a heat exchanger when frost grows on the tubes and fins was used first to simulate the heat exchanger performance under dry conditions.

Note that "dry" here does not mean that the air is absolutely dry. It only means that during the experiments, no steam was added into the chamber. So under these dry conditions, the air inlet relative humidity could reach nearly 60% or more, depending on the humidity when the experiments started inside the room where the experimental chamber was located. A very small amount of frost formed on the surface of the heat exchanger under these dry conditions. Its effect on the performance of the heat exchanger is assumed to be negligible.

Thirteen data sets are used in the validation of the model. The test conditions are listed in Table 3.1, which shows the (30—480 minutes) time-averaged values of the parameters. Actually, all the parameters fluctuated during the averaging period due to some unpredictable factors in the experiments. These small fluctuations were documented by Carlson (2001).

Table 3.1 Test conditions for model validation under dry conditions

Data Set	Air inlet temperature T_{ain} (°C)	Refrigerant inlet temperature: T_{rin} (°C)	Air inlet dew point temperature T_{dp} (°C)	Air face velocity: vel_{air} (m/s)	Refrigerant mass flow rate: $\dot{m}_{ref}$ (kg/s)
Case 1	-0.3	-10.7	-7.9	1.3	0.37
Case 2	-18	-26.3	-21.5	1.3	0.35
Case 3	-19	-30.9	-23.9	2.3	0.51
Case 4	-19	-29.0	-23.6	1.5	0.50
Case 5	-0.9	-11.0	-6.8	2.3	0.53
Case 6	-1.0	-11.0	8.2	1.5	0.54
Case 7	-1.8	-13.0	-10.0	0.6	0.55
Case 8	-1.2	-11.7	-9.4	0.6	0.36
Case 9	-1.9	-11.5	-7.8	1.5	0.37
Case 10	-0.1	-10.5	-5.6	2.3	0.37
Case 11	0.7	-10.5	-3.6	2.3	0.20
Case 12	-0.8	-11.4	-5.6	1.5	0.20
Case 13	-0.5	-10.3	-7.0	0.6	0.2

Capacity is the most important characteristic of heat exchangers. A model for predicting the performance of heat exchangers will not be successful if it cannot predict the capacity correctly.

Three independent methods were used to calculate the capacity of the heat exchanger in the experiments: an air, a refrigerant and a chamber energy balance (Carlson 2001). In dry conditions, these balances are given by:

$$Q_{ref} = \dot{m}_{ref}\, c_{p,ref}\left(T_{rout} - T_{rin}\right) - Q_{tubes} \tag{3.1}$$

$$\dot{Q}_{air} = \dot{m}_{air} c_{p,air} (T_{ain} - T_{aout}) - Q_{windtunnel} \tag{3.2}$$

$$Q_{chamber} = UA_{chamber} \cdot \Delta T_{walls} + W_{blower} + W_{heater} + W_{precoler} \tag{3.3}$$

These three calculations of capacity were in very close agreement (RMS 2.4%) at the dry operating conditions. However, $Q_{chamber}$ is usually not stable compared with Q_{ref} and Q_{air} because the heater is on and off very frequently. The mass flow rate of the steam entering the chamber is not measured, so the chamber balance cannot be used under frosted conditions (Carlson, 2001). Only Q_{ref} and Q_{air} are used in the comparison.

In the model, the capacity of the heat exchanger is calculated by summarizing over the eight finite elements (tube rows) with the following equation:

$$Q = \sum_{k=1}^{8} \dot{m}_{air} c_{p,air,k} (T_{ain,k} - T_{aout,k}) \tag{3.4}$$

When compared with the experimental data, good agreement is obtained for the predicted capacity of the heat exchanger, as shown in Figure 3.1.
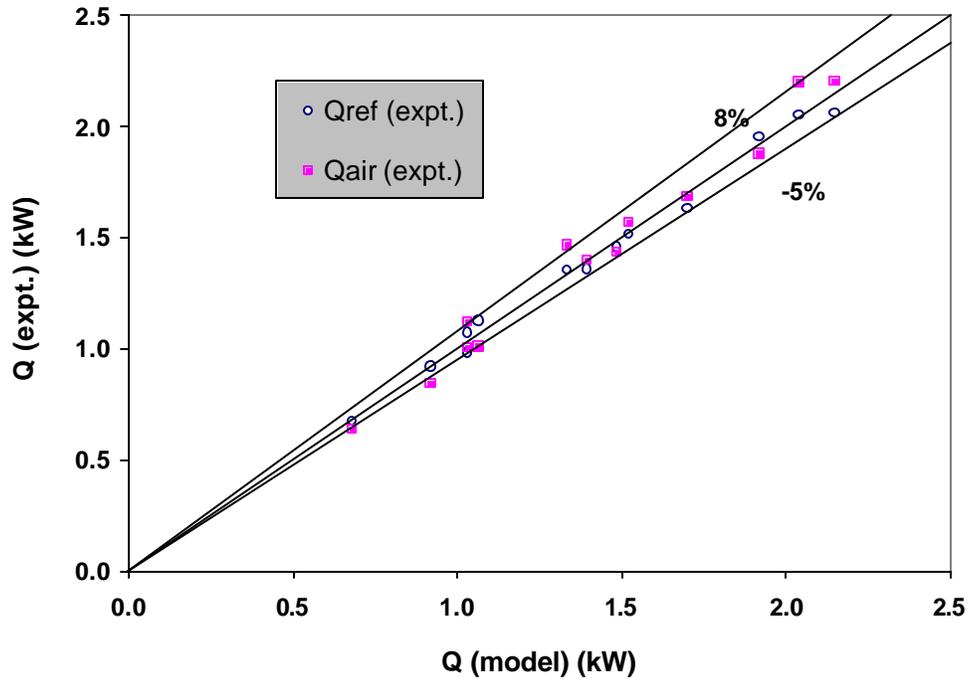
Figure 3.1 Comparison of the heat exchanger capacity

Two UA values were calculated in the experiments—one comes from Q_{ref} and the other, from Q_{air}:

$$UA_{ref} = \frac{Q_{ref}}{LMTD} \tag{3.5}$$

$$UA_{air} = \frac{Q_{air}}{LMTD} \tag{3.6}$$

Where $LMTD = \dfrac{\left(T_{ain} - T_{rout}\right) - \left(T_{aout} - T_{rin}\right)}{\ln \dfrac{\left(T_{ain} - T_{rout}\right)}{\left(T_{aout} - T_{rin}\right)}}$ (3.7)

The predicted UA is given by: $UA = \displaystyle\sum_{k=1}^{8} \dfrac{Q_k}{LMTD_k}$ (3.8)

Where k=1,2…8 is the row number

Q_k is the capacity of each tube row.

$$LMTD_k = \dfrac{\left(T_{ain,k} - T_{rout,k}\right) - \left(T_{aout,k} - T_{rin,k}\right)}{\ln \dfrac{\left(T_{ain,k} - T_{rout,k}\right)}{\left(T_{aout,k} - T_{rin,k}\right)}}$$ (3.9)

Figure 3.2 illustrates comparison of UA values between the simulation results and the experimental data, and the two matched well.
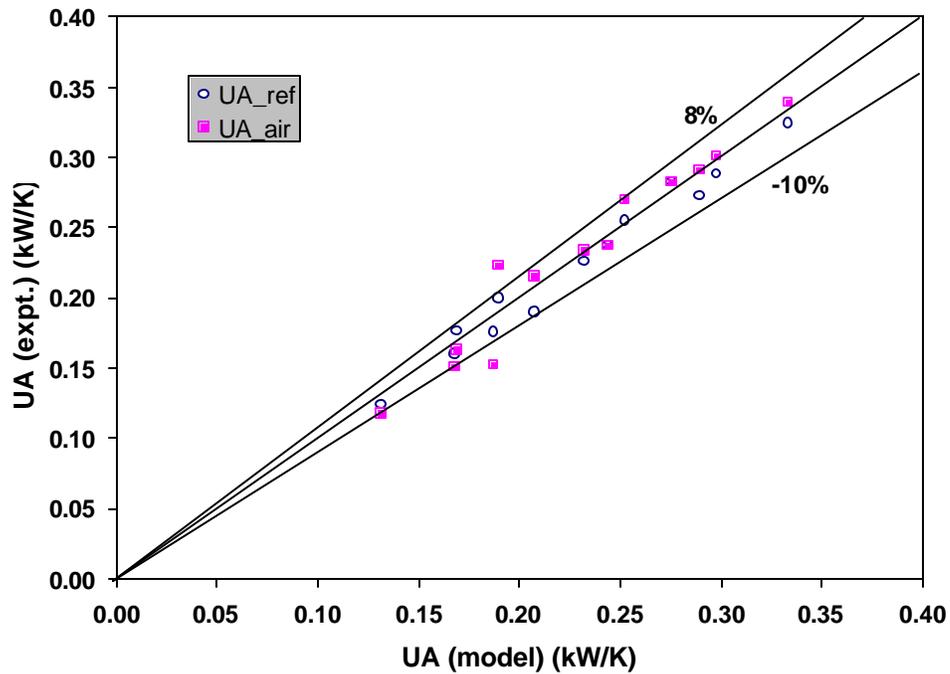
Figure 3.2 Comparison of UA values

Comparisons are also made for the average air and refrigerant exit temperatures measured during the experiment and predicted by the model, shown in Figure 3.3 and 3.4. As it can be seen from the figure, the model prediction of the air and refrigerant exit temperature accurately matched those measured by the experiment.
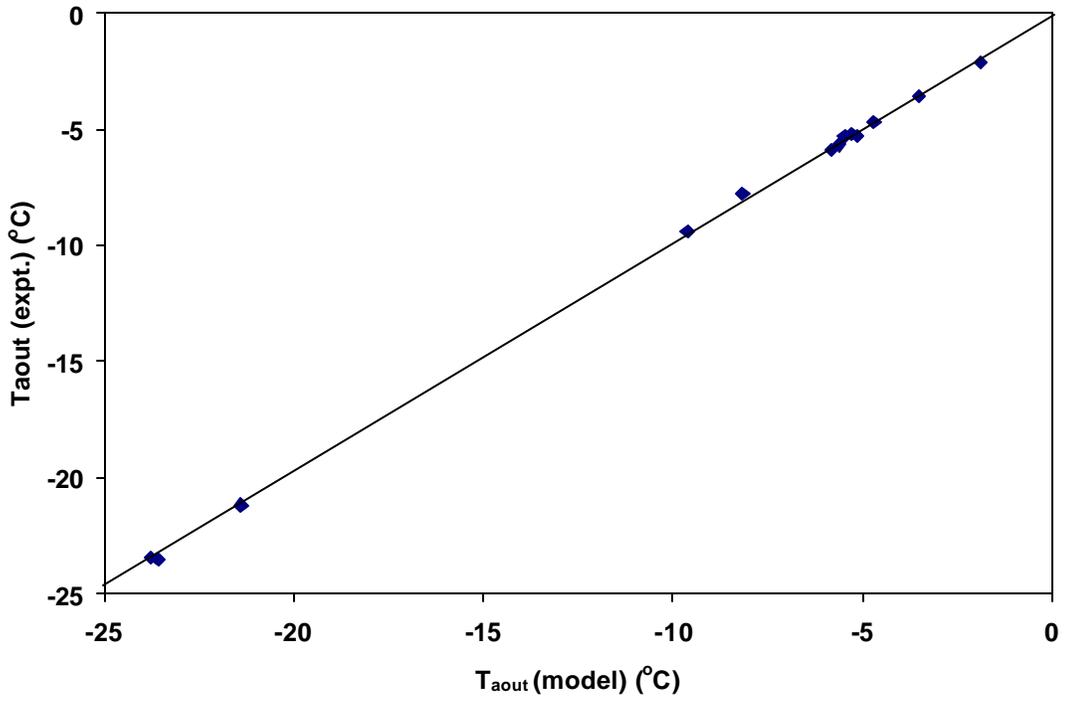
Figure 3.3 Comparison of air exit temperature
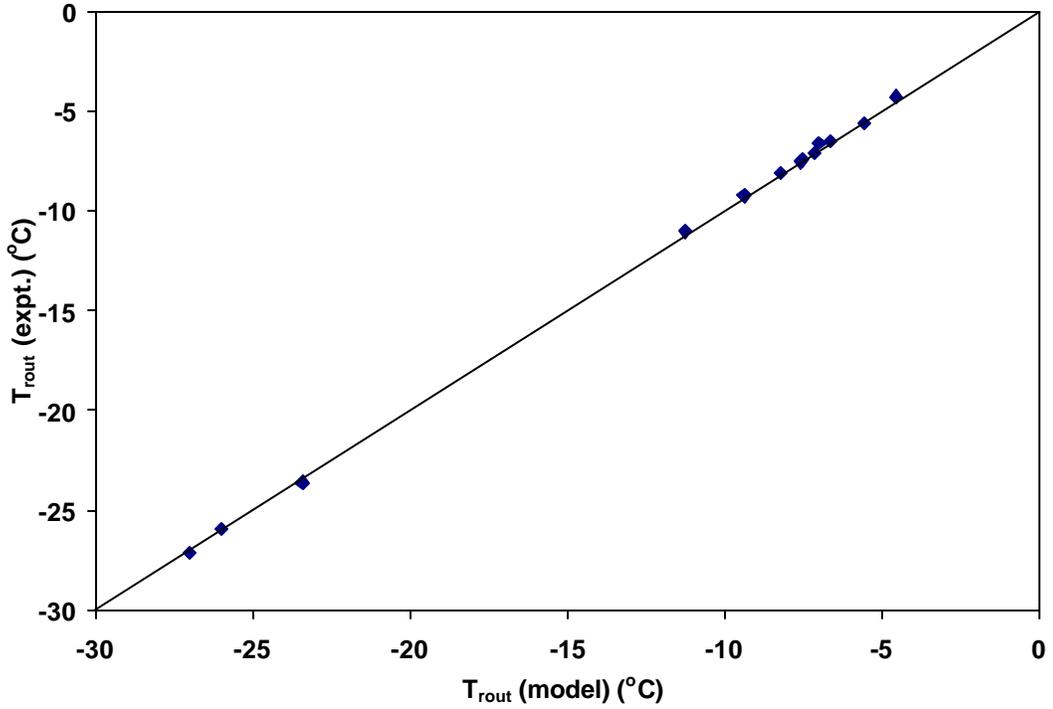
Figure 3.4 Comparison of refrigerant exit temperature

3.2 Model validation under frosted conditions

Ten data sets (Case 1 to Case 10 in Table 3.2) are designed to validate the model under frosted conditions, as described in Appendix C. Another data set (Case 11) was added to provide more information. Their operating conditions are listed in Table 3.2.

Table 3.2 Operating conditions for model validation under frosted conditions

Data Set	Air inlet temperature T_{ain}(°C)	Refrigerant inlet temperature: T_{rin} (°C)	Air inlet relative humidity: RH_{in}	Air velocity: vel_{air} (m/s)	Refrigerant mass flow rate: $\overset{\bullet}{m}_{ref}$ (kg/s)
Case 1	0	-10	90%	1.3	0.45
Case 2	0	-10	90%	1.3	0.2
Case 3	0	-10	90%	1.3	0.26
Case 4	0	-30	90%	2.2	0.5
Case 5	-20	-30	70%	2.2	0.5
Case 6	-20	-30	70%	1.3	0.5
Case 7	0	-10	90%	0.9	0.5
Case 8	0	-10	80%	0.9	0.5
Case 9	0	-10	70%	0.9	0.5
Case 10	-20	-30	70%	0.9	0.5
Case 11	-8	-32	90%	0.6	0.5

For clarity, each data set is named using the following format: air inlet temperature/refrigerant inlet temperature/air inlet relative humidity/air velocity/refrigerant mass flow rate. For example, 0/-10/90/1.3/0.45 represents Case 1. This format is used throughout the report.

As in Table 3.1, each value of the operating parameters shown in Table 3.2 is a time-averaged value obtained after steady state was reached. All the parameters actually fluctuated with time and the magnitudes of fluctuations vary from one experiment to another. For details see Appendix D.

To validate the model, measured data input to the model are: air inlet temperature and humidity, air mass flow rate, refrigerant inlet temperature, and refrigerant mass flow rate.

3.2.1 Model validation for a typical experiment

Consider a typical case 0/-10/90/0.9/0.5 (Case 8) for example, the predicted air outlet temperature is compared with T_{nozzle} in Figure 3.5 and the comparison of the refrigerant outlet temperatures is shown in Figure 3.6. Carlson (2001) described the comparison of T_{nozzle} and the average outlet temperature of the six thermocouples and they agreed within RMS 0.2 °C. Note that the variations in outlet temperature reflect variations in the input air and refrigerant inlet temperature.
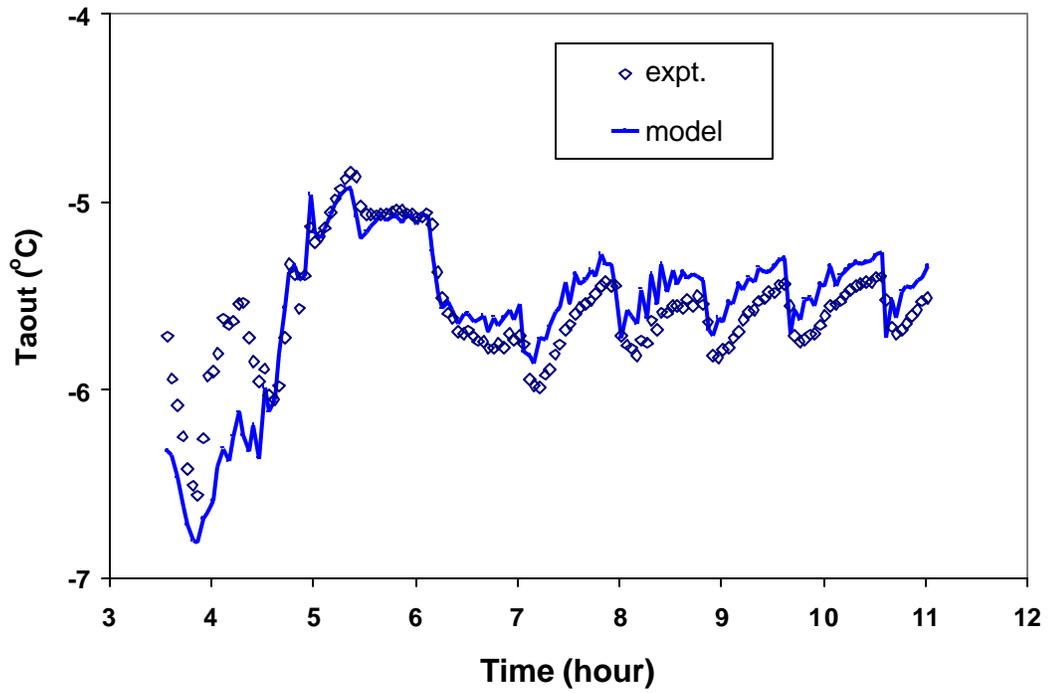
Figure 3.5 Comparison of air outlet temperature for 0/-10/90/0.9/0.5
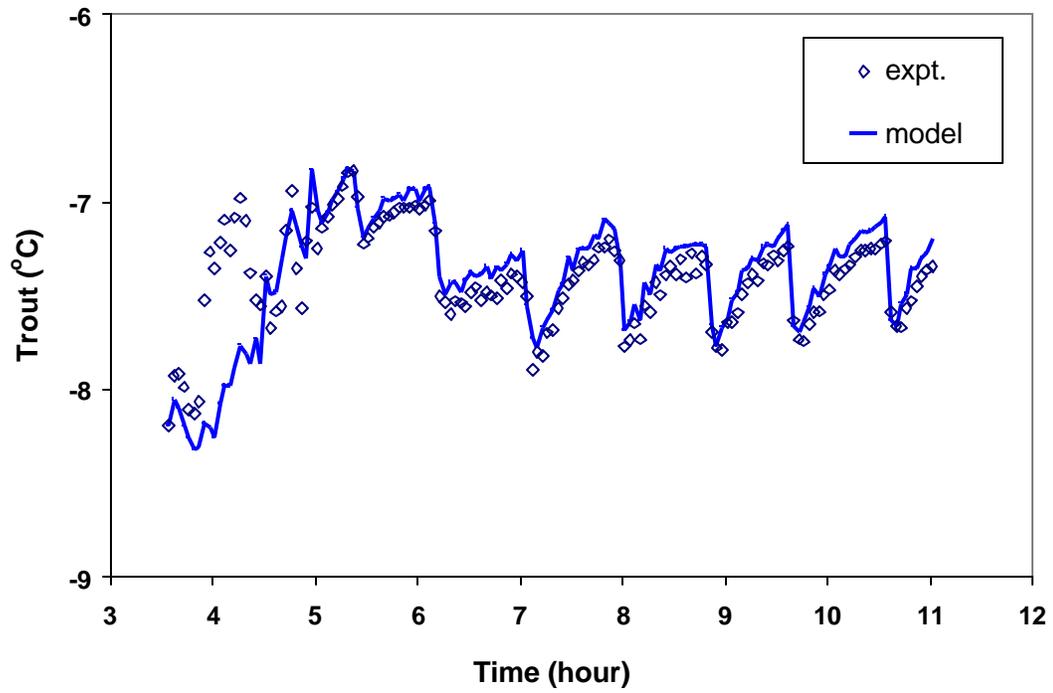
Figure 3.6 Comparison of averaged refrigerant outlet temperature for 0/-10/90/0.9/0.5

When frost grows on the tubes and fins of the heat exchanger, mass is transferred from the humid air to the frost layer. Thus, the total load of the heat exchanger consists of two parts—sensible load and latent load.

The equations used to calculate the three loads—total load Q, sensible load Q_{sens} and latent load Q_{latent} —are listed in Table 3.3.

Table 3.3 Equations used to calculate load in the experiments and model

	Experiments (Carlson, 2001)	Model
Sensible load	$Q_{sens} = \dot{m}_{air}\, c_{p,air}\left(T_{ain} - T_{nozzle}\right) - Q_{windtunnel}$ (3.10)	$Q_{sens} = \sum_{k=1}^{8} \dot{m}_{air}\, c_{p,air,k}\left(T_{ain,k} - T_{aout,k}\right)$ k=1,2,…8, row number (3.14)
Latent load	$Q_{latent} = \dot{m}_{air}\left(w_{in} - w_{out}\right)h_{sg}$ (3.11)	$Q_{latent} = \sum_{k=1}^{8} \dot{m}_{air}\left(w_{in,k} - w_{out,k}\right)h_{sg,k}$ (3.15)
Total load	$Q_{ref} = \dot{m}_{ref}\, c_{p,ref}\left(T_{rout} - T_{rin}\right) - Q_{tubes}$ (3.12) $Q_{air} = Q_{sens} + Q_{latent}$ (3.13)	$Q = Q_{sens} + Q_{latent}$ (3.16)

For the present case, the comparisons of the total load, sensible load and latent load with time along with measured uncertainties are shown in Figures 3.7, 3.8 and 3.9 respectively. The variations in output variables reflect variations in the measured input air and refrigerant inlet temperature and air inlet humidity.

Notice that time does not start from 0 in these graphs. The reason is that a pulldown period is needed to cool the inlet air from the ambient temperature to the desired temperature (in this case, it is 0 °C). The length of this period depends on both the ambient conditions and actual operations during the experiment, e.g., the time to turn on the heater and humidifier and achieve new steady state. Refer to Carlson (2001) for more information about experiments. In Case 8, the pulldown period was about 3.5 hours.
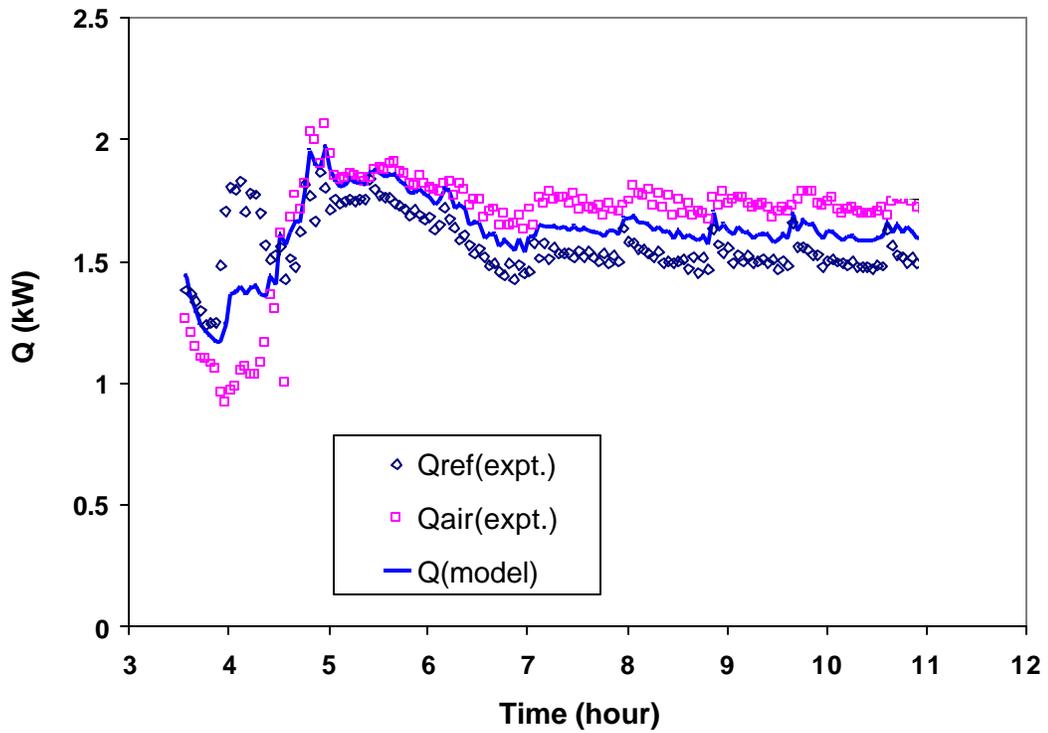
Figure 3.7 Comparison of the total load for 0/-10/90/0.9/0.5
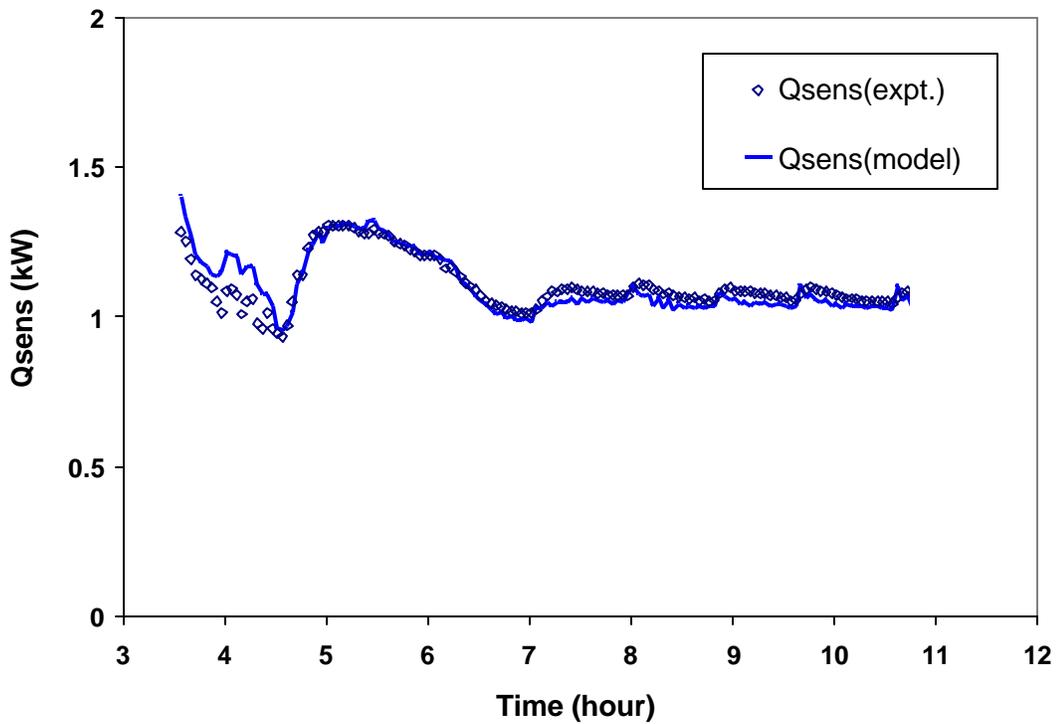
Figure 3.8 Comparison of the sensible load for 0/-10/90/0.9/0.5
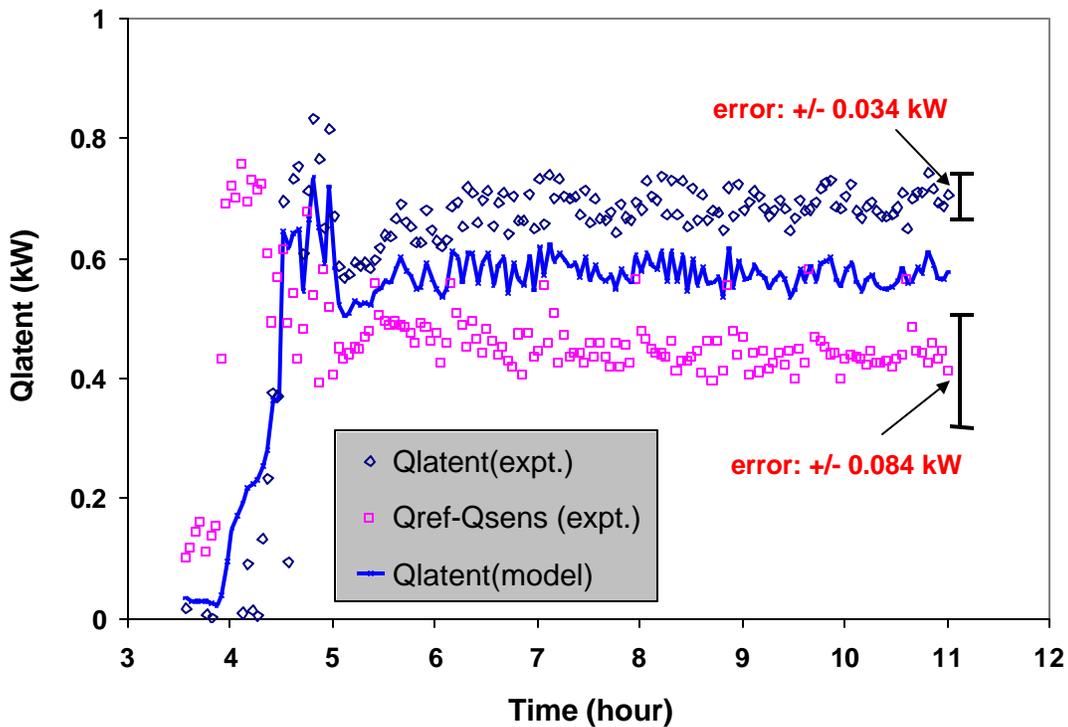
Figure 3.9 Comparison of the latent load for 0/-10/90/0.9/0.5

Because there were some problems with the air humidity measurement that may affect the accuracy of the latent load obtained experimentally from Eqn. 3.11, the predicted latent load is also compared with (Q_{ref} - Q_{sens}) in Figure 3.9. However, the latter calculation includes possible error due to the difference between air and refrigerant-side energy balance, which was found to be 0.15 kW approximately.

The air inlet and outlet humidity is obtained from the dew point measurement using two General Eastern dew point meters. The problems are:

- The location of the inlet dew point meter was not exactly at the air inlet; instead it was placed outside the wind tunnel 1.5 m downstream and 0.3 m above the top of the heat exchanger;

- Inlet air temperature stratification was observed in some experiments. It is reasonable to believe that the air humidity was also not uniform at the inlet, which caused the uneven vertical frost distribution among the nine circuits (Carlson, 2001). So, this measured dew point was not the real inlet humidity;

- There was also outlet air temperature and humidity stratification according to the experimental data. So the dew point meter at the outlet only measured one point and could not tell what was happening in the other locations.

All these problems add to the aforementioned measurement uncertainties affecting the accuracy of the latent load and frost mass calculations. They can also explain the discrepancy in the comparison of the latent load and frost mass in the experiments and model. The uneven-vertical-frost-distribution issue was not addressed in the

model that currently assumes the nine circuits are exactly identical. An inlet air mixer should be added and the dew point meter should be relocated for future experiments.

3.2.2 Model validation for eleven experiments

Owing to different operating conditions each experiment was carried out for different number of hours. For air supply temperature of 0 °C the experiments were carried out usually until the coils were fully frosted, while for air supply temperature of –20 °C the experiments were conducted for at least 24 hours of operation, so there was a different amount of frost accumulation at the end of the each experiment. Therefore for all experiments with air inlet temperature of 0 °C, comparisons were made at the time when 2.5 kg of frost was formed on the heat exchanger as per scale measurement. While for cases with air inlet temperature of –20 °C, comparison was made at 1.5 kg (approximately) of frost.

The comparisons for all eleven data sets are shown in Figures 3.10, 3.11 and 3.12 for the total load, sensible load and latent load respectively.
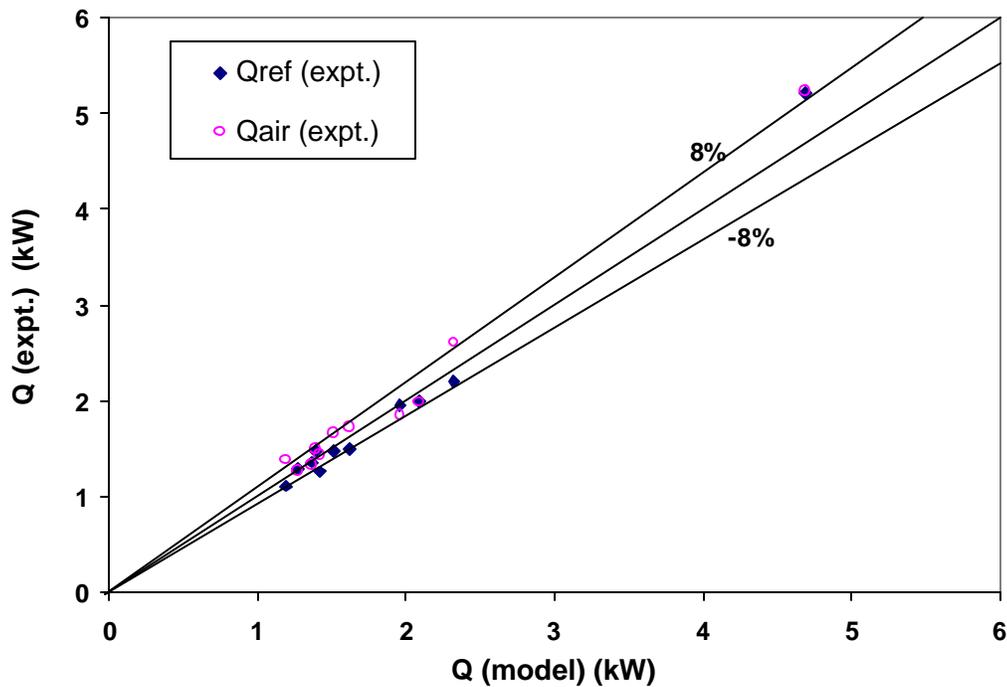

Figure 3.10 Validation of the total heat transfer for all data sets
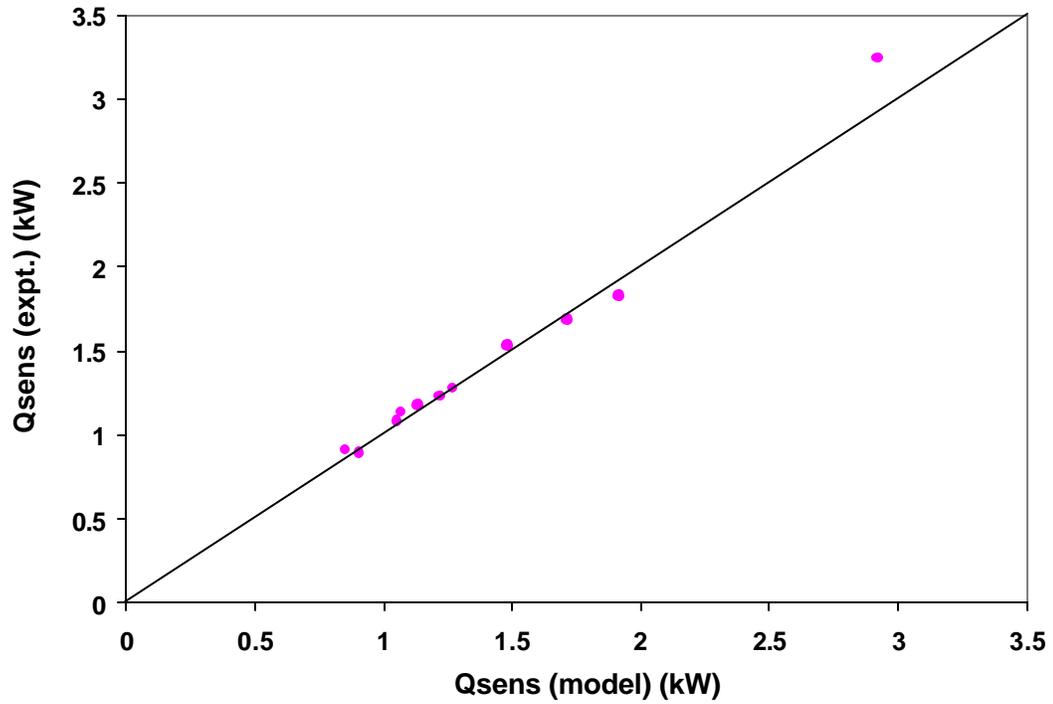
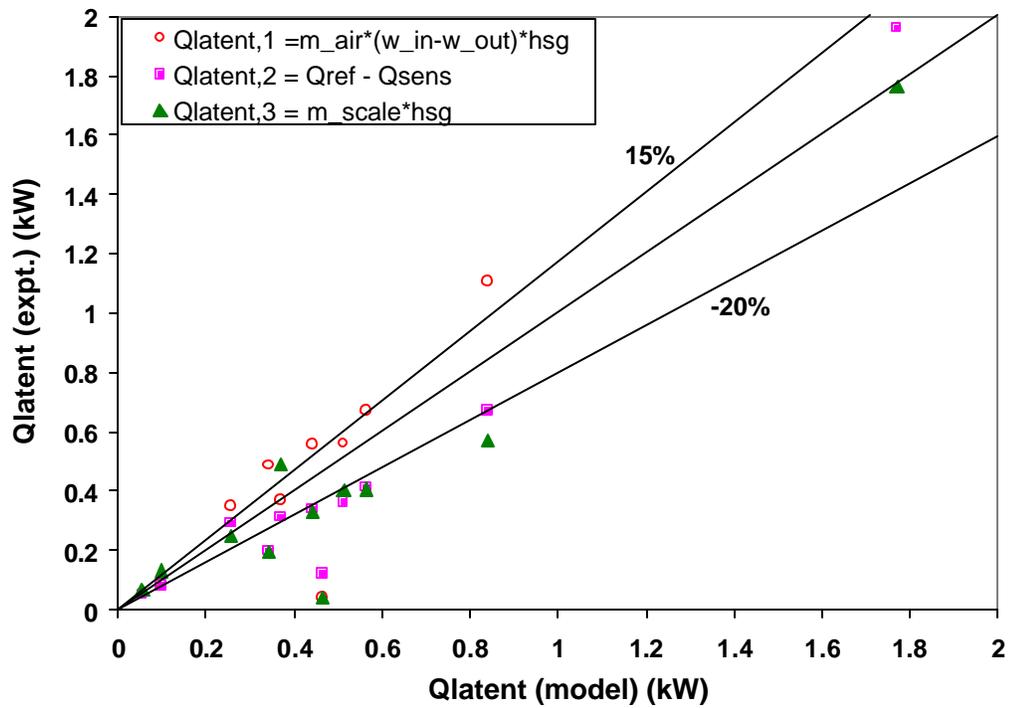Figure 3.11 Validation of the sensible load for all data sets

Figure 3.12 Validation of the latent load for all data sets

Results for capacities and temperatures (air and averaged refrigerant outlet temperatures) in each data set are summarized in Table 3.4. Please refer to Carlson (2001) for the measurement error of each instrument.

δ is the averaged difference between the predicted value and experimental data as shown in Eqn. (3.17):

$$\boldsymbol{d} = avg(X_{m,k} - X_{e,k}) \tag{3.17}$$

APD is the percentage of δ over the experimental data, as defined in Eqn. (3.18):

$$APD = avg\frac{\left|X_{m,k} - X_{e,k}\right|}{X_{e,k}} \tag{3.18}$$

RMS is the root mean squared error as shown in Eqn. (3.19):

$$RMS = \frac{\sum_{k=1}^{N}(X_{m,k} - X_{e,k})^2}{N} \tag{3.19}$$

N is the number of experimental data points used in the comparison.

Table 3.4 Comparison of loads, air and refrigerant outlet temperatures

S. No	Data set	Q (kW)		Q$_{sens}$ (kW)		Q$_{latent}$ (kW) *		T$_{aout}$ (^{o}C)		T$_{rout}$ (^{o}C)	
		APD	RMS	APD	RMS	APD	RMS	δ	RMS	δ	RMS
1.	0/-10/90/1.3/0.45	6%	0.13	3%	0.06	25%	0.28	0.2	0.2	0.1	0.1
2.	0/-10/90/1.3/0.2	7%	0.08	8%	0.08	29%	0.14	0.2	0.2	-0.2	0.2
3.	0/-10/90/1.3/0.26	13%	0.16	2%	0.02	8%	0.04	0	0.1	0.4	0.4
4.	0/-30/90/2.2/0.5	9%	0.47	6%	0.23	8%	0.16	0.7	0.8	-1	1
5.	-20/-30/70/2.2/0.5	1%	0.03	6%	0.11	27%	0.01	0.3	0.3	0	0.1
6.	-20/-30/70/1.3/0.5	1%	0.02	2%	0.03	11%	0.01	0.3	0.3	0.1	0.1
7.	0/-10/90/0.9/0.5	6%	0.1	2%	0.03	16%	0.1	0.1	0.2	0.1	0.1
8.	0/-10/80/0.9/0.5	2%	0.03	3%	0.04	17%	0.09	0.2	0.2	-0.1	0.1
9.	0/-10/70/0.9/0.5	5%	0.07	3%	0.04	26%	0.1	0.2	0.2	0.2	0.2
10.	-20/-30/70/0.9/0.5	1%	0.02	2%	0.03	5%	0.01	0	0.1	-0.1	0.1
11.	-8/-32/90/0.6/0.5	2%	0.07	2%	0.05	7%	0.03	-1.0	1.0	-0.2	0.2

* Q$_{latent}$ comes from Eqn. (3.11).

Generally, we see good agreement between the simulation results and experimental data with the exception of a few data sets (data set 2, 3, and 4) for total capacity and a few (set 1, 2, 5 and 9) for latent load capacity. The difference can be attributed to the dew point meter issue, the inlet air temperature and humidity stratification and the

uneven vertical frost distribution that may have affected the accuracy of the total capacity and latent load calculations. Figure 3.13 shows the variation of refrigerant outlet temperatures with time for case 4 (0/-30/90/2.2/0.5). The model assumes that each of the nine cross counter flow refrigerant circuits have the same refrigerant temperatures and thus the frost is evenly distributed from top to bottom of the heat exchanger. This assumption failed in some of the experiments conducted with air supply temperatures of 0 °C, due to the air temperature and humidity stratification perpendicular to the air flow at inlet of the heat exchanger. Figure 3.14 shows the variation of air inlet temperatures with time for case 4. It is found that the air supply temperature is not uniform, with warmer air at the top than at the bottom. It is due to this reason and also humidity stratification (due to improper mixing of steam inside the chamber) that causes more frost to grow on top of the heat exchanger than at the bottom, subsequently reducing more free flow area at the top and thus higher air velocities (higher air side heat transfer coefficient) causing higher frost growth at the top. In this way the cycle repeats itself causing more and more non-uniformity in the refrigerant outlet and air supply temperatures and hence the deviation between the model prediction and the experimental observations. For cases with air supply temperatures of –20 °C, the frost growth rate was very low and so the effects of air and humidity stratification were lesser and hence there is good agreement between the model and experiment. Again for dry cases there was no humidity addition and thus good agreement was obtained between model prediction and experimental data.
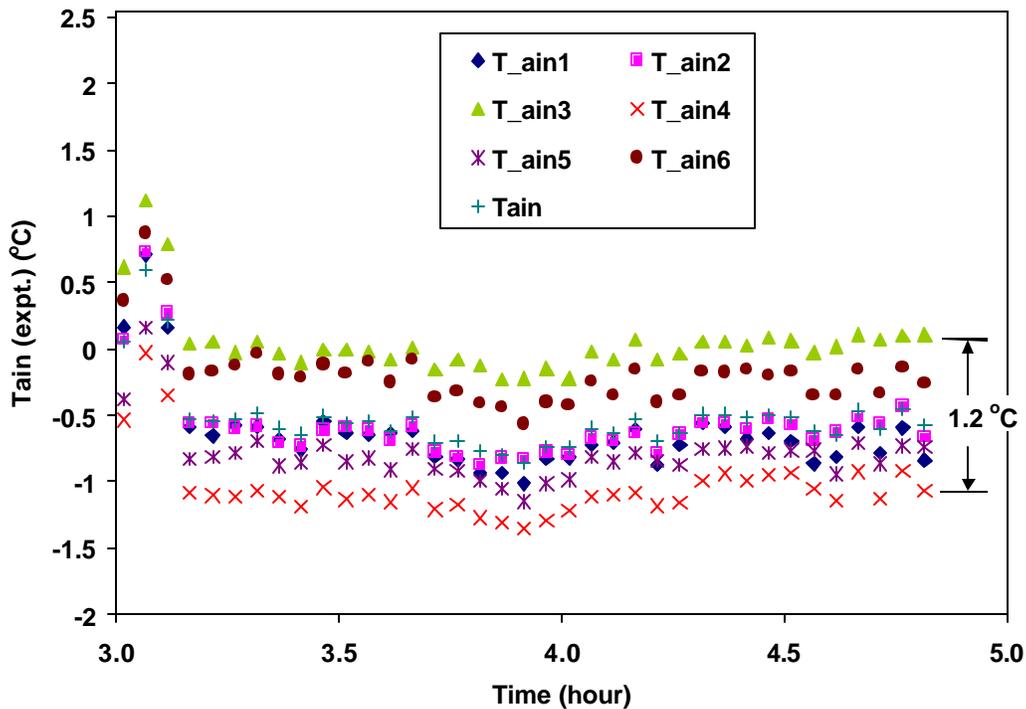

Figure 3.13 Refrigerant outlet temperatures (experimental) for case 4 (0/-30/90/2.2/0.5)
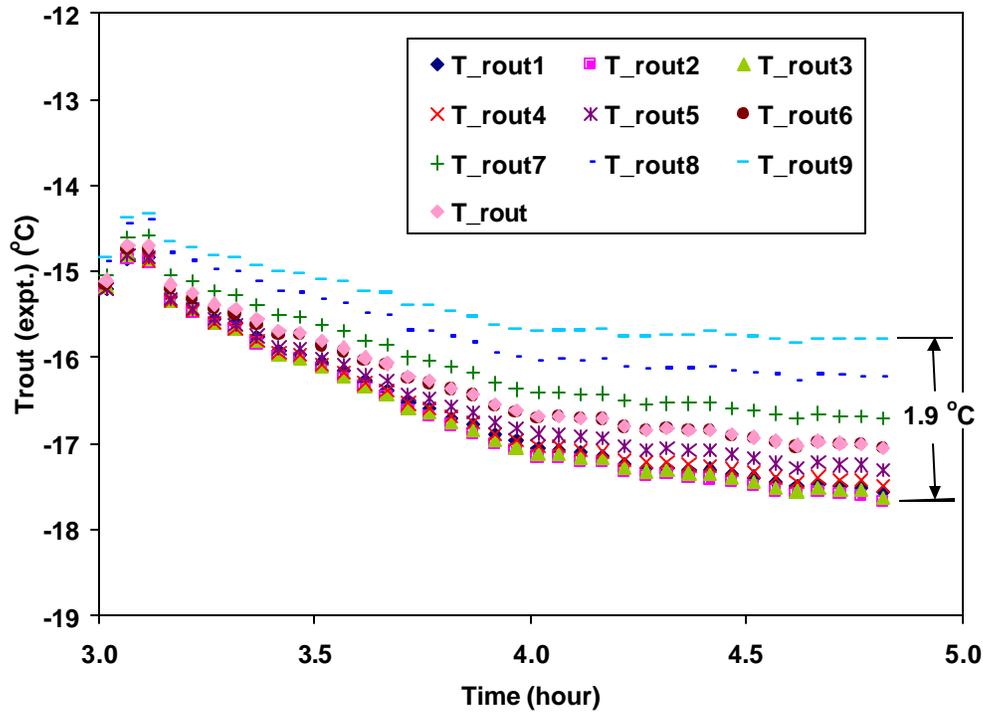
Figure 3.14 Air inlet temperatures (experimental) for case 4 (0/-30/90/2.2/0.5)

Table 3.5 shows total, sensible and latent heat transfer for all the eleven cases with values taken at the time when 2.5 kg of frost formed on the heat exchanger (as per scale measurement) for experiments with air supply temperature of 0 °C and 1.5 kg for cases with air supply temperature of –20 °C. The refrigerant side heat transfer is selected for total capacity values; the sensible heat transfer is taken from the measured air side values while the latent heat values are based on the scale measurements.

Table 3.5 Total, sensible and latent heat transfer for all the cases

Data Set	Time (hours)	Q_{total} (kW)	Q_{sens} (KW)	SHR (Q_{sens}/Q_{total})	Qlatent (KW)
0/-10/90/1.3/0.45	3.45	2.204	1.532	0.70	0.5717
0/-10/90/1.3/0.2	10.20	1.110	0.911	0.82	0.193
0/-10/90/1.3/0.26	4.90	1.257	0.894	0.71	0.402
0/-30/90/2.2/0.5	0.85	5.210	3.24	0.62	1.763
-20/-30/70/2.2/0.5	25.10	1.952	1.83	0.94	0.041
-20/-30/70/1.3/0.5	17.65	1.285	1.232	0.96	0.067
0/-10/90/0.9/0.5	4.85	1.494	1.081	0.72	0.407
0/-10/80/0.9/0.5	5.95	1.475	1.135	0.77	0.331
0/-10/70/0.9/0.5	7.85	1.471	1.178	0.80	0.251
-20/-30/70/0.9/0.5	9.05	1.359	1.278	0.94	0.131
-8/-32/90/0.6/0.5	2.25	1.994	1.680	0.85	0.491

<u>3.2.3 Air side pressure drop validation with time</u>

      Four pressure drops were measured in the experiments to track the change of the air side pressure drop at four locations along the centerline of the experimental rows of the heat exchanger, as shown in Figure 3.15.
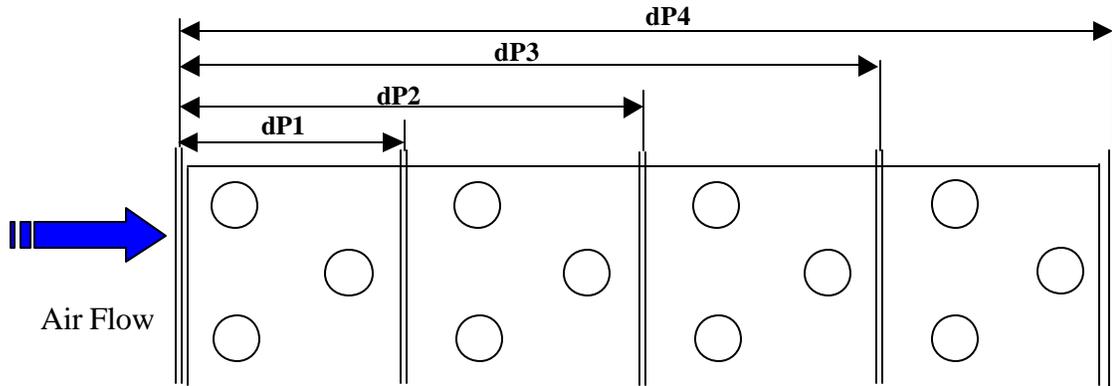

Figure 3.15 Air side pressure drop measurement

      Figure 3.16 compares the measured pressure drop with the predicted results for 0/-10/90/0.9/0.5. The model prediction the measured pressure drop for this particular case is very close.

      In most cases, good agreement was obtained in the comparison of air side pressure drop. However, for a few cases the pressure drop measurements were not accurate owing to improper alignment of the pressure sensors and so the model predictions were not in good agreement. During operation, for cases with higher air velocities, the pressure sensors got inclined from their initial vertical position giving rise to error in measuring the pressure drop across rows. Please refer to Appendix D for the validation results for each data set.
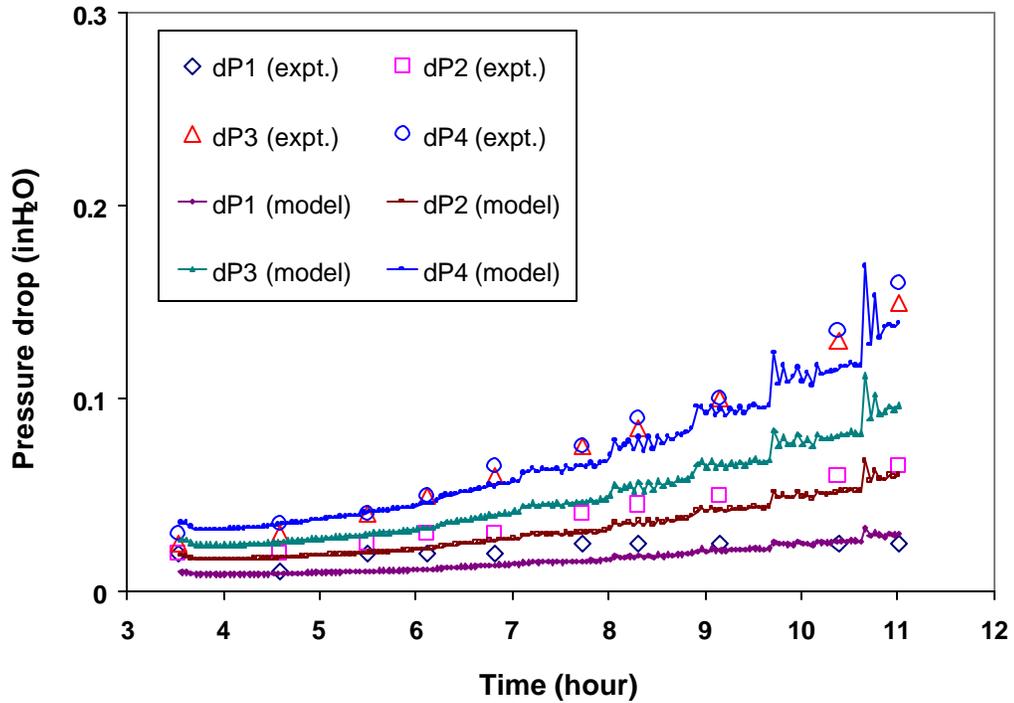
Figure 3.16 Comparison of air side pressure drop for 0/-10/90/0.9/0.5

3.2.4 Model validation of frost mass and thickness

        In all experiments, three independent methods were used to measure the frost mass. First, the heat exchanger rests on a scale, which shows how the total mass of frost increases with time. Second, defrosted water is collected after the experiment, which gives the total amount of frost that grows on the whole heat exchanger. The third method is to use the inlet and outlet dew point meters to calculate frosting rate (kg/s):

$$\dot{m}_{fr} = \dot{m}_{air}\left(w_{in} - w_{out}\right))\tag{3.20}$$

        In the model, the frosting rate is calculated for each of the eight tube rows and added together, as shown in the following equation:

$$\dot{m}_{fr} = \sum_{k=1}^{8}\dot{m}_{air}\left(w_{in,k} - w_{out,k}\right)\tag{3.21}$$

The same time interval was used in the experiments and the model (i.e., three minutes). For these comparisons, the model inputs the actual (3-minute average) experimental data recorded during the experiments (T_{ain}, RH_{in}, T_{rin}, $\dot{m}_{air}$, $\dot{m}_{ref}$).

        Figure 3.17 compares the predicted frost mass to that obtained from the experiment (0/-10/90/0.9/0.5) using the two methods mentioned above. The error shown for the final frost mass calculated from the dew point meters came from the ±0.2 °C uncertainty of the dew point measurements. Only two of the three experimental methods matched well with each other—the scale reading and mass of water collected (see Carlson (2001) for details), while

29

the frost mass calculated from the dew point measurement is almost twice as much as what the scale shows. The predicted result usually falls between these two for most of the cases.
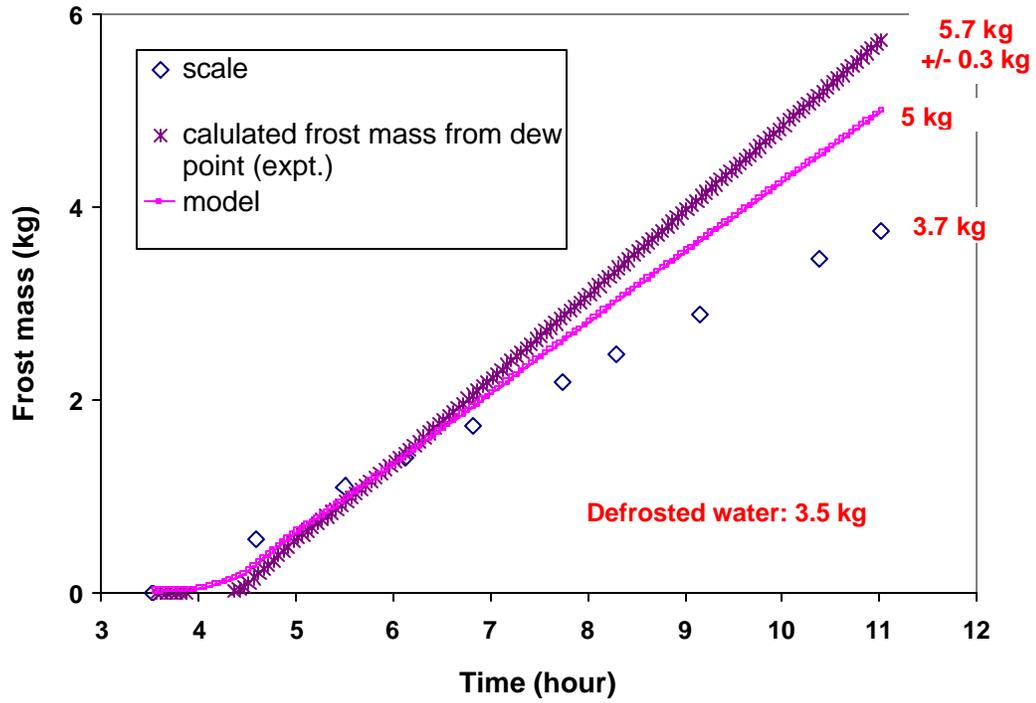

Figure 3.17 Comparison of the frosting rate for 0/-10/90/0.9/0.5

This discrepancy is due to the same problems discussed when predicted latent load was compared with the experimental data. The model was using the measured inlet dew point (RH_{in}) as one of its inputs and the predicted frosting rate tends to be within about 20% of the experimental results calculated using the dew point meters. The difference between these two is shown in Figure 3.18.
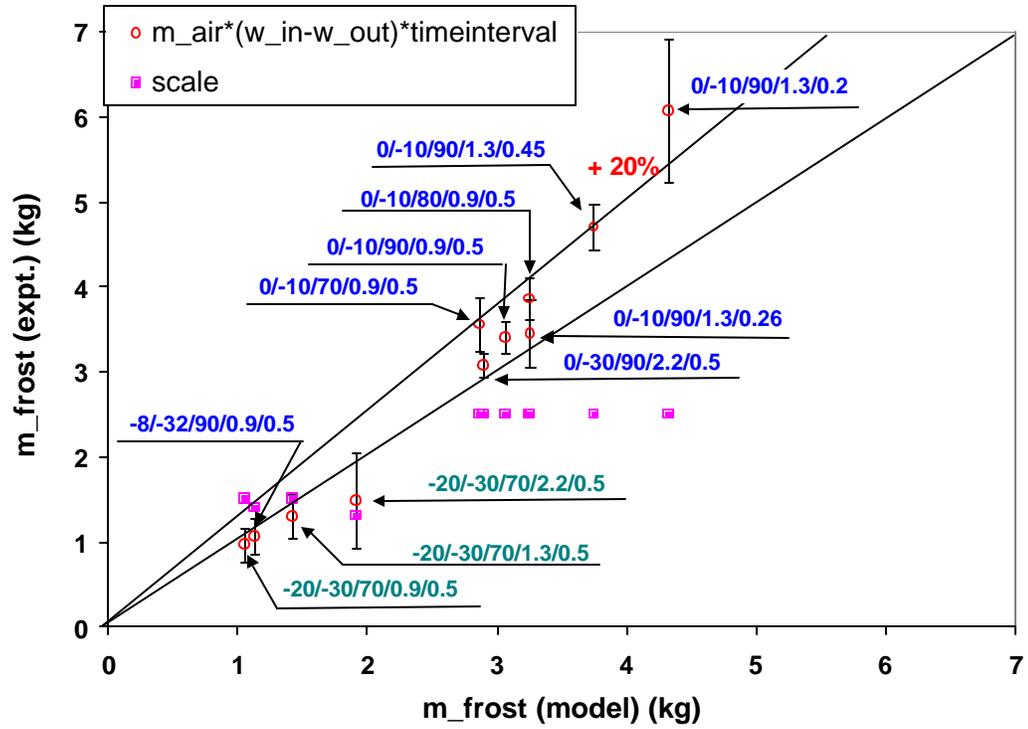
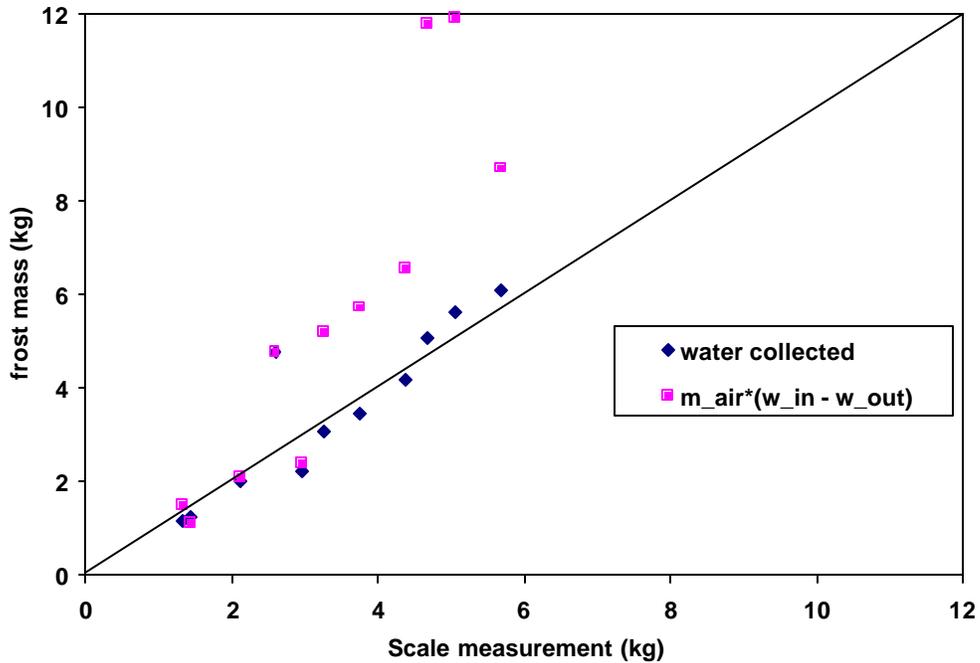Figure 3.18 Comparison of frost mass for all data sets

Figure 3.19 Comparison of experimental frost mass measurement for all data sets

Figure 3.19 shows the comparison of the measured mass transfer by scale, defrosted water and dew point measurements. From the figure it can be seen that the mass transfer from dew point measurements is over predicting that measured by scale. However, the defrosted water measurements are in close agreement with that of scale.

No instruments were used in the experiments to measure the frost thickness due to the difficulty in measuring the frost thickness in full-scale heat exchangers. Instead, the thickness was measured with the pictures taken of each row from time to time. Figure 3.20 shows the photos of rows 1, 3, 5 and 7 at the end of the 11-hour experiment (0/-10/90/0.9/0.5).
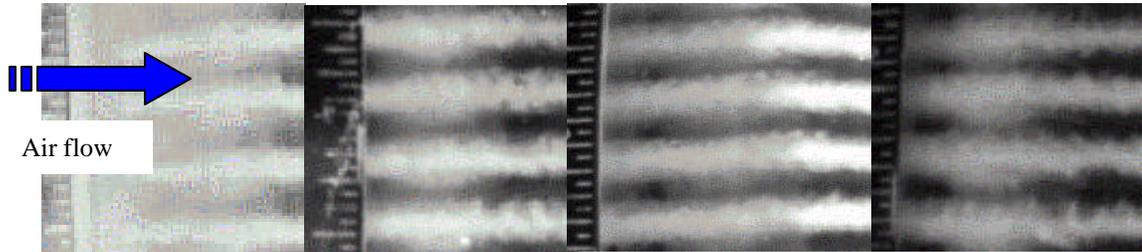

Figure 3.20 Frost pictures for 0/-10/90/0.9/0.5 (top view)

It can be seen that a ruler was placed before each of the four rows to help measure the frost thickness. Even so, it is very difficult to measure the thickness from these photos because the ruler is not accurate enough and the pictures are sometimes very obscure or dark to read. The uncertainty was very large, about ±1/32'' (±0.79mm).

The measured frost thickness is compared to the predicted values for 0/-10/90/0.9/0.5 case in Figure 3.21. Similar fair agreement was obtained in the other cases, which can be found in Appendix D.
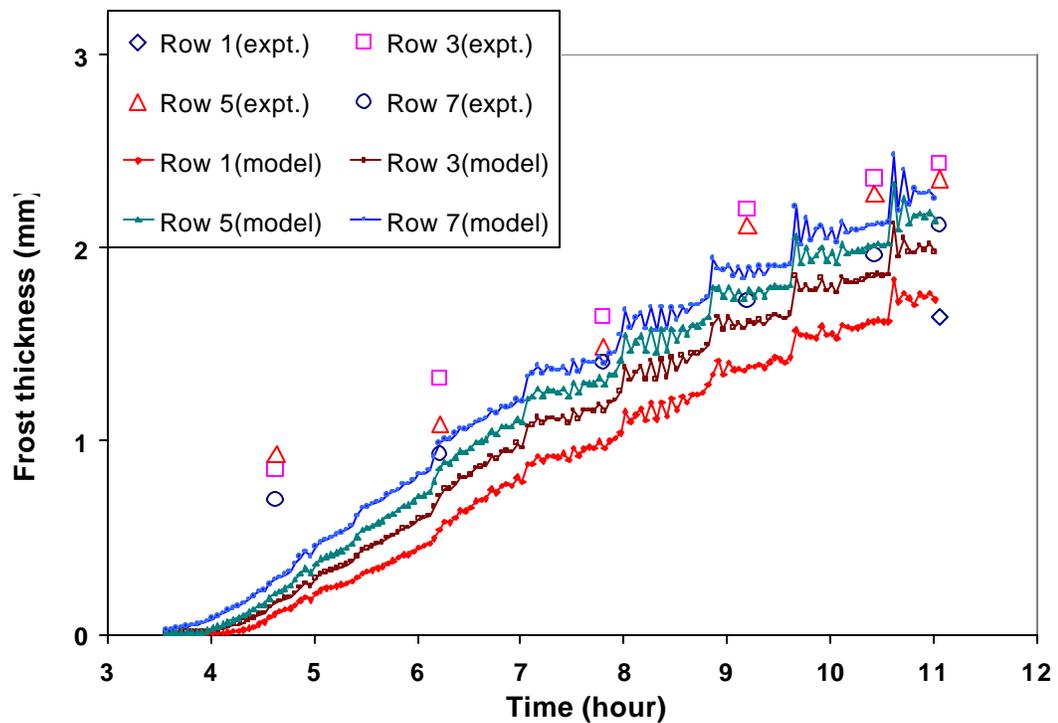

Figure 3.21 Comparison of frost thickness for 0/-10/90/0.9/0.5

3.3 Discussion

From the comparisons presented above and in Appendix D, it can be found that the model results agree very well with data under both dry and frosted conditions. Capacity, airside pressure drop, mass of frost, mass of frost thickness etc. can be well predicted.

Next, we present some interesting results from the model.

One of the goals of this research is to identify and analyze the factors affecting the frost deposition pattern (FDP) with the ultimate objective of finding ways to control the frost to be uniformly distributed across the surface of the heat exchangers and decrease the blockage effect of the frost on the air flow and thus increase the time interval between defrost.

FDP depends on the geometry of the heat exchanger and operating conditions. For a particular heat exchanger, the operating conditions play the most important role in causing different FDPs.

A wide range of FDPs has been observed on this heat exchanger. In some cases, more frost would form at the leading edge. Model results show that air velocity, air inlet humidity, and surface temperature (determined by refrigerant mass flow rate, inlet refrigerant temperature and air inlet temperature) all affect the FDP, as shown in Figures 3.22, 3.23, 3.24 and 3.25. From Figure 3.22 we see that low air velocity, high air inlet humidity, high refrigerant mass flow rate (i.e., smaller refrigerant temperature rise) causes more frost to form on the front rows. Changing in the air inlet humidity with other parameters remaining constant (figure 3.23), it is observed that the frost deposition pattern does not change much, however the amount of frost deposited increases with an increase in the air inlet humidity. Again from figure 3.24, it can be seen that for a secondary refrigerant the mass flow rate of refrigerant has little effect on the FDP as compared to the effect of changing velocity depicted in figure 3.22. Finally, decreasing the air supply causes more frost to grow on the front rows than the back as shown in figure 3.25 and visa-versa. Keeping these observations in mind would help us achieve design the proper operating conditions, which could lead to uniform frost distribution as well as desired performance of the heat exchanger.
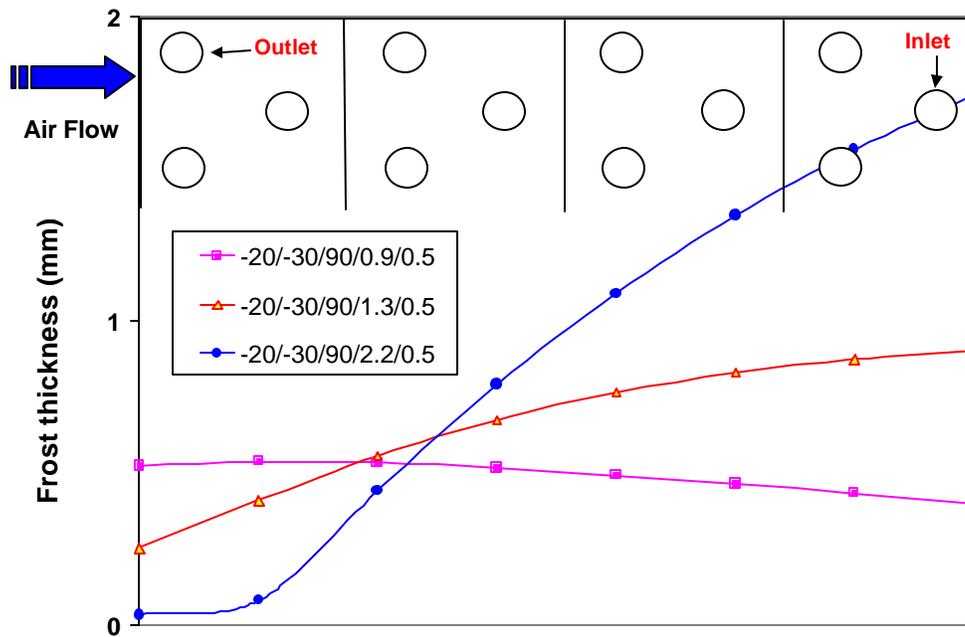
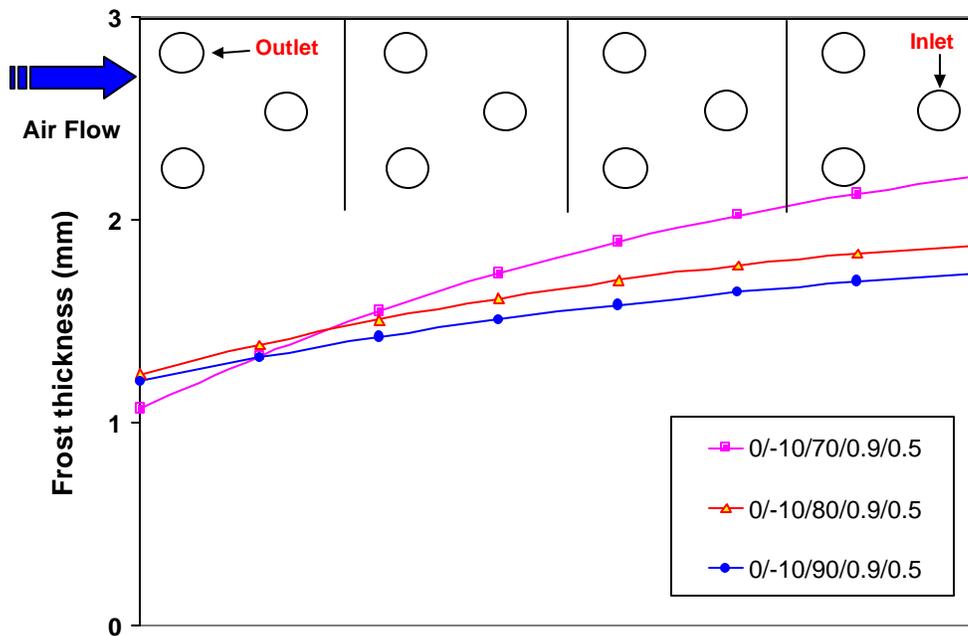Figure 3.22 Effect of air velocity on FDP

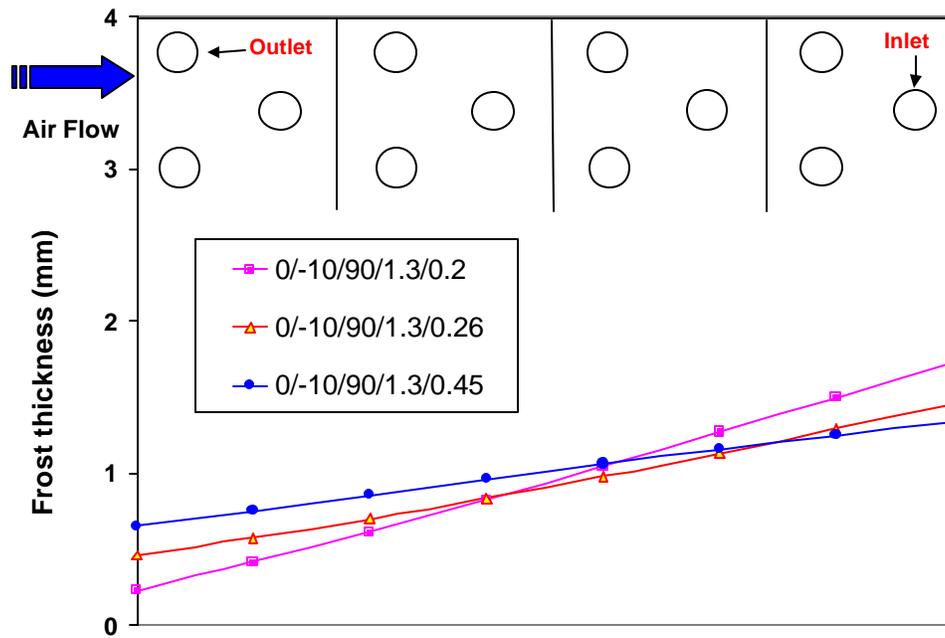Figure 3.23 Effect of air inlet humidity on FDP
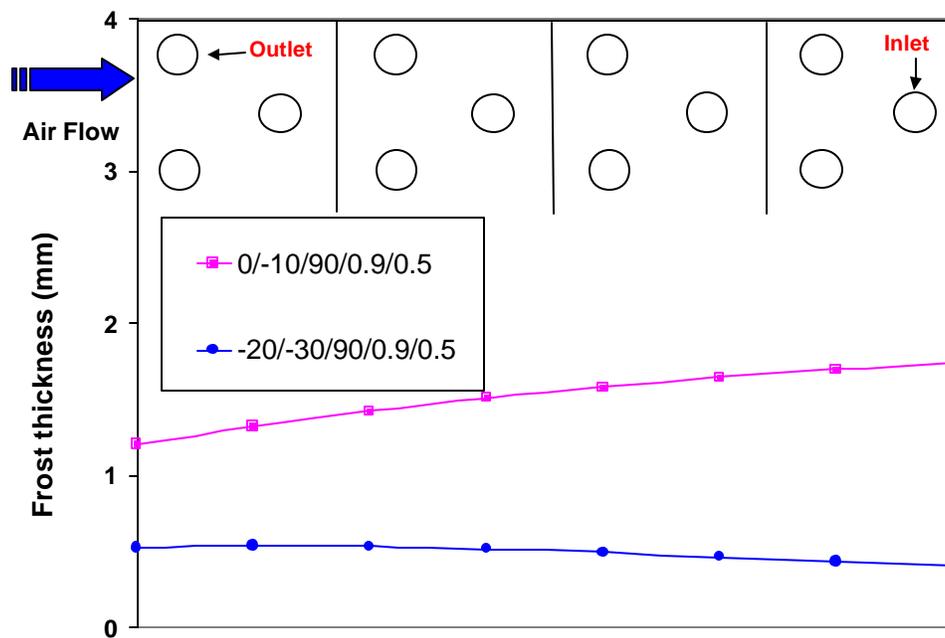
Figure 3.24 Effect of refrigerant mass flow rate on FDP

Figure 3.25 Effect of air inlet temperature on FDP

3.4 Conclusions and recommendations for future work

This report provides a good model and insight for predicting the performance of a full-scale heat exchanger with plain fins under frosted conditions. Experimental model was successful overall. Outlet air temperatures were predicted within the range of experimental uncertainty as shown in Table 3.4. Thus the model's ability to predict the sensible heat transfer during frosting conditions is excellent. Prediction of the latent heat transfer was far less accurate (APD's of 5 to 29%), apparently due to poor placement of the inlet due point measurement, which overestimated mass transfer (for most of the cases) compared to the other two direct measurement techniques employed as shown in Figure 3.19. Since the inlet dew point measurement (placed in the middle of the evaporator chamber) was closer to the steam addition there exists a strong possibility that the measured inlet dew point was higher than the actual dew point at the exact inlet of the heat exchanger. Consequently, the temperature difference between the inlet and outlet dew point measurement was higher than the actual and hence could account for the much higher prediction of the frost mass deposition using the dew point measurement as compared to scale measurement. For future experiments this measurement error can be significantly reduced by sampling the air at the exact inlet of heat exchanger for inlet dew point measurement. Since the model was forced to rely on the inlet dew point measurement, its prediction of mass transfer agreed more closely (~20 %) with that obtained from the dew point measurement as shown in Figure 3.18.

Interestingly, despite the inlet dew point uncertainty, the model prediction of total (sensible plus latent) capacity agreed with refrigerant side heat transfer within the limits of experimental error, as indicated by the predictions of the refrigerant exit temperature shown in Table 3.4. For most of the experiments, the SHR (Sensible Heat Ratio) was so large, 70 to 96% as shown in Table 3.5 that errors in predicting mass transfer did not have significant effects on Q_{total}. However, the effects are still important because of the effect of frost on rate of degradation of Q_{sens}.

In future efforts could be made in predicting the optimal defrost time for a display case heat exchanger using this model and also extend the present model to other heat exchanger geometries, for example staggered fin arrangements. Also, present model can be modified to predict the effect of the previously discussed parameters on FDP for direct expansion coil type heat exchangers. Finally, if the frost/defrost model could be generalized to many kinds of heat exchangers including micro-channel heat exchangers and fin surface enhancements, great progress could be made in the management and control of frost in the refrigeration system.

Chapter 4: Simulation of the Performance of the Heat Exchanger under the Effect of a Fan Curve

4.1 Introduction

The heat exchanger described in Chapters 2 and 3 was designed based on the geometry of heat exchangers that are typically used in the supermarket display cases (Carlson, 2001). In this chapter, it is placed into a virtual duct and runs under the control of two identical fans working in parallel as shown in Figure 4.1. This is the typical configuration of supermarket display cases (Terrell, 1999).
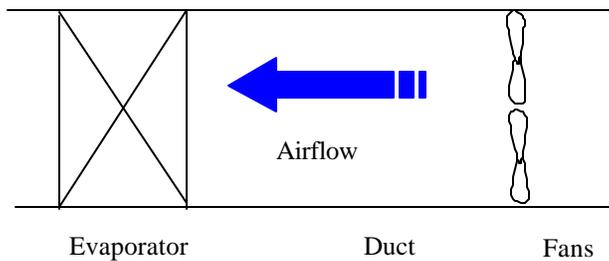

.

Figure 4.1 Schematic of the supermarket display case

Typically, two fans of 5W SP type are installed in a display case refrigerator manufactured by Tyler. The fan curve for each of the fan provided by Kempiak (2001) is shown in Figure 4.2. Figure 4.3 shows the fan curve for two fans (each of the type shown in figure 4.2) operating in parallel.

$$y = -2E\text{-}07x^3 + 3E\text{-}05x^2 - 0.0026x + 0.15$$
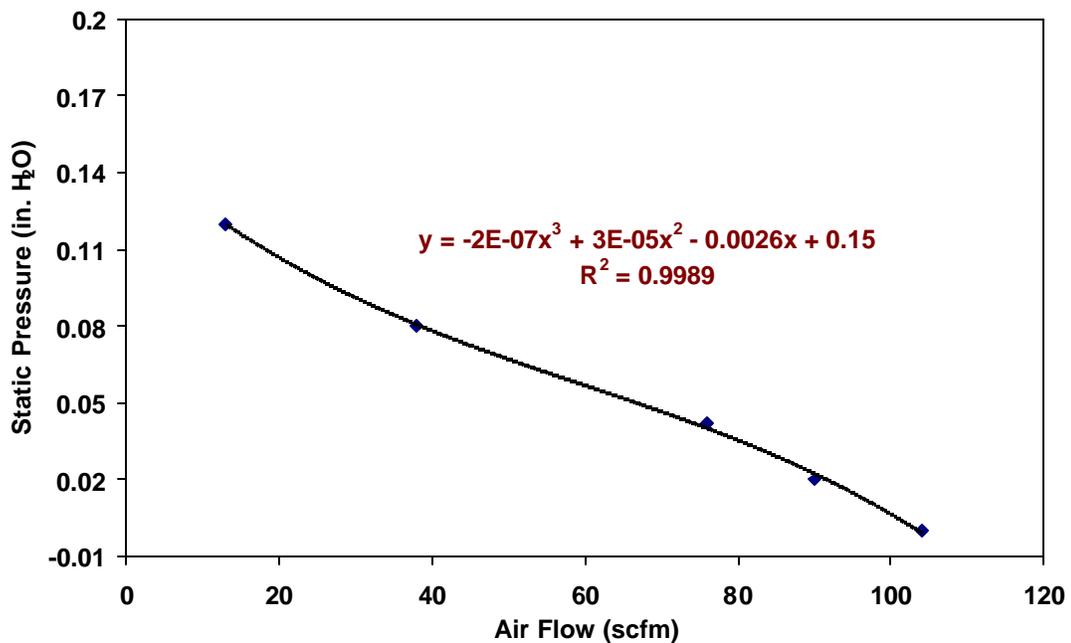$$R^2 = 0.9989$$
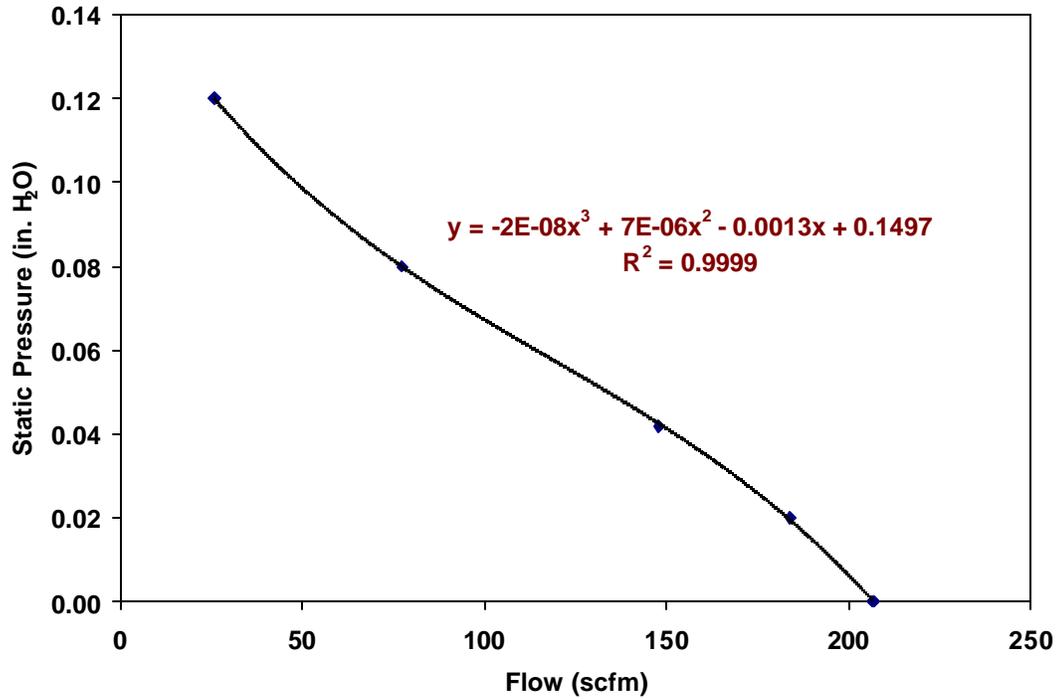
Figure 4.2 Fan curve (Kempiak, 2001)

Figure 4.3 Fan Curve for two fans in parallel

Since these fans operate in parallel inside the duct, the relationship between pressure drop across fan and the volumetric air flow rate across the heat exchanger can be expressed by the following relation

$$dP_{fan} = -2*10^{-8}*\dot{V}_{air}^{3} + 7*10^{-6}*\dot{V}_{air}^{2} - 0.0013*\dot{V}_{air} + 0.1497 \tag{4.1}$$

Where, dP_{fan} = Pressure drop across the fan, inH_2O

$\dot{V}_{ait}$ =   Volumetric flow rate of air, CFM

Also, the pressure loss due to airflow in the duct is given by

$$dP_{duct} = \frac{1}{2} \cdot C_d \cdot \mathbf{r}_{air} \cdot vel_{air}^{2} \tag{4.2}$$

Where, dP_{duct} = Pressure loss across the duct, inH_2O

C_d =   Dimensionless pressure loss coefficient

vel_{air} = Air face velocity, fpm

      Mao et al. (1997) studied a similar heat exchanger typically used in a supermarket display case, with a face velocity of 0.5 m/s and corresponding volumetric flow rate of 162 CFM. At this flow rate, the pressure drop across the heat exchanger (predicted by the model) and fan curve were 0.01 inH_2O and 0.037 inH_2O respectively. Therefore, the pressure drop in the duct was 0.027 inH_2O and C_d is determined to be 45.13 from Eqn.(4.2). Actually,

our heat exchanger was designed based on the geometry and performance of their heat exchanger. The virtual duct shown in Figure 4.1 is also very similar to their duct. So C_d=45.13 is used in the simulation.

4.2 Simulation model

To the quasi-steady frosting model was added a fan curve equation to simulate the performance of the heat exchanger in this scenario.

Carlson (2001) presented the typical display case operating conditions. Only the meat case condition is simulated here (i.e., air inlet temperature at about 2 °C and refrigerant inlet temperature around -6.7 °C). Since a single-phase refrigerant (HFE 7100) is used in the heat exchanger, its mass flow rate could be adjusted to simulate both the DX coils and the indirect coils. Table 4.1 lists the two conditions used in the simulation. The first one is used to simulate the DX coil with a very large mass flow rate of refrigerant and hence small temperature glide. The second with relatively low mass flow rate of refrigerant is used to simulate the operations of a secondary refrigerant (large temperature glide). The refrigerant inlet temperature is chosen to achieve exactly the same sensible capacity for both coils (here, $Q_{sens} = 0.65$ kW).

Table 4.1 Operating conditions for two simulation cases

Operating conditions	DX	Secondary
Air inlet temperature (°C) : T_{ain}	2	2
Refrigerant inlet temperature (°C) : T_{rin}	-5.3	-7.4
Air inlet relative humidity: RH_{in}	90%	90%
Initial air volumetric flow rate (CFM): $\overset{\bullet}{V}_{air}$	179	179
Refrigerant mass flow rate (kg/s): $\overset{\bullet}{m}_{ref}$	2.6	0.35

As in Chapter 3, these two simulation cases are named using the format: air inlet temperature/refrigerant inlet temperature/air inlet relative humidity/air velocity/ refrigerant mass flow rate. Therefore, the DX coil is named as 2/-5.3/90/0.5/2.6 and the secondary refrigerant case, 2/-7.4/90/0.5/0.35.

4.3 Results and discussion

For a simulation period of fourteen and a half hours Figures 4.4 and Figure 4.5 depict the fan curve for DX coil and indirect refrigeration respectively. As seen in Figure 4.4 and 4.5, the increase in the pressure drop across the fan with time for DX case is 1.5 times that across indirect case. Also, at the end of simulation period, the CFM drops by 49% for DX coil while for indirect refrigeration it drops by 22% as shown in Figure 4.6, for the operating conditions described in Table 4.1. Thus for the same capacity and air supply temperature, the indirect refrigeration can sustain longer time between defrosts as compared to the DX case, if the decrease in volumetric flow rate is considered as the criterion for initiating defrost.
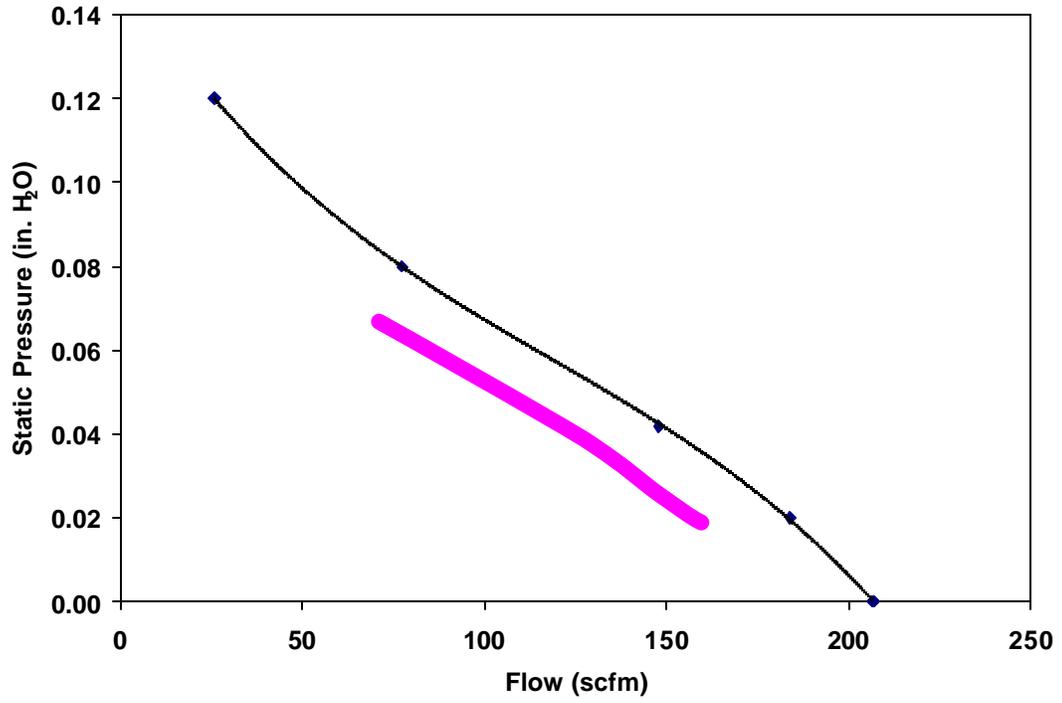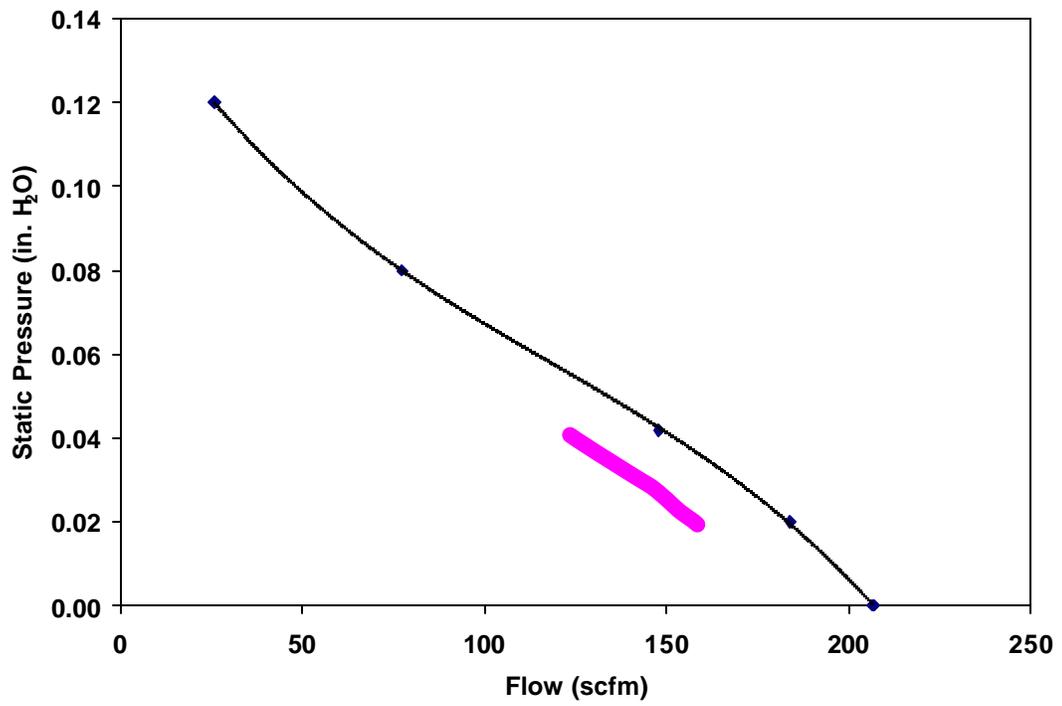
Figure 4.4 Fan operating range (DX)
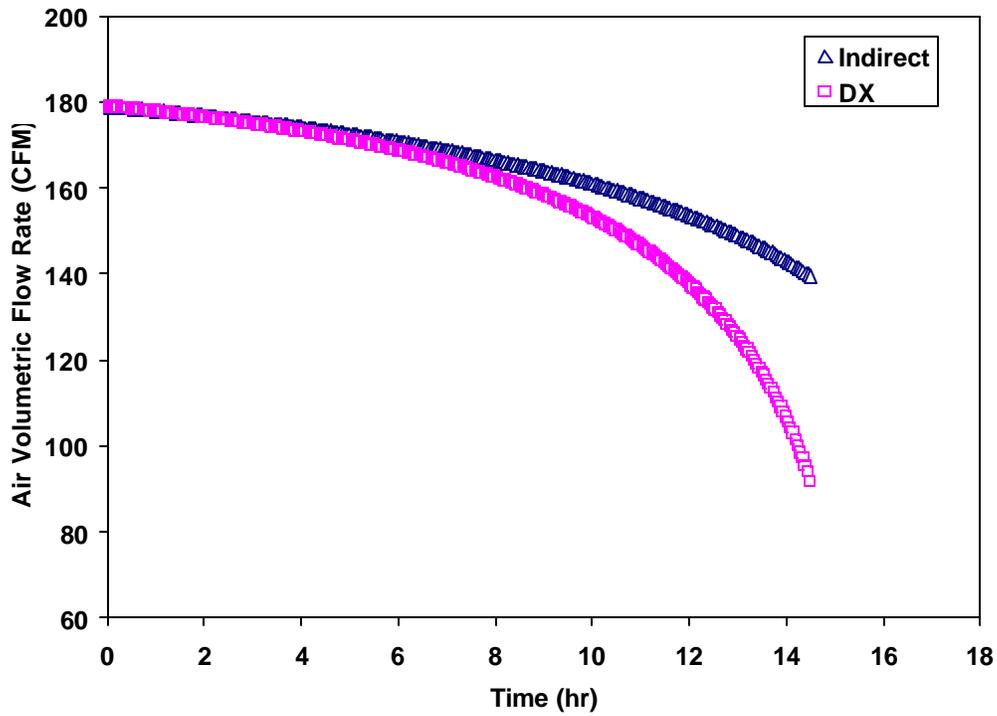

Figure 4.5 Fan operating range (Indirect)

Figure 4.6 Degradation of the volumetric air flow rate

Figure 4.7 shows the decrease in the capacity of the heat exchanger with time for both the cases. It can be seen that 23% drop in total capacity of the heat exchanger is encountered in DX case four hours before that in indirect case. The sensible capacity of the heat exchanger is also affected by the frost in the same way as total capacity for both the cases, as shown in Figure 4.8. Hence, if drop in capacity is considered as the defrost criterion then also the indirect refrigeration system offers longer operation periods and hence lesser number of defrosts than DX case.
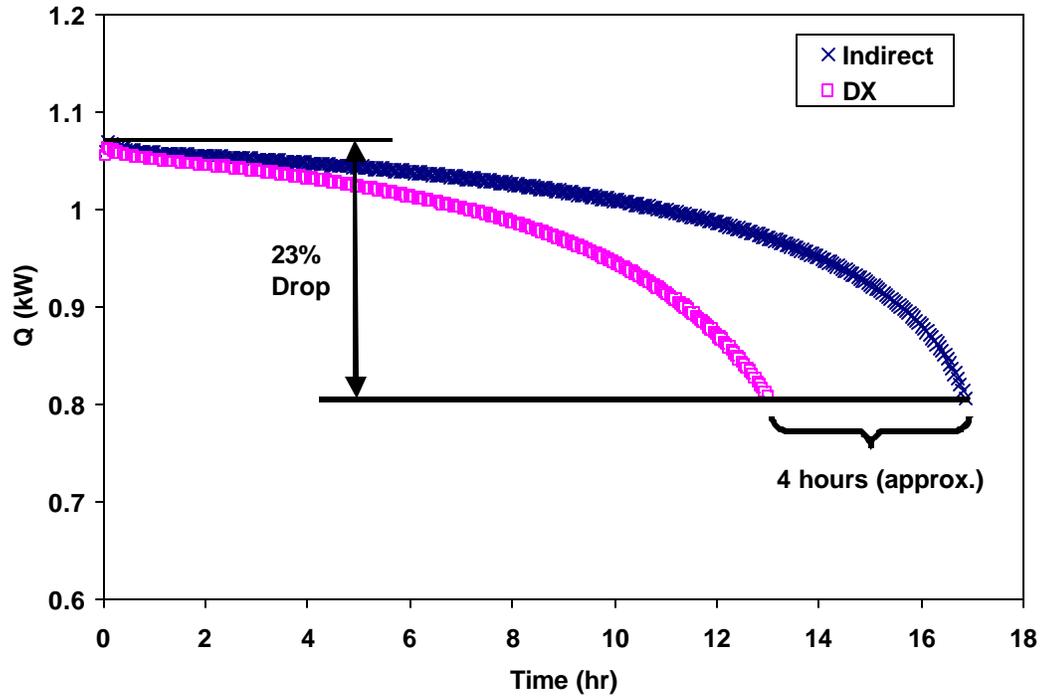
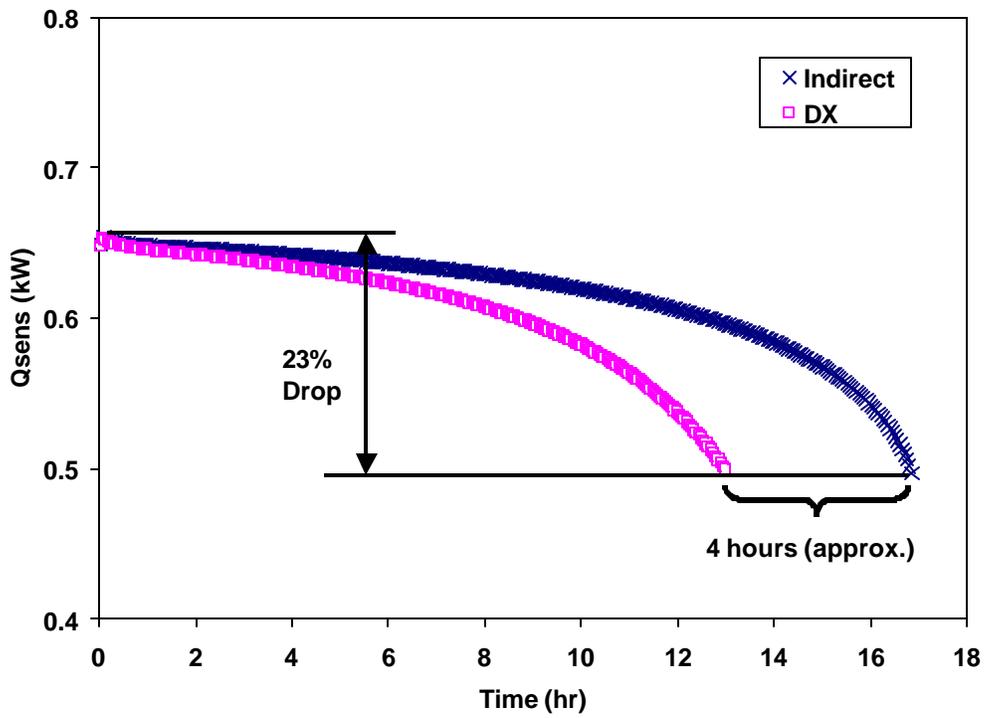Figure 4.7 Degradation of total capacity

Figure 4.8 Degradation of the sensible capacity

Meanwhile, although the frosting rate for the whole heat exchanger is the same for both cases as shown in Figure 4.9, the frost distribution pattern is totally different. In the DX coil case, the amount of frost that grows on the leading-edge row at the end of simulation period is almost seven and a half times that on the trailing edge row, as shown in Figure 4.10. In contrast, the amount of frost growth on the leading-edge row for indirect refrigeration is two times that on the trailing edge row at the end of simulation. Also the amount of frost growth on the leading edge for DX case is 50% more than that for indirect refrigeration, while at the trailing edge the frost growth for indirect case is twice as much as DX case.
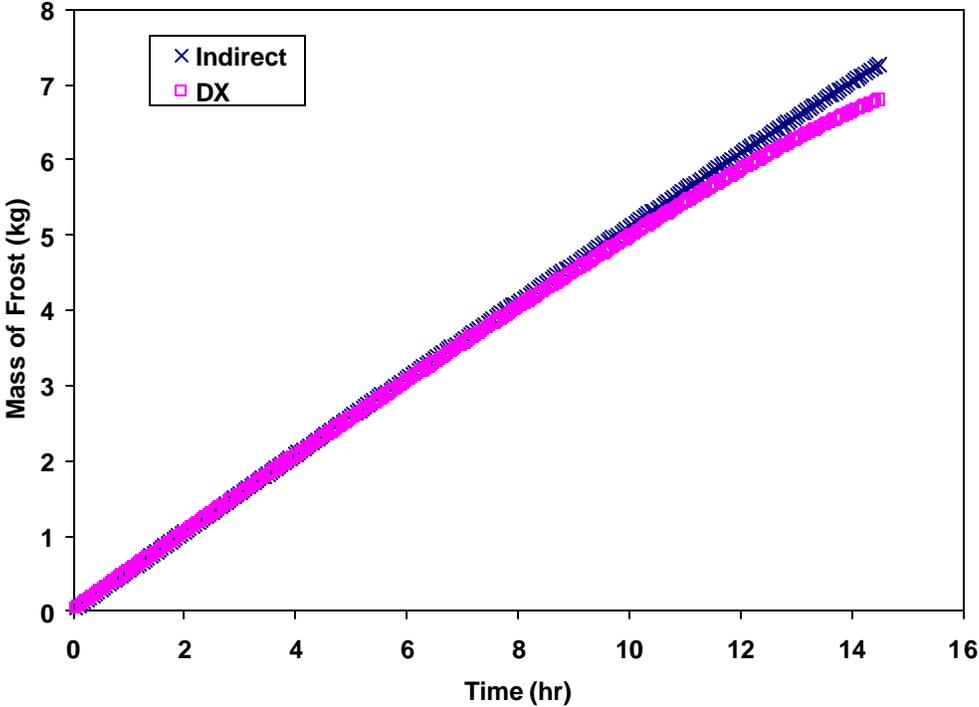

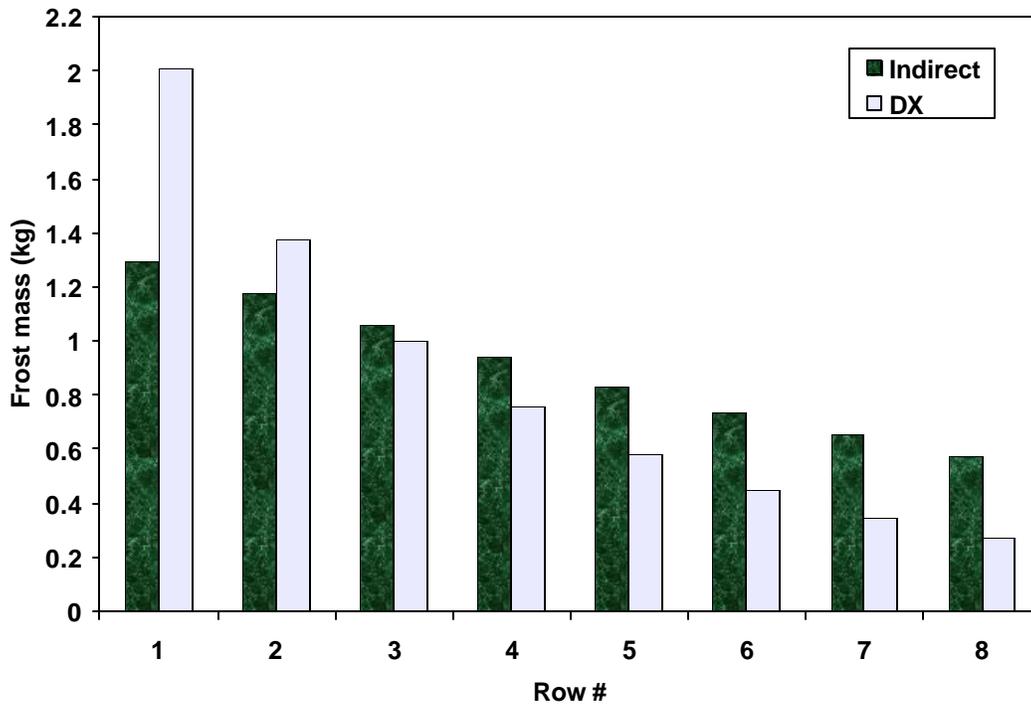Figure 4.9 Total frost deposition rate

Figure 4.10   Frost mass deposition patterns

The different frost deposition patterns can be explained by examining the absolute humidity glides as shown in Figure 4.10 for the DX coil and Figure 4.11 for the secondary refrigerant case. The absolute humidity difference between the humid air and saturated surface is the driving force for frost formation. The higher the difference is, the more frost grows on the surface of the heat exchanger. From these two graphs, we can see that large absolute humidity difference at the leading edge causes most of the frost to form in the DX coil case. The absolute humidity glide is affected by the temperature glide, which can be adjusted to control the frost mass distribution.
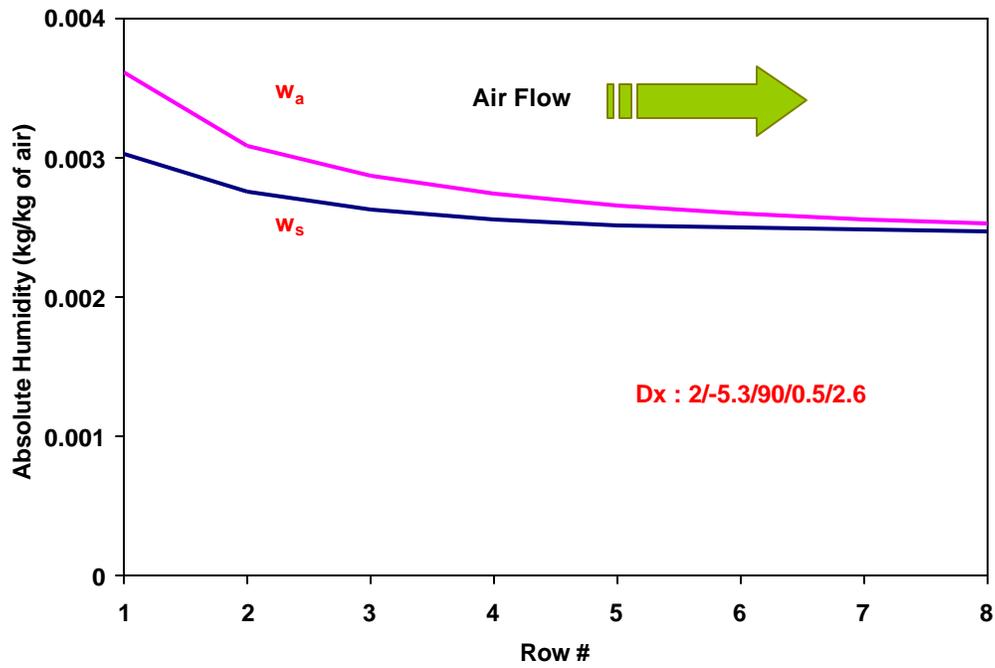
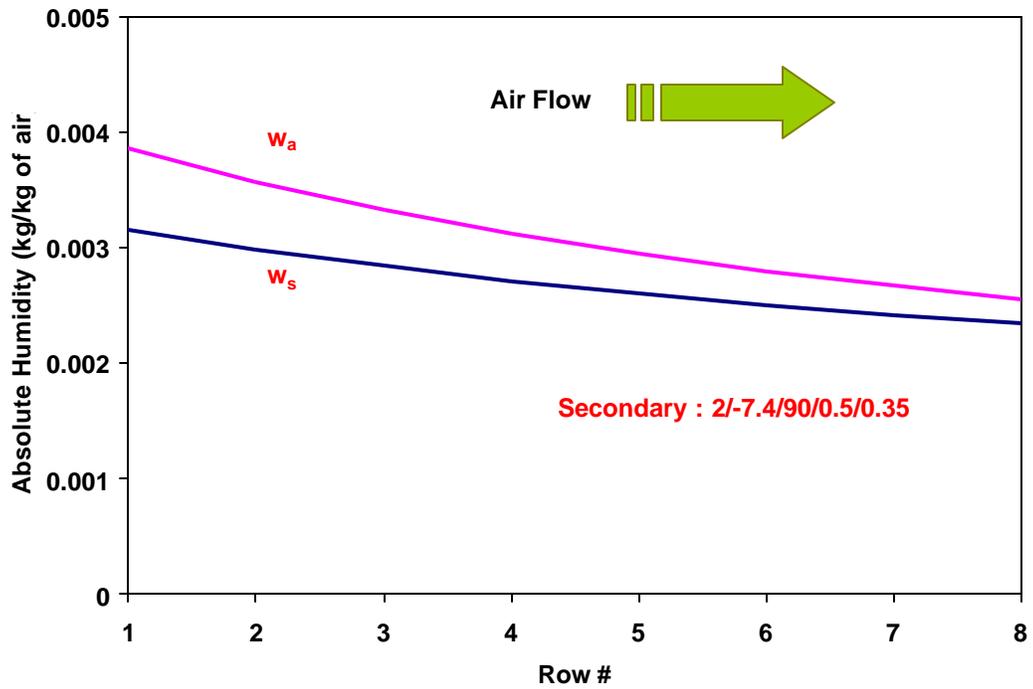Figure 4.11 Absolute humidity glide for the DX coil

Figure 4.12 Absolute humidity glide for the secondary refrigerant

In reality, we care more about frost thickness distribution than frost mass distribution because it is the one that actually affects the air free flow area and heat transfer coefficient, and therefore affects the capacity and air side pressure drop which will determine the air mass flow rate under the control of a fan curve. Figure 4.13 shows the frost thickness on the eight tube rows at the end of simulation period for these two cases. The variation in the frost thickness distribution is totally different for both the cases as the temperature difference is more at the leading edge and much less at the trailing edge for the DX coil in comparison with the almost constant temperature difference of secondary refrigerant coil. For DX case, the frost thickness is much more at the leading edge than at the trailing edge owing to much larger absolute humidity difference at the leading edge as shown in Figure 4.11. In contrast, the secondary refrigeration has an almost uniform frost thickness distribution from the leading edge to the trailing edge owing to less variation in the absolute humidity glide as shown in Figure 4.12. In spite of higher absolute humidity difference at the leading edge than at the trailing edge, the frost thickness is higher at the trailing edge than at the leading edge for indirect refrigeration. This is due to the variation in density of the frost from leading edge
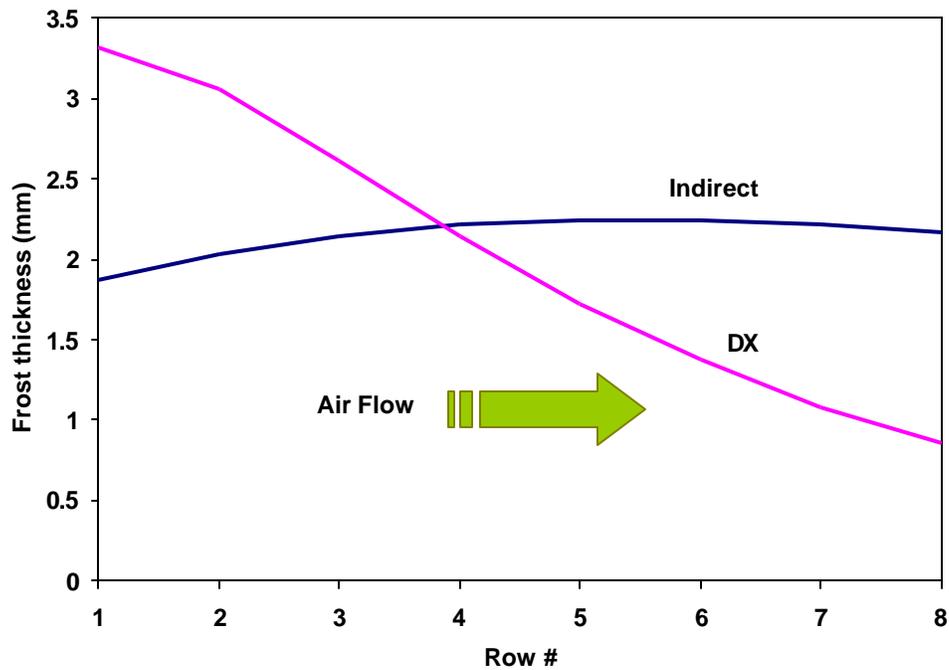

Figure 4.13 Comparison of frost thickness distribution

to the trailing edge as shown in Figure 4.14. As shown, variation in the density of the frost along the rows is higher in case of indirect refrigeration as compared to DX coil. Also the frost density is higher at the leading edge for indirect case than the DX case and visa-versa.
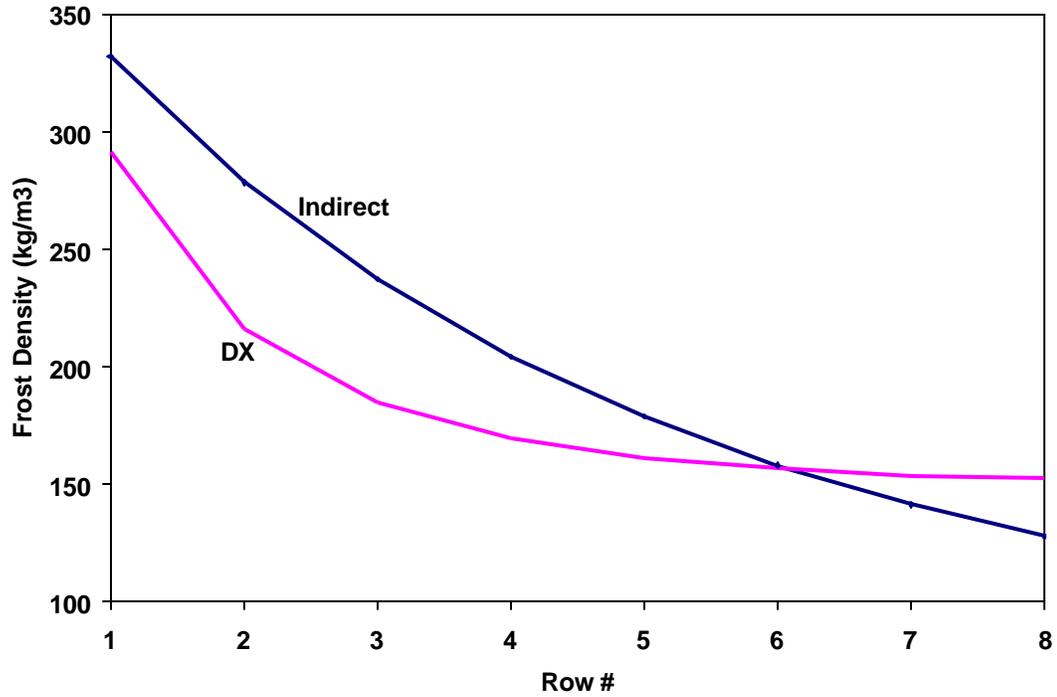
Figure 4.14 Frost Density Distribution for both cases

Figure 4.15 and 4.16 show the air, wall and refrigerant temperature distribution across the rows at the end of simulation period for DX and indirect refrigeration cases respectively. Owing to the higher temperature difference between air and the wall at the leading edge for the DX coil, frost mass deposition is higher at the leading edge than the trailing edge. For the secondary refrigerant case, the frost mass deposition is nearly constant across the rows because of the nearly constant temperature difference between air and wall as shown in Figure 4.14.
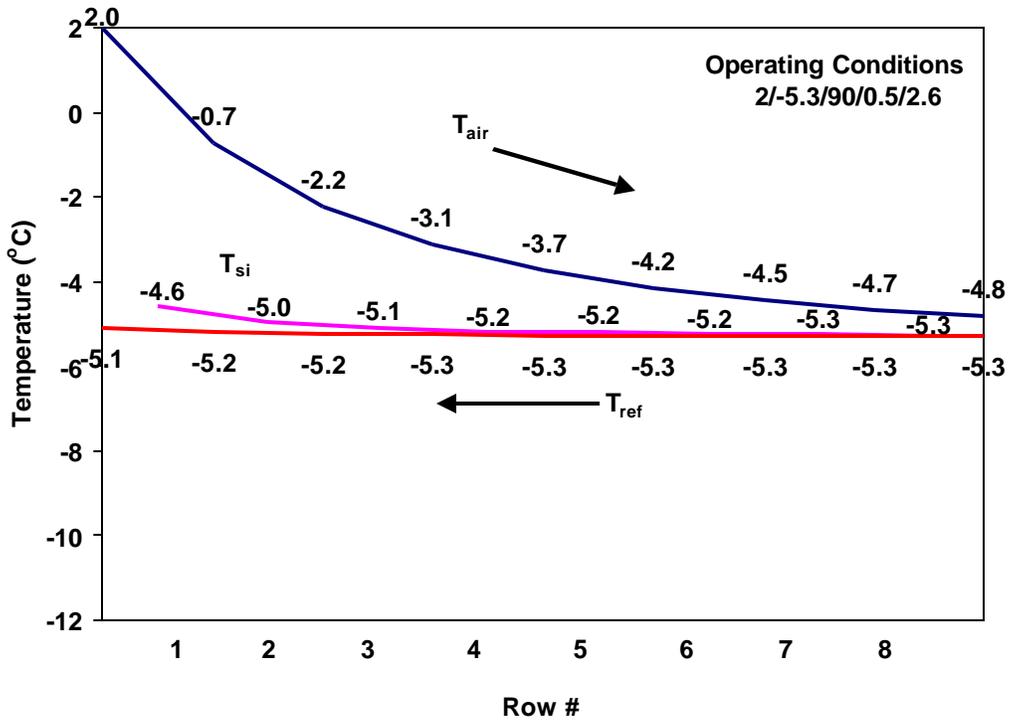
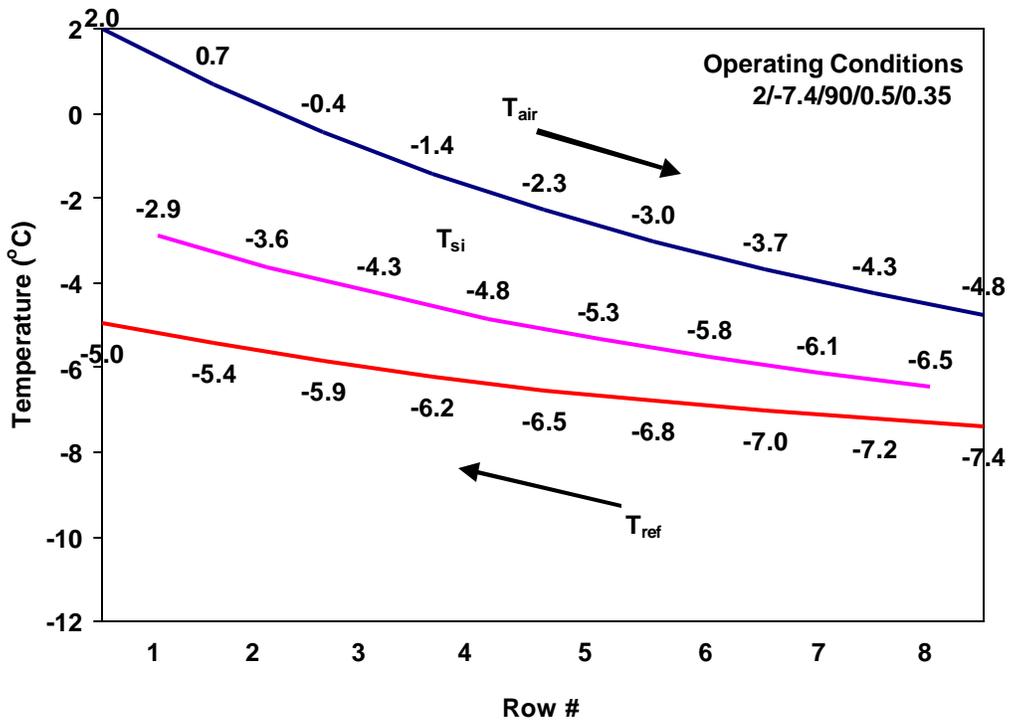Figure 4.15 Temperatures for DX coil

Figure 4.16 Temperatures for indirect refrigeration

4.4 Conclusion and future recommendations

After comparing the pressure drop, volumetric flow, sensible capacity and frost thickness distribution for DX and indirect refrigeration for the operating conditions specified in Table 4.1, it can be concluded that indirect refrigeration offers longer time between successive defrosts due a more uniform frost distribution pattern. However, the DX behavior predicted by the current model and presented in this analysis is based on very high mass flow rate of secondary refrigerant causing a negligible refrigerant temperature glide to simulate DX behavior. It does not include the effects of refrigerant pressure drop and changing heat transfer coefficient (refrigerant side), which are a typical of DX refrigeration system. In future, the current model could be extended to include actual DX behavior, incorporating the heat transfer and pressure drop correlations of a two phase refrigerant, thereby combining effectively the features of DX and indirect refrigeration to obtain the most favorable operating conditions for uniform frost growth across the heat exchanger and thus minimize the frequency of defrosts.

Bibliography

1. Bridges B.D. and C.W. Bullard. 1995. Simulation of Room Air Conditioner Performance. MS thesis, ACRC TR-79, University of Illinois at Urbana-Champaign, IL.

2. Chen, H., L. Thomas, and R.W. Besant. 2000. Modeling Frost Characteristics on Heat Exchanger Fins: Pt. I, Numerical Model. ASHRAE Transactions, 106, Pt.2.

3. Chen, H., L. Thomas, and R.W. Besant. 2000. Modeling Frost Characteristics on Heat Exchanger Fins: Pt. II, Model Validation and Limitations. ASHRAE Transactions, 106, Pt.2.

4. Chen, H., R.W. Besant, and Y.X. Tao. 1999. Frost Characteristics And Heat Transfer On A Flat Plate Under Freezer Operating Conditions: Pt. II, Numerical Modeling And Comparisons With Data. ASHRAE Transactions, 105, Pt. 2: 252-259.

5. Chen, H., L. Thomas, and R.W. Besant. 1999. Measurement of Frost Characteristics on Heat Exchanger Fins, Part II: Data and Analysis. ASHRAE Transactions, 105, Pt.2.

6. Dietenberger, M.A. 1983. Generalized Correlation of the Water Frost Thermal Conductivity. Int. J. Heat Mass Transfer, 26(4): 607-619.

7. Dyer, J. M., B.D. Storey, J.L. Hoke, A.M. Jacobi, and J.G. Georgiadis. 2000. An Experimental Investigation of Effect of Hydrophobicity on the Rate of Frost Growth in Laminar Channel Flows. ASHRAE Transactions, 106, Pt.1.

8. Elmahdy, A.H., and R.C. Biggs. 1983. Efficiency of Extended Surfaces with Simultaneous Heat and Mass Transfer. ASHRAE Transactions, Vol. 89:135-143.

9. Emery, A. F., and B.L. Siegel. 1990. Experimental Measurements of the Effects of Frost Formation on Heat Exchanger Performance. ASME – HTD, Vol.139: 1-7.

10. Gnielinski, V. 1976. New Equations for Heat and Mass Transfer in Turbulent Pipe and Channel Flow. Int. Chem.Eng.,16:359-368.

11. Gray D.L., and R.L. Webb. 1986. Heat transfer and friction correlations for plate finned-tube heat exchangers having plain fins. Proc 8th Heat Transfer conference: 2745-2750.

12. Hayashi Y., Aoki K., Yuhura H., 1976. Study of Frost Formation Based on a Theoretical Model of the Frost Layer. Trans. Japan Society Mechanical Engineers, Vol. 40:885-899.

13. Hayashi, Y., A. Aoki, S. Adachi, and K. Hori. 1977. Study of Frost Properties Correlation with Frost Formation Types. Journal of Heat transfer, 99: 239-245.

14. Hoke, J.L., J.G. Georgiadis, and A.M. Jacobi. 2000. The Interaction between the Substrate and Frost Layer through Condensate distribution. Ph.D. Dissertation. Univ. of Illinois at Urbana-Champaign.

15. Inan, C. 1999. Heat and Mass Transfer through a Domestic Refrigerator and Evaluation of Evaporator Performance under Frosted Conditions. Ph.D. Dissertation. Istanbul Technical University, Univ. of Illinois at Urbana-Champaign.

16. Incropera, F.P., and D.P. DeWitt. 1996. Fundamentals of Heat and Mass Transfer. John Wiley & Sons, 4th Edition.

17. Kays, W.M., and M.E. Crawford. 1993. Convective Heat and Mass Transfer. McGraw-Hill, Inc. 3rd Edition.

18. Kim, N.H., B. Youn, and R.L. Webb. 1999. Air-Side Heat Transfer and Friction Correlations for Plain Fin-and-Tube Heat Exchangers with Staggered Tube Arrangements. Transactions of ASME, Vol.121: 662-667.

19. Kondepudi, S. N., and D. L. O'Neal. 1989. Performance of Finned Tube Heat Exchangers under Frosting Conditions. ASME – HTD, Vol.123: 193-200.

20. Kondepudi, S. N., D.L. O'Neal. 1987. The Effect of Frost Growth on Extended Surface Heat Exchanger Performance—a Review. ASHRAE Transactions, 93(2): 258-274.

21. Korte, C.M., and A.M. Jacobi. 1997. Condensate Retention and Shedding Effects on Air-Side Heat Exchanger Performance. ACRC, University of Illinois at Urbana-Champaign.

22. McQuiston, F.C. 1978a. Heat Mass and Momentum Transfer Data for Five Plate-Fin Tube Transfer Surface. ASHRAE Transactions, 84(1): 266-293.

23. McQuiston, F.C. 1978b. Correlation of Heat Mass and Momentum Transport Coefficients for Plate-Fin-Tube Heat Transfer Surfaces with Staggered Tubes. ASHRAE Transactions, 84(1): 293-309.

24. Mao Y., R.W. Besant, and H. Chen. 1999. Frost Characteristics and Heat Transfer on a Flat Plate under Freezer Operating Conditions: Pt. I, Experimentation and Correlations. ASHRAE Transactions, 105, Pt. 2: 231-251.

25. Mao Y., R.W. Besant, and K.S. Rezkallah. 1992. Measurement and Correlations of Frost Properties with Airflow over a Flat Plate. ASHRAE Transactions, 98, Pt.2: 65-78.

26. Mao, Y., W.J. Terrell Jr., R.C. Reef, and P.S. Hrnjak. 1997. New Coolant for Indirect Refrigeration Based on Potassium Formate. ACRC, University of Illinois at Urbana-Champaign, IL.

27. Ogawa, K., N. Tanaka, and M.Takeshita. 1993. Performance Improvement of Plate Fin-and-tube Heat Exchangers under Frosting Conditions. ASHRAE Transactions, 99: 762-771.

28. O'Neal, D.L., and D.R. Tree. 1985. A Review of Frost Formation in Simple Geometries. ASHRAE Transactions, 91: 267-281.

29. Oskarsson, S.P. 1990. Evaporator Model for Operation with Dry, Wet and Frosted Finned Surfaces, Pt. I and II. ASHRAE Transactions, 96(1): 373-392.

30. Oskarsson, S.O., K.I. Krakow, and S. Lin. 1990. Evaporator Models for Operation with Dry, Wet and Frosted Finned Surfaces, Pt. I: Heat transfer and Fluid Flow Theory, ASHRAE Transactions 96, Pt.1: 373-380

31. Oskarsson, S.O., K.I. Krakow, and S. Lin. 1990. Evaporator Models for Operation with Dry, Wet and Frosted Finned Surfaces, Pt. II: Evaporator Models and Verification, ASHRAE Transactions 96, Pt.1: 381-392

32. Ostin, R., and S. Andersson. 1991. Frost Growth Parameters in a Forced Air Stream. Int. J. Heat Mass Transfer, Vol. 34(4-5): 1009-1017.

33. Padki, M.M., S.A. Sherif, and R.M. Nelson. 1989. A Simple Method for Modeling the Frost Formation Phenomenon in Different Geometries. ASHRAE Transactions, 95, Pt.2: 1127-1137.

34. Pira, J.V., C.W. Bullard, and A.M. Jacobi. 2000. An Evaluation of Heat Exchangers Using System Information and PEC. MS thesis. ACRC, University of Illinois at Urbana-Champaign.

35. Rite, R.W., and R.R. Crawford. 1991. A Parametric Study of the Factors Governing the Rate of Frost Accumulation on Domestic Refrigeration-freezer Finned-tube Evaporator. ASHRAE Transactions, 97, Pt.2: 438-446.

36. Sami, S.M., and T. Duong. 1989. Mass and Heat Transfer during Frost Growth. ASHRAE Transactions, 95, Pt.1: 158-165.

37. Sekhar, N.K., and D.L. O'Neal. 1993. A Simplified Model of Pin Fin Heat Exchangers Under Frosting Conditions. ASHRAE Transactions, 99, Pt.1: 754-761.

38. Stasiulevicius, J., A. Skrinska and A. Zukauskas. 1988. Heat Transfer on Finned Tube Bundles in Cross flow. Hemisphere Publishing Corporation.

39. Stoecker, W.F., and J.W. Jones. 1982. Refrigeration and Air Conditioning. 2nd Edition. McGraw-Hill, Inc.

40. Storey, B.D., and A.M. Jacobi. 1999. The Effect of Streamwise Vortices on the Frost Growth Rate in Developing Laminar Channel Flows. International Journal of Heat and Mass Transfer 42: 3787-3802.

41. Tao, Y.X., Y. Mao, and R.W. Besant. 1994. Frost Growth Characteristics on Heat Exchanger Surfaces: Measurement and Simulation Studies. ASME, HTD-Vol.286: 29-38.

42. Tao, Y.X., R.W. Besant, and K. S. Rezkallah. 1993. A Mathematical Model for Predicting the Densification and Growth of Frost on a Flat Plate. Int. J. Heat Mass Transfer, Vol. 36(2): 353-363.

43. Thomas, L., H. Chen, and R.W. Besant. 1999. Measurement of Frost Characteristics on Heat Exchanger Fins, Part I: Test Facilities and Instrumentation. ASHRAE Transactions, 105, Pt.2.

44. Terrell Jr., W.J. 1995. Evaluation of Secondary Fluids for Use in Low-temperature Supermarket Applications. MS thesis. ACRC, University of Illinois at Urbana-Champaign.

45. Threlkeld, J.L. 1970. Thermal Environmental Engineering (2nd Edition). Prentice-Hall, New York, N.Y.

46. Wattelet, J.P., and J.C. Chato. 1994. Heat Transfer Flow Regimes of Refrigerants in a Horizontal - tube Evaporator. University of Illinois at Urbana-Champaign, ACRC TR-55.

47. Wang, C. C., and C. T. Chang. 1998. Heat and Mass Transfer for Plate Fin-and-Tube Heat Exchangers, With and Without Hydrophilic Coating. Int. J. Heat and Mass Transfer, 41: 3109-3120.

48. Wang, C. C., Y. J. Chang, Y. C. Hsieh, and Y. T. Lin. 1996. Sensible Heat and Friction Characteristics of Plate Fin-and-Tube Heat Exchangers Having Plane Fins. Int. J. of Refrigeration, 19(4): 223-230.

49. Wang, C. C., Y.C. Hsieh, and Y. T. Lin. 1997. Performance of Plate Finned Tube Heat Exchangers under Dehumidifying Conditions. Journal of Heat Transfer, 119: 109-117.

50. Webb, R.L. 1990. Air-side Heat Transfer Correlations for Flat and Wavy Plate Fin-and-tube Geometries. ASHRAE Transactions, 96(2): 445-449.

51. Xiao, Q., and W.Q.Tao. 1990. Effect of Fin Spacing on Heat Transfer and Pressure Drop of Two-Row Corrugated-fin and Tube Heat Exchanger. Heat Mass Transfer, Vol. 17: 577-586

52. Yonko, J.D., and C.F. Sepsy. 1967. An Investigation of the Thermal Conductivity of Frost while Forming on a Flat Horizontal Plate. ASHRAE Transactions 73, Pt. II: I.1.1-I.1.11.

Appendix A   Fin Surface Efficiency

A.1 Fin surface efficiency under dry conditions

The surface efficiency under dry conditions is obtained from the fin efficiency with an area-weighting factor (Incropera and DeWitt, 1990):

$$\boldsymbol{h}_{suf} = 1 - \frac{A_{fin}}{A_o}\left(1 - \boldsymbol{h}_f\right) \tag{A.1}$$

Where A_{fin} fin surface area

$A_o = A_{fin} + A_t$ total heat transfer area

A_t tube outer surface area

$\boldsymbol{h}_f$ fin efficiency

$\boldsymbol{h}_{suf}$ surface efficiency

Because of the staggered tubes in the evaporator, the fin efficiency $\boldsymbol{h}_f$ is calculated using the sector method with conduction. As shown in Figure A.1, the hexagonal area of fins around each tube is divided into eight zones. Each zone is then divided into four sectors. The number of sectors can be increased for better approximation
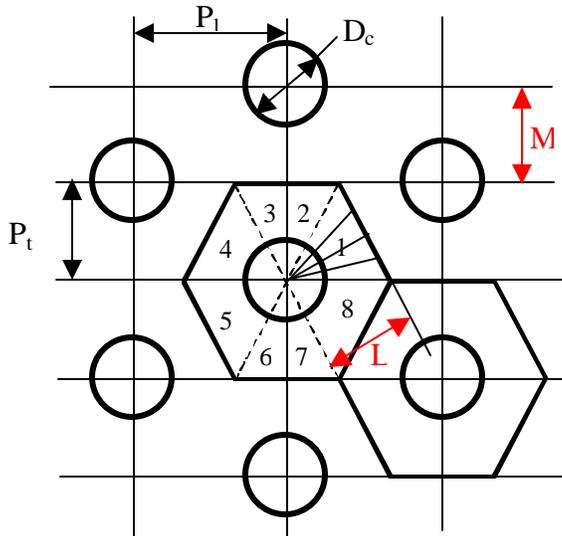
Figure A.1 Sector method (plain-fin)

The total fin efficiency can be calculated by the sum of the multiplication of fin efficiencies for each sector in each zone and S_n divided by the sum of surface areas of all eight sectors in each zone.

$$h_f = \frac{\sum\limits_{n=1}^{N} S_n h_n}{\sum\limits_{n=1}^{N} S_n}$$

(A.2)

Where S_n surface area of each sector (see below for calculation)

h_n is given in terms of modified Bessel functions:

$$h_n = \frac{2r_i}{m(r_{oo,n}^2 - r_i^2)} \left[\frac{K_1(mr_i)I_1(mr_{oo,n}) - K_1(mr_{oo,n})I_1(mr_i)}{K_1(mr_{oo,n})I_0(mr_i) + K_0(mr_i)I_1(mr_{oo,n})} \right]$$

(A.3)

$$m = \sqrt{\frac{2h_a}{k_{fin}F_{th}}}$$, fin parameter

h_a airside heat transfer coefficient, $W/m^2 \cdot K$

k_{fin} fin conductivity, $kW/m \cdot K$

F_{th} fin thickness, m

n = 1, 2, 3, 4

N=4 (number of sectors in each zone)

Two radii are needed for the sector method. One is the inner radius r_i that depends on the fin-tube connection. ARI Standard 410 (1981) recommends the following equation for plate-type fins with collars touching the adjacent fin.

$$r_i = \frac{D_c}{2} + F_{th}$$

(A.4)

Where r_i inner radius (different from tube inner radius)

     D_c tube outer diameter

The other radius r_o is outer radius, which comes from the approximation of area of the hexagonal using that of a circle with radius equal to r_o (Korte and Jacobi, 1997). r_o is obtained from $r_{o,n} = R_n \, r_i$, where R_n is the radius ratio and n represents zone 1 to 8.

R_n and S_n are calculated differently in sectors for zone 2, 3, 6, and 7 from sectors for zone 1, 4, 5, and 8. For zone 2, 3, 6, and 7:

$$R_n = \frac{M}{r_i} \sqrt{\left(\frac{2n-1}{2N}\right)^2 + \left(\frac{L}{M}\right)^2}$$

(A.5)

$$S_n = \frac{r_i^2}{2}\left(R_n^2 - 1\right)\left[\tan^{-1}\left(\frac{nM}{NL}\right) - \tan^{-1}\left(\frac{(n-1)M}{NL}\right)\right]$$ (A.6)

Where n = 1, 2,3,4 and N=4, and $M = \dfrac{P_t}{2}, \quad L = \dfrac{P_l}{2}$.

For zone 1, 4, 5, and 8:

$$R_n = \frac{M}{r_i}\sqrt{\left(\frac{2n-1}{2N}\right)^2\left(\frac{L}{M}\right)^2 + 1}$$ (A.7)

$$S_n = \frac{r_i^2}{2}\left(R_n^2 - 1\right)\left[\tan^{-1}\left(\frac{nL}{NM}\right) - \tan^{-1}\left(\frac{(n-1)L}{NM}\right)\right]$$ (A.8)

Where n = 1,2, 3,4 and N=4.

A.2 Fin surface efficiency under frosted conditions

Though many efforts have been devoted to study of fin surface efficiency under dehumidifying conditions, the available literature on frosted heat exchangers still offers very limited information. Therefore, for the present study the wet fin surface efficiency is determined by analyzing the heat balance across an element of thickness dx m, shown in Figure A.2. The heat balance states that the rate of heat flow entering the fin element at positon 1 from the end of the fin plus the heat transferred by conduction from the frost surface to the element.
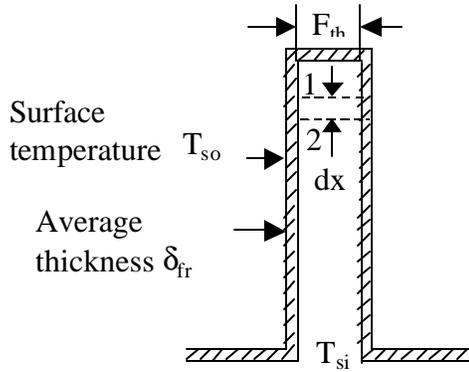
Figure A.2 Wet Fin surface Efficiency

The heat balance for the fin element is

$$k_{fin}\frac{f_{th}}{2}z\left(\frac{dT_f}{dx}\right)_1 + k_{fr}zdx\left(\frac{T_{so}-T_f}{d_{fr}}\right) = k_{fin}\frac{f_{th}}{2}z\left(\frac{dT_f}{dx}\right)_2$$ (A9)

$$k_{fin} \frac{f_{th}}{2} \left[\left(\frac{dT_f}{dx} \right)_2 - \left(\frac{dT_f}{dx} \right)_1 \right] = k_{fr} dx \left(\frac{T_{so} - T_f}{d_{fr}} \right) \qquad (A10)$$

where

T_f temperature of fin, ^{o}C

The wet fin surface efficiency determination is similar to that of dry fin surface efficiency except that the fin parameter, m as obtained form Eq. (A10) is now defined as

$$m = \sqrt{\frac{k_{fr}}{d_{fr} k_{fin} \frac{F_{th}}{2}}} \qquad (A11)$$

The variation of frosted fin surface efficiency with frost thickness for one operating conditions, 0/-10/90/1.3/0.45 is shown in Figure A.4 It can be seen that when the frost thickness grows from 0 to 1mm the fin surface efficiency increases rapidly reaching 98% after 1mm of frost has been deposited on the fins. Eventually the fin surface efficiency reaches 100% with the frost thickness of 3.5 to 4mm, with the heat exchanger being blocked completely. Thus it can be concluded that once 1mm of frost gets deposited on the fin, the reduction in heat transfer due to insulating effect (lower thermal conductivity of frost) of frost causes the entire fin to be at the base temperature.
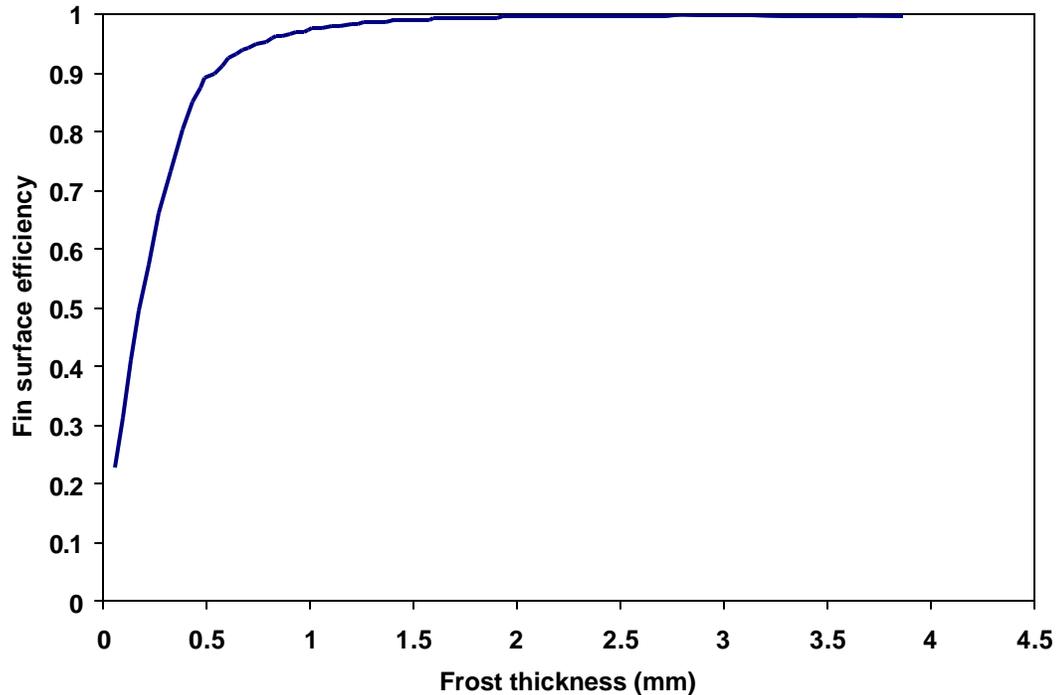
Figure A.4 Variation of predicted fin surface efficiency with frost thickness for 0/-10/90/1.3/-0.45.

Appendix B: Heat Transfer and Pressure Drop Correlations

B.1 Air side heat transfer coefficient correlations
1)   Wang and Chang (1998)

$$h_{a,wang} = j_{wang} \cdot G_{max} \cdot C_{p,a} \cdot \Pr^{-\frac{2}{3}} \tag{B.1}$$

$$j_4 = 0.357 \, \mathrm{Re}_{D_c}^{-0.328} \left(\frac{P_t}{P_l} \right)^{-0.502} \left(\frac{F_s}{D_c} \right)^{0.0312} \left(\frac{P_l}{D_c} \right)^{-1.28} \tag{B.2}$$

$$\frac{j_N}{j_4} = 0.991 \cdot \left[2.24 \cdot \mathrm{Re}_{D_c}^{-0.092} \cdot \left(\frac{N}{4} \right)^{-0.031} \right]^{0.607 \cdot (4-N)} \tag{B.3}$$

2)   Wang, Chang, Hsieh, and Lin (1996)

$$j = 0.394 \, \mathrm{Re}_{Dc}^{-0.392} \left(\frac{F_{th}}{D_c} \right)^{-0.0449} NP^{-0.0897} \left(\frac{F_p}{D_c} \right)^{0.212} \tag{B.4}$$

3)   Kim, Youn and Webb (1999)

$$h_{a,kim} = j_{kim} \cdot G_{max} \cdot C_{p,a} \cdot \Pr^{-\frac{2}{3}} \tag{B.5}$$

$$j_{N=3} = 0.163 \, \mathrm{Re}_D^{-0.369} \left(\frac{P_t}{P_l} \right)^{0.106} \left(\frac{F_s}{D} \right)^{0.0138} \left(\frac{P_t}{D} \right)^{0.13} \tag{B.6}$$

$$\frac{j_{N=1,2}}{j_{N=3}} = 1.043 \cdot \left[\mathrm{Re}_D^{-0.14} \left(\frac{P_t}{P_l} \right)^{-0.564} \left(\frac{F_s}{D} \right)^{-0.123} \left(\frac{P_t}{D} \right)^{1.17} \right]^{(3-N)} \tag{B.7}$$

The comparison of the limitations of each correlation and the experimental conditions is shown in Table B.1.

Table B.1 Air side heat transfer coefficient correlations

		Limitation on Correlations	Experimental conditions
Wang and Chang (1998)		NP = 2 $1.54 < P_l / D_c < 1.63$ $Re_{Dc} > 2000$ $F_s = 1.4 \sim 1.22$ mm $D_c = 7.52$ mm or 10.23 mm $P_t = 20.4$ mm or 21 mm $P_l = 12.7$mm or 16.7 mm	NP = 8 $P_l / D_c = 2.6$ $500 < Re_{Dc} < 25000$ $F_s = 8$ mm $D_c = 12.7$ mm $P_t = 38.1$ mm $P_l = 33$ mm
Wang, Chang, Hsieh, and Lin (1996)		$800 < Re_{Dc} < 7500$ $0.13 < F_{th} < 0.2$ mm $1.74 < F_p < 3.20$ $D_c = 10.23$ mm $P_t = 25.4$ mm	$500 < Re_{Dc} < 25000$ $F_{th} = 0.2$ mm $F_p = 3$ $D_c = 12.7$ mm $P_t = 38.1$ mm
Kim, Youn and Webb (1999)	NP=1,2	$591 \le Re_{Dc} \le 14430$ $1.154 \le P_t / P_l \le 1.654$ $2.399 \le P_t / D_c \le 2.877$ $0.135 \le (F_s\text{-}F_{th}) / D_c \le 0.3$	
	NP $\ge$ 3	$505 \le Re_{Dc} \le 24707$ $0.857 \le P_t / P_l \le 1.654$ $1.996 \le P_t / D_c \le 2.881$ $0.081 \le (F_s\text{-}F_{th}) / D_c \le 0.641$	$573 < Re_{Dc} < 1957$ $P_t / P_l = 1.155$ $P_t / D_c \le 3$ $(F_s\text{-}F_{th}) / D_c = 0.61$

B.2 Air side pressure drop correlations

The air side pressure drop can be calculated using the following equation (Kays and London, 1998):

$$\Delta P = \frac{G_{max}^{2}}{2} \cdot v_1 \cdot \left[\left(K_c + 1 - s^2 \right) + 2 \cdot \left(\frac{v_2}{v_1} - 1\right) + f \cdot \frac{A_o}{A_{free}} \cdot \frac{v_m}{v_1} - (1 - s^2 - K_e)\frac{v_2}{v_1} \right] \quad (B.8)$$

Where G_{max} max air velocity (based on minimum flow area), kg/m^2-s

       v_1 specific volume of inlet air (m^3/kg)

       v_2 specific volume of inlet air (m^3/kg)

       v_m man specific volume (m^3/kg)

       A_o total heat transfer area

       A_{free} free flow area

       f friction factor

$$s = \frac{A_{free}}{A_{frontal}} \quad \text{ratio of free flow area to frontal area}$$

$$K_c \quad \text{entrance loss coefficient}$$

$$K_e \quad \text{exit loss coefficient}$$

K_c and K_e, evaluated on the assumption of uniform velocity in the duct, are functions of the contraction and expansion geometry and , in some cases, of the Reynolds number in the tubes. Kays and London (1998) presented some analytical values of these coefficients for a number of simple entrance and exit geometries. In our study, $K_c = 0.6$ and $K_e = 0.15$ were used based on the analysis of Kays and London (1998).

The available literature provides two air side friction factor correlations for plain fin heat exchangers with round tubes—Kim, Youn and Webb (1999), Wang et al. (1996) applicable to the range of geometry and operating conditions used in the display case.

1)   Wang et al. (1996)

$$f = 1.039 \cdot \mathrm{Re}_{D_c}^{-0.418} \cdot \left(\frac{F_{th}}{D_c}\right)^{-0.104} \cdot N^{-0.0935} \cdot \left(\frac{F_s}{D_c}\right)^{0.197} \tag{B.9}$$

Their test conditions are:

$$F_{th} = 0.13 \, or \, 0.2 mm, \qquad F_s = 1.74 \sim 3.21 mm,$$

$$D_c = 10.23 mm, \qquad P_t = 25.4 mm,$$

$$P_l = 22 mm, \qquad NP = 2, 4, 6$$

$$800 < \mathrm{Re}_{Dc} < 7500$$

2)   Kim, Youn and Webb (1999)

$$f = f_f \cdot \frac{A_{fin}}{A_o} + f_t \cdot \left(1 - \frac{A_{fin}}{A_o}\right) \cdot \left(1 - \frac{F_{th}}{F_p}\right) \tag{B.10}$$

$$\text{Where } f_t = \frac{4}{p} \cdot \left(0.25 + \frac{0.118}{\left[\frac{P_t}{D} - 1\right]^{1.08}} \mathrm{Re}_D^{-0.16}\right) \cdot \left(\frac{P_t}{D} - 1\right) \tag{B.11}$$

$$f_f = 1.455 \cdot \mathrm{Re}_D^{-0.656} \cdot \left(\frac{P_t}{P_l}\right)^{-0.347} \cdot \left(\frac{F_s}{D}\right)^{-0.134} \cdot \left(\frac{P_t}{D}\right)^{1.23} \tag{B.12}$$

The limitations in the correlations are the same as listed in air side heat transfer correlations (Kim, Youn and Webb (1999)).

B.3 Refrigerant heat transfer correlations

The Gnielinski correlation for fully developed (hydro-dynamically and thermally) turbulent flow in a smooth circular tube is used. The correlation is expressed in Equation B.13.

$$Nu = \frac{(f/8)(Re_{di}-1000)Pr_{ref}}{1+12.7(f/8)^{1/2}\left(Pr_{ref}^{2/3}-1\right)} \tag{B.13}$$

Where   f   friction factor

        Re_{di} Reynolds number based on inner tube diameter

        Pr_{ref} Refrigerant Prandtl number

This correlation is valid for $0.5 < Pr < 10^6$, $2300 < Re_{di} < 5\mathrm{x}10^6$.

The friction factor comes from the following equations:

$$Term = 2.457 \; \ln \; \frac{1}{(7/Re_{di})^{0.9} + 0.27 \; Re\,lrough} \tag{B.14}$$

$$A = Term^{16} \tag{B.15}$$

$$B = \left(37530/Re_{di}\right)^{16} \tag{B.16}$$

$$Term_2 = \frac{1}{(A+B)^{3/2}} \tag{B.17}$$

$$Term_1 = \frac{8}{Re_{di}} \tag{B.18}$$

$$f = 8 \; (Term_1^{12} + Term_2)^{1/12} \tag{B.19}$$

Relrough is the relative roughness of the tube surface and can be expressed in Eqn. B.20 (ASHARE Fundamentals, 1987):

$$Re\,lrough = \frac{1.5*10^{-6}}{di} \tag{B.20}$$

Generally speaking, the thermal entry length x_{fd} in turbulent flow will affect the heat transfer coefficient. Incropera and DeWitt (1996) defined x_{fd} as: $\frac{x_{fd}}{di} = 10$. Kays and Crawford (1993) analyzed the effect of thermal-entry-length on the heat transfer coefficient for turbulent flow in a circular tube. They found that for small Prandtl numbers, this effect is very pronounced and increases with Reynolds number. However, at Prandtl number above 1, the thermal-entry-length effect becomes less and less important.

Their results show that at Pr=10 and Re=100,000, when x/di=0, Nu_x/Nu_{fd}=1.05; when x/di =10, Nu_x/Nu_{fd} =1.02; when x/di=20, Nu_x/Nu_{fd}=1.01; and at x/di > 30, the local Nusselt number is almost the same as the fully developed flow Nusselt number, which means Nu_x/Nu_{fd}=1.00.

In our experiments, the length of each refrigerant pass is L=0.70m and the inner diameter of tubes is di=0.011m, so L/di=64. Assuming the Reynolds number is 100,000, then Nu_x/Nu_{fd} =(1.05*10+1.02*10+1.01*10+1*(64-30))/64 = 1.01, which means that the entry-length effect is only 1% for Re=100,000. Since at lower Reynolds numbers it should be even smaller, then the effect of thermal-entry-length on refrigerant heat transfer coefficients is negligible in this study since the range of the Reynolds number is 3000~8000 in the experiments. So, Gnielinski correlation was directly used without any corrections in the model.

Appendix C: Test Matrix

This Appendix shows the results of simulations made prior to conducting the experiments, in order to identify the operating conditions that would result in different frost deposition pattern, sensible heat, latent heat etc.

Simulations in this appendix were made using the earlier version of the model, which relied on some assumptions and correlations that have since been replaced by others. The results are qualitatively similar to those obtained with latest version of model that is documented in the body of this report.

The frost deposition pattern (FDP) depends on the geometry of the heat exchanger and operating conditions. For a particular heat exchanger, the operating conditions will play the most important role in causing different FDPs.

The running conditions can be described by the following five parameters and their typical values are given in Table C.1.

Table C.1 Five parameters and their typical values for running conditions

Parameters for running conditions	Typical values
Air inlet temperature (°C): T_{ain}	0, -20
Refrigerant inlet temperature (°C): T_{rin}	T_{ain} -10
Air inlet RH: RH_{in}	70%, 80%, 90%
Air velocity (m/s): vel_{air}	0.6, 0.9, 1.3, 2.2
Refrigerant temperature rise (°C): ΔT_{ref}	1, 3, 5 (or max that is reachable)

These parameters affect the FDP on this particular heat exchanger very differently. Among them, the air face velocity (or Reynolds number) is the most important factor.

Table C.2 lists four running conditions at four different air face velocity: 0.6m/s, 0.9m/s, 1.3m/s and 2.2m/s respectively with other parameters remaining the same (T_{ain}=-20 °C, T_{rin} = -30 °C, RH_{in} =70%, m_{ref} =0.5 kg/s). The small graph shown at the right hand of each test run shows the predicted mass of frost accumulated on the four rows after 10 hours with Row 1 being the air inlet and Row 4 air outlet.

It can be seen from Table C.2 that a higher velocity "pushes" frost deposition to the trailing edge. More specifically, at 0.6 m/s, there is more frost on the first row. But with 0.9 m/s, the most-frosted rows have changed to the second and third row. Note that under this condition, a more evenly distributed frost pattern is obtained. As we continue to increase the velocity, more frost grows on the back rows with very little frost on the first row at 2.2m/s.

Table C.2 Effect of air face velocity on FDP

$T_{ain} = -20\,^{\circ}C,\ T_{rin} = -30\,^{\circ}C,\ RH_{in} = 70\%,\ \dot{m}_{ref} = 0.5\ kg/s$

Tain	Trin	RH_in	vel_air	d_Tref	(m_ref)
-20	-30	70%	0.6	1.8	0.5
Row	1	2	3	4	
m_fr (g)	202	183	150	116	

Tain	Trin	RH_in	vel_air	d_Tref	(m_ref)
-20	-30	70%	0.9	2.3	0.5
Row	1	2	3	4	
m_fr (g)	189	217	214	196	

Tain	Trin	RH_in	vel_air	d_Tref	(m_ref)
-20	-30	70%	1.3	2.76	0.5
Row	1	2	3	4	
m_fr (g)	156	222	254	261	

Tain	Trin	RH_in	vel_air	d_Tref	(m_ref)
-20	-30	70%	2.2	3.4	0.5
Row	1	2	3	4	
m_fr (g)	80	185	271	333	

Due to limitation of the experimental setup, a minimum capacity of the heat exchanger (Q_{min}) is required to run the tests successfully, which should be larger than or at least equal to the sum of transmission load through the chamber wall (Q_t) and the capacity of the blower (W_{blower}). According to Diane et al. (2001), at $T_{ain} = 0\,^{\circ}C$, $Q_t = 0.41$ kW and $T_{ain} = -20\,^{\circ}C$, $Q_t = 0.85$ kW; W_{blower} is about 0.38 kW at lower velocity ($vel_{air} \le 1.3$ m/s) and 1.3 kW at 2.2 m/s. So at $T_{ain} = 0\,^{\circ}C$ and low air velocity ($vel_{air} \le 1.3$ m/s), the minimum capacity of the heat exchanger: $Q_{min} = 0.79$ kW; at $T_{ain} = 0\,^{\circ}C$ and $vel_{air} = 2.2$ m/s, $Q_{min} = 1.71$ kW; at $T_{ain} = -20\,^{\circ}C$ and low air velocity ($vel_{air} \le 1.3$ m/s), $Q_{min} = 1.23$ kW; at $T_{ain} = -20\,^{\circ}C$ and $vel_{air} = 2.2$ m/s, $Q_{min} = 2.15$ kW. In Table C.2, when the air velocity is 0.6 m/s, the total capacity of the heat exchanger is only 0.93 kW, lower than the minimum capacity required. So this case is not achievable in experiments. Only 0.9 m/s, 1.3 m/s, and 2.2 m/s running conditions are included in the tentative test matrix.

In the experiments, a single-phase refrigerant is chosen so that the refrigerant temperature glide can be controlled. Changing the refrigerant mass flow rate will change the temperature glide. For example, a low flow rate

will lead to a parallel temperature glide between the air side and refrigerant side while a high flow rate will give a very flat temperature glide, which can be used to simulate DX coils.

The effect of ΔT_{ref} (i.e., refrigerant temperature glide) on the FDP is shown in Table C.3 where four different ΔT_{ref}'s have been used.

Table C.3 Effect of refrigerant temperature glide on FDP

$T_{ain}= 0\ °C$, $T_{rin} =-10\ °C$, $RH_{in} =90\%$, $vel_{air} =1.3$ m/s

Tain	Trin	RH_in	vel_air	d_Tref	(m_ref)
0	-10	90%	1.3	5.3	0.2
Row	1	2	3	4	
m_fr (g)	712	1030	1265	1413	

Tain	Trin	RH_in	vel_air	d_Tref	(m_ref)
0	-10	90%	1.3	5	0.26
Row	1	2	3	4	
m_fr (g)	1024	1337	1547	1672	

Tain	Trin	RH_in	vel_air	d_Tref	(m_ref)
0	-10	90%	1.3	4	0.45
Row	1	2	3	4	
m_fr (g)	1783	1980	1990	1894	

Tain	Trin	RH_in	vel_air	d_Tref	(m_ref)
0	-10	90%	1.3	1	2.6
Row	1	2	3	4	
m_fr (g)	2637	2053	1527	1138	
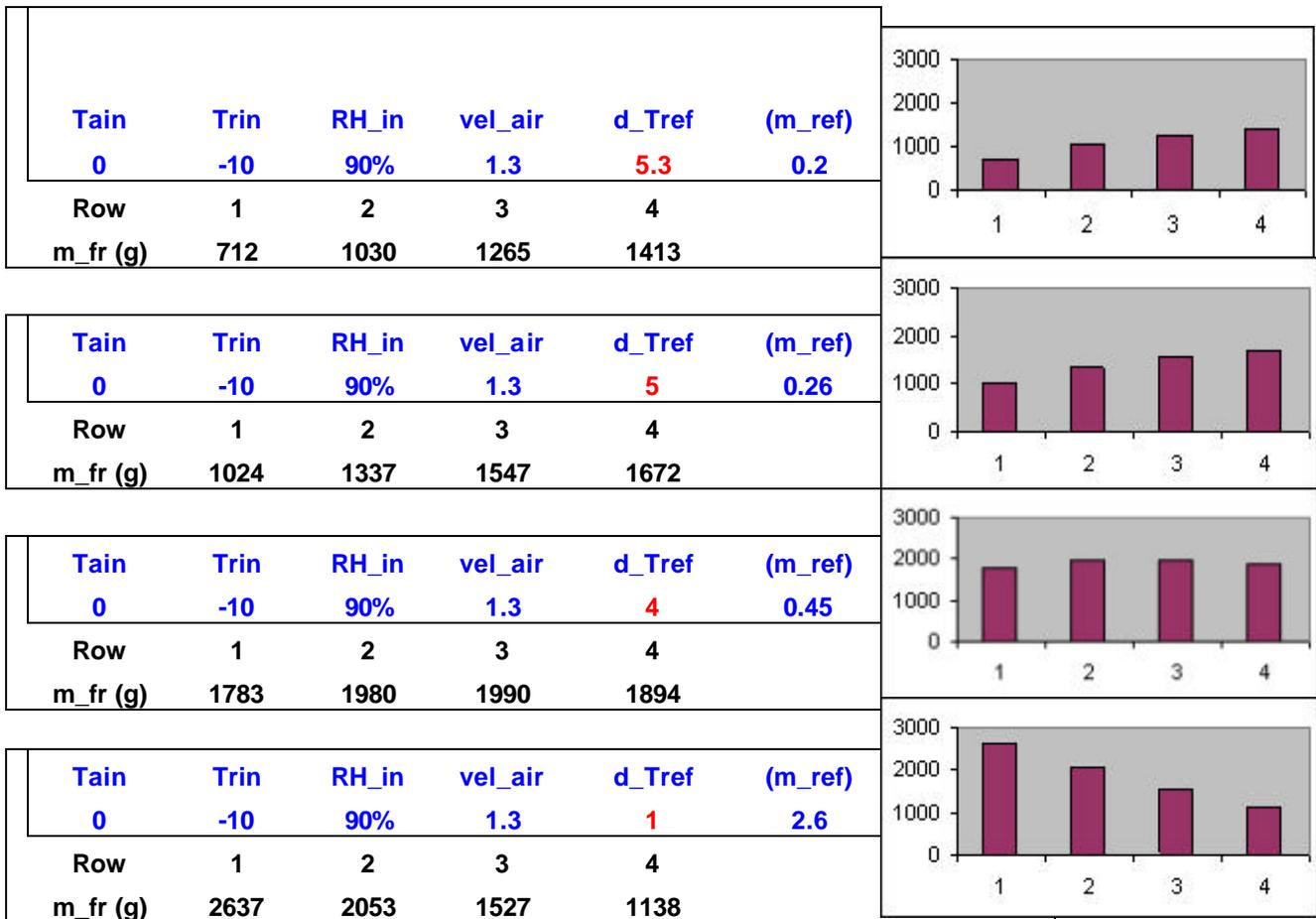
Table C.3 shows that at high refrigerant temperature drop (low mass flow rate), there is little frost on the first row and a large amount of frost on the back rows. With a decrease in temperature drop, more frost starts to grow on the middle rows and then on the leading edge of the heat exchanger. At high mass flow rate, the temperature glide is almost flat (only 1 °C drop), which can simulate a DX coil with more of the frost growing on the front rows and little frost on the back rows. However, because the maximum refrigerant mass flow rate that can be reached in the experiments is about 0.5 kg/s, only the first three of the four tests are actually achievable and thus included in the tentative test matrix**.**

Beside air face velocity and refrigerant temperature glide, air inlet humidity also affects the FDP. For 0 °C and –20 °C, the absolute humidity corresponding to the three relative humidity levels are shown in Figure C.1:
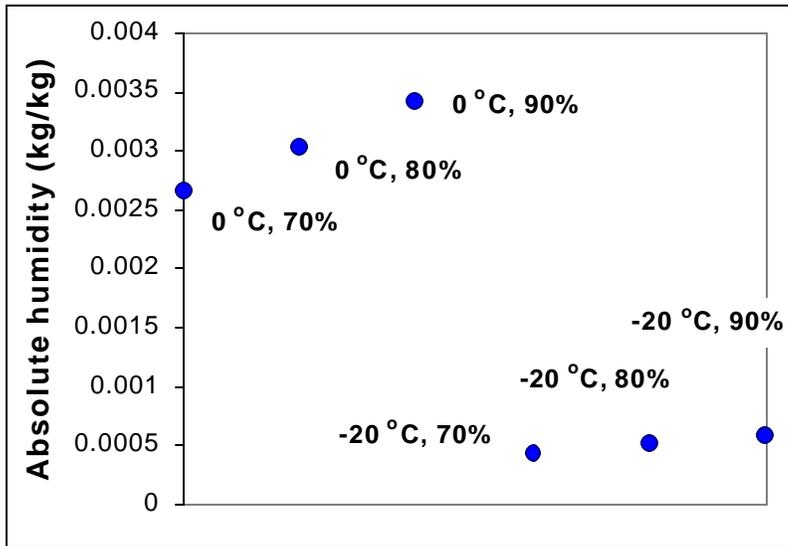
Figure C.1 Absolute humidity

It can be seen that under –20 °C, the absolute humidities for 70%, 80% and 90% are very close to one another. Changing relative humidity will not dramatically change FDP. At 0 °C, FDPs are different when the relative humidity changes. Table C.4 shows the predicted frost deposition patterns under three different humidities.

It is easy to understand that the higher the air inlet humidity is, the more frost will grow on the heat exchanger since more water vapor will be removed from the humid air when it passes through the cold coils. But it is very interesting to see how frost distributes across the heat exchanger. At high humidity, more frost tends to grow on the front rows. As the humidity decreases, the back rows starts to get more frost.

These three cases are included in the tentative test matrix.

Table C.4 Effect of air inlet relative humidity on FDP

T_{ain}=0 °C, T_{rin} =-10 °C, vel_{air} =0.9 m/s, ΔT_{ref} =3 °C

Tain	Trin	RH_in	vel_air	d_Tref	(m_ref)
0	-10	90%	0.9	3.1	0.5
Row	1	2	3	4	
m_fr (g)	2001	1920	1653	1376	

Tain	Trin	RH_in	vel_air	d_Tref	(m_ref)
0	-10	80%	0.9	3	0.48
Row	1	2	3	4	
m_fr (g)	1172	1359	1332	1198	

Tain	Trin	RH_in	vel_air	d_Tref	(m_ref)
0	-10	70%	0.9	3	0.4
Row	1	2	3	4	
m_fr (g)	340	686	896	967	
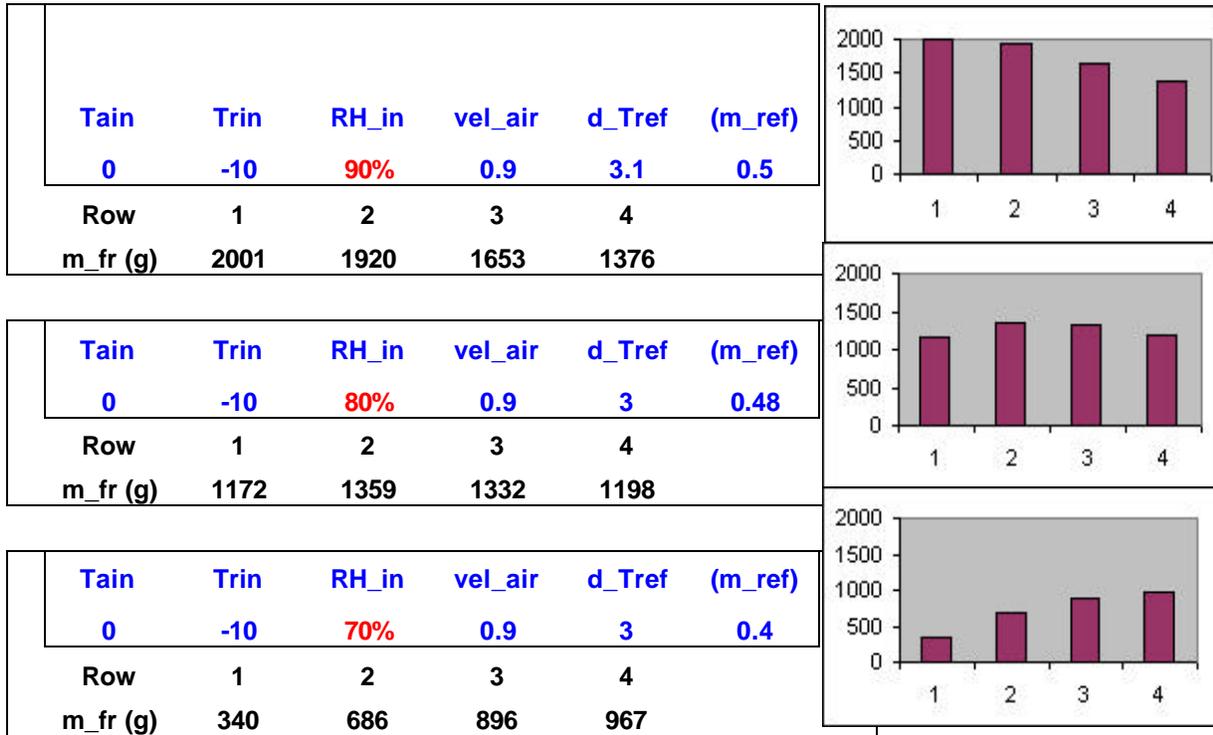
The temperature difference between T_{ain} and T_{rin} also affects FDP. In Table C.5, three running conditions with different (T_{ain} - T_{rin}) (8 °C, 10 °C, and 12 °C respectively) are shown here while other parameters remain the same (T_{ain}=0 °C, RH_{in} =90%, vel_{air} =1.3m/s, ΔT_{ref} =4.2 °C). The graph on the right hand of each test run shows the frost mass on the four rows after 10 hours with Row 1 being the air inlet and Row 4 air outlet. As can be seen from Table C.5, larger difference between T_{ain} and T_{rin} would "push" the frost distribution towards the inlet. However, because the maximum refrigerant mass flow rate is about 0.55 kg/s, only the first two of the three tests are achievable. Since the effects of (T_{ain} - T_{rin}) are not important, they will be neglected and T_{ain} - T_{rin} =10 °C will continue to be used.

Table C.5 Effect of (T_{ain} - T_{rin}) on FDP

T_{ain}=0 °C, RH_{in} =90%, V_{air} =1.3m/s, ΔT_{ref} =4.2 °C

Tain	Trin	RH_in	vel_air	d_Tref	(m_ref)
0	-8	90%	1.3	4.2	0.18
Row	1	2	3	4	
m_fr (g)	371	650	874	1037	

Tain	Trin	RH_in	vel_air	d_Tref	(m_ref)
0	-10	90%	1.3	4.2	0.4
Row	1	2	3	4	
m_fr (g)	1621	1853	1918	1877	

Tain	Trin	RH_in	vel_air	d_Tref	(m_ref)
0	-12	90%	1.3	4.2	0.55
Row	1	2	3	4	
m_fr (g)	2247	2309	2131	1892	
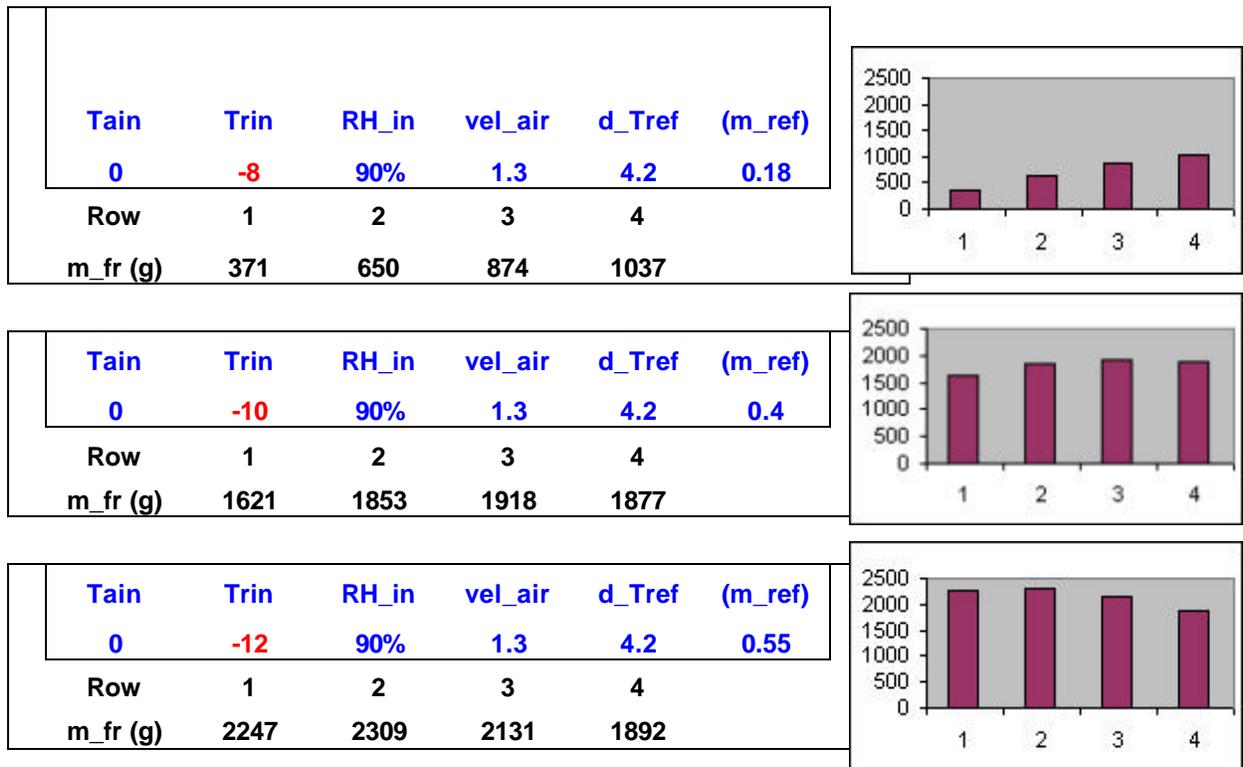
Table C.6 summarizes all the test runs that were just mentioned and are achievable in the experiments and gives a tentative text matrix:

Table C.6 Tentative test matrix

Test runs	Tain	Trin	RH_in	vel_air	d_Tref	(m_ref)	FDP
1	-20	-30	70%	0.9	2.3	0.5	Uniform
2	-20	-30	70%	1.3	2.8	0.5	Back
3	-20	-30	70%	2.2	3.4	0.5	Back
4	0	-10	90%	1.3	5.3	0.2	Back
5	0	-10	90%	1.3	5	0.26	Back
6	0	-10	90%	1.3	4	0.45	Uniform
7	0	-10	90%	0.9	3.1	0.5	Front
8	0	-10	80%	0.9	3	0.48	Middle
9	0	-10	70%	0.9	3	0.4	Back

It can be seen from Table C.6 that under most running conditions, more frost grows on the back rows. By changing some operating parameters, near-uniform frost distribution can be achieved in two of the nine conditions,

e.g., Test No.1 and No.6. It does not happen often that frost forms on the middle rows. Even in Test No.8, the middle rows only get slightly more frost than the front and back rows.

Another frost deposition pattern—more frost at the leading edge—only occurred in Test No.7 with slightly more frost on the front rows than on the other rows. To design a more typical test to show that absolutely more frost could grow at the leading edge, some conclusions from the previous discussion about the effects of several operating parameters on the FDP should be reviewed here. What could "push" more frost distribution towards the front rows? From the discussion above, the answer is low air velocity, high air inlet humidity, high refrigerant mass flow rate (i.e., smaller refrigerant temperature rise) and larger temperature difference between air inlet and refrigerant inlet. Then, what if these conditions are all satisfied with the limitation of the current experimental setup, i.e., run a test with the lowest air velocity at 0.6 m/s, the highest air inlet humidity at 90%, the highest refrigerant mass flow rate at 0.5 kg/s, and the largest temperature difference between air inlet and refrigerant inlet at 30 °C (i.e., $T_{ain}= 0$ °C and $T_{rin}= -30$ °C)? The FDP is exactly what we want—five times more frost grows on the first row of the heat exchanger than the fourth row. The result is shown in Table C.7 and this test run is added to the test matrix.

The total amount of frost is not very large. The reason is that frost grows so fast on the heat exchanger that it totally blocks the air free flow area in just 4.5 hours, while most of the other previous tests mentioned above runs for 10 hours without blocking the air free flow area.

Table C.7 One case of more frost forming at the leading edge

$T_{ain}= 0$ °C, $T_{rin}= -30$ °C, $RH_{in} =90\%$, $vel_{air} =0.6$ m/s, $\dot{m}_{ref} =0.5$ kg/s

Tain	Trin	RH_in	vel_air	d_Tref	(m_ref)
0	-30	90%	0.6	6.8	0.5
Row	1	2	3	4	
m_fr (g)	2501	1396	794	469	
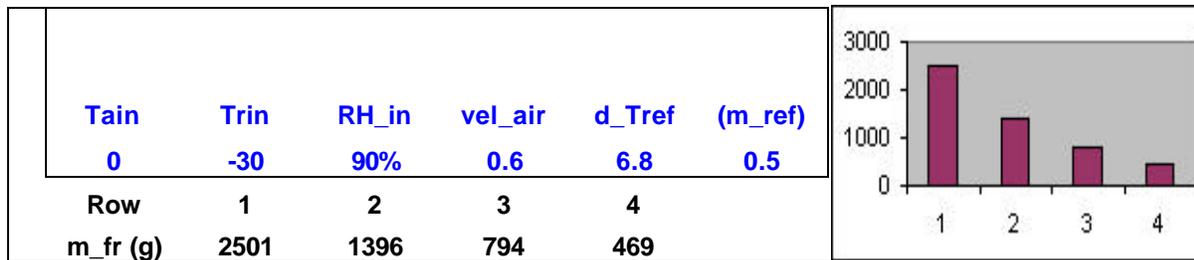
The tentative test matrix is obtained when effect of several operating parameters on the FDP is considered. On the other hand, the test matrix should be representative among all the running conditions listed in Table C.6. For example, it should contain the maximum (and minimum)-capacity running condition, maximum (and min) –airside-pressure-drop case, and maximum (and min)-mass-of-frost case. Because the more frost grows on the heat exchanger, usually the larger airside pressure drop will be, only the capacity of the heat exchanger and the mass of frost need to be considered.

Forty-five test conditions were simulated and studied with the refrigerant inlet temperature 10 ^{o}C always lower than air inlet temperature. Figures C.2 and C.3 show the total heat transfer rate and mass of frost respectively. The X axis of both figures shows the number of data points. The dotted line is the minimum capacity required due to the limitation of the current experimental setup, as mentioned above when the effect of air velocity on the FDP

was discussed. So any point below this dotted line is not achievable. The circles show the nine test runs shown in the tentative test matrix (Table C.6).
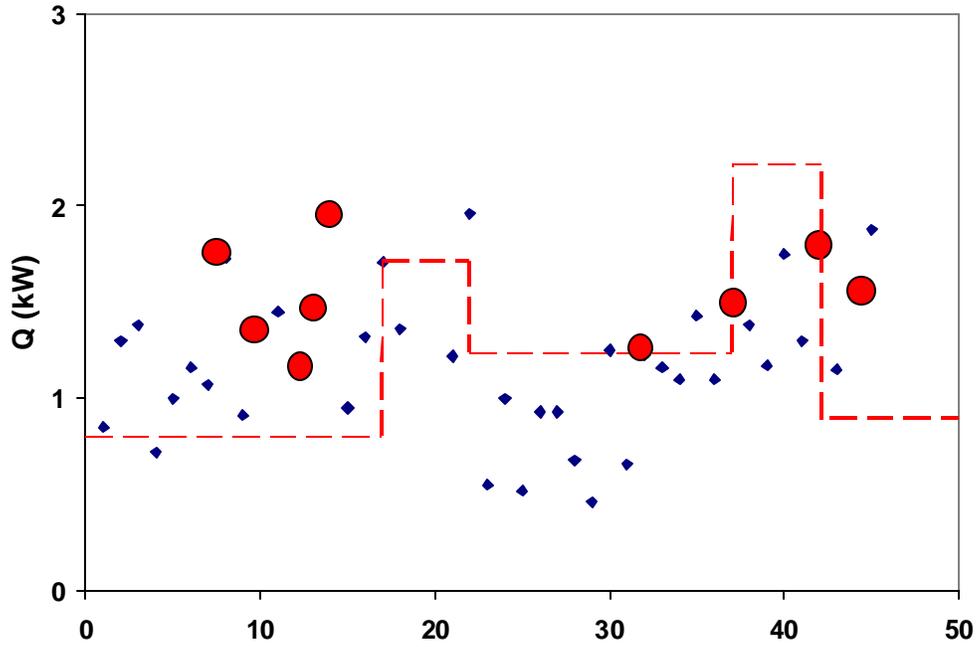
Figure C.2 Capacity in forty-five simulated cases with T_{ain} - T_{rin} =10 ℃
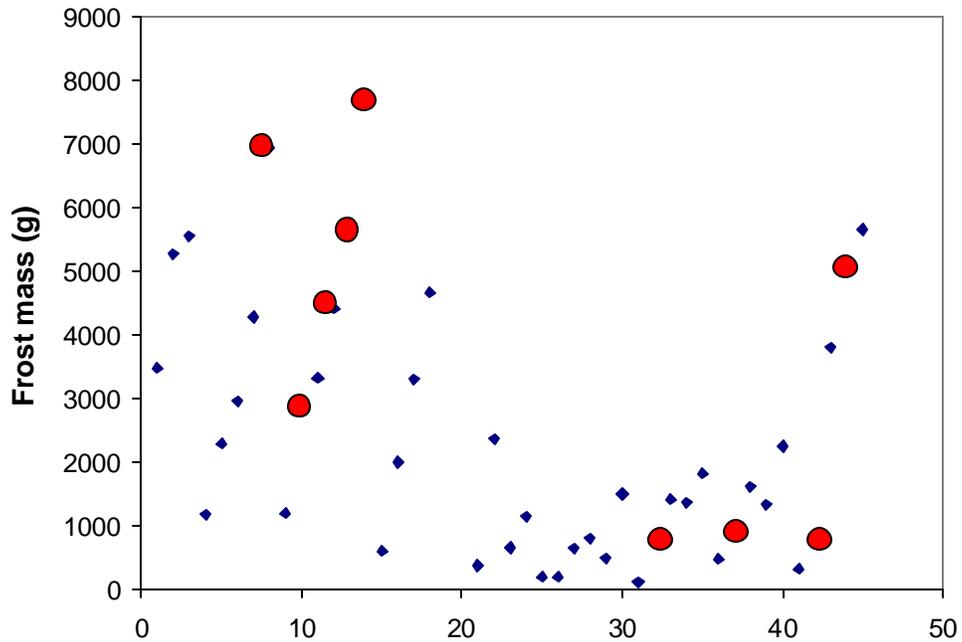
Figure C.3 Mass of frost in forty-five simulated cases with T_{ain} - T_{rin} =10 ℃

Figures C.2 and C.3 show that the nine test runs chosen as test matrix can represent most of the operating conditions that are achievable. However, another maximum-capacity-and-maximum-frost-mass test run, which is shown in Table C.8 with the total heat transfer rate of 6.7 kW and total mass of frost of nearly 11 kg, needs to be added into Table C.6 to make the test matrix complete.

The final test matrix is shown in Table C.9.

Table C.8 Maximum-capacity-and-maximum-frost-mass case

	Tain	Trin	RH_in	vel_air	d_Tref	(m_ref)	
	0	-30	90%	2.2	12.6	0.5	
Row	1	2	3	4			
m_fr (g)	3115	3126	2906	2577			

Table C.9 Final test matrix

Test runs	Tain	Trin	RH_in	vel_air	d_Tref	(m_ref)	FDP
1	-20	-30	70%	0.9	2.3	0.5	Uniform
2	-20	-30	70%	1.3	2.8	0.5	Back
3	-20	-30	70%	2.2	3.4	0.5	Back
4	0	-10	90%	1.3	5.3	0.2	Back
5	0	-10	90%	1.3	5	0.26	Back
6	0	-10	90%	1.3	4	0.45	Uniform
7	0	-10	90%	0.9	3.1	0.5	Front
8	0	-10	80%	0.9	3	0.48	Middle
9	0	-10	70%	0.9	3	0.4	Back
10	0	-30	90%	0.6	6.8	0.5	Front
11	0	-30	90%	2.2	12.6	0.5	Front

Appendix D   Complete Validation Results under Frosted Conditions

D.1 Validation results for 0/-10/90/1.3/0.45
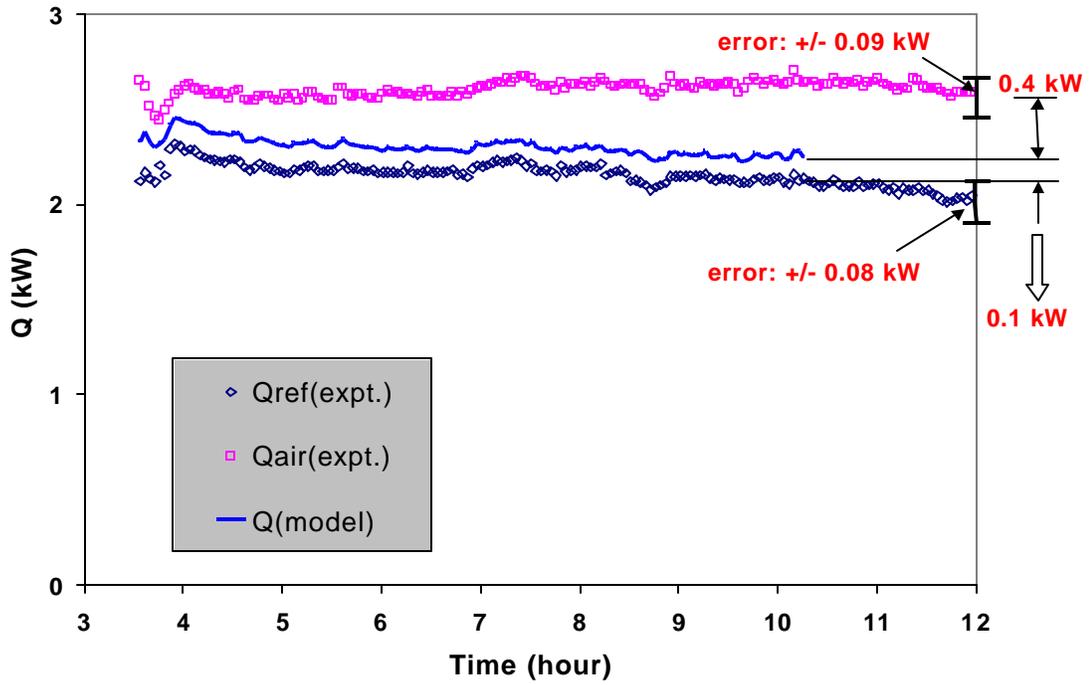
Figure D.1 Comparison of the total load for 0/-10/90/1.3/0.45
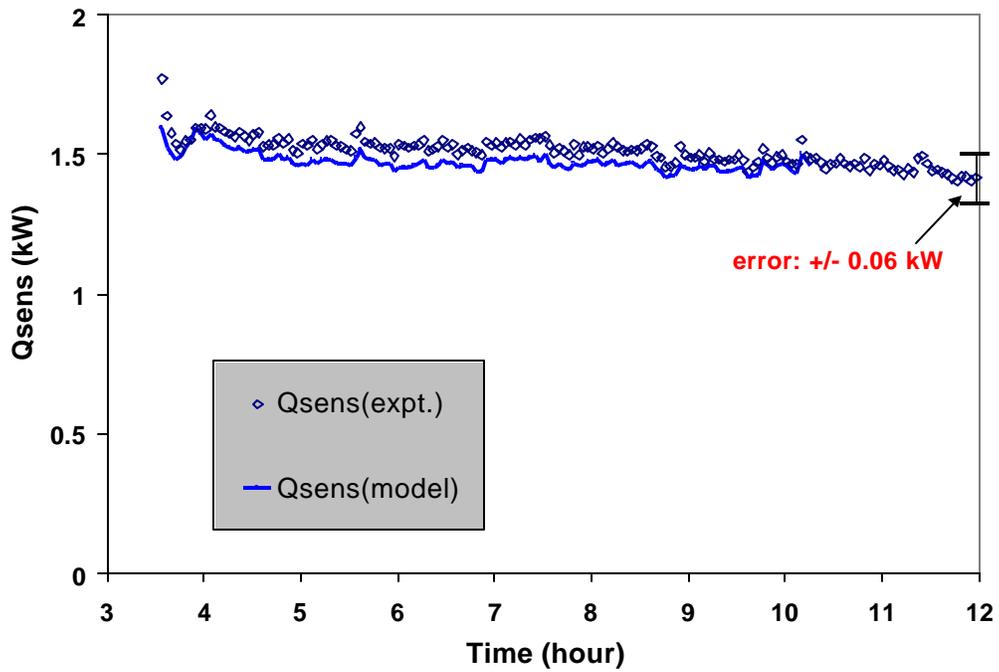
Figure D.2 Comparison of the sensible load for 0/-10/90/1.3/0.45
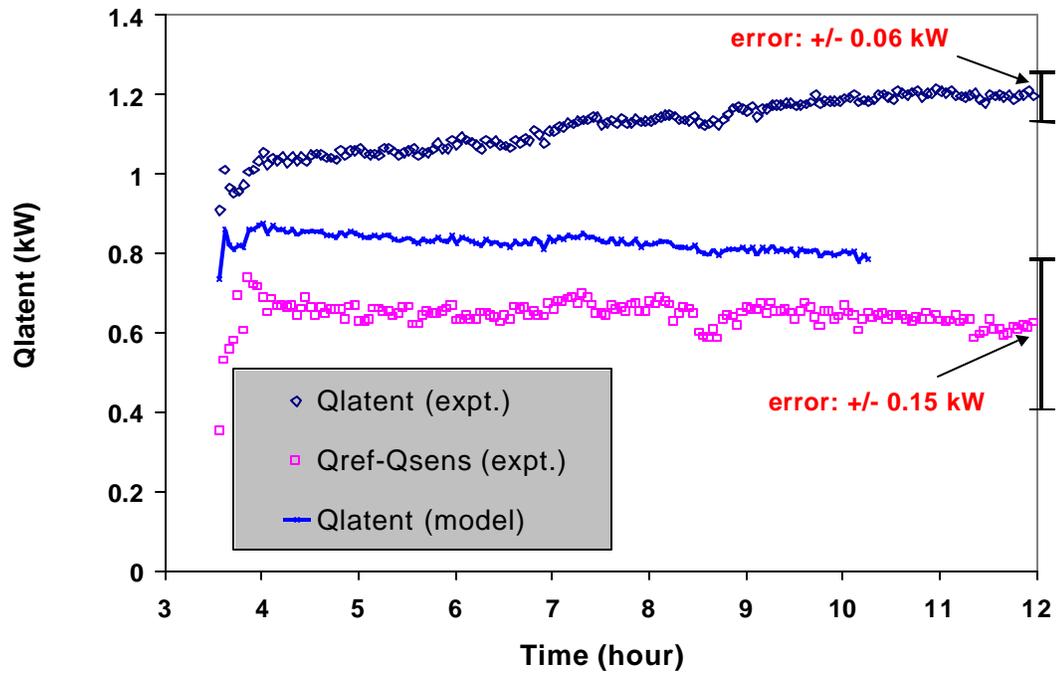
Figure D.3 Comparison of the latent load for 0/-10/90/1.3/0.45
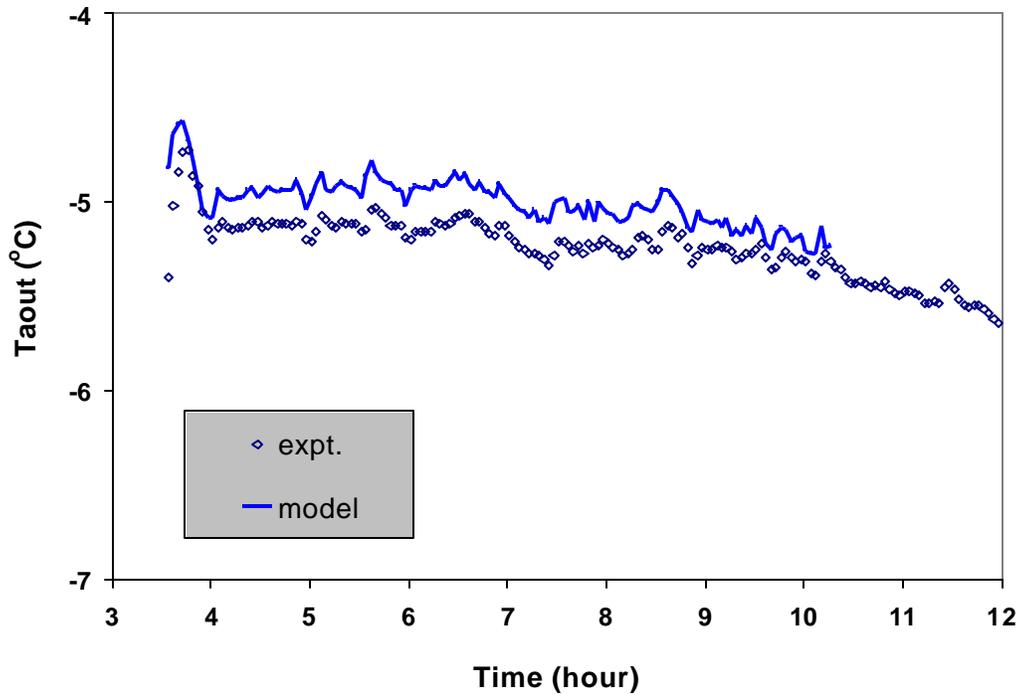
Figure D.4 Comparison of the air outlet temperature for 0/-10/90/1.3/0.45
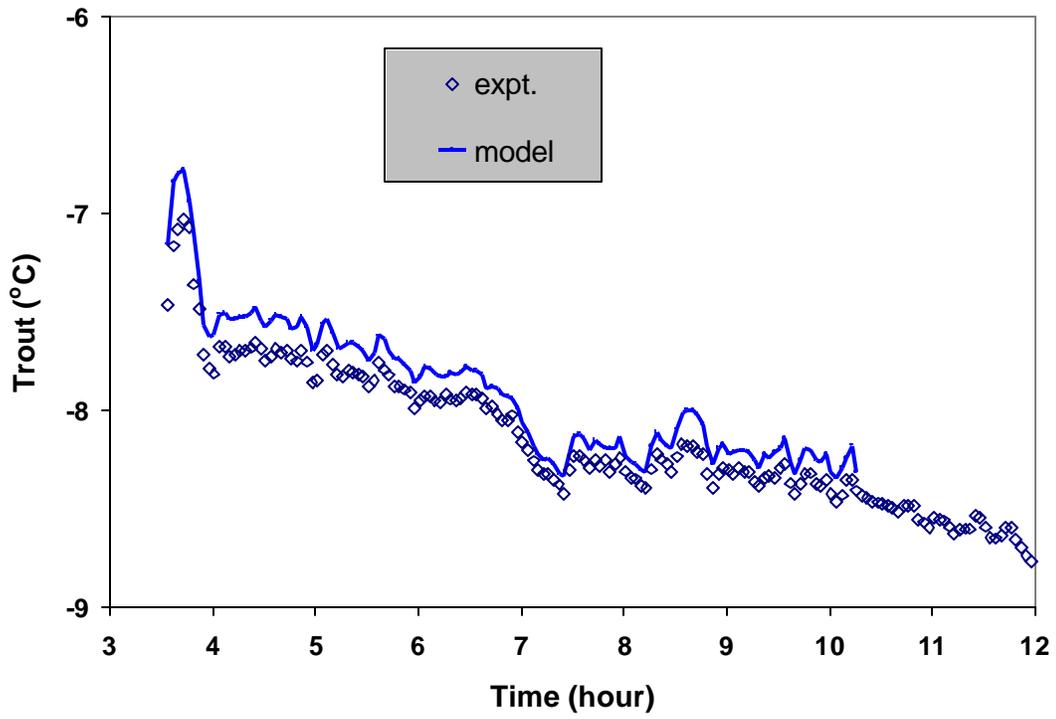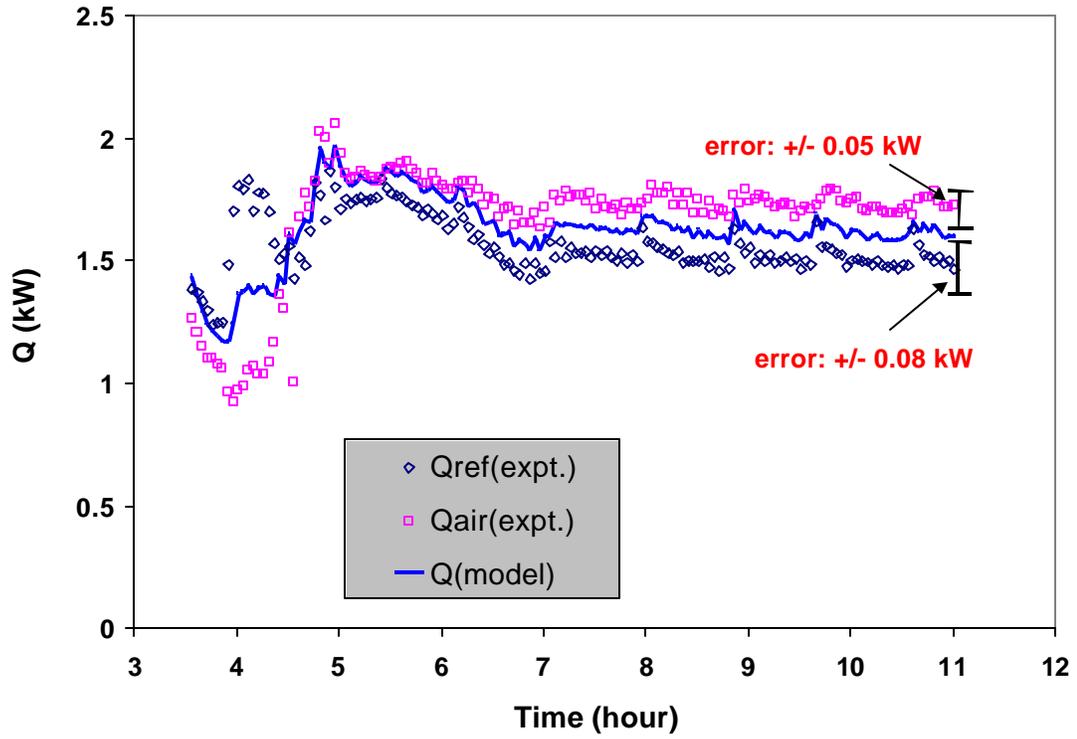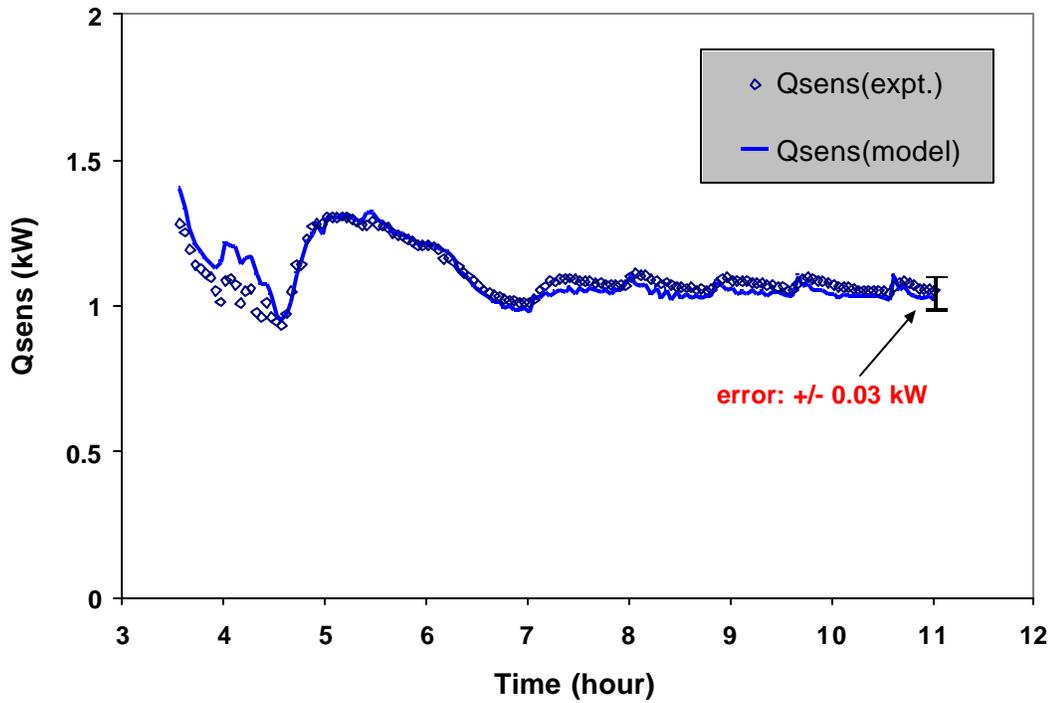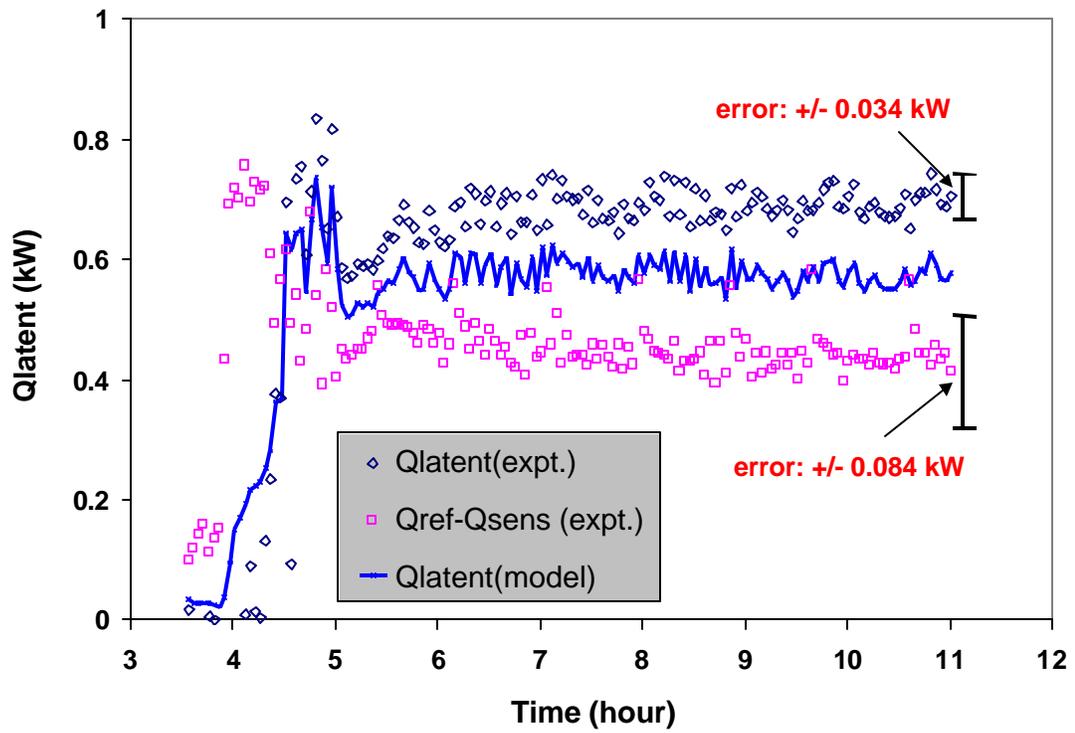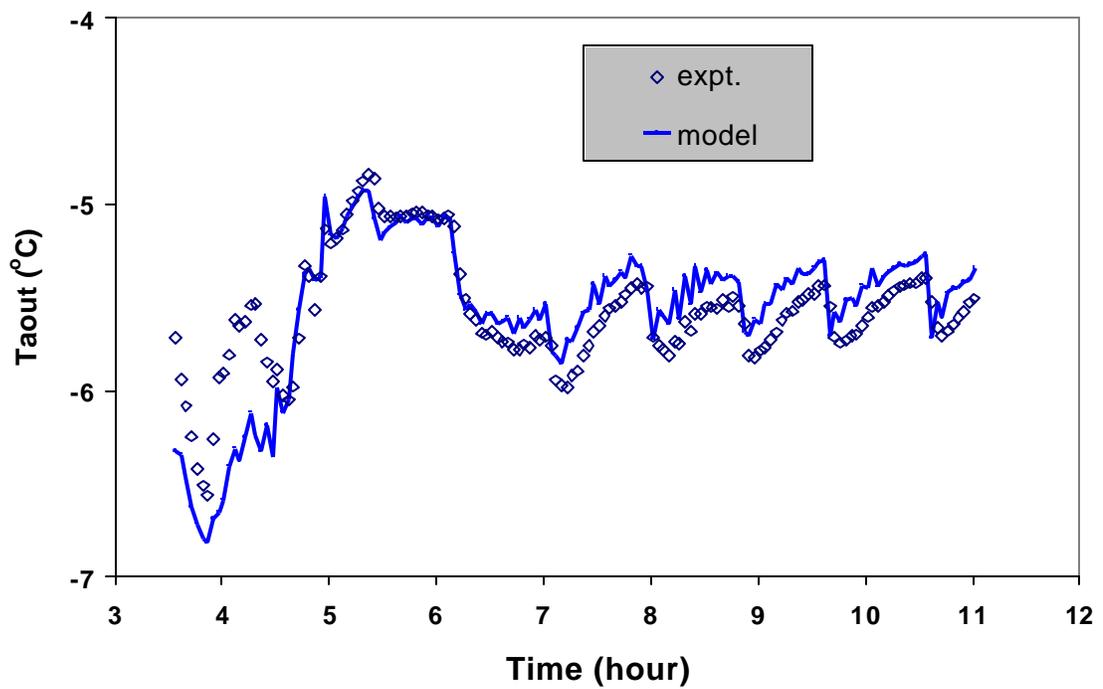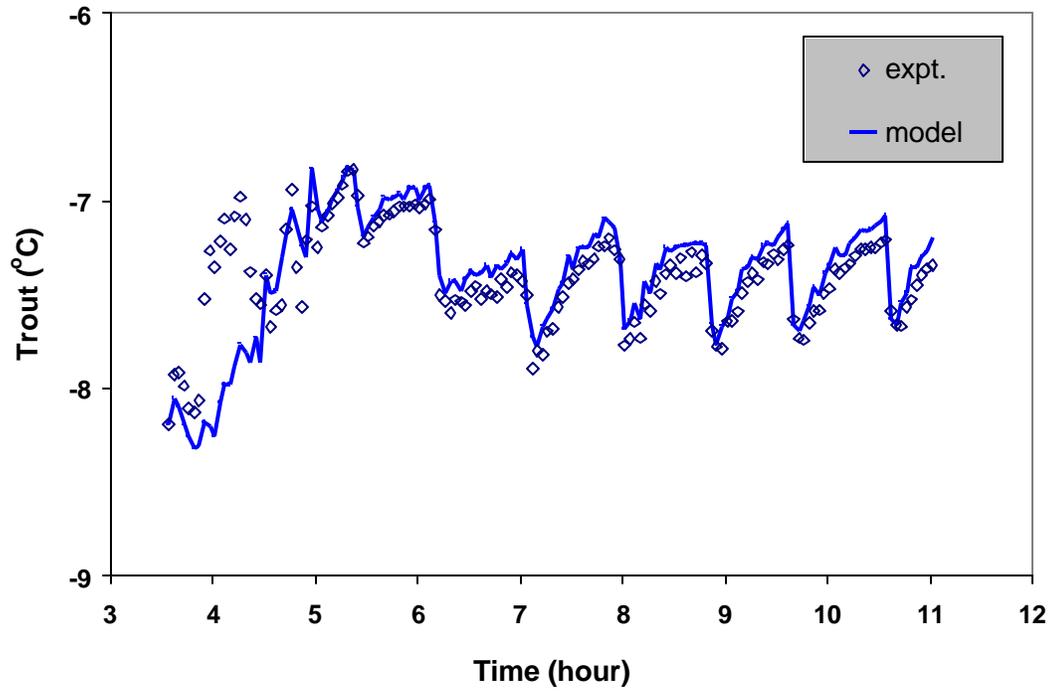
Figure D.5 Comparison of the refrigerant outlet temperature for 0/-10/90/1.3/0.45
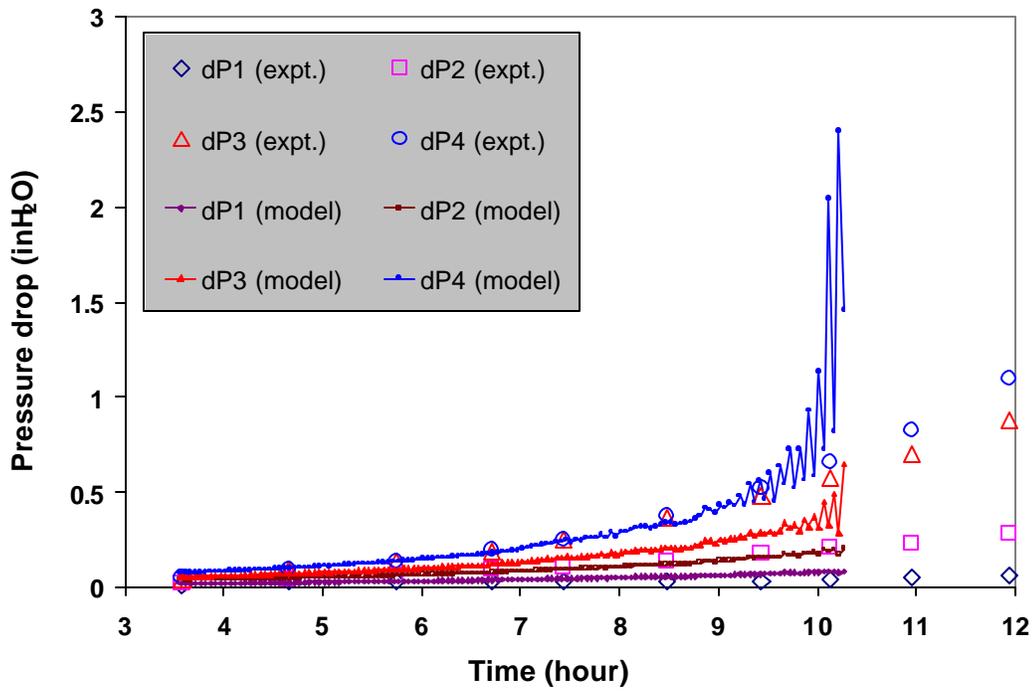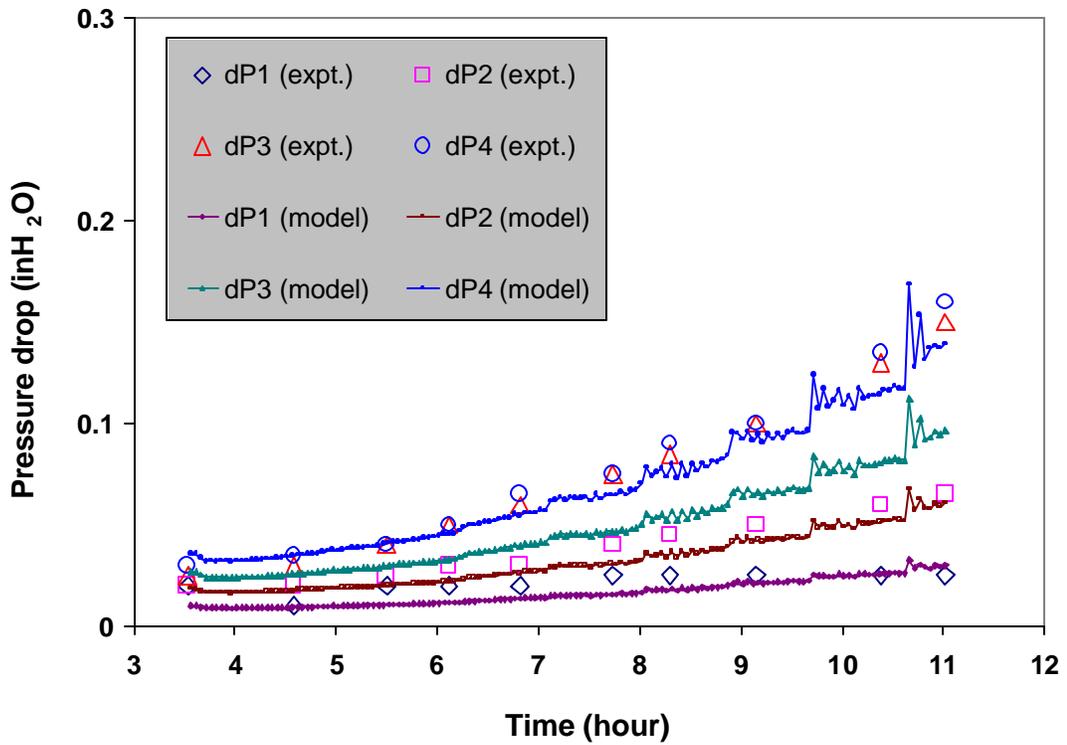

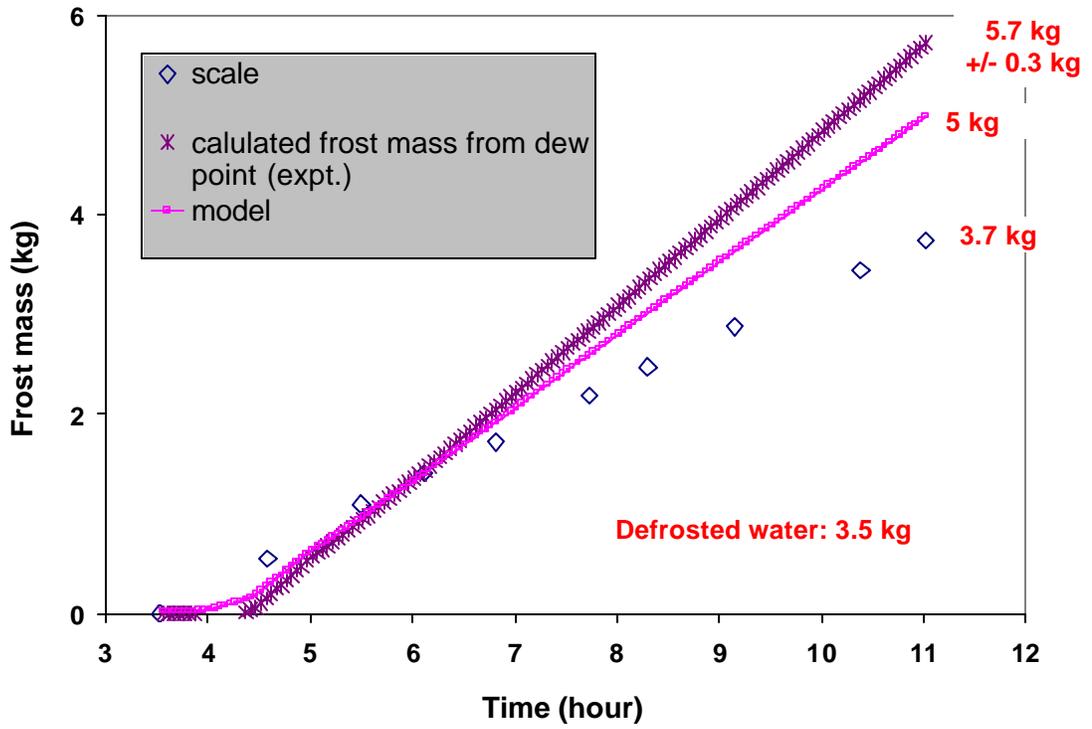Figure D.6 Comparison of the air side pressure drop for 0/-10/90/1.3/0.45
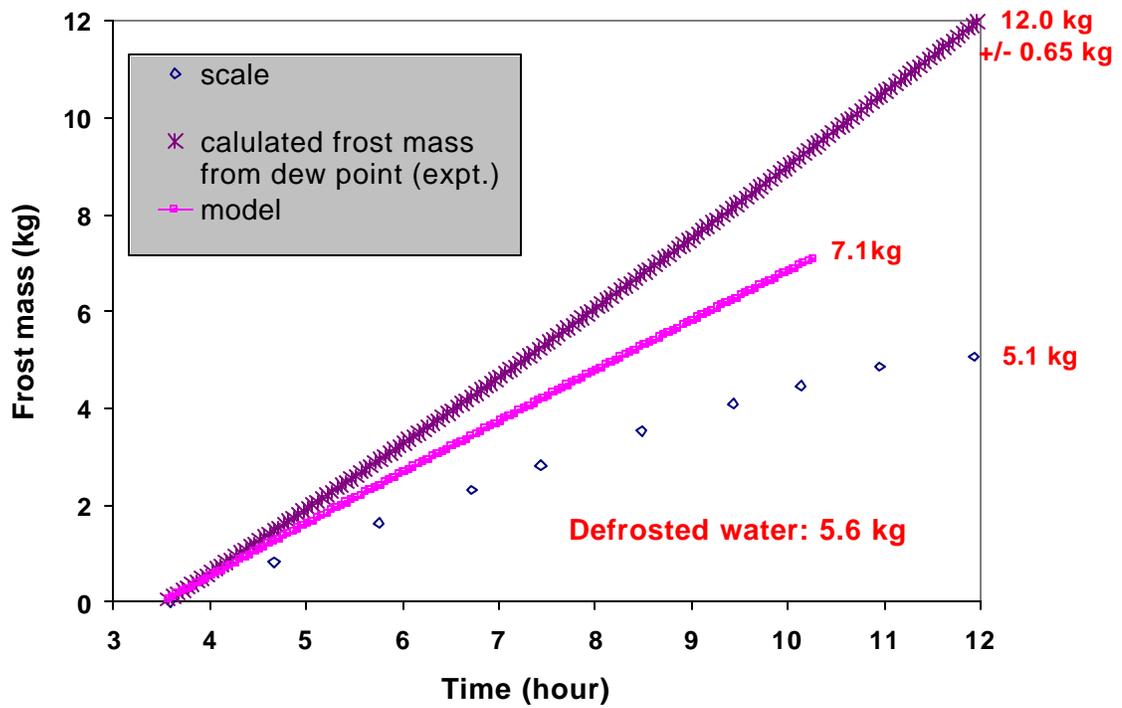
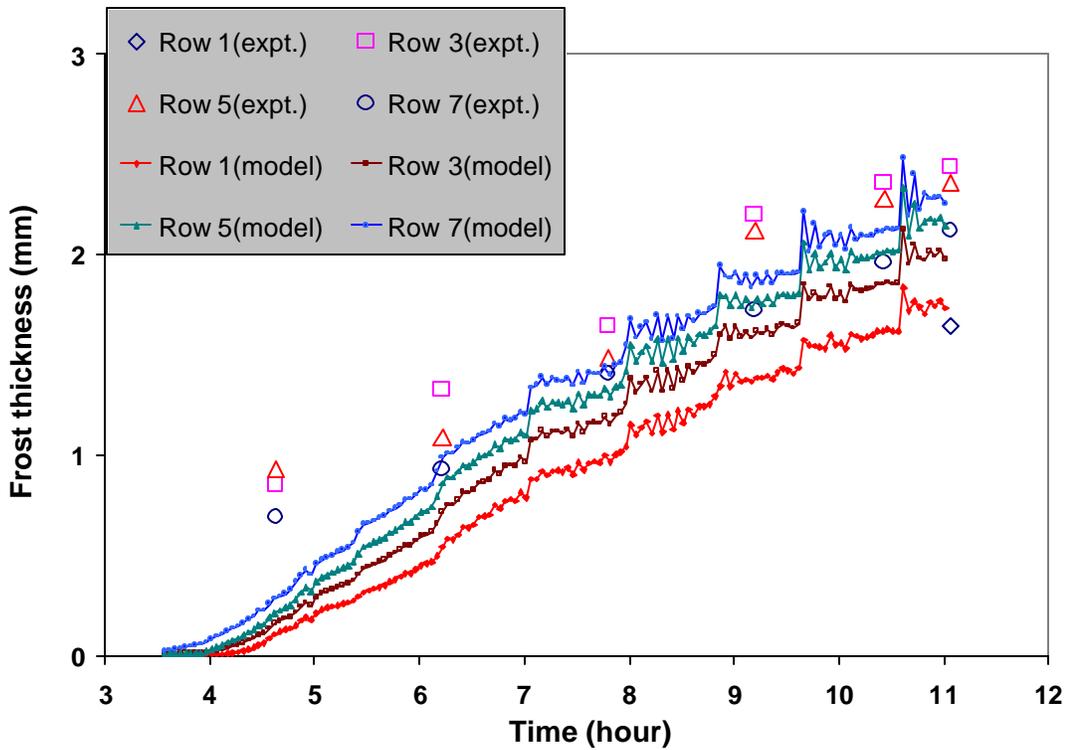Figure D.7 Comparison of the frosting rate for 0/-10/90/1.3/0.45
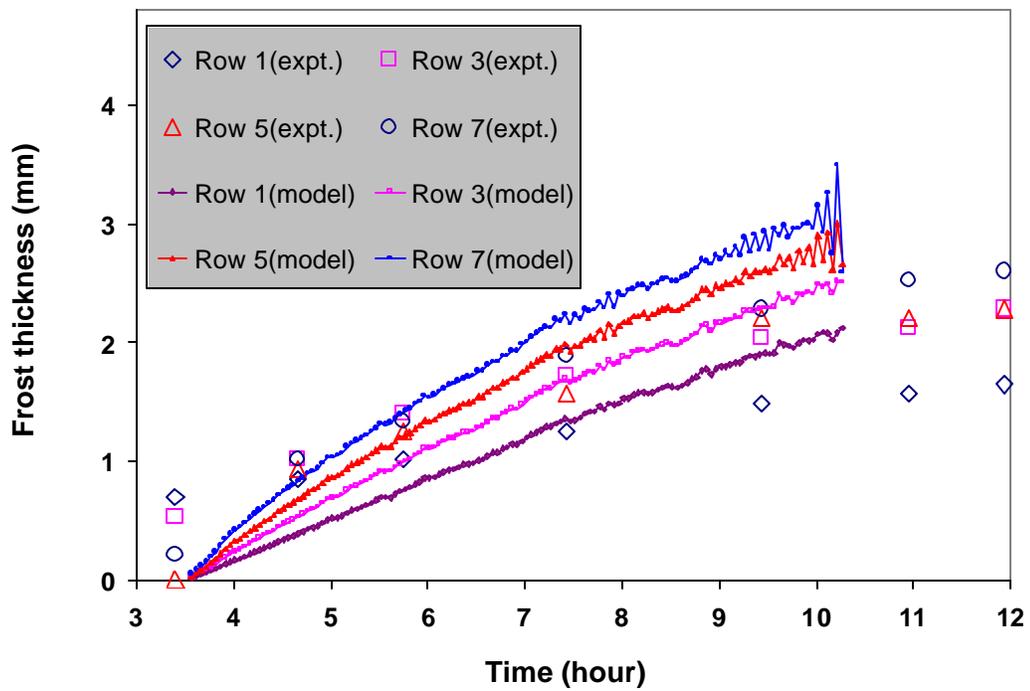
Figure D.8 Comparison of the frost thickness for 0/-10/90/1.3/0.45
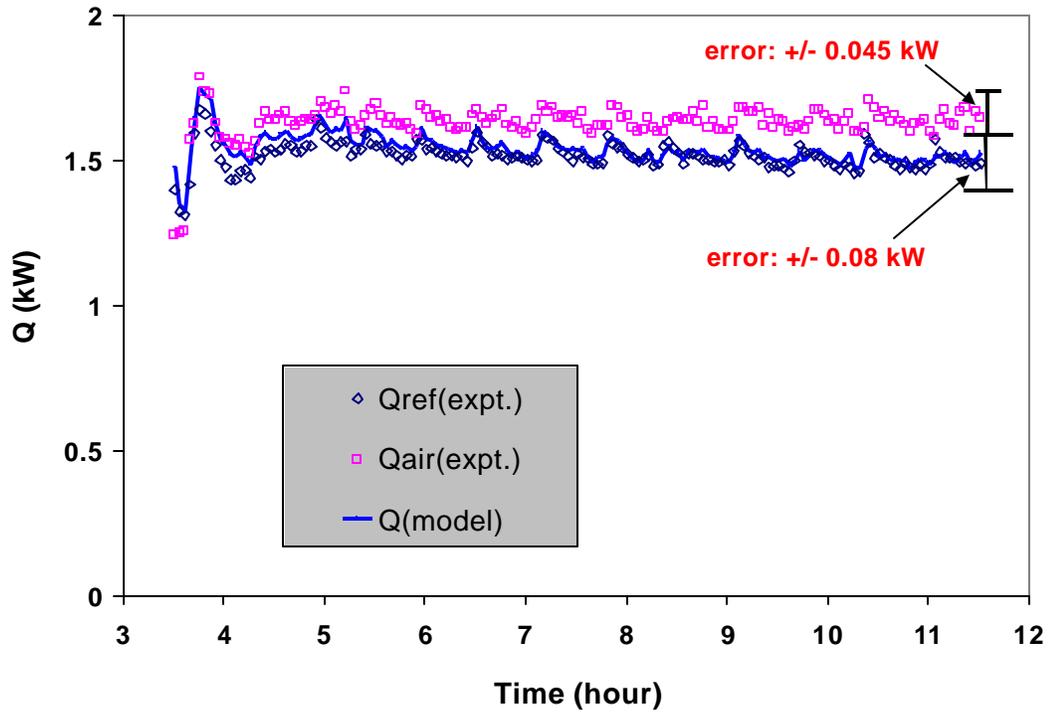
D.2 Validation results for 0/-10/90/1.3/0.2
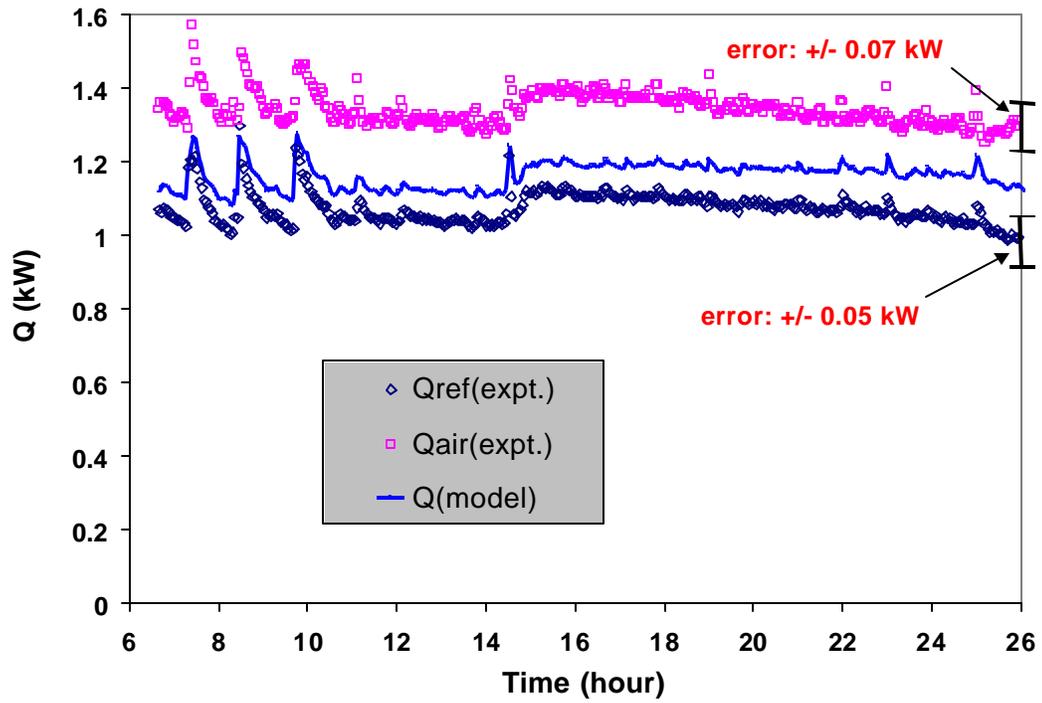
Figure D.9 Comparison of the total load for 0/-10/90/1.3/0.2
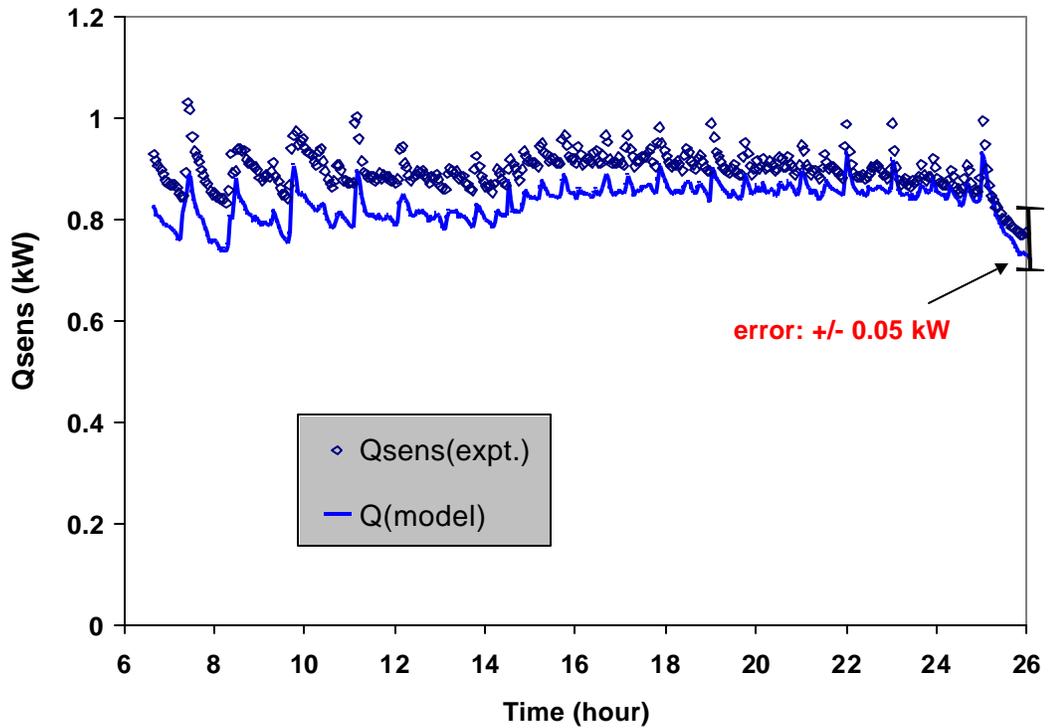
Figure D.10 Comparison of the sensible load for 0/-10/90/1.3/0.2

75
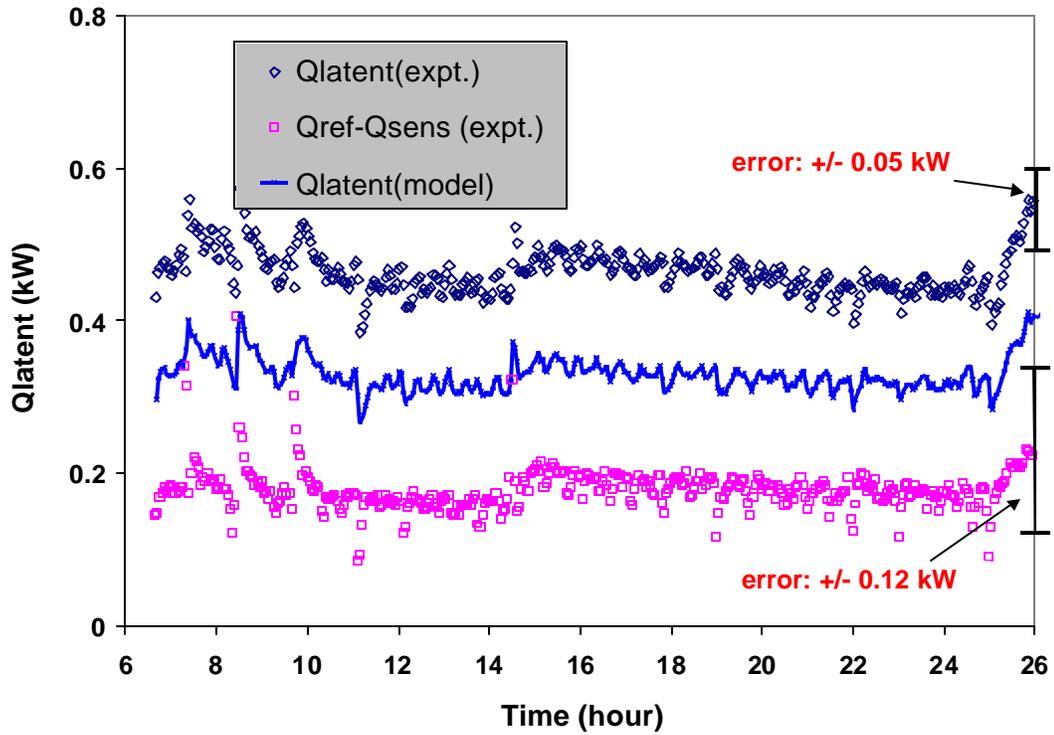
Figure D.11 Comparison of the latent load for 0/-10/90/1.3/0.2
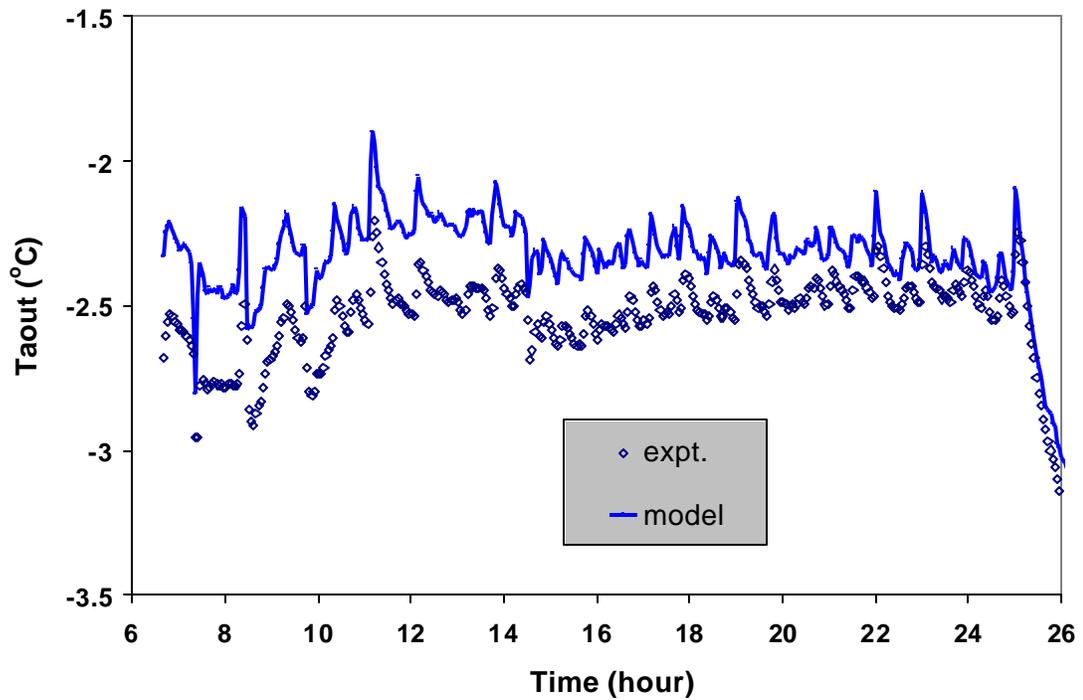
Figure D.12 Comparison of the air outlet temperature for 0/-10/90/1.3/0.2
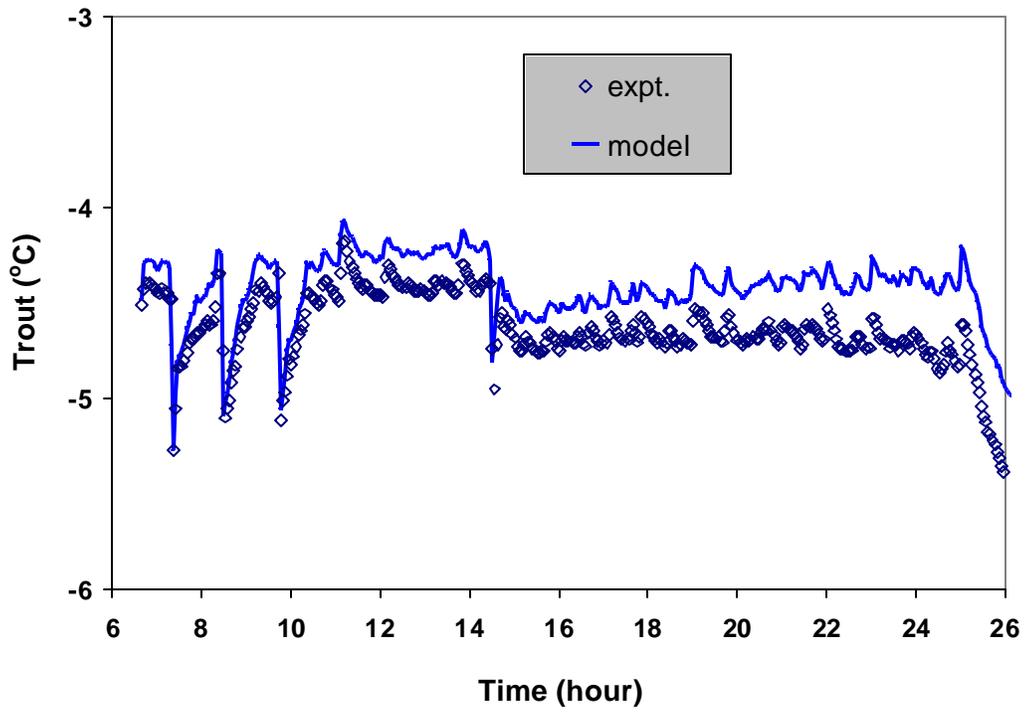
Figure D.13 Comparison of the refrigerant outlet temperature for 0/-10/90/1.3/0.2
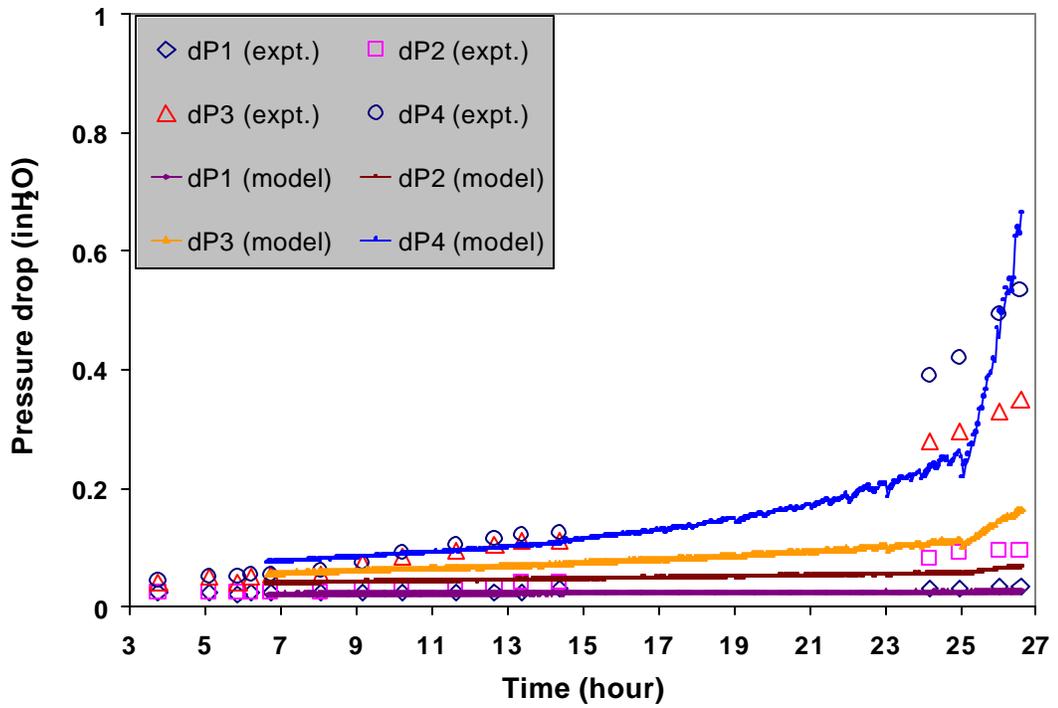
Figure D.14 Comparison of the air side pressure drop for0/-10/90/1.3/0.2
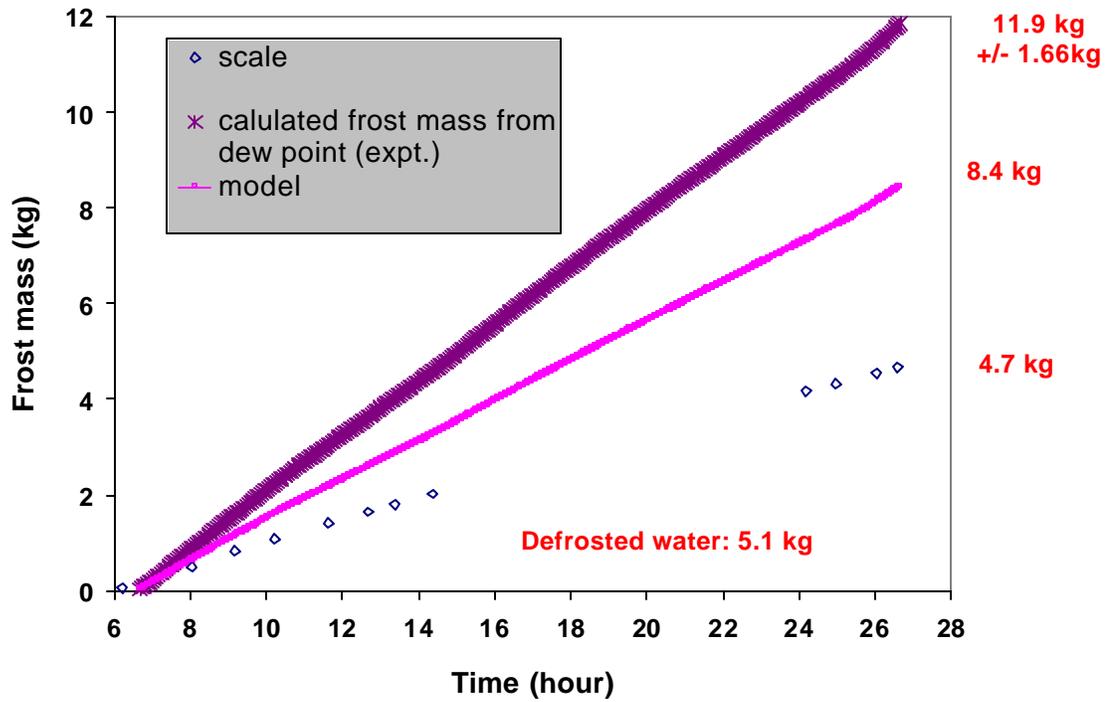
Figure D.15 Comparison of the frosting rate for 0/-10/90/1.3/0.2
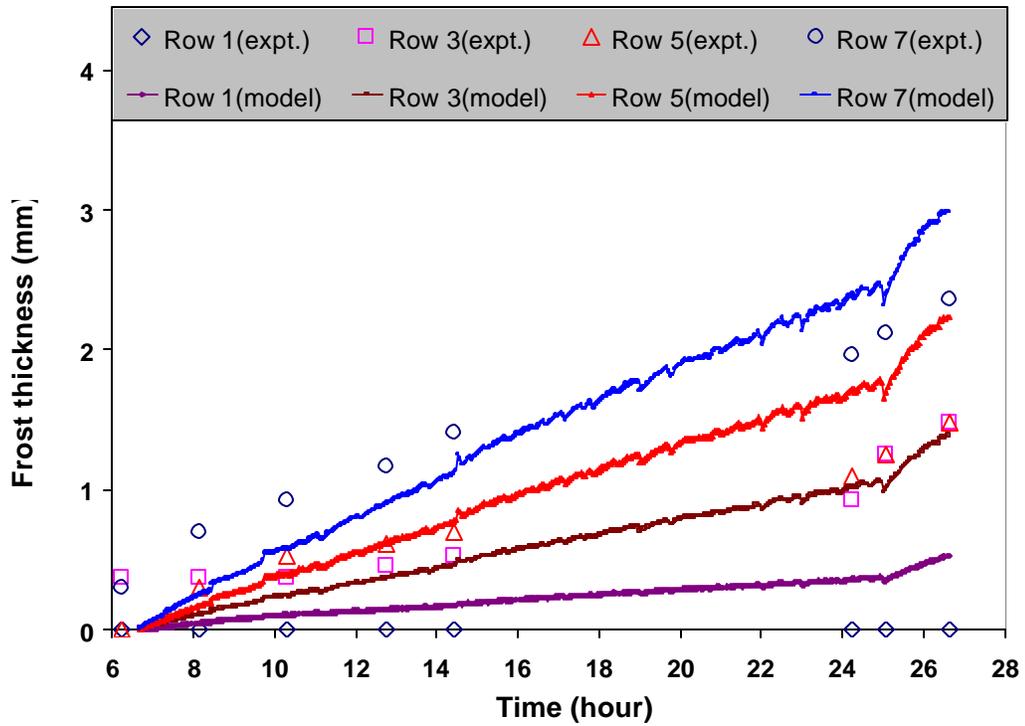
Figure D.16 Comparison of the frost thickness for 0/-10/90/1.3/0.2

D.3 Validation results for 0/-10/90/1.3/0.26
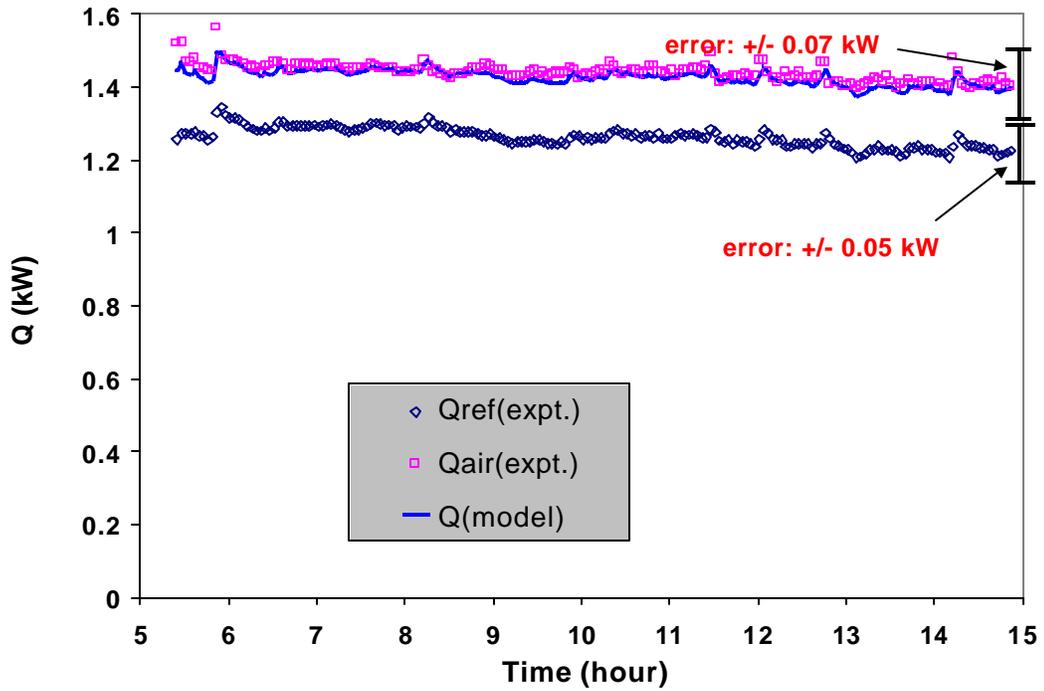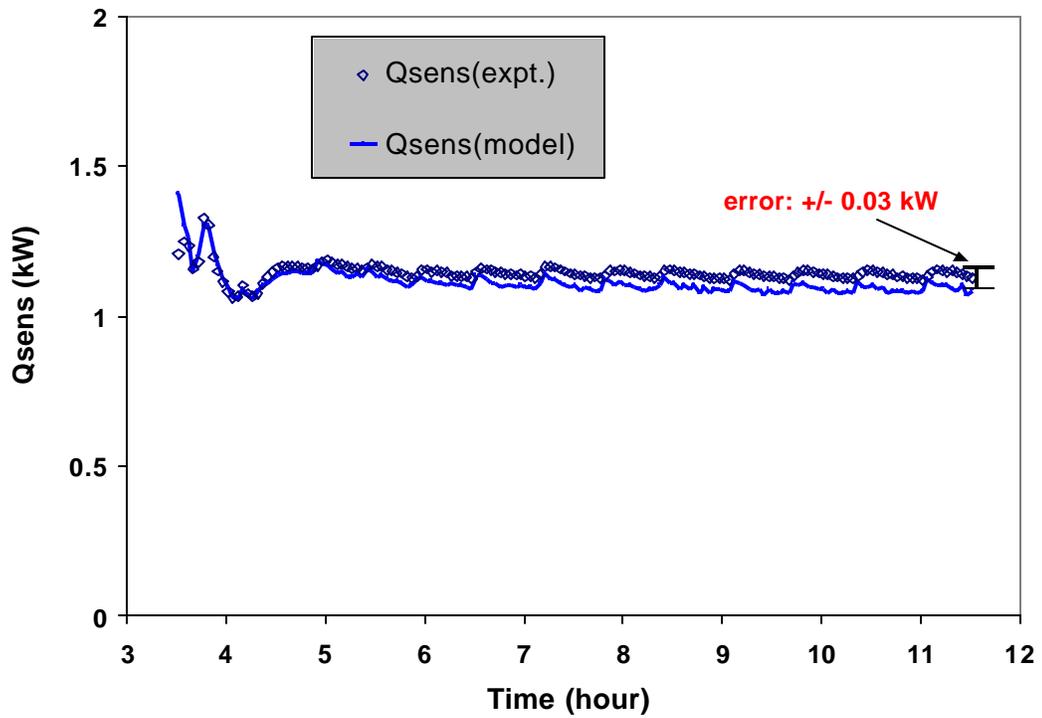

Figure D.17 Comparison of the total load for 0/-10/90/1.3/0.26
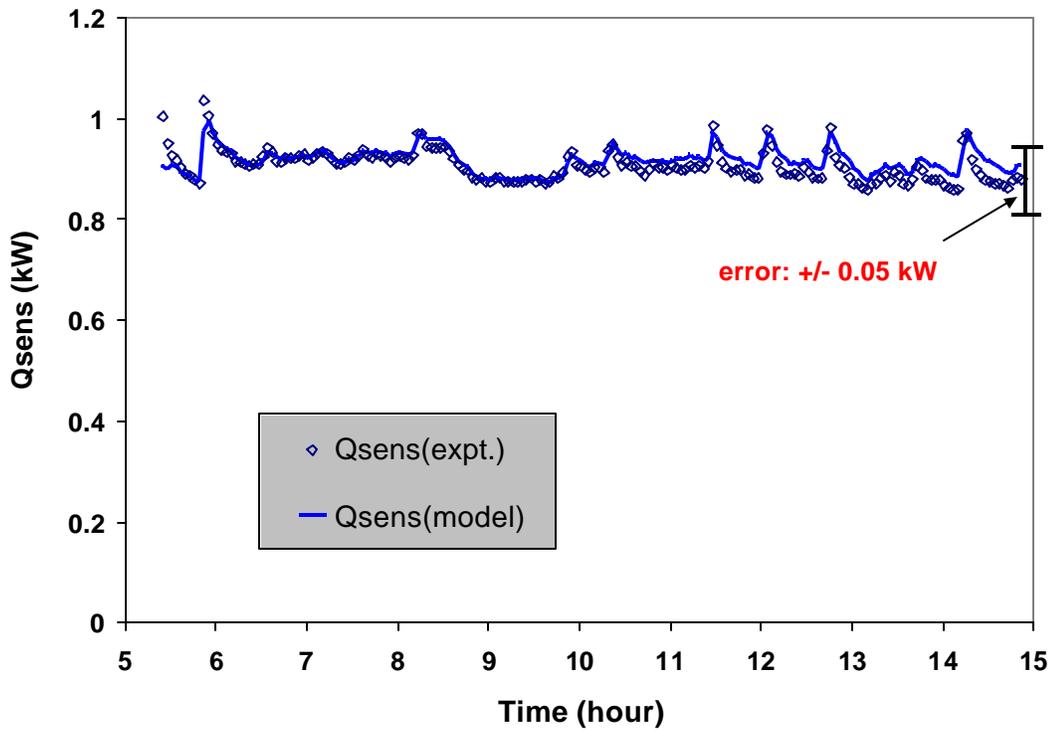
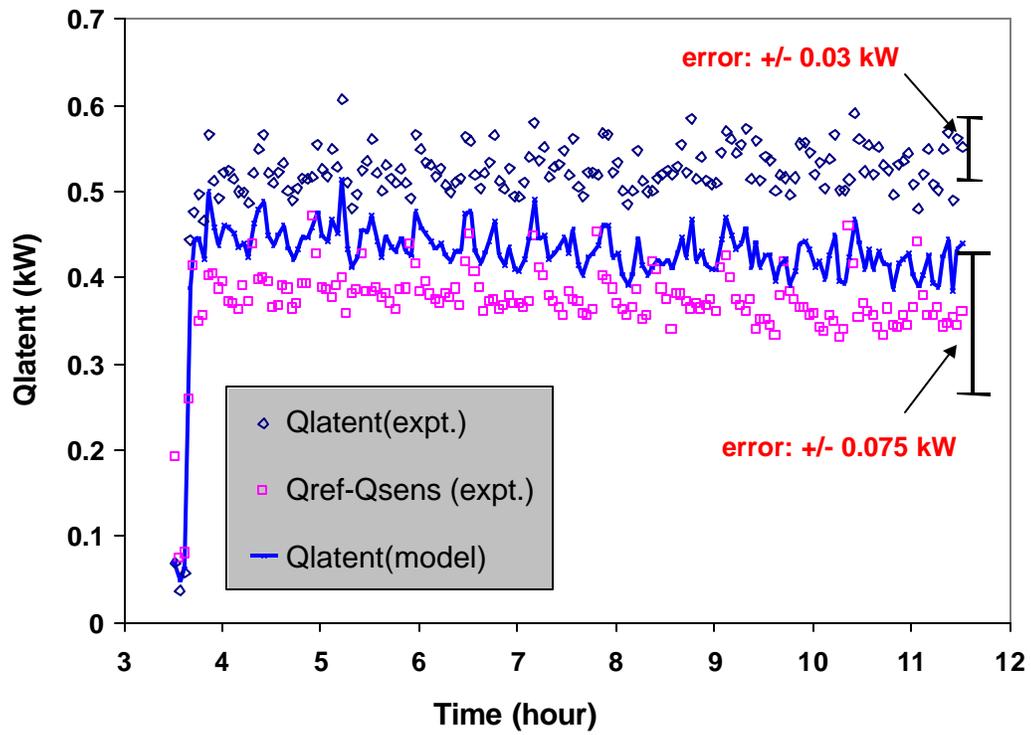Figure D.18 Comparison of the sensible load for 0/-10/90/1.3/0.26
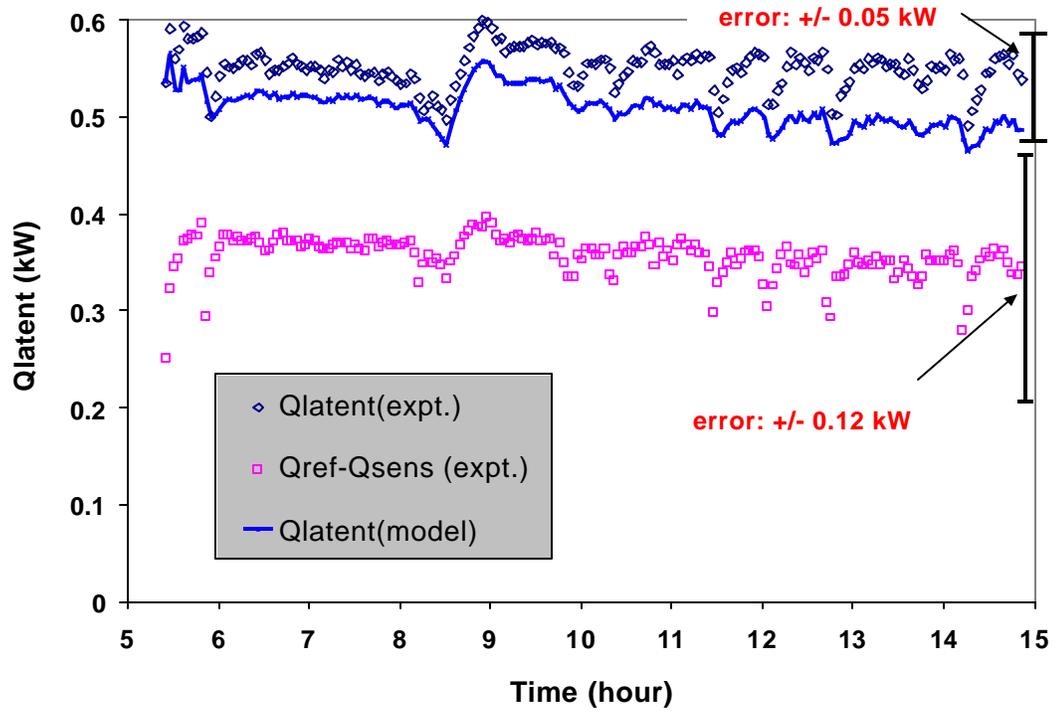
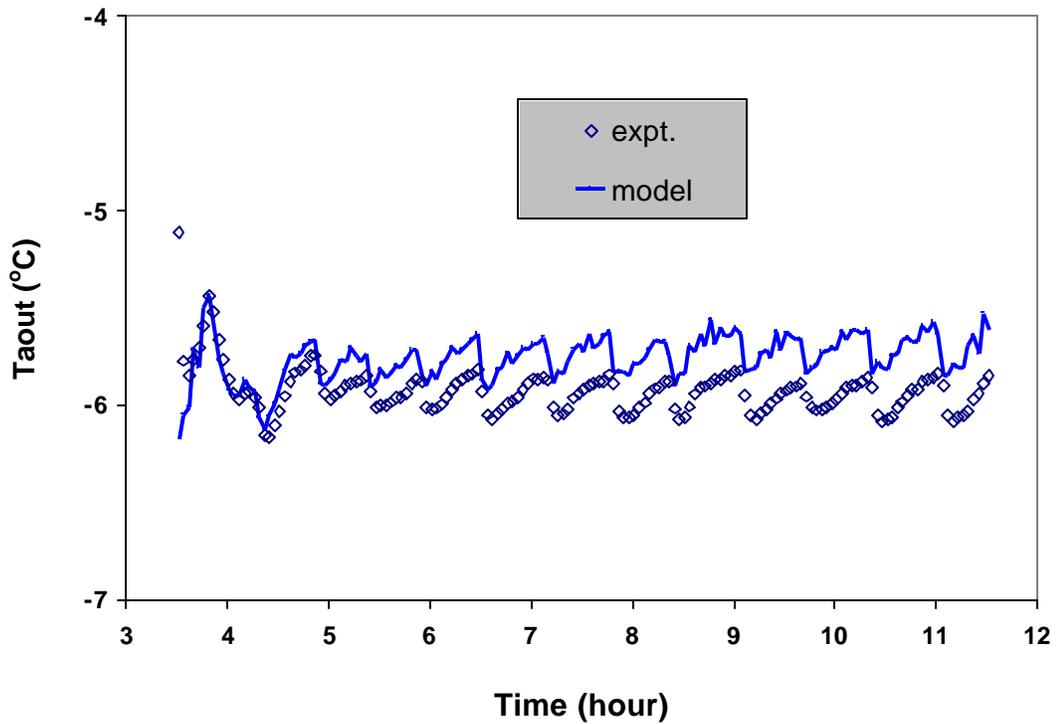Figure D.19 Comparison of the latent load for 0/-10/90/1.3/0.26
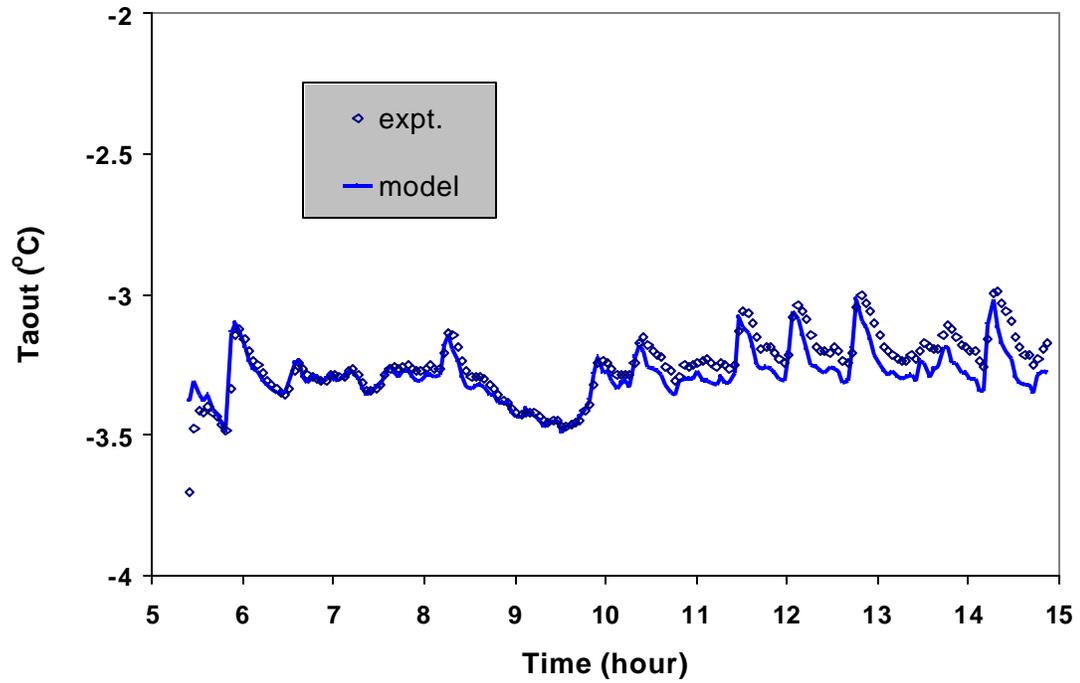
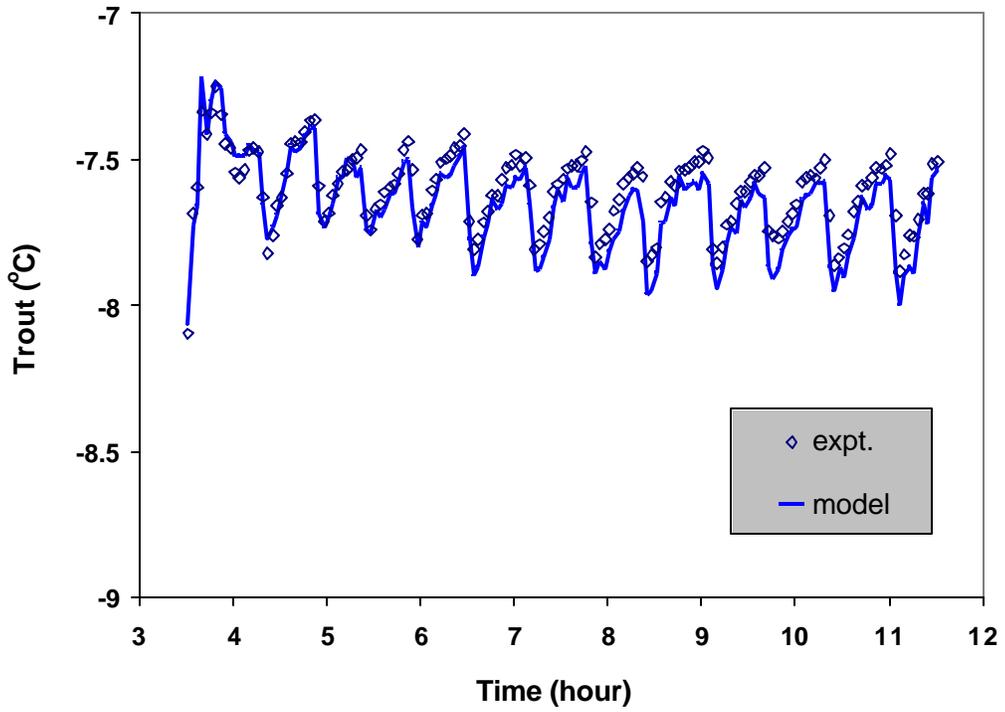Figure D.20 Comparison of the air outlet temperature for 0/-10/90/1.3/0.26
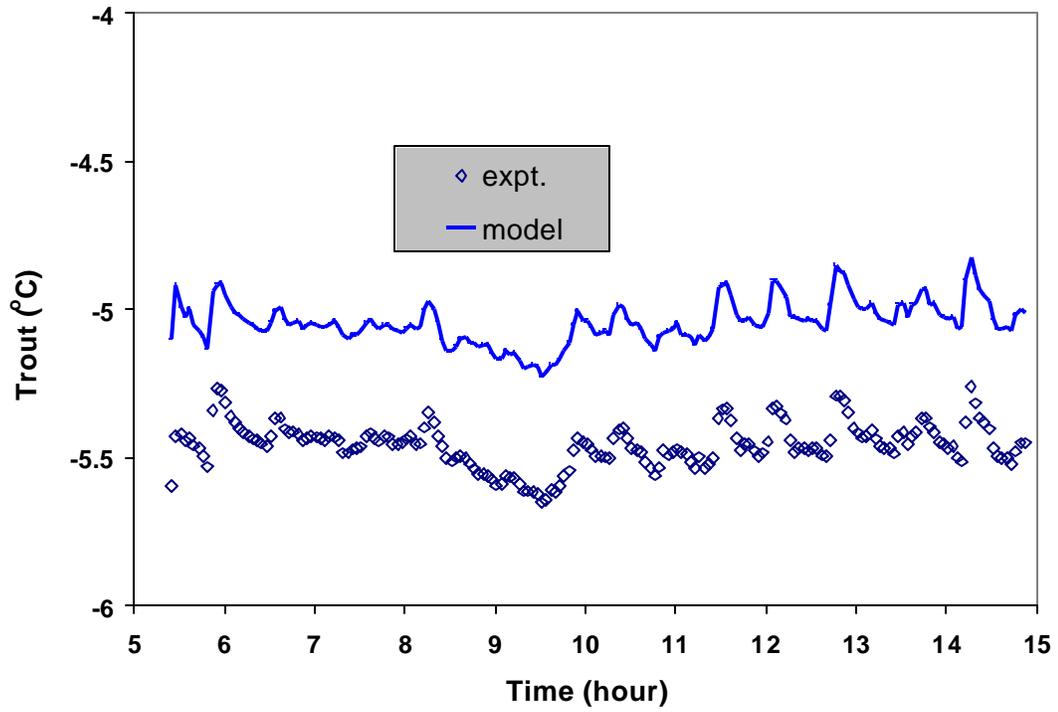
Figure D.21 Comparison of the refrigerant outlet temperature for 0/-10/90/1.3/0.26
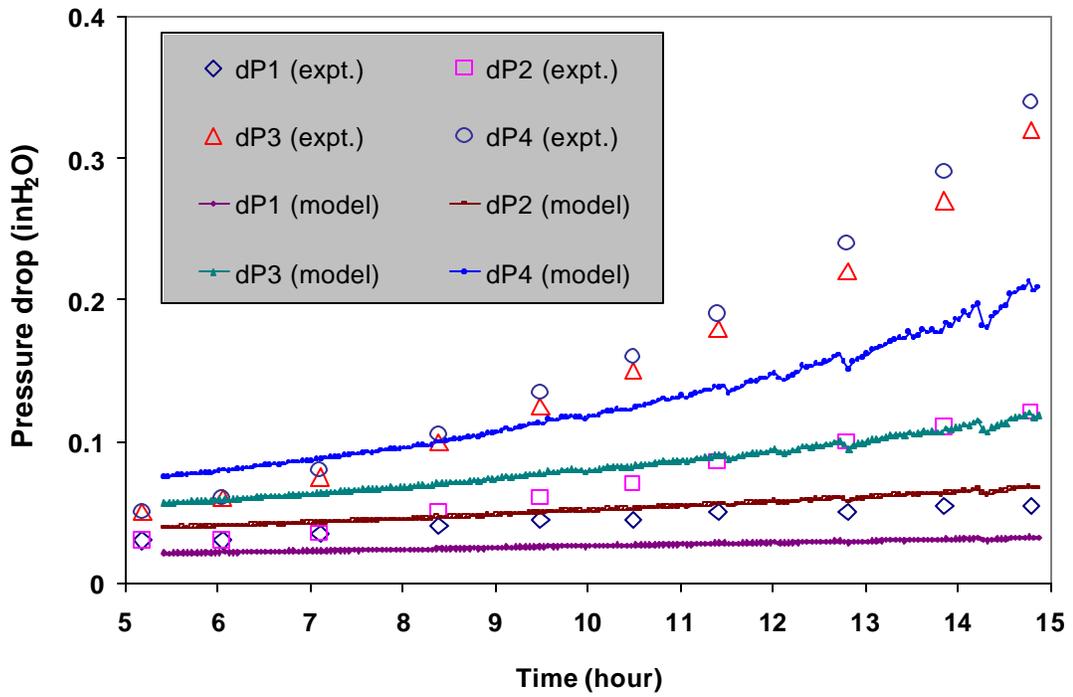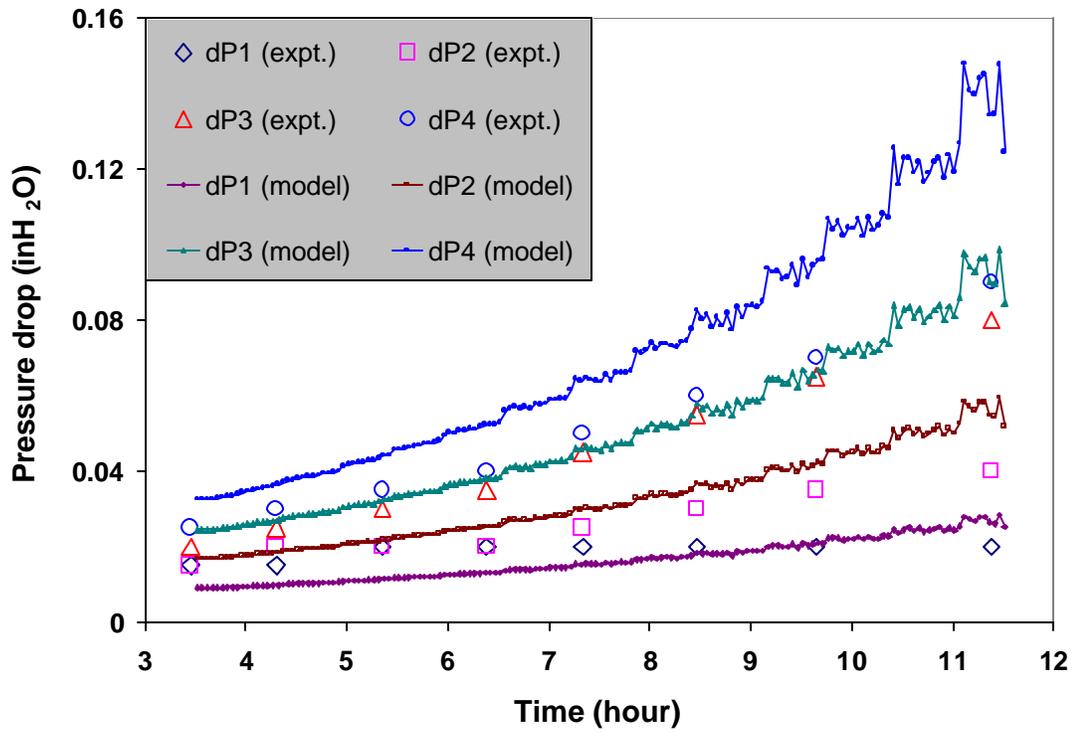

Figure D.22 Comparison of the air side pressure drop for 0/-10/90/1.3/0.26
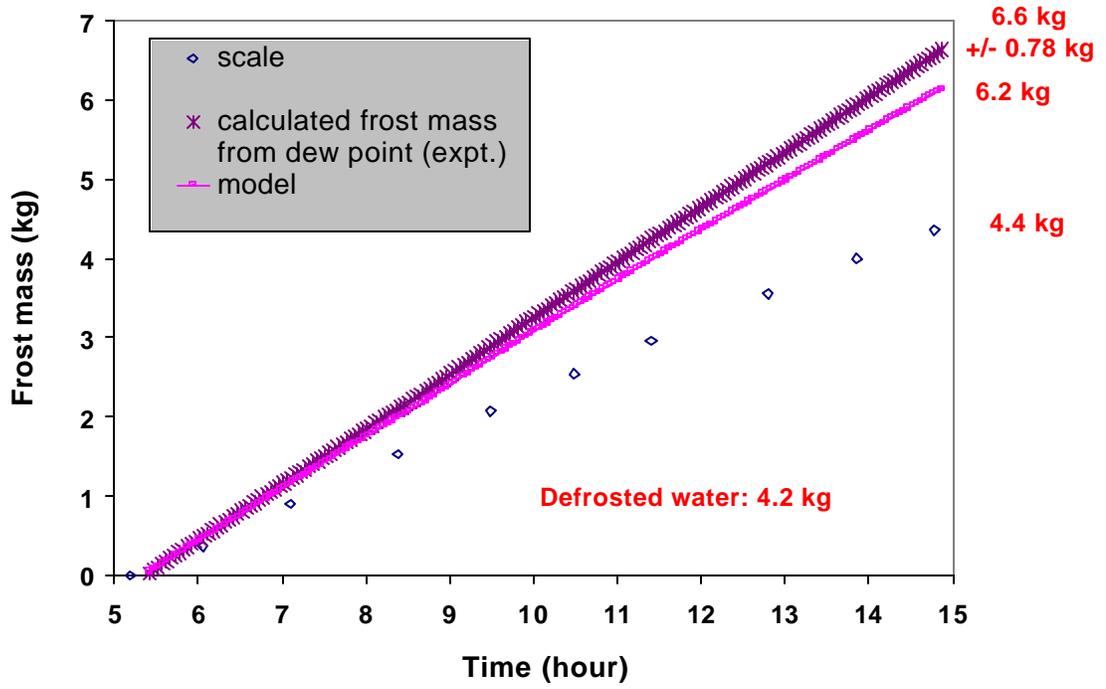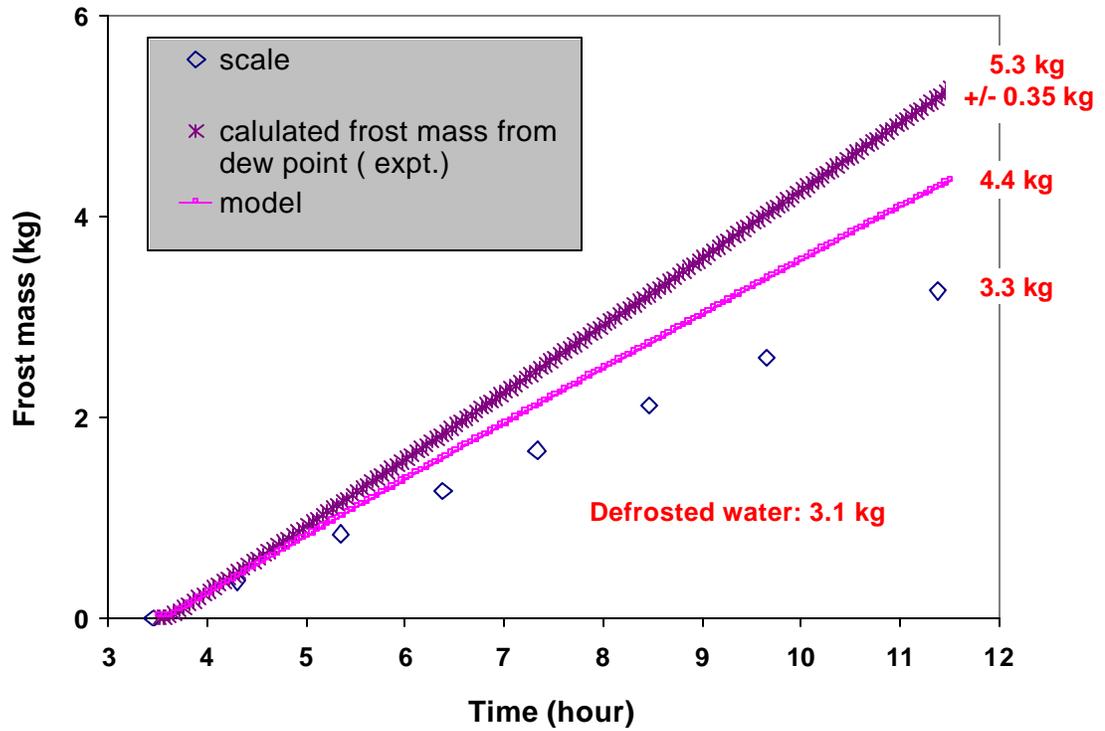
Figure D.23 Comparison of the frosting rate for 0/-10/90/1.3/0.26
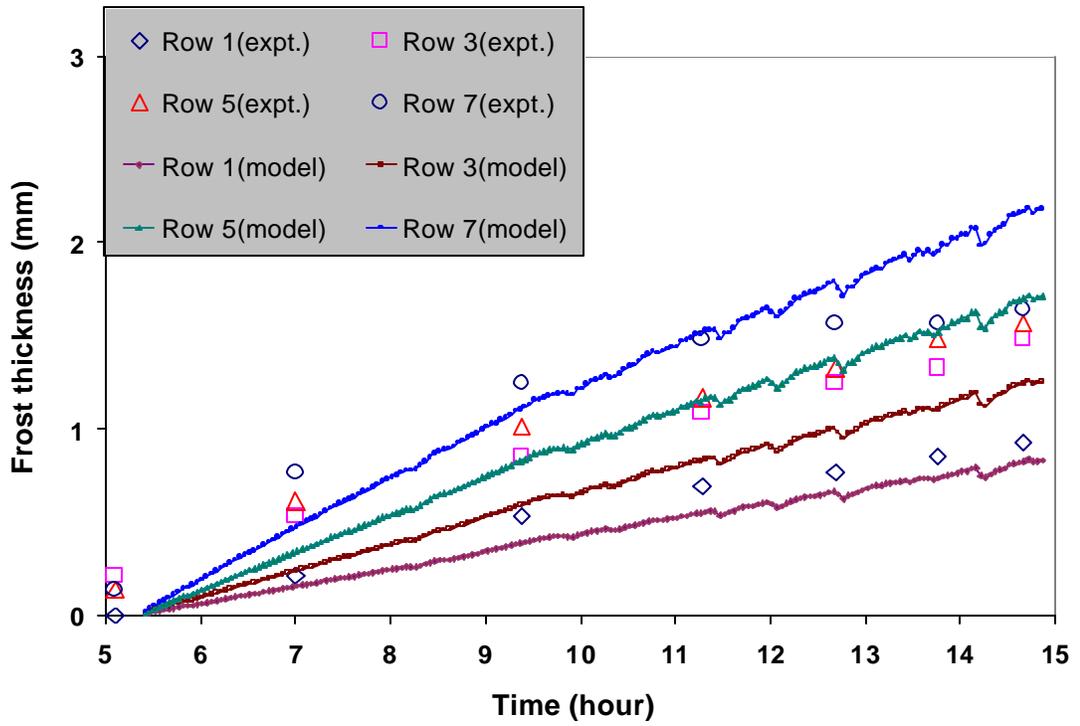
Figure D.24 Comparison of the frost thickness for 0/-10/90/1.3/0.26

D.4 Validation results for 0/-30/90/2.2/0.5
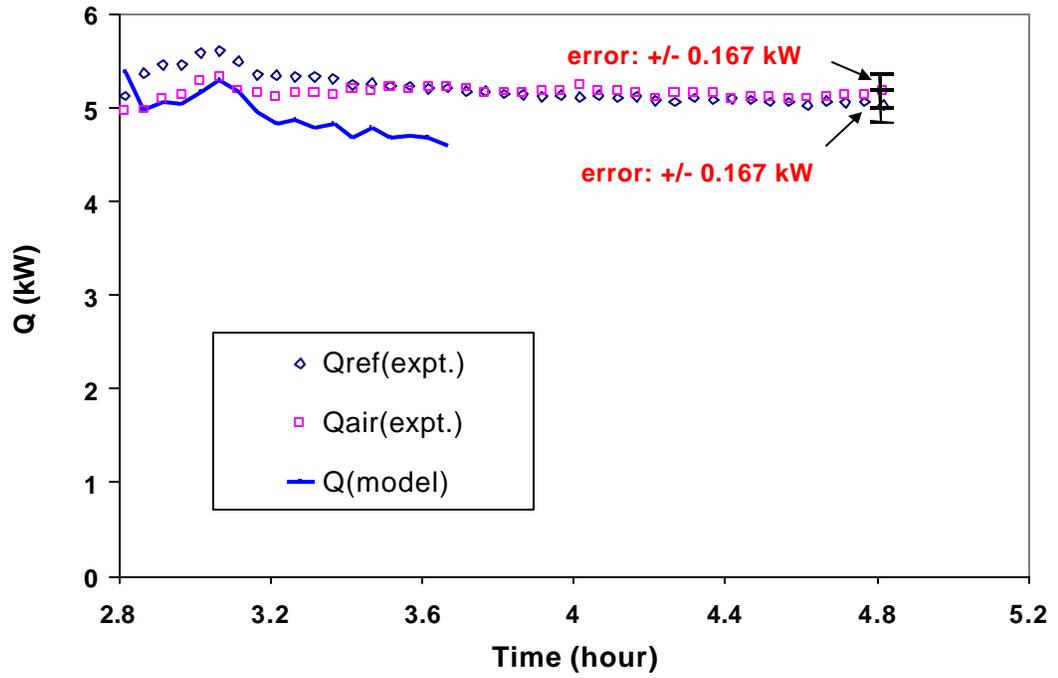
Figure D.25 Comparison of the total load for 0/-30/90/2.2/0.5
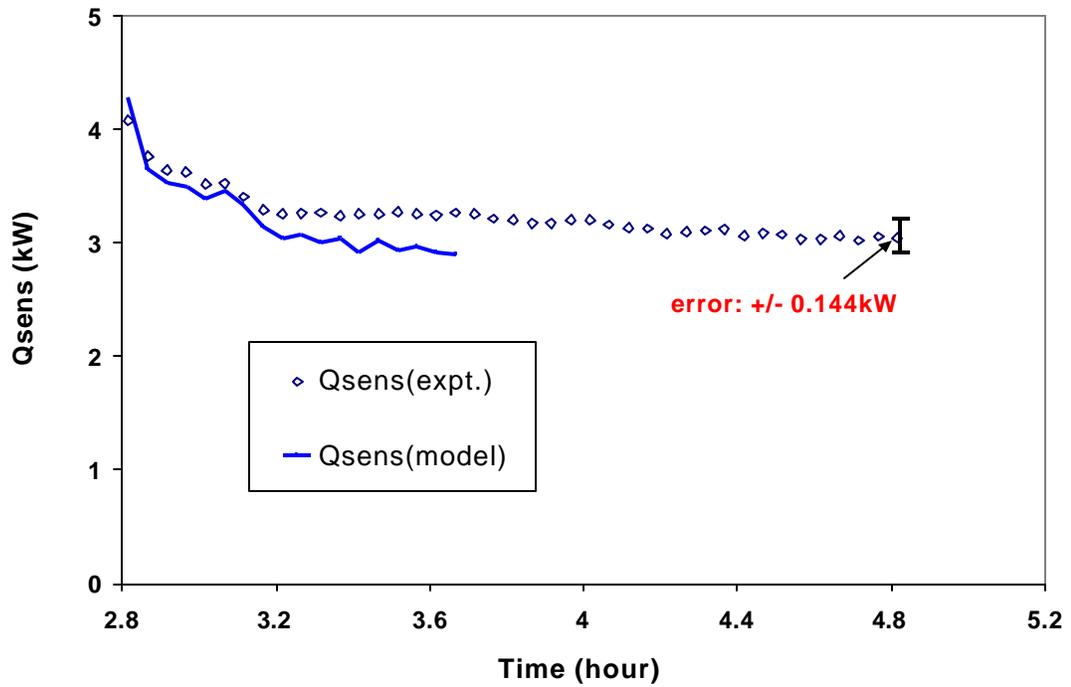
Figure D.26 Comparison of the sensible load for 0/-30/90/2.2/0.5
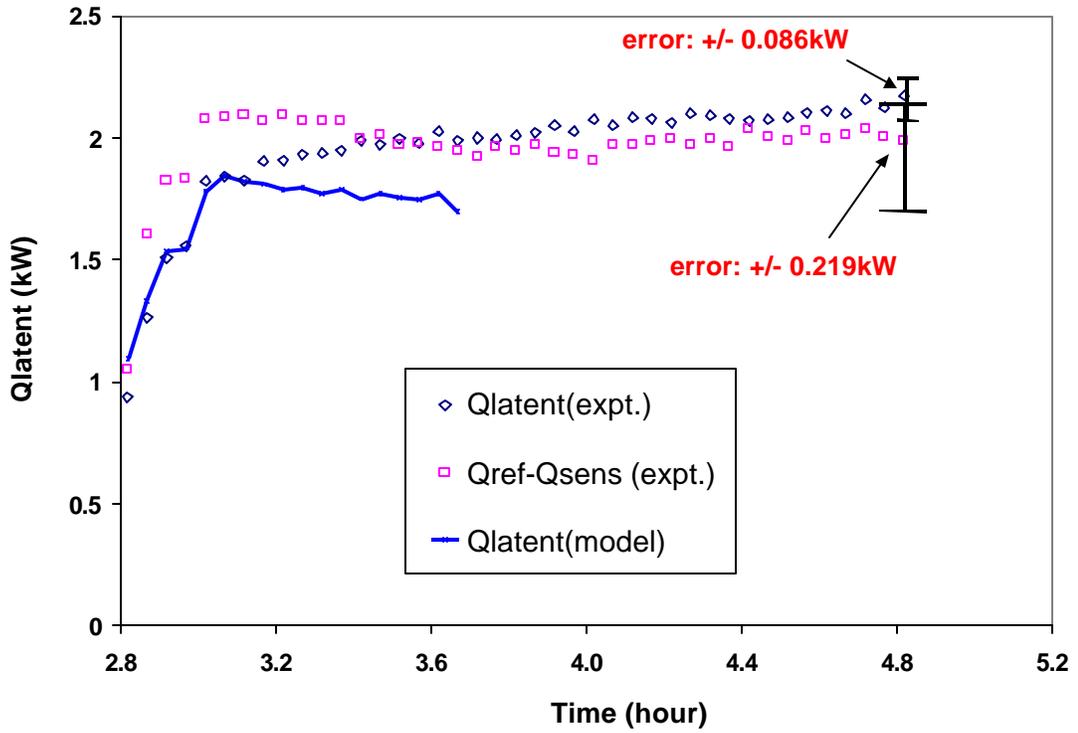
Figure D.27 Comparison of the latent load for 0/-30/90/2.2/0.5
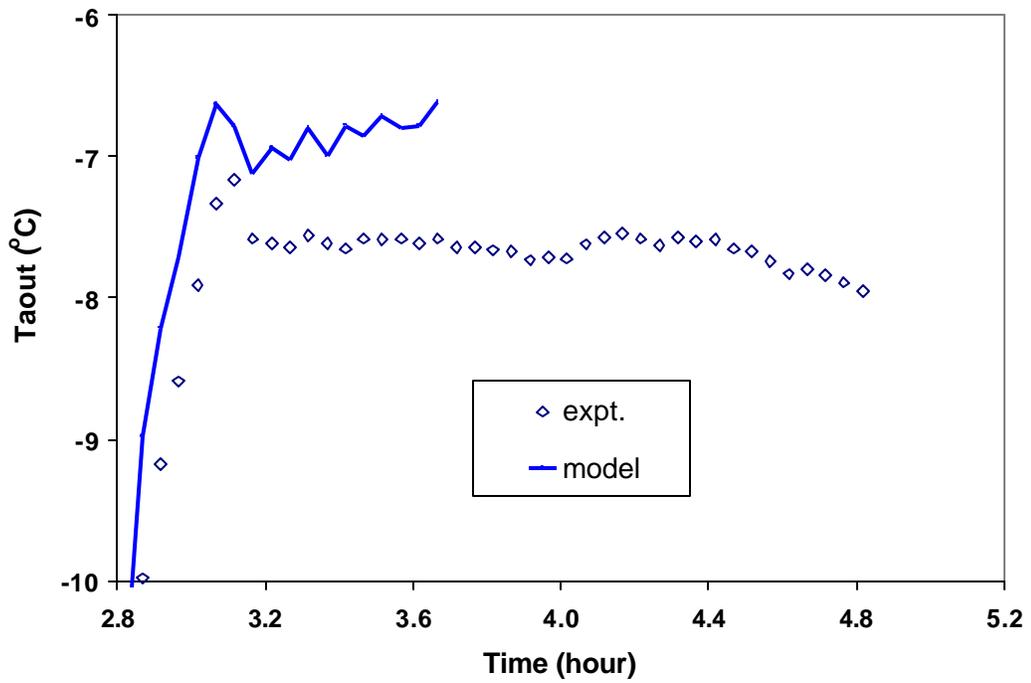
Figure D.28 Comparison of the air outlet temperature for 0/-30/90/2.2/0.5
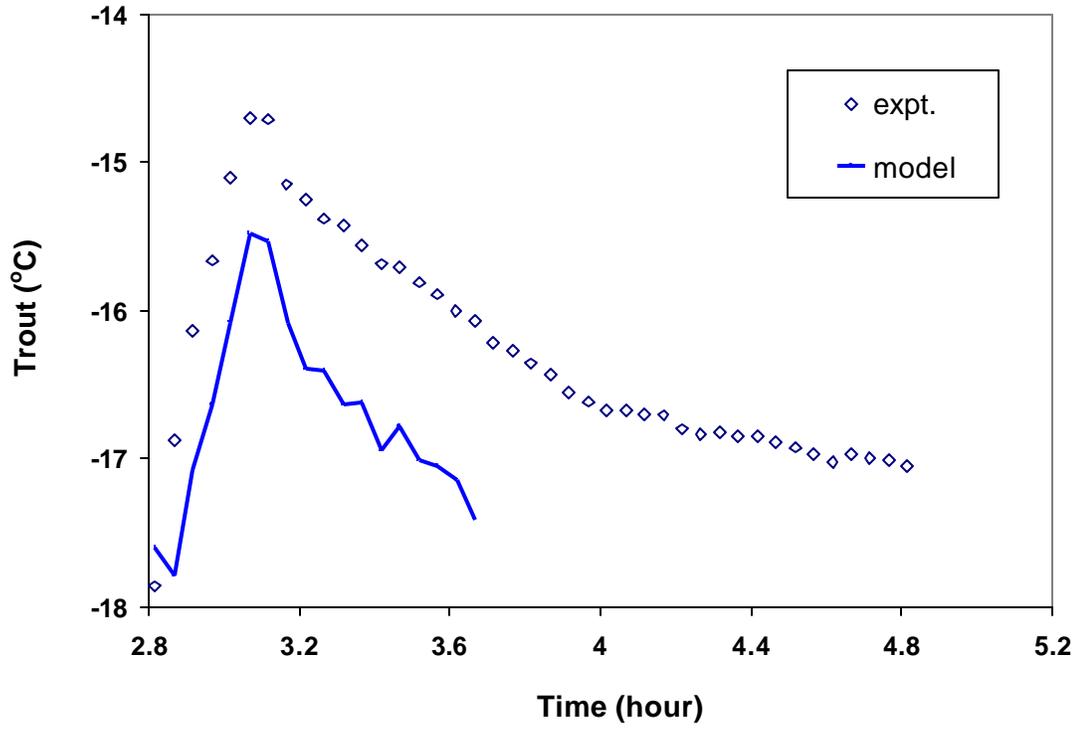
Figure D.29 Comparison of the refrigerant outlet temperature for 0/-30/90/2.2/0.5
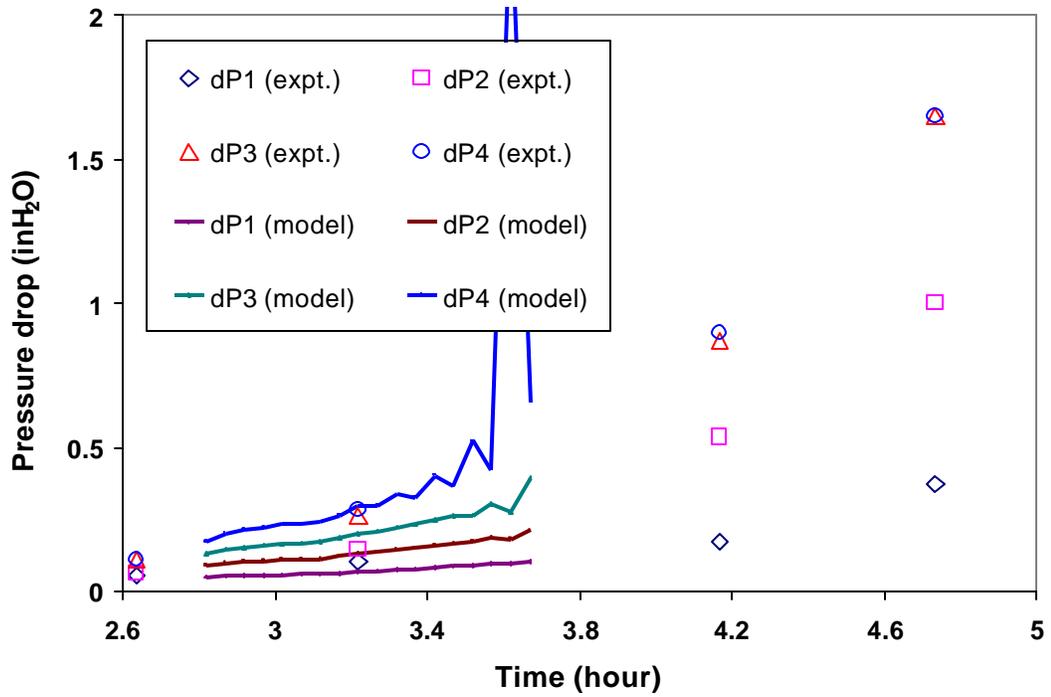
Figure D.30 Comparison of the air side pressure drop for 0/-30/90/2.2/0.5
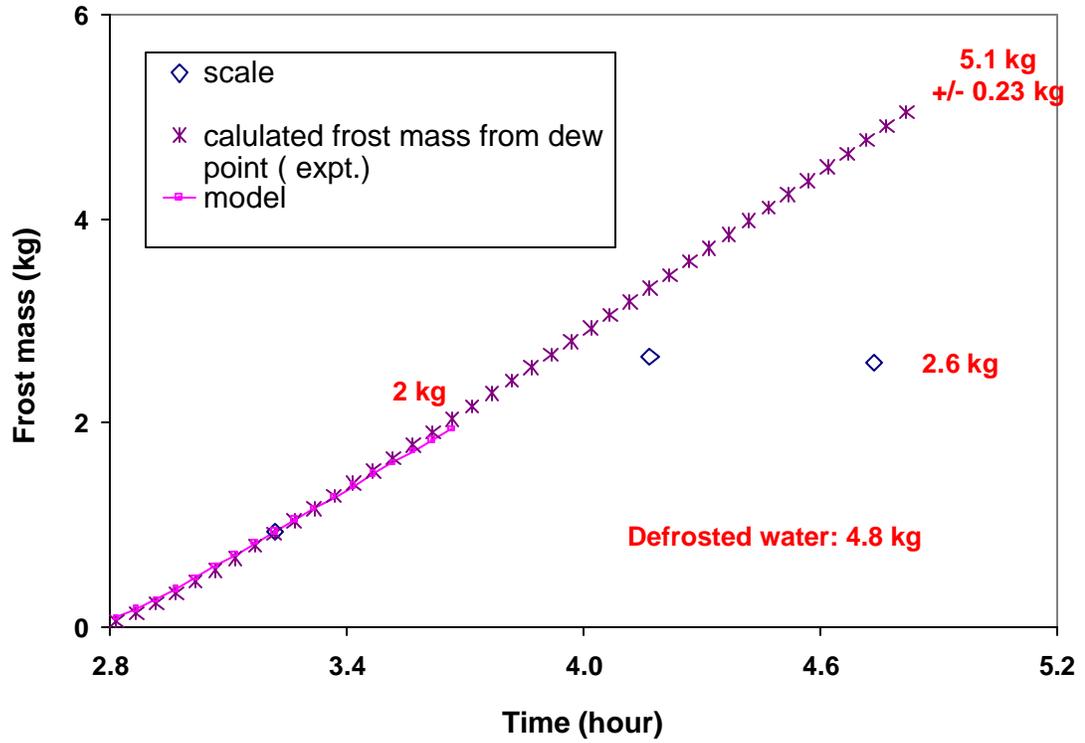
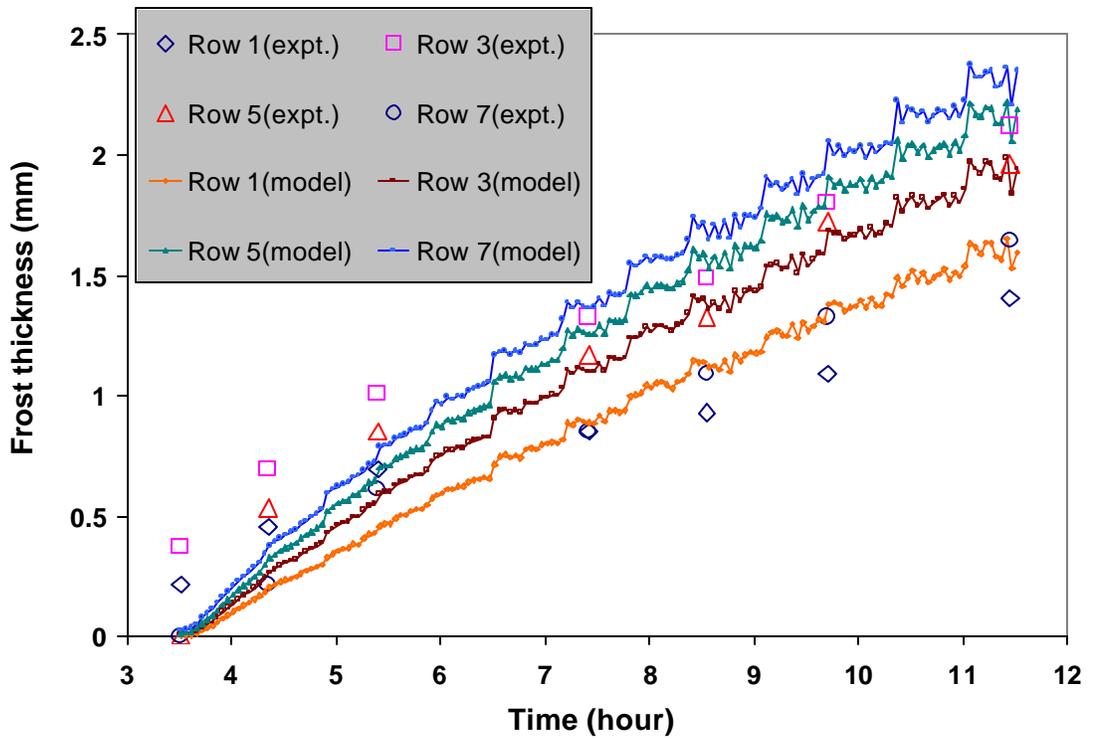Figure D.31 Comparison of the frosting rate for 0/-30/90/2.2/0.5
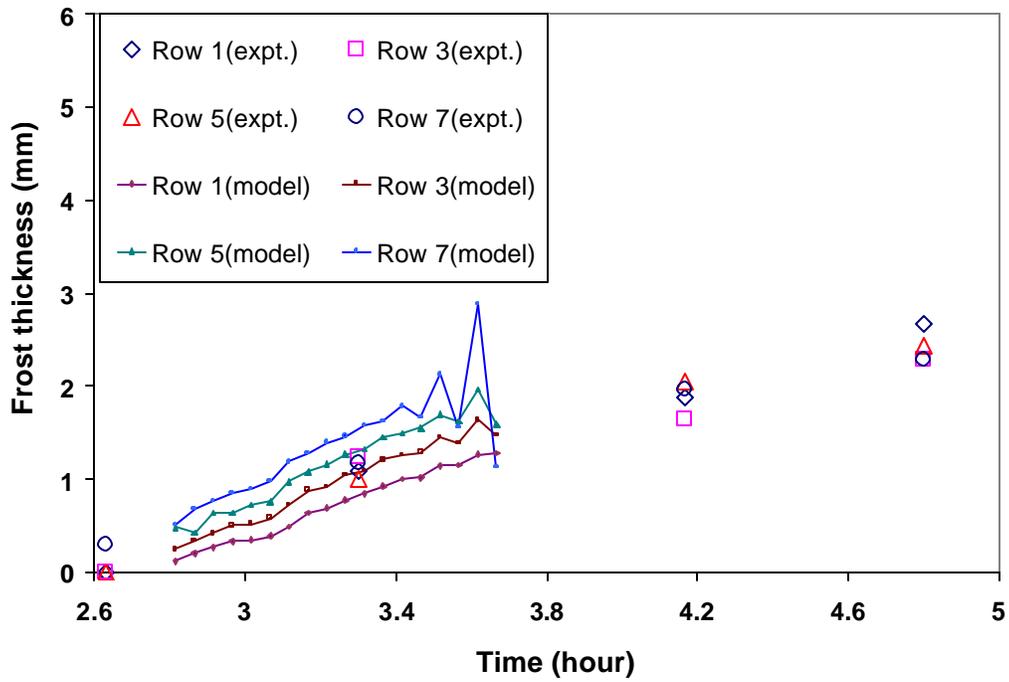
Figure D.32 Comparison of the frost thickness for 0/-30/90/2.2/0.5

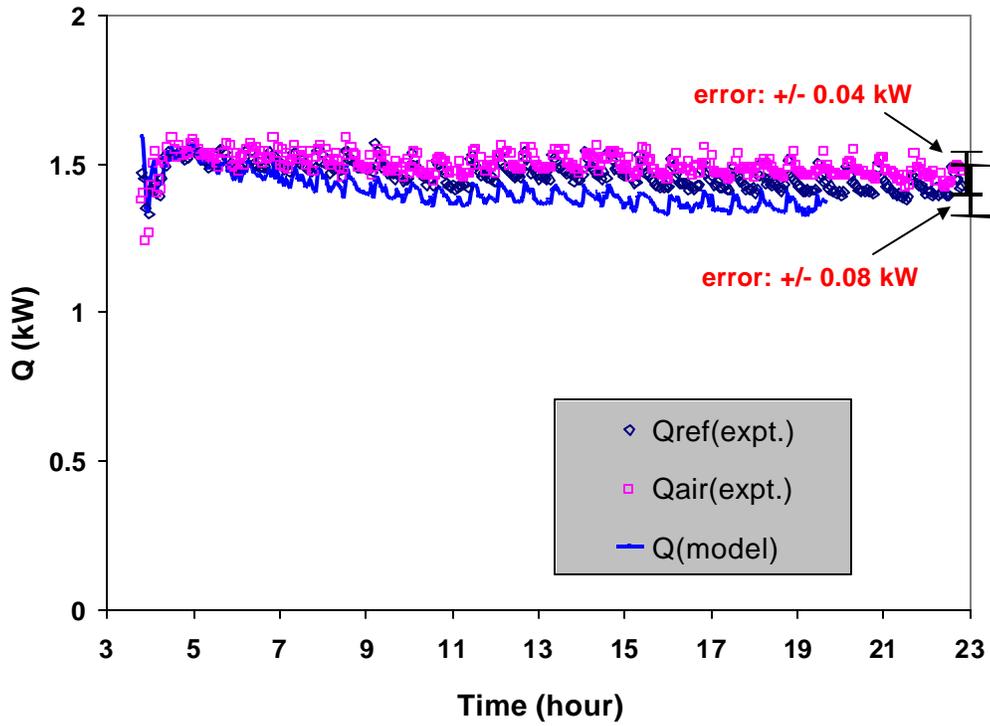**D.5 Validation results for -20/-30/70/2.2/0.5**
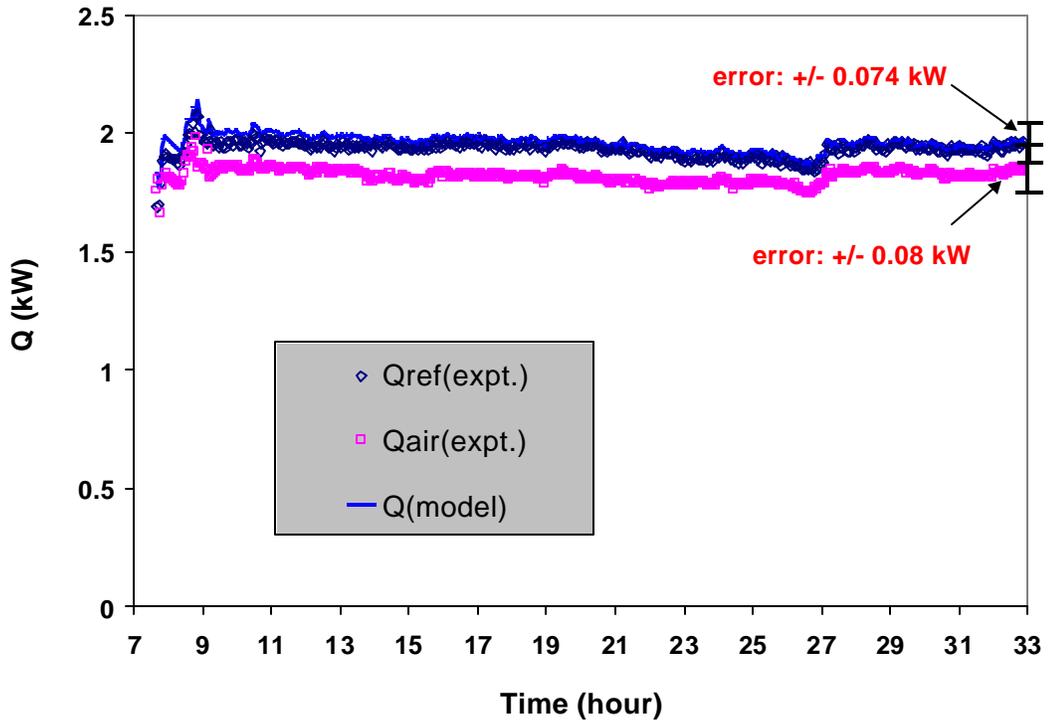
Figure D.33 Comparison of the total load for -20/-30/70/2.2/0.5
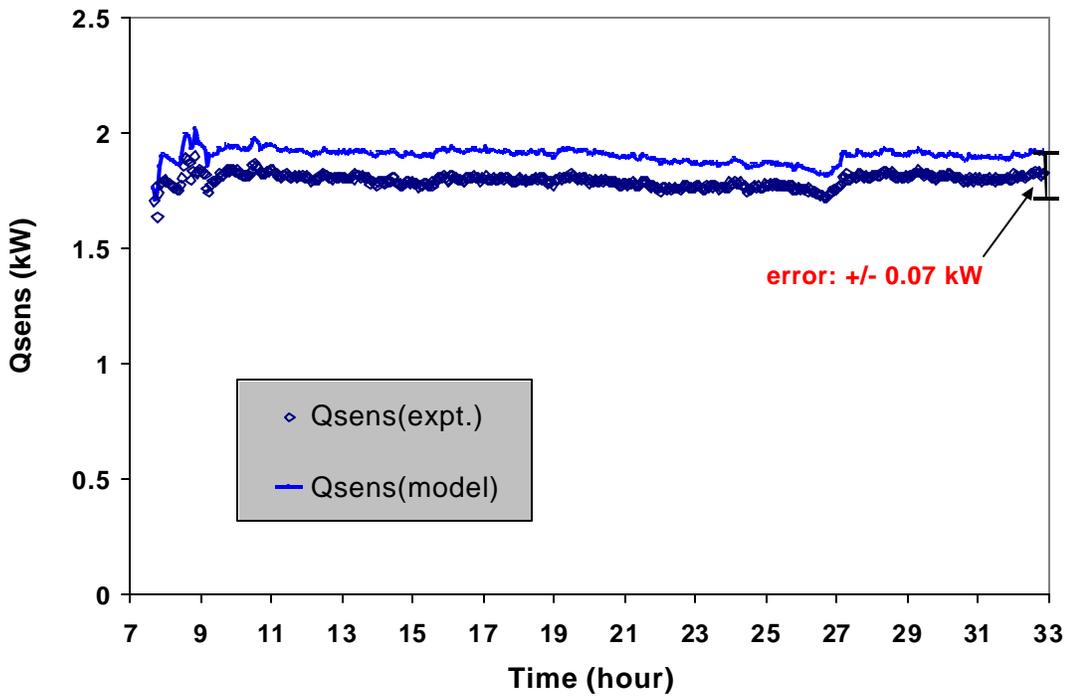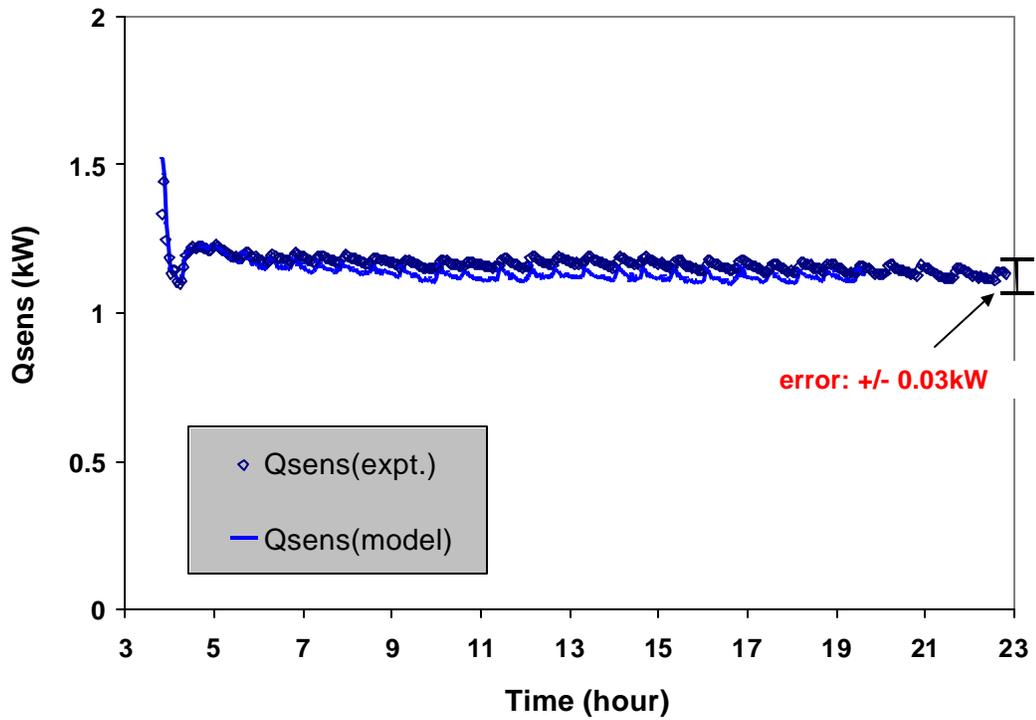

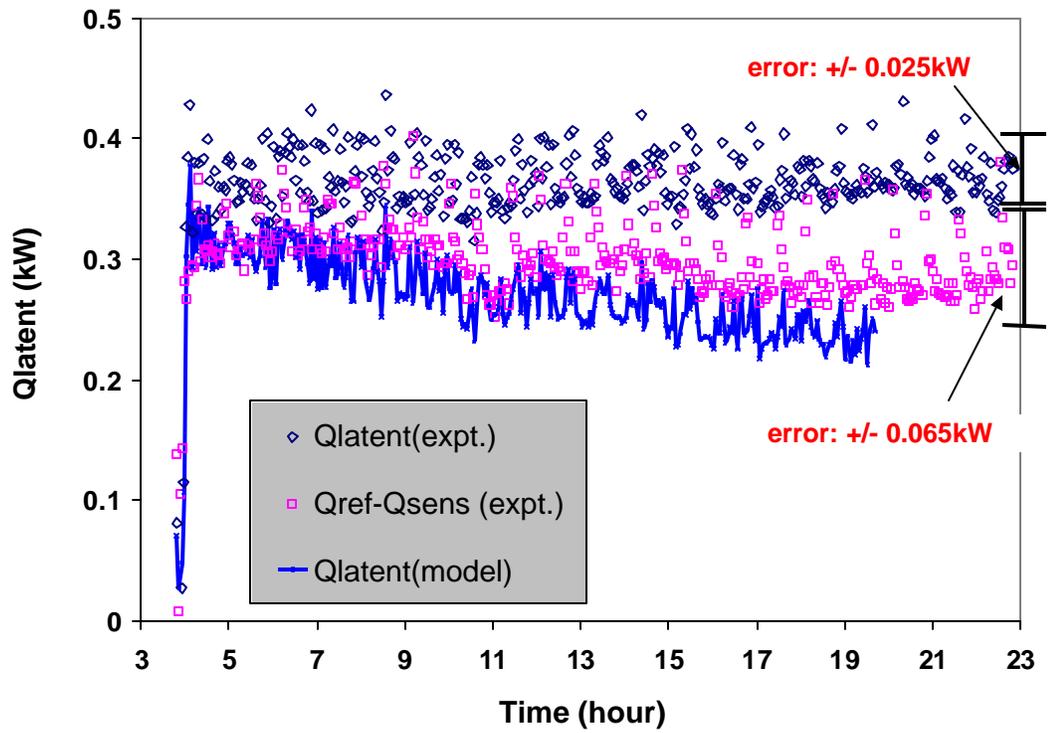Figure D.34 Comparison of the sensible load for -20/-30/70/2.2/0.5
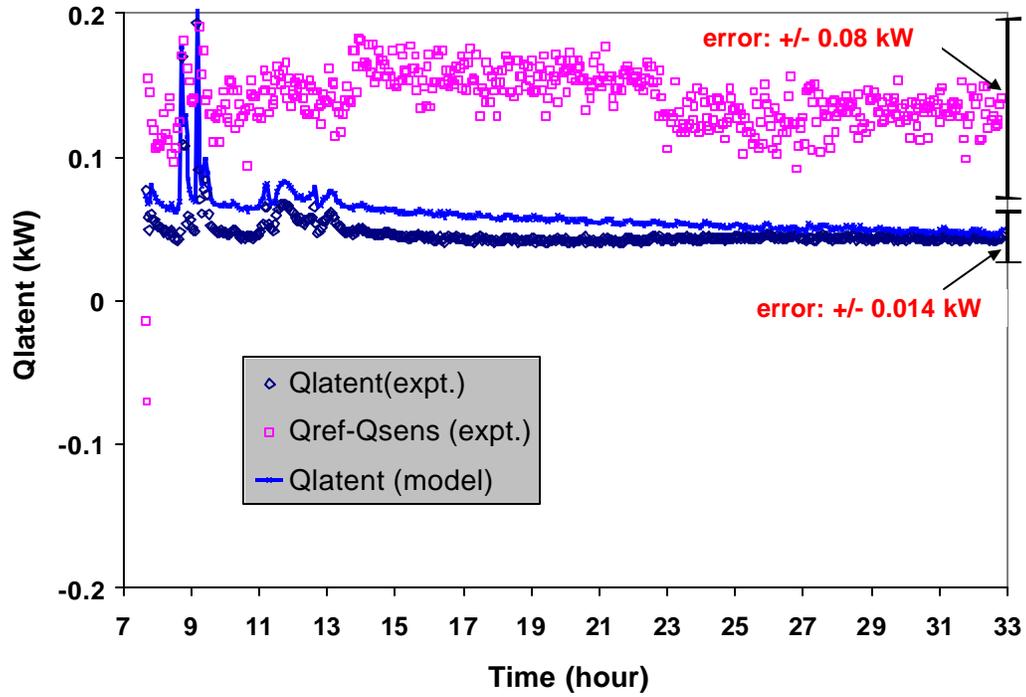
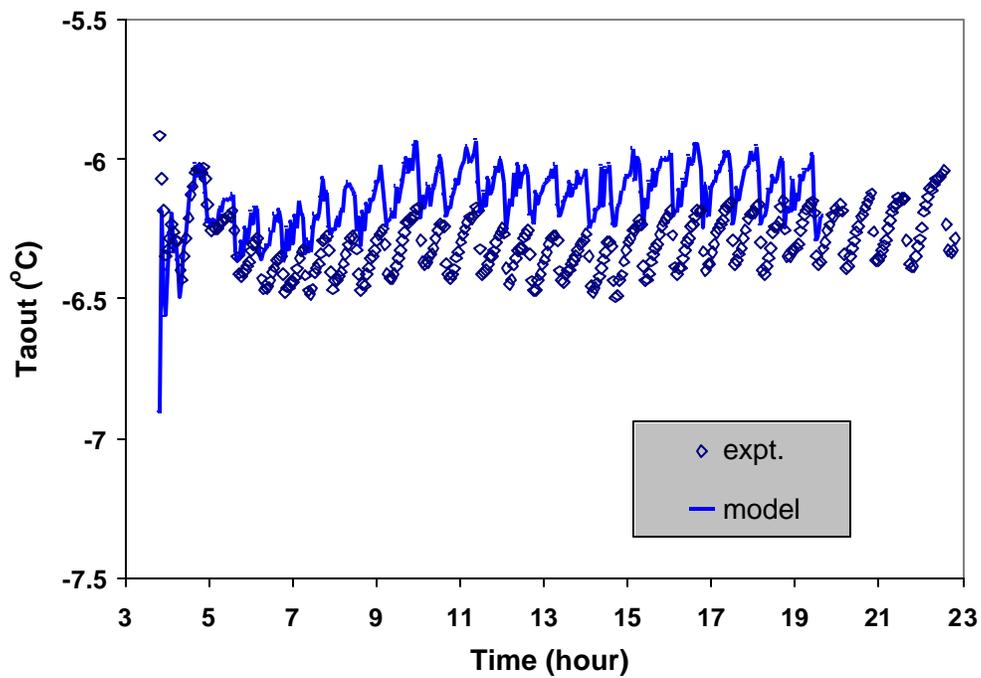Figure D.35 Comparison of the latent load for -20/-30/70/2.2/0.5
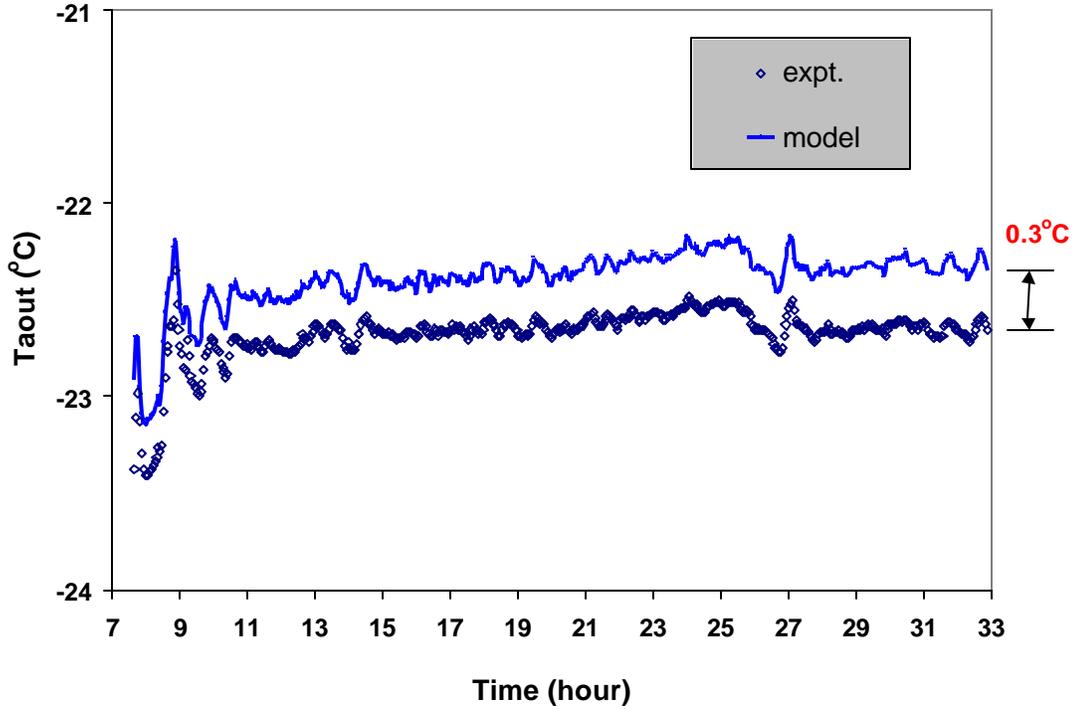
Figure D.36 Comparison of the air outlet temperature for -20/-30/70/2.2/0.5
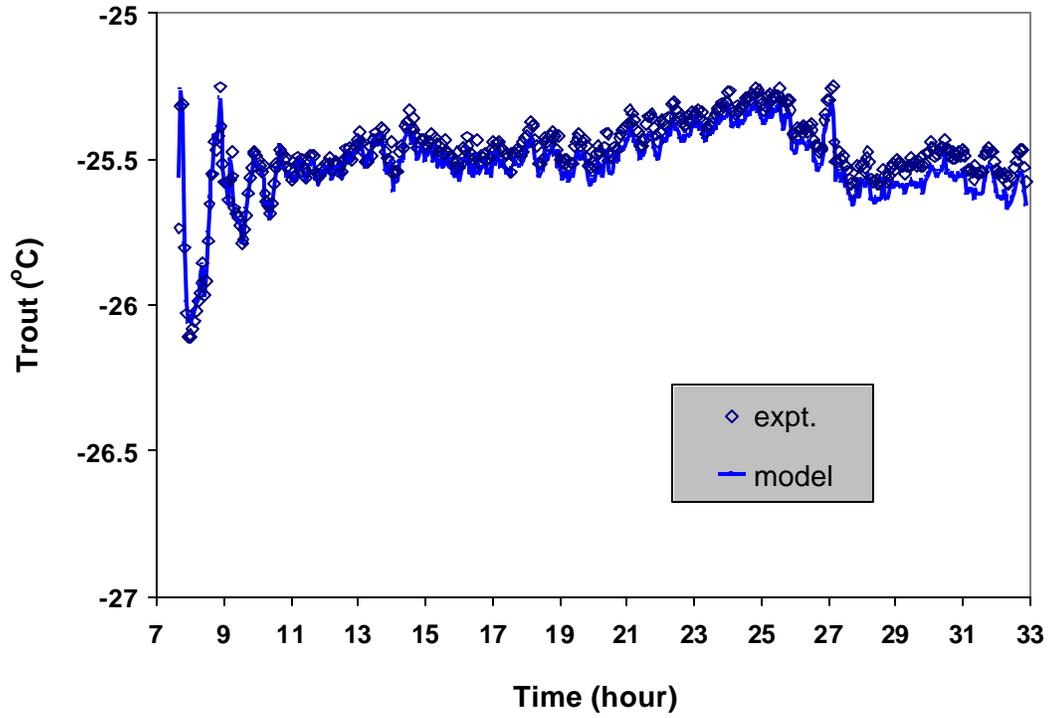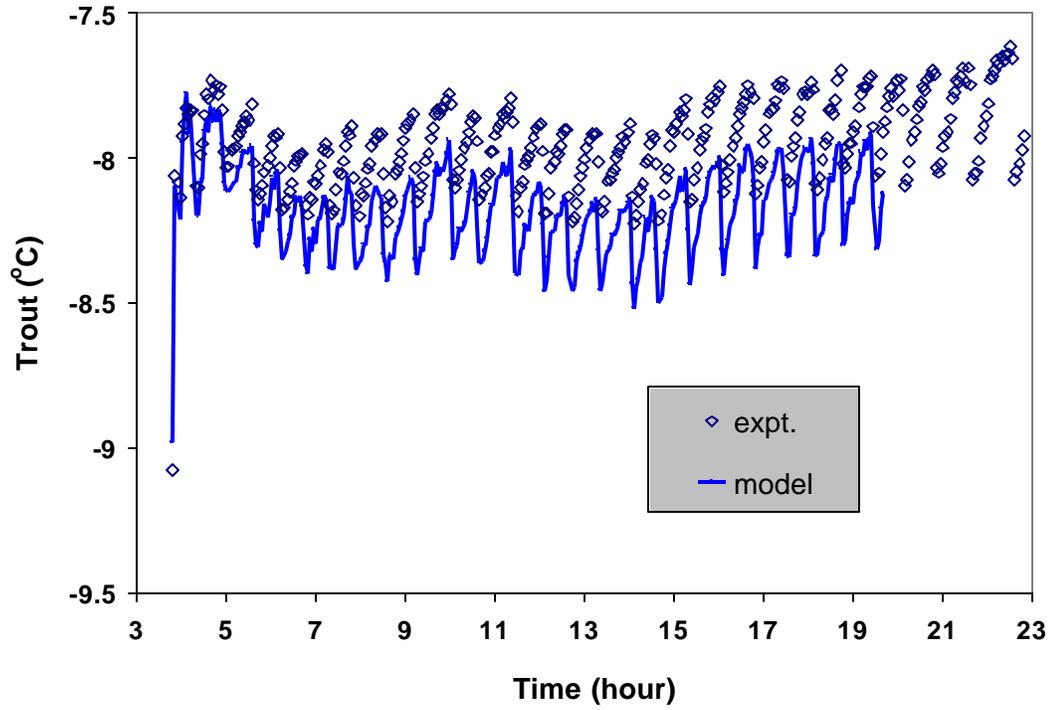
Figure D.37 Comparison of the refrigerant outlet temperature for -20/-30/70/2.2/0.5
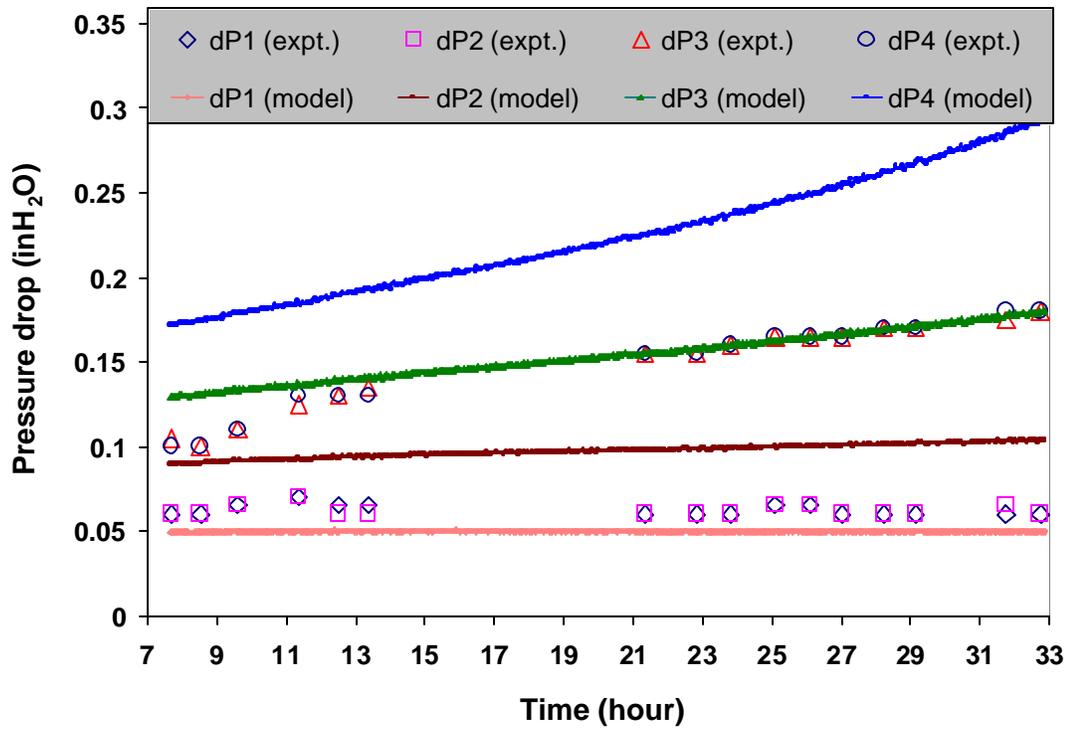
Figure D.38 Comparison of the air side pressure drop for -20/-30/70/2.2/0.5
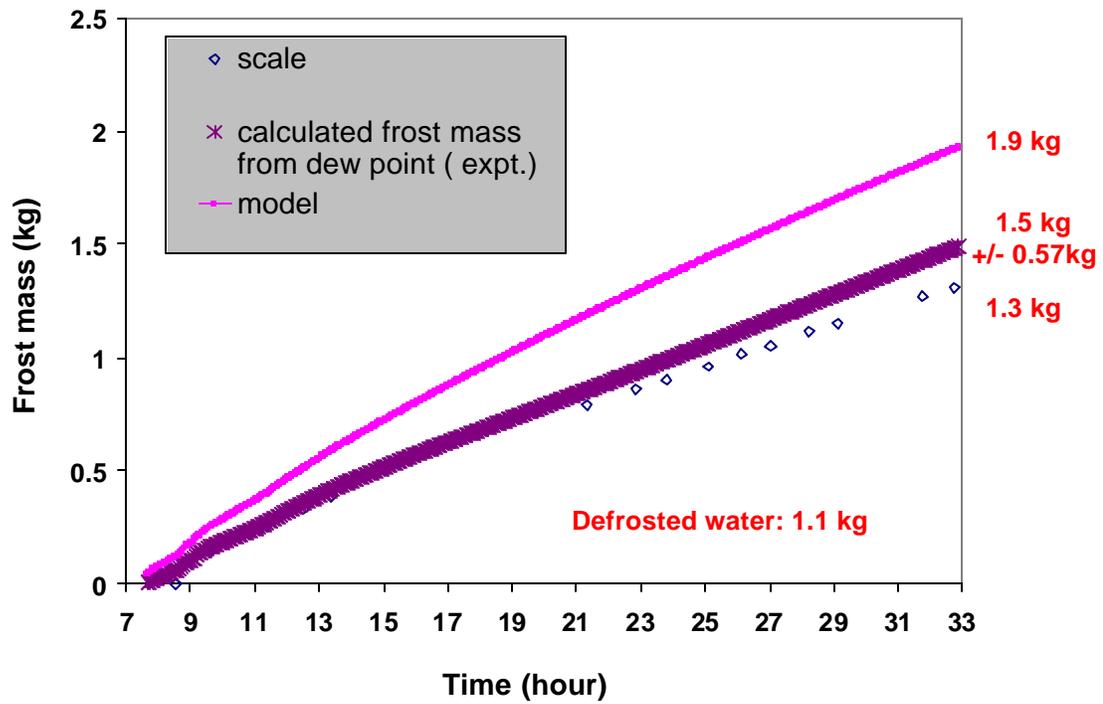
Figure D.39 Comparison of the frosting rate for -20/-30/70/2.2/0.5
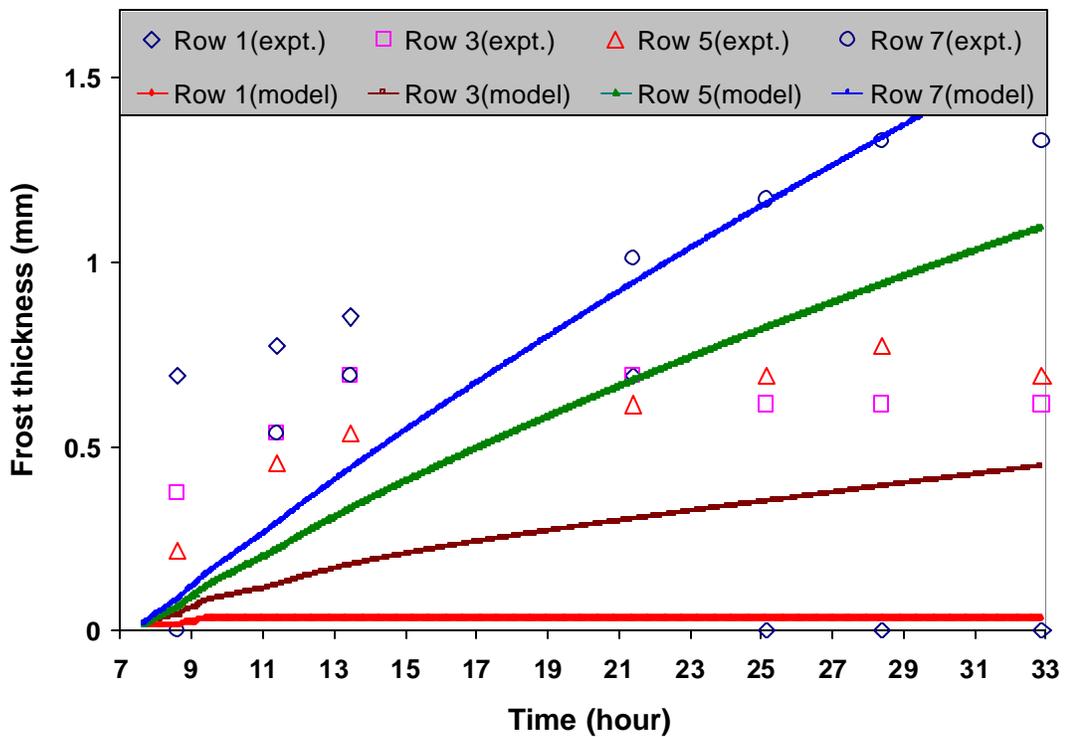
Figure D.40 Comparison of the frost thickness for -20/-30/70/2.2/0.5

D.6 Validation results for -20/-30/70/1.3/0.5
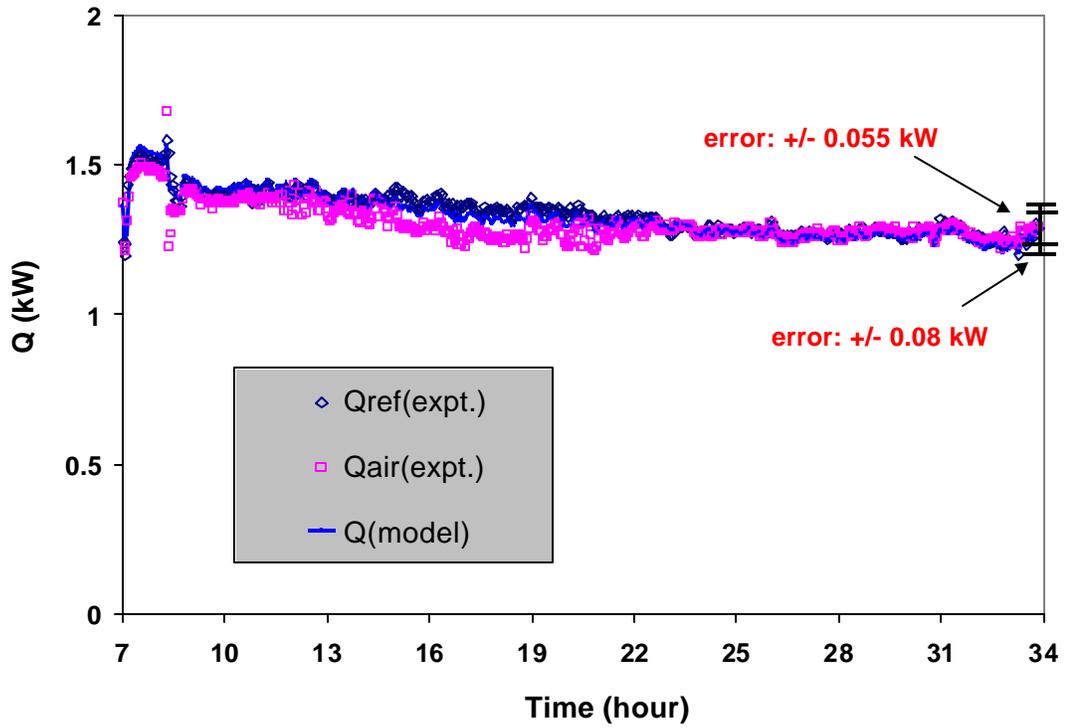
Figure D.41 Comparison of the total load for -20/-30/70/1.3/0.5
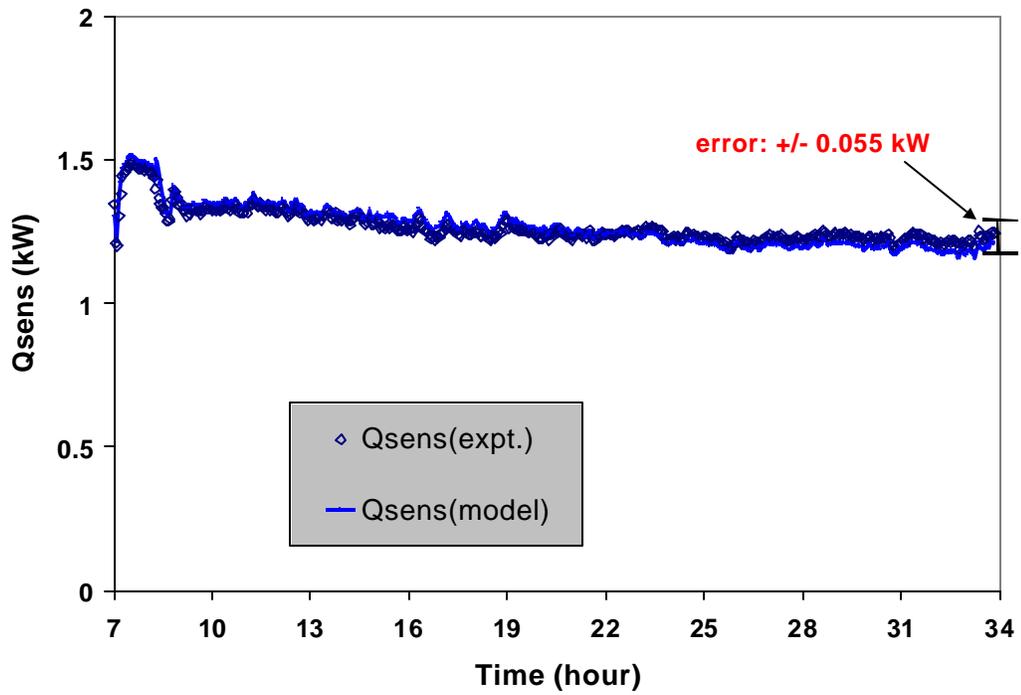
Figure D.42 Comparison of the sensible load for -20/-30/70/1.3/0.5
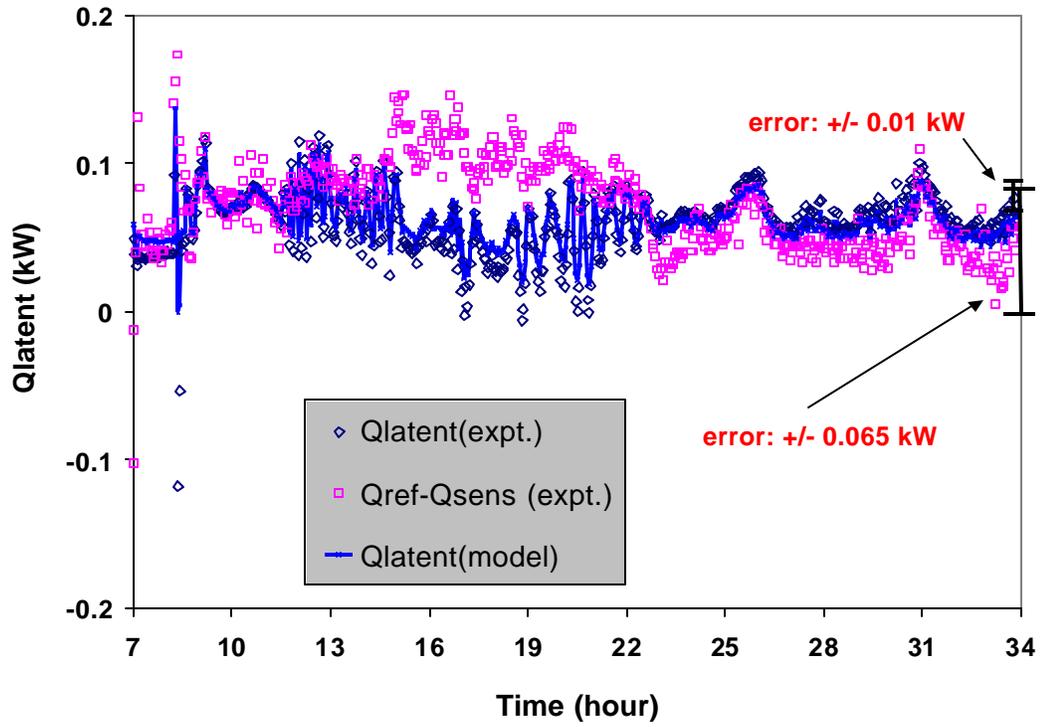
Figure D.43 Comparison of the latent load for -20/-30/70/1.3/0.5
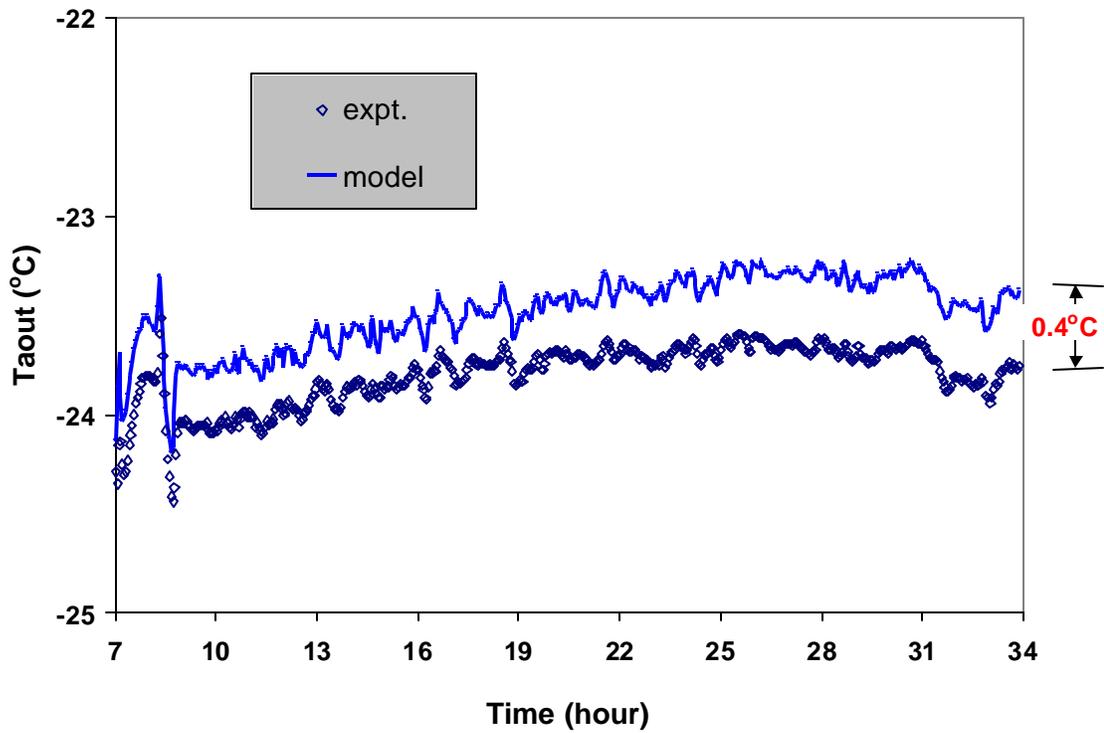
Figure D.44 Comparison of the air outlet temperature for -20/-30/70/1.3/0.5
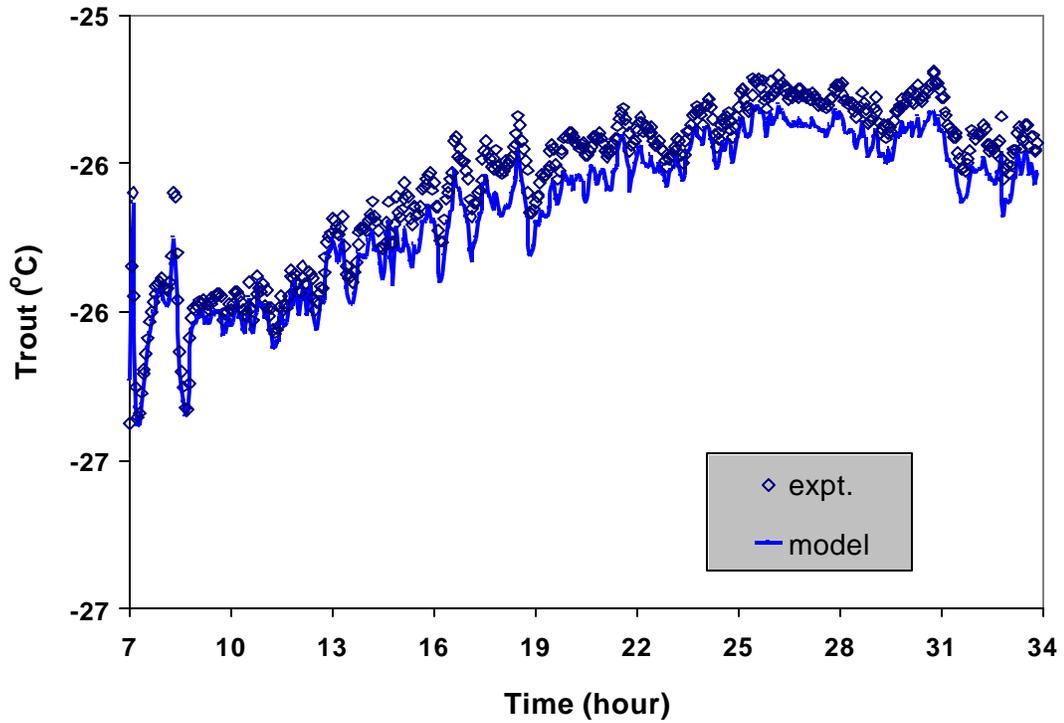
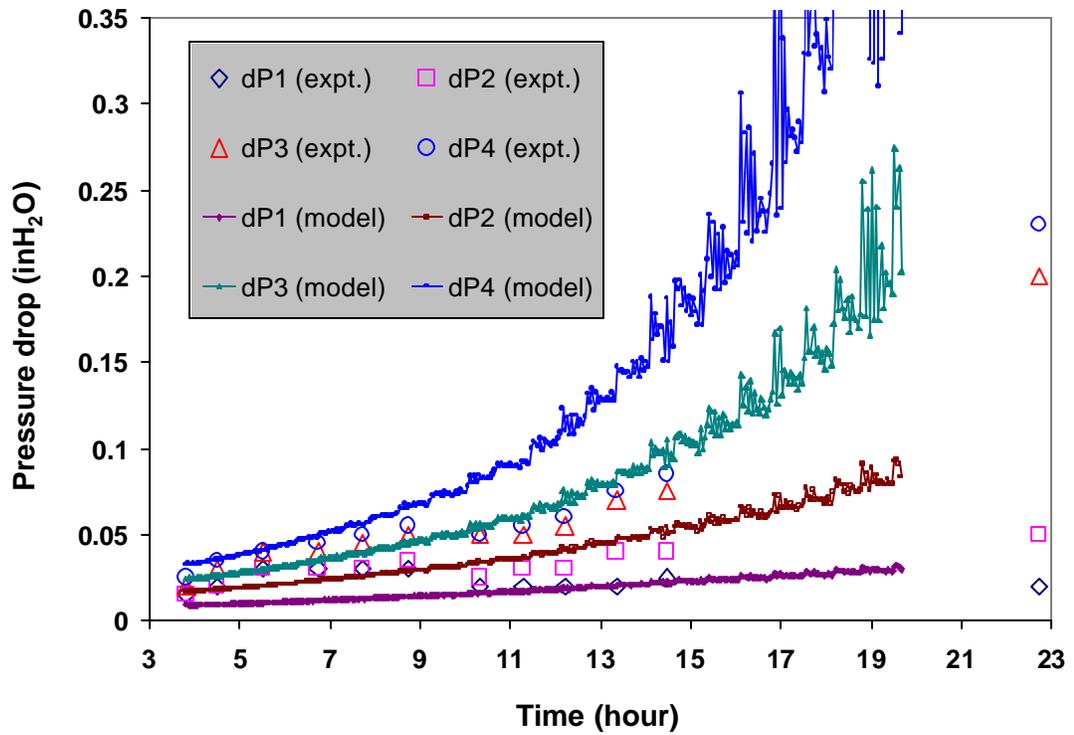Figure D.45 Comparison of the refrigerant outlet temperature for -20/-30/70/1.3/0.5
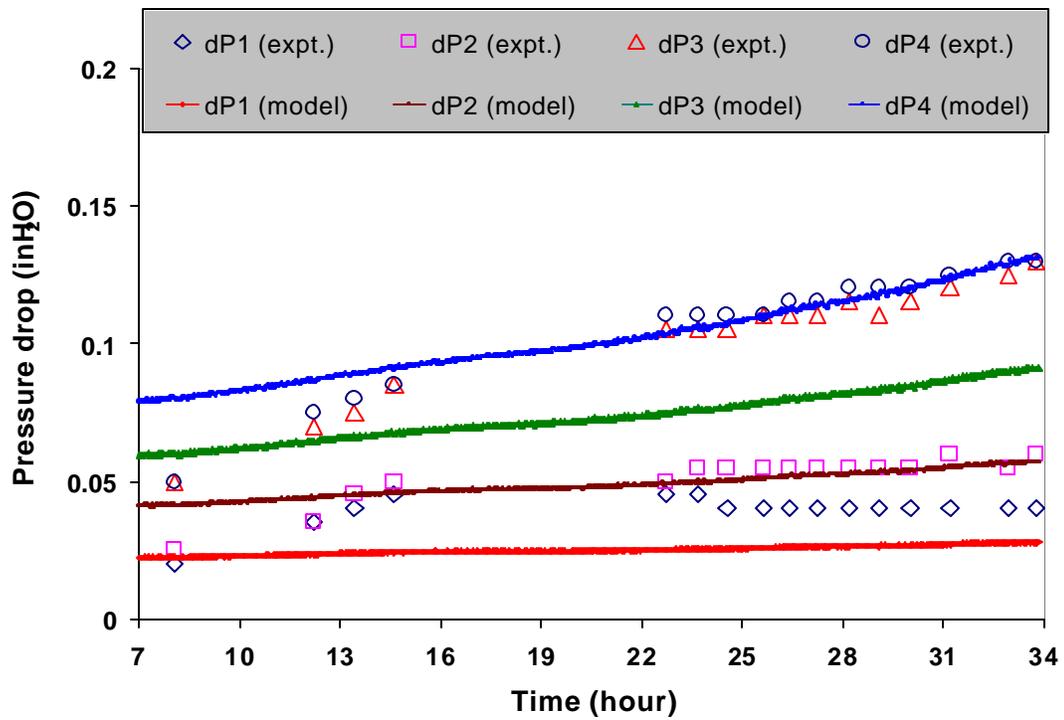
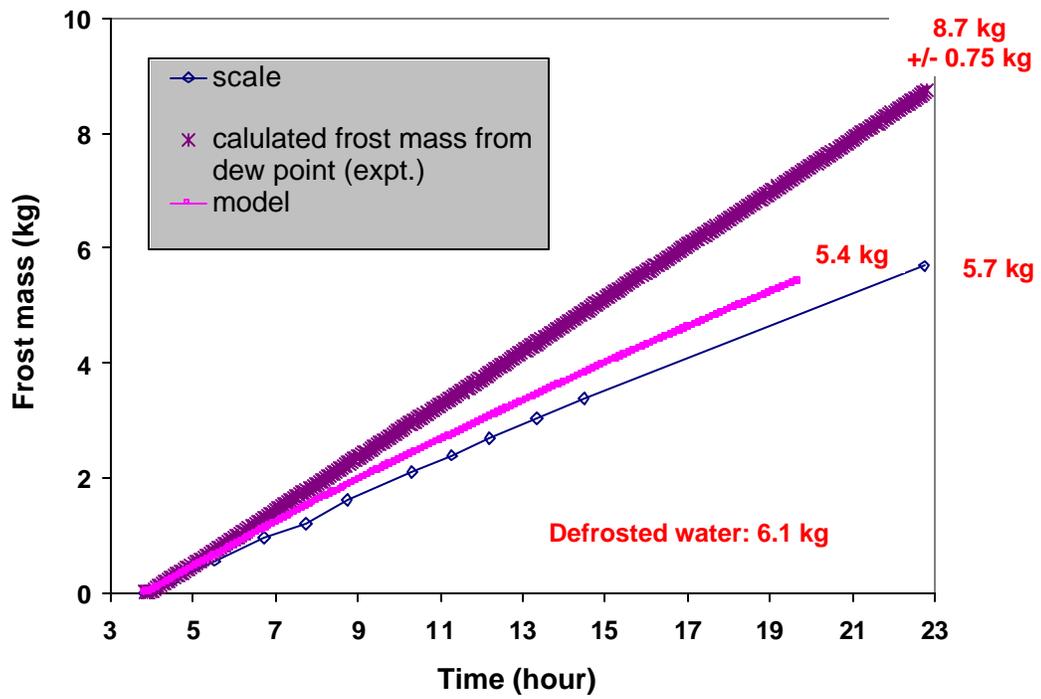Figure D.46 Comparison of the air side pressure drop for -20/-30/70/1.3/0.5
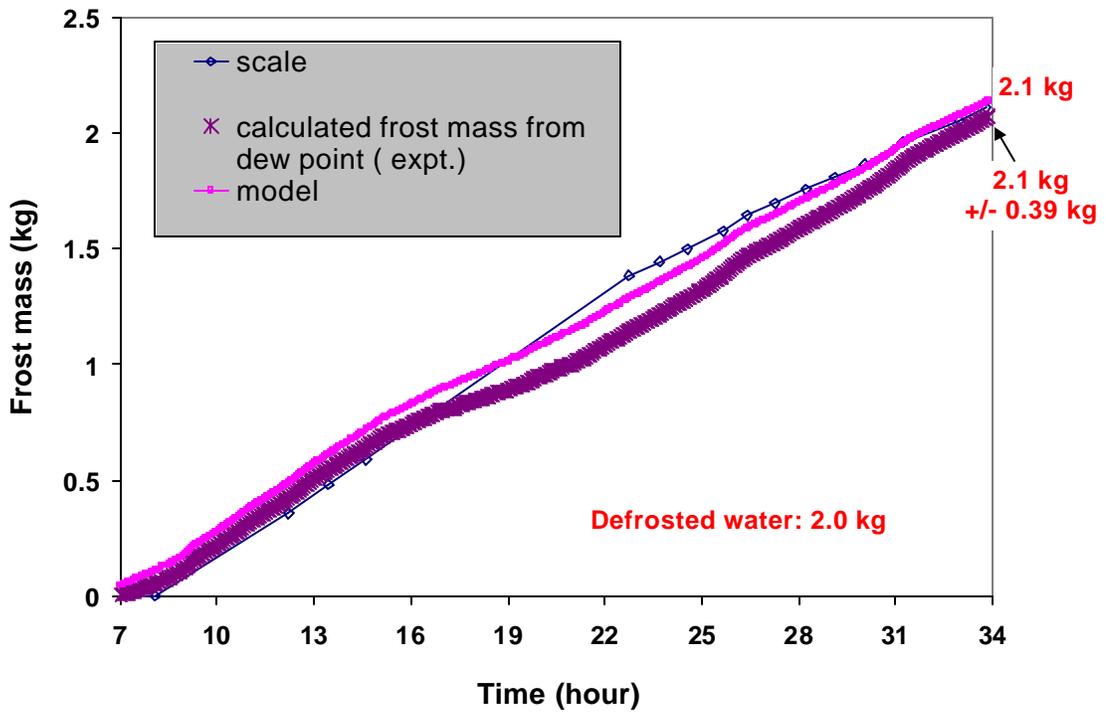
Figure D.47 Comparison of the frosting rate for -20/-30/70/1.3/0.5
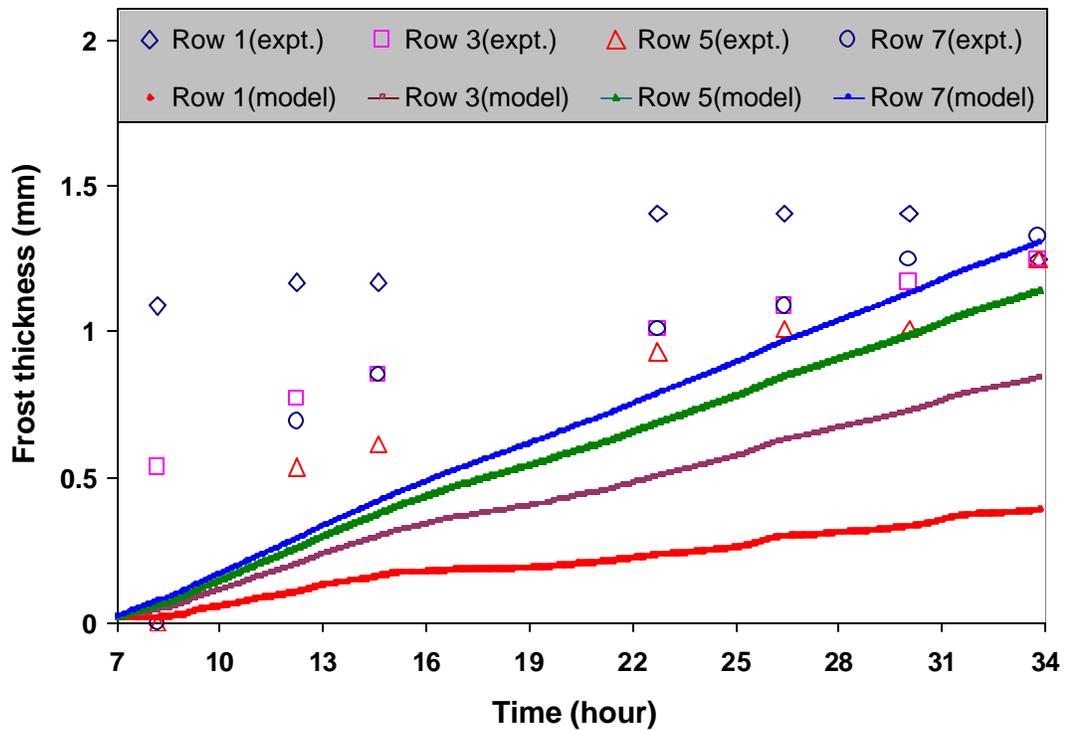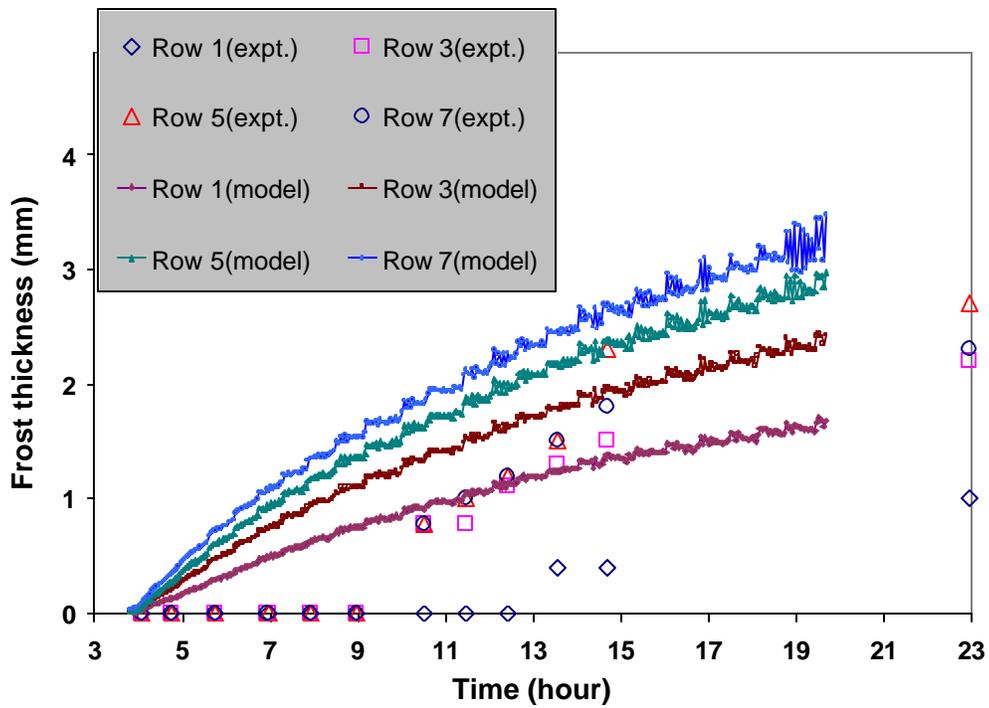

Figure D.48 Comparison of the frost thickness for -20/-30/70/1.3/0.5

D.7 Validation results for 0/-10/90/0.9/0.5

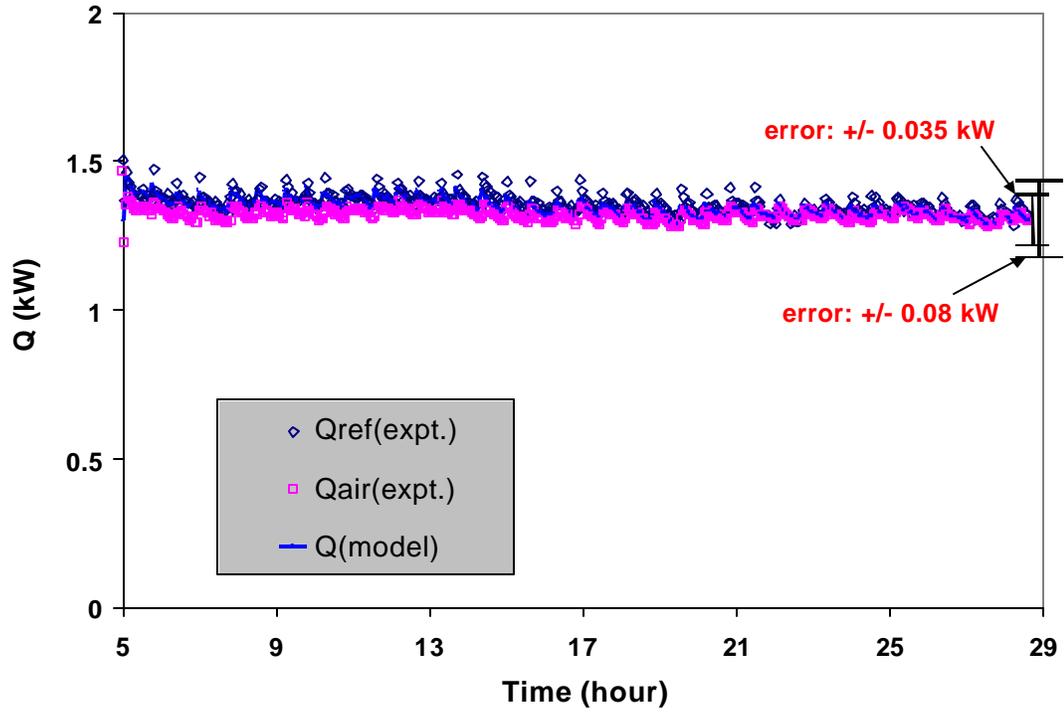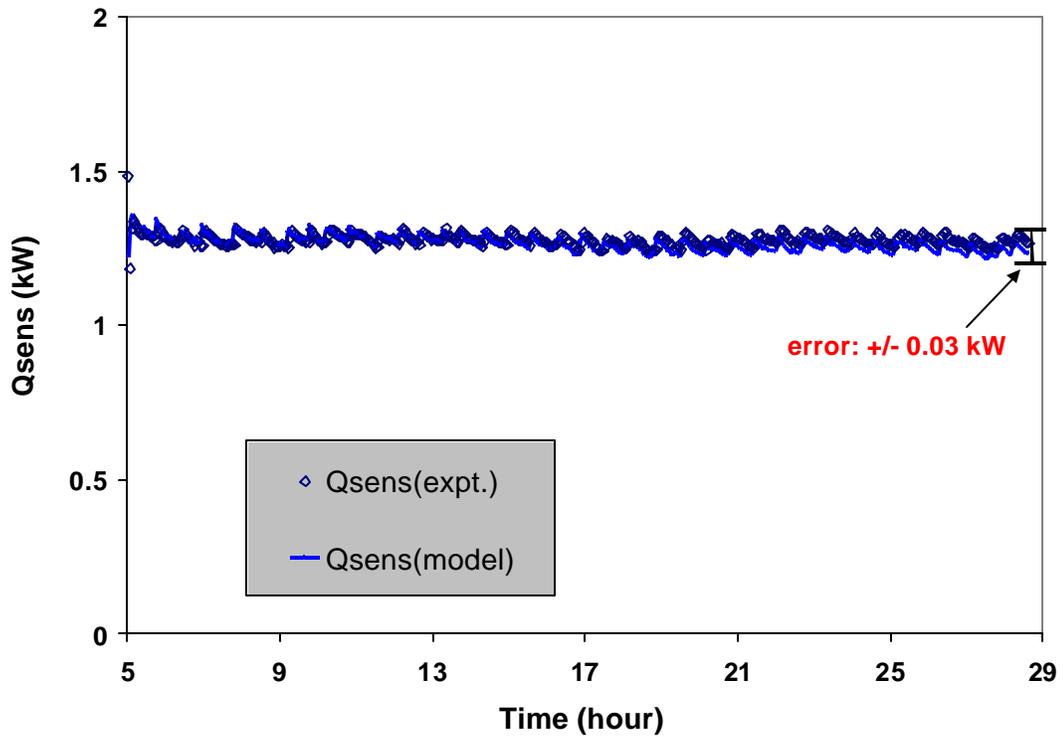Figure D.49 Comparison of the total load for 0/-10/90/0.9/0.5

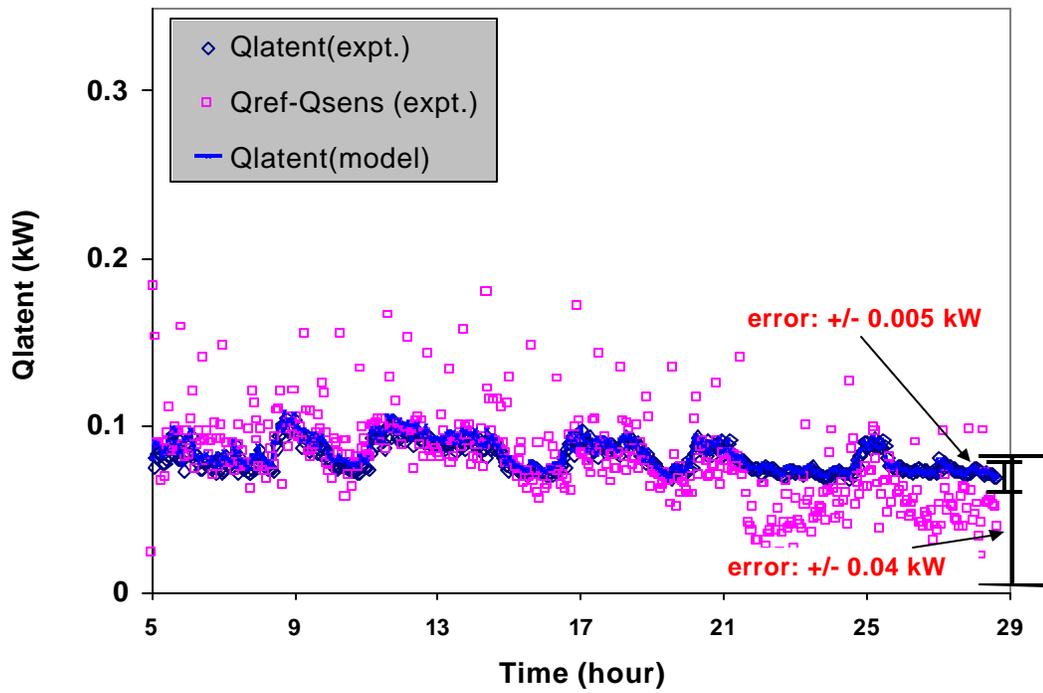Figure D.50 Comparison of the sensible load for 0/-10/90/0.9/0.5

95

Figure D.51 Comparison of the latent load for 0/-10/90/0.9/0.5

Figure D.52 Comparison of the air outlet temperature for 0/-10/90/0.9/0.5

Figure D.53 Comparison of the refrigerant outlet temperature for 0/-10/90/0.9/0.5

Figure D.54 Comparison of the air side pressure drop for 0/-10/90/0.9/0.5

Figure D.55 Comparison of the frosting rate for 0/-10/90/0.9/0.5

Figure D.56 Comparison of the frost thickness for 0/-10/90/0.9/0.5

D.8 Validation results for 0/-10/80/0.9/0.5

Figure D.57 Comparison of the total load for 0/-10/80/0.9/0.5

Figure D.58 Comparison of the sensible load for 0/-10/80/0.9/0.5

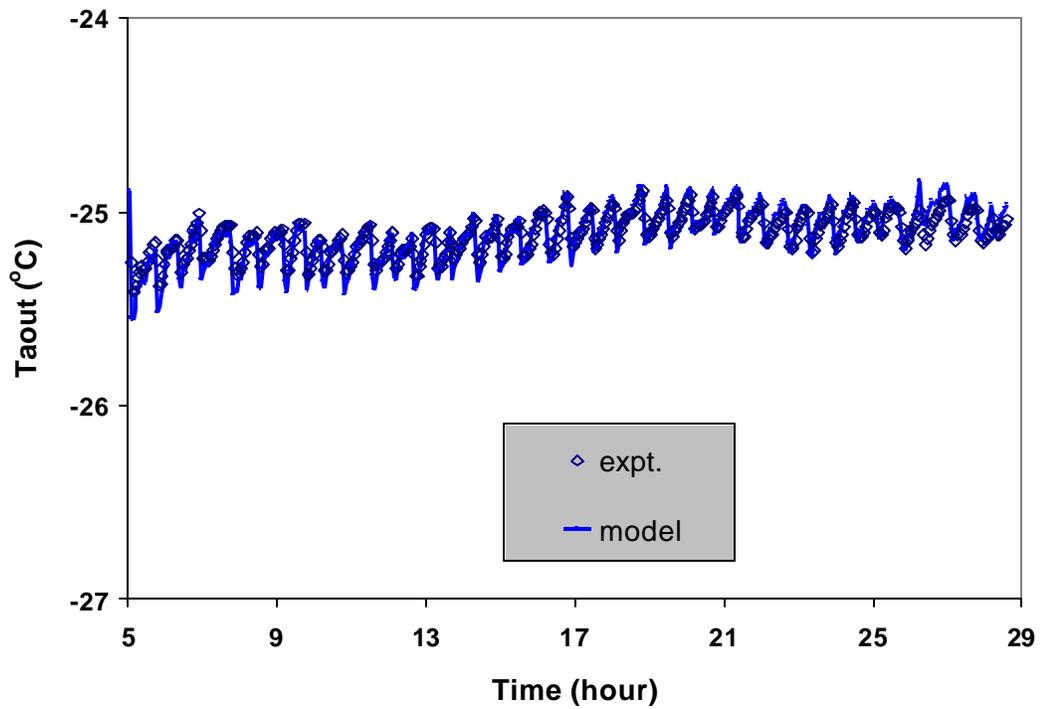Figure D.59 Comparison of the latent load for 0/-10/80/0.9/0.5

Figure D.60 Comparison of the air outlet temperature for 0/-10/80/0.9/0.5
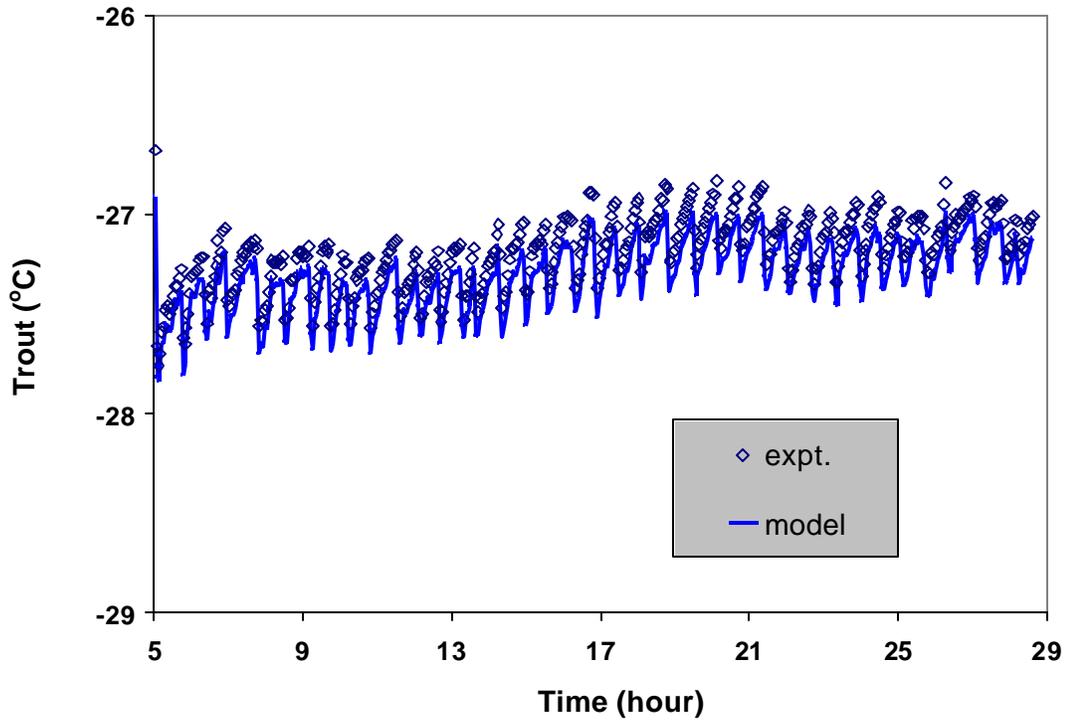
Figure D.61 Comparison of the refrigerant outlet temperature for 0/-10/80/0.9/0.5

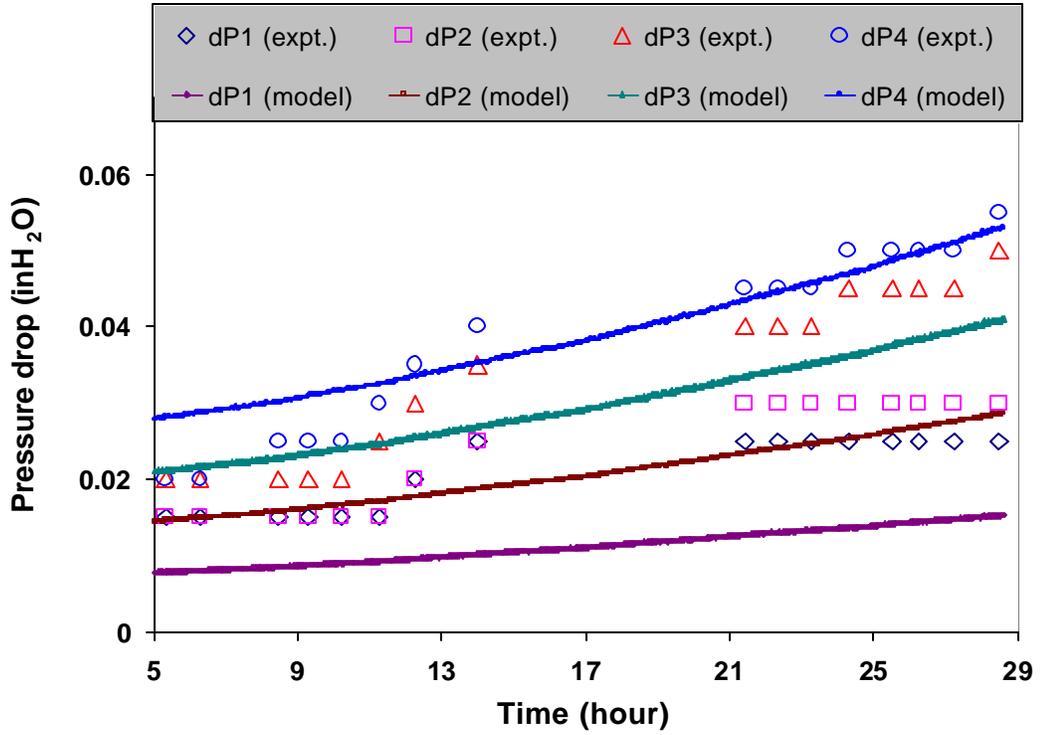

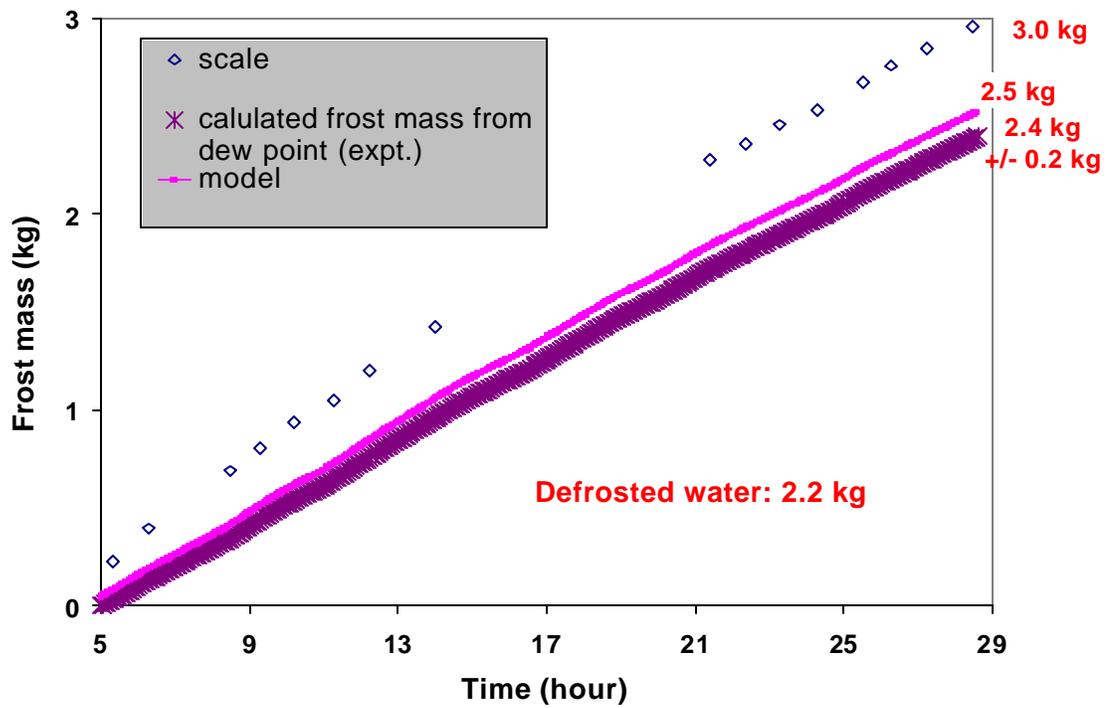Figure D.62 Comparison of the air side pressure drop for 0/-10/80/0.9/0.5

Figure D.63 Comparison of the frosting rate for 0/-10/80/0.9/0.5

Figure D.64 Comparison of the frost thickness for 0/-10/80/0.9/0.5

D.9 Validation results for 0/-10/70/0.9/0.5

Figure D.65 Comparison of the total load for 0/-10/70/0.9/0.5

Figure D.66 Comparison of the sensible load for 0/-10/70/0.9/0.5

Figure D.67 Comparison of the latent load for 0/-10/70/0.9/0.5

Figure D.68 Comparison of the air outlet temperature for 0/-10/70/0.9/0.5

Figure D.69 Comparison of the refrigerant outlet temperature for 0/-10/70/0.9/0.5

Figure D.70 Comparison of the air side pressure drop for 0/-10/70/0.9/0.5

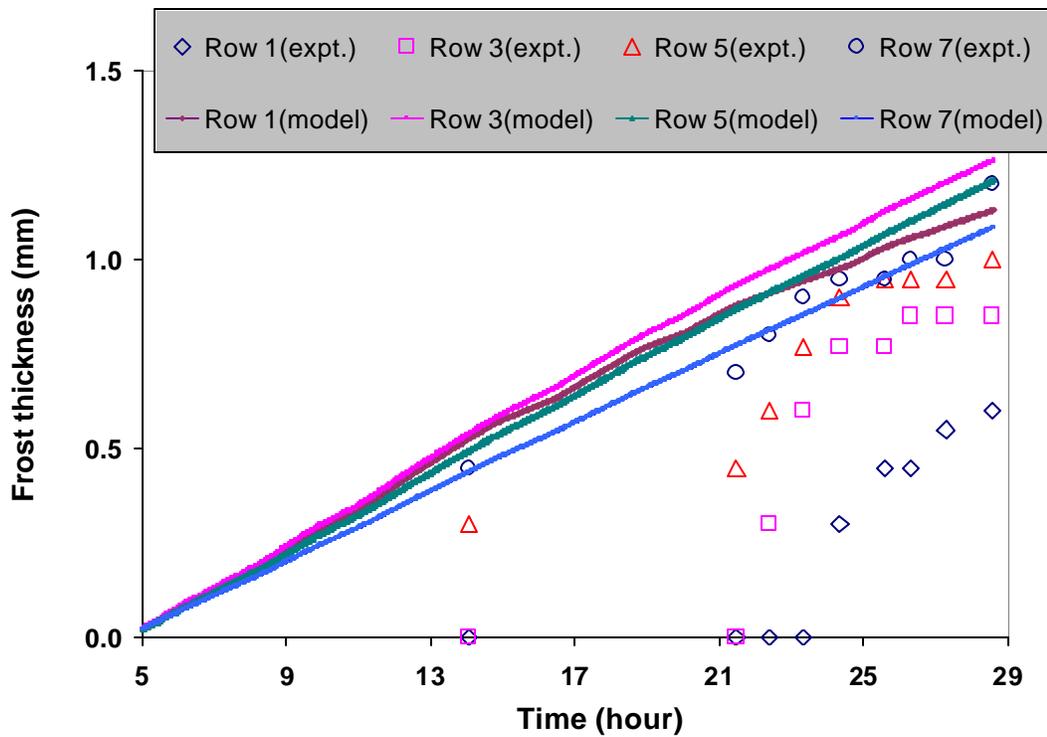Figure D.71 Comparison of the frosting rate for 0/-10/70/0.9/0.5

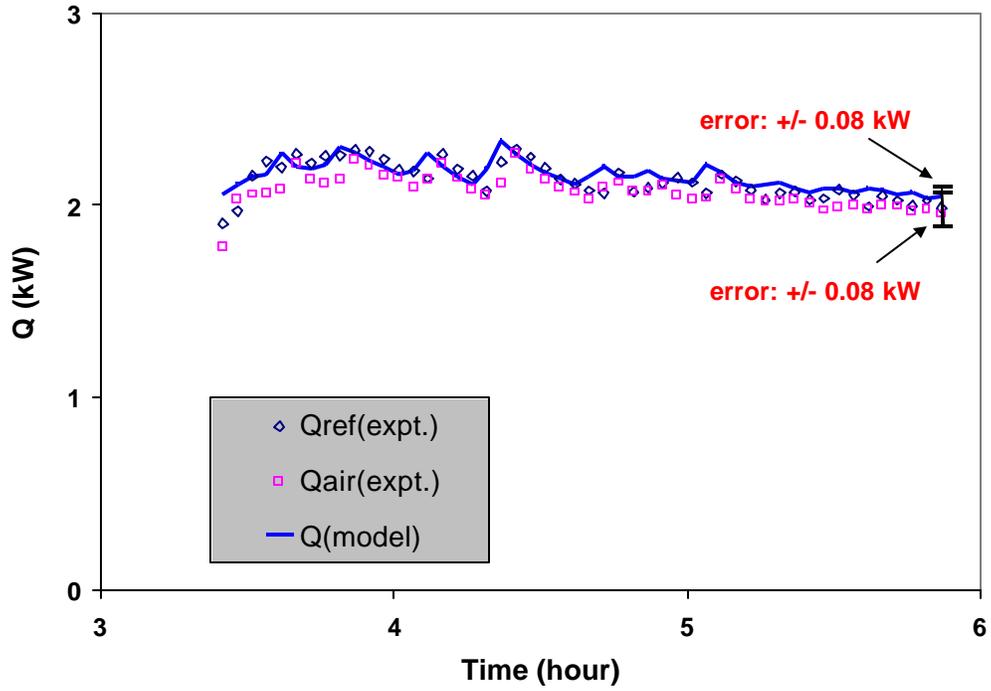Figure D.72 Comparison of the frost thickness for 0/-10/70/0.9/0.5

Figure D.73 Comparison of the total load for -20/-30/70/0.9/0.5
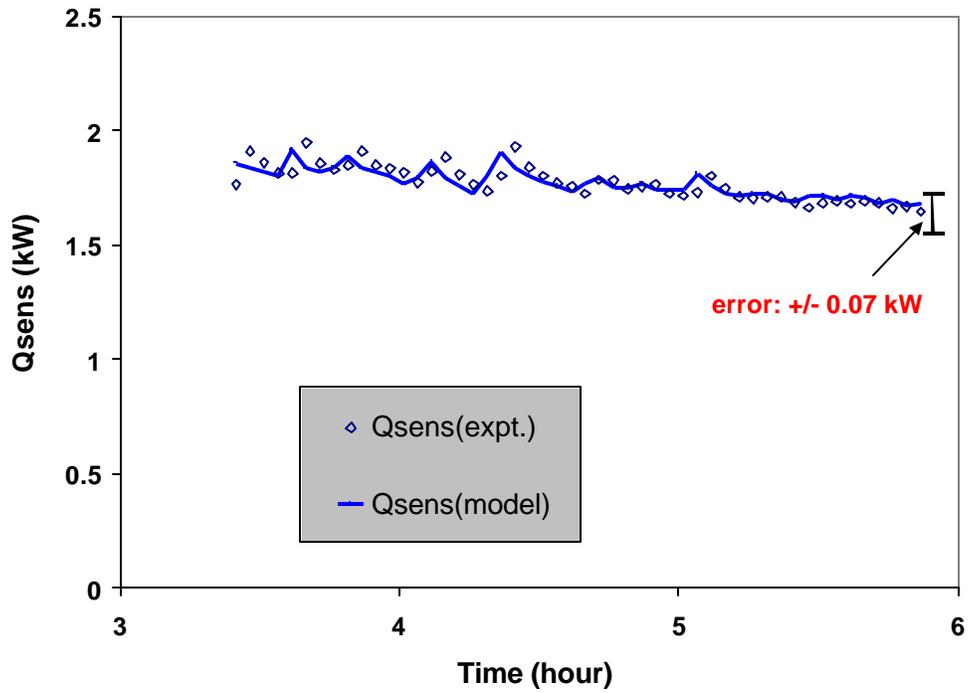

Figure D.74 Comparison of the sensible load for -20/-30/70/0.9/0.5
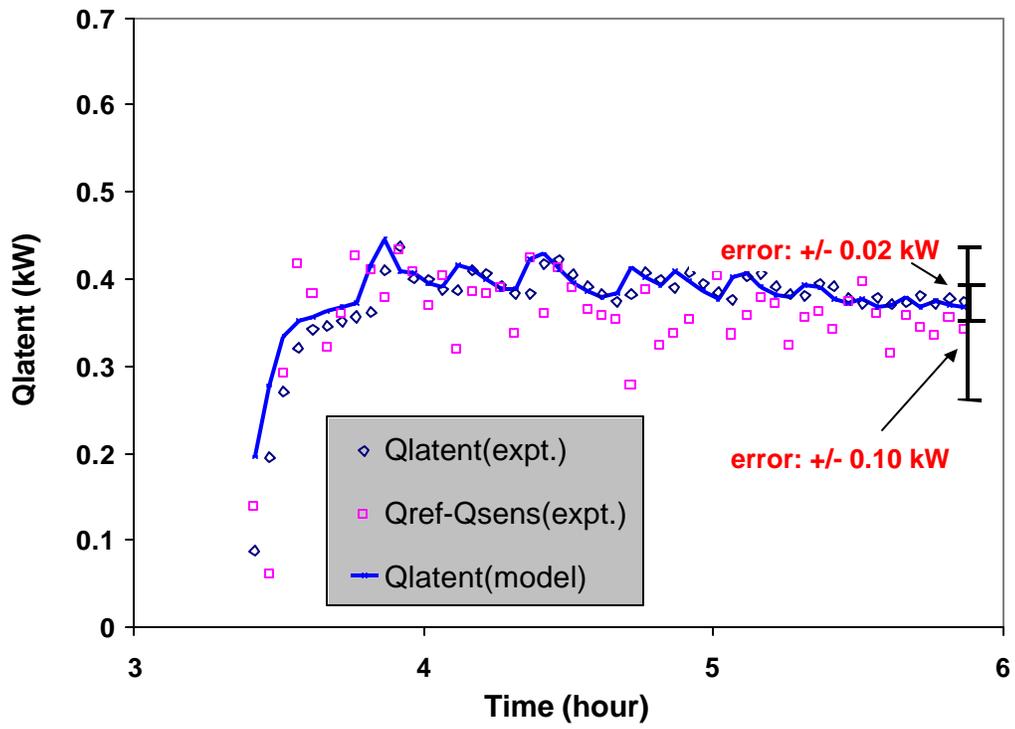
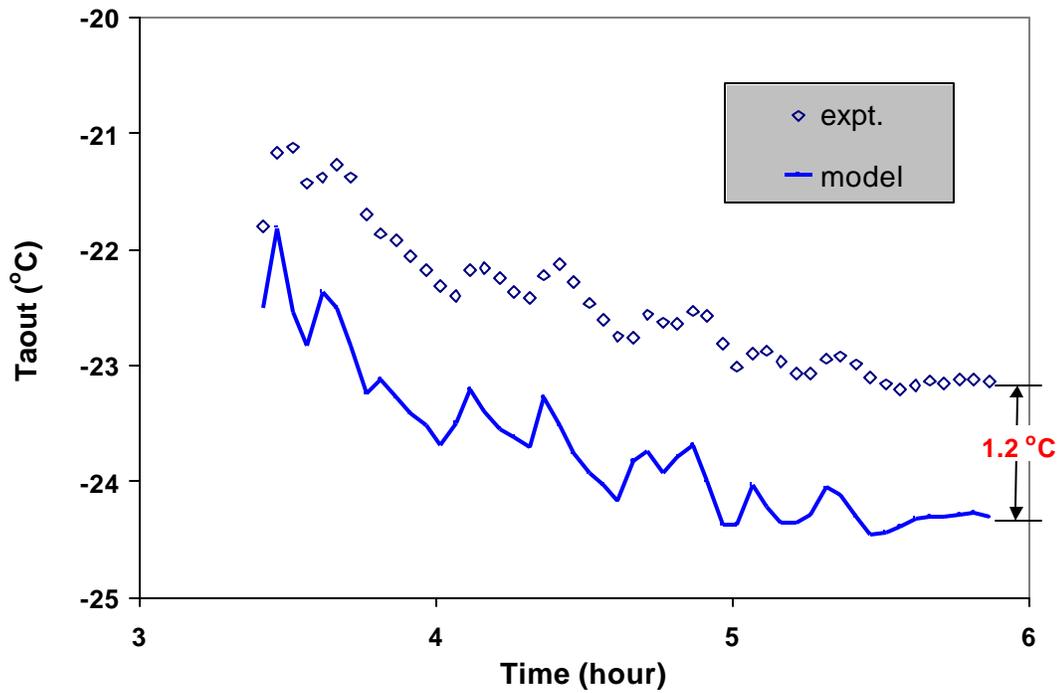Figure D.75 Comparison of the latent load for -20/-30/70/0.9/0.5

Figure D.76 Comparison of the air outlet temperature for -20/-30/70/0.9/0.5

Figure D.77 Comparison of the refrigerant outlet temperature for -20/-30/70/0.9/0.5

Figure D.78 Comparison of the air side pressure drop for -20/-30/70/0.9/0.5

Figure D.79 Comparison of the frosting rate for -20/-30/70/0.9/0.5

Figure D.80 Comparison of the frost thickness for -20/-30/70/0.9/0.5

D.11 Validation results for -8/-32/90/0.6/0.5

Figure D.81 Comparison of the total load for -8/-32/90/0.6/0.5

Figure D.82 Comparison of the sensible load for -8/-32/90/0.6/0.5

111

Figure D.83 Comparison of the latent load for -8/-32/90/0.6/0.5

Figure D.84 Comparison of the air outlet temperature for -8/-32/90/0.6/0.5
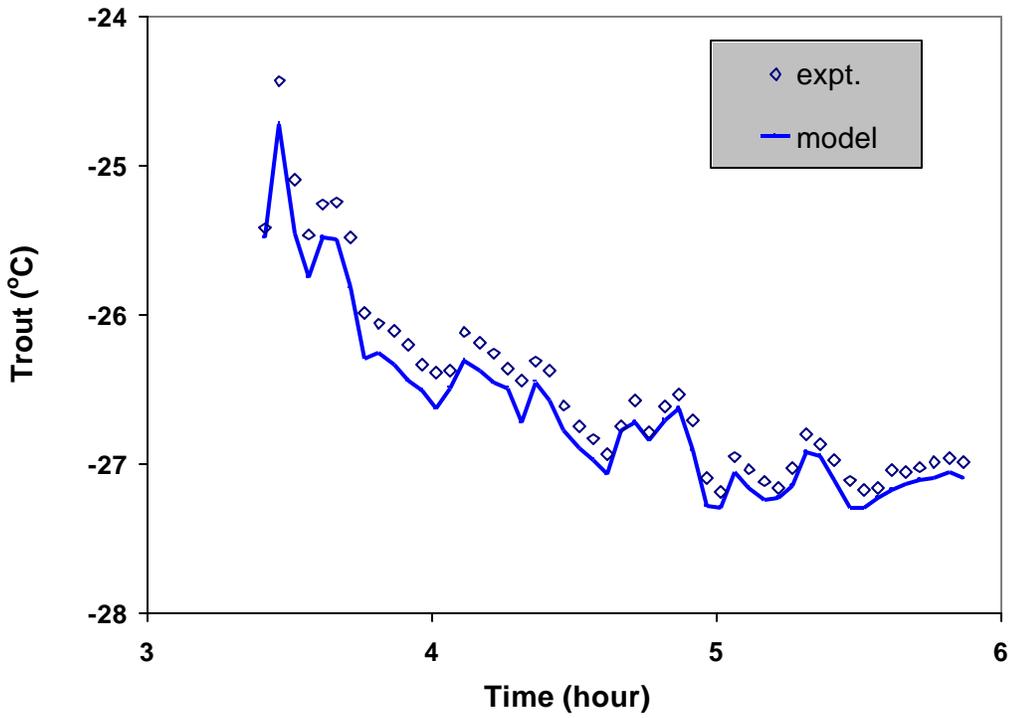
Figure D.85 Comparison of the refrigerant outlet temperature for -8/-32/90/0.6/0.5
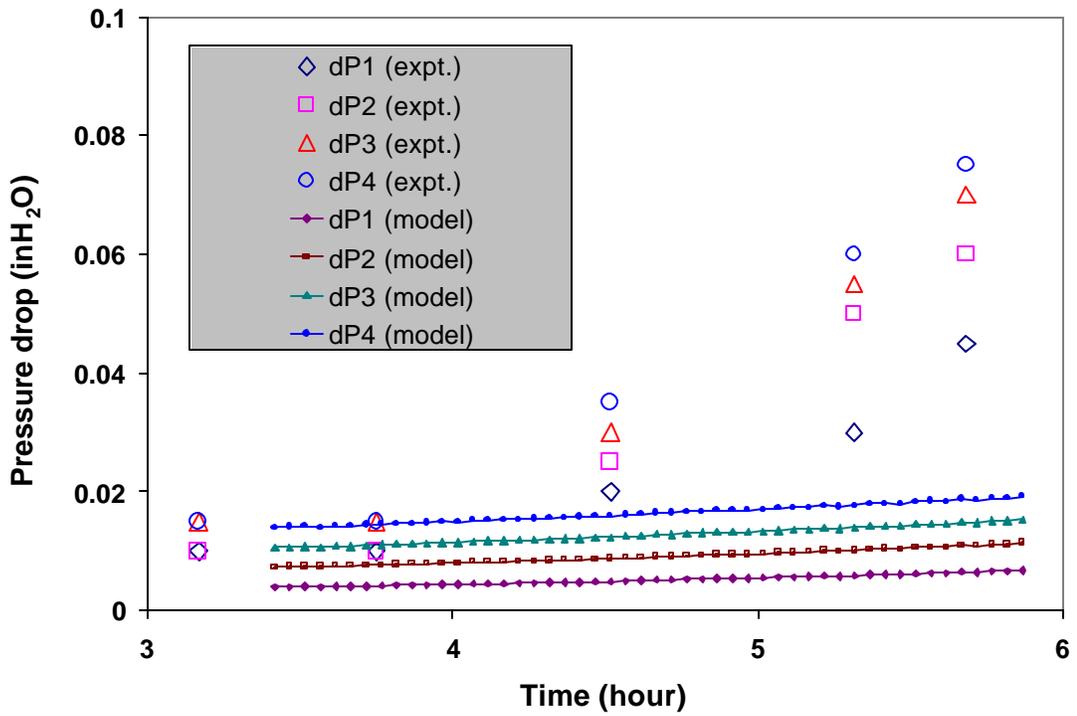

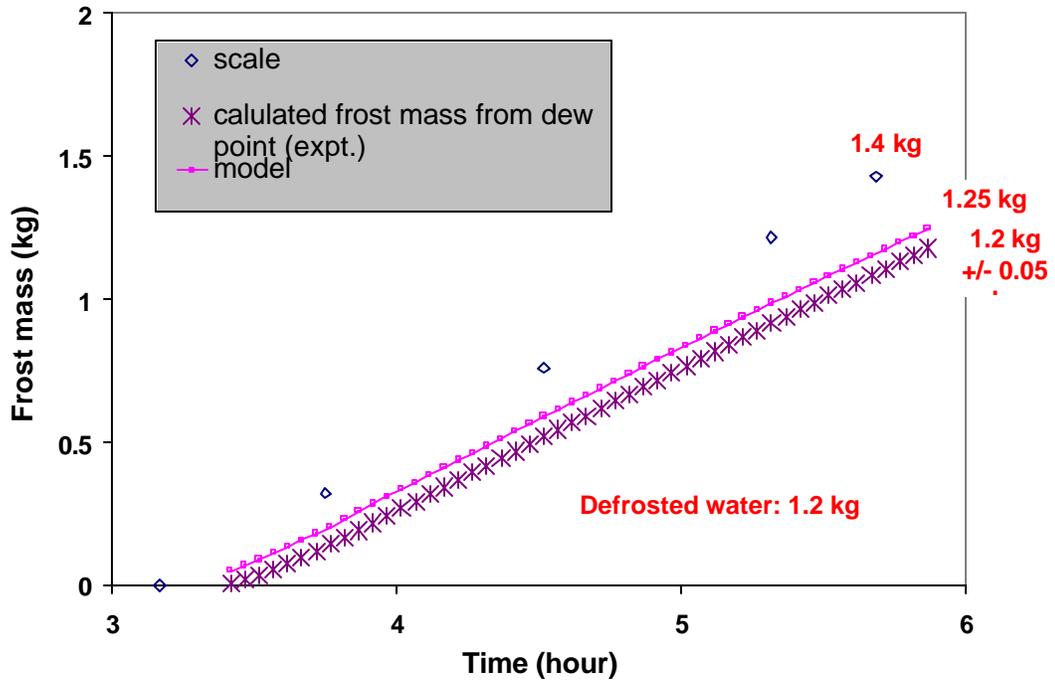Figure D.86 Comparison of the air side pressure drop for -8/-32/90/0.6/0.5

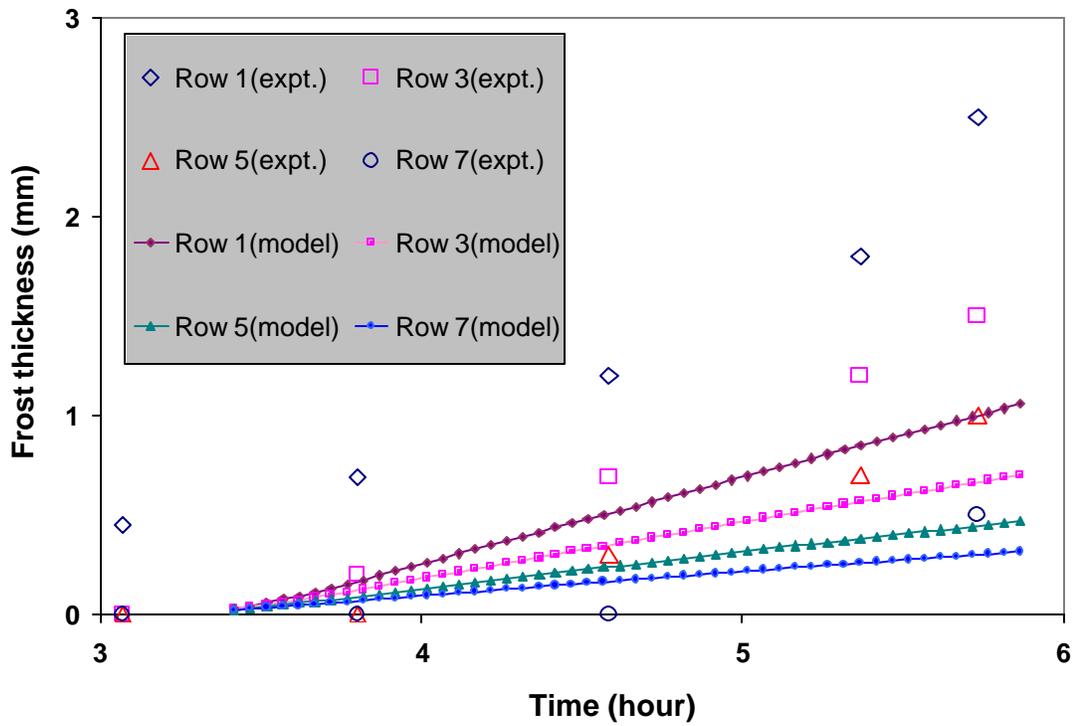Figure D.87 Comparison of the frosting rate for -8/-32/90/0.6/0.5

Figure D.88 Comparison of the frost thickness for -8/-32/90/0.6/0.5